การใช้ประโยชน์จากมีเทนและคาร์บอนไดออกไซด์ในการผลิตกระแสไฮโดรเจนเข้มข้น

นายธีระทัศน์ ศักดิ์วราธรณ์

วิทยานิพนธ์นี้เป็นส่วนหนึ่งของการศึกษาตามหลักสูตรปริญญาวิทยาศาสตรดุษฎีบัณฑิต
สาขาวิชาเคมีเทคนิค ภาควิชาเคมีเทคนิค
คณะวิทยาศาสตร์ จุฬาลงกรณ์มหาวิทยาลัย
ปีการศึกษา 2557

UTILIZATION OF METHANE AND CARBON DIOXIDE TO PRODUCE HYDROGEN-RICH STREAM

Mr. Theerathad Sakwarathorn

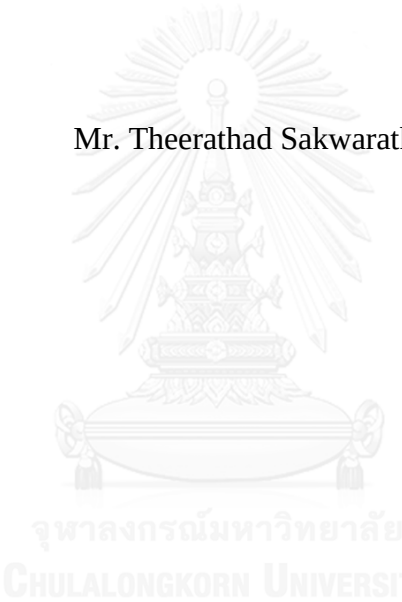

A Dissertation Submitted in Partial Fulfillment of the Requirements
for the Degree of Doctor of Philosophy Program in Chemical Technology
Department of Chemical Technology
Faculty of Science
Chulalongkorn University
Academic Year 2014

Thesis Title	UTILIZATION OF METHANE AND CARBON DIOXIDE TO PRODUCE HYDROGEN-RICH STREAM
By	Mr. Theerathad Sakwarathorn
Field of Study	Chemical Technology
Thesis Advisor	Associate Professor Nuttaya Pongstabodee, Ph.D.
Thesis Co-Advisor	Associate Professor Viwat Vchirawongkwin, Dr.rer.nat.
	Professor Bernd Michael Rode, Dr.rer.nat.

Accepted by the Faculty of Science, Chulalongkorn University in Partial Fulfillment of the Requirements for the Doctoral Degree

.....Dean of the Faculty of Science
(Professor Supot Hannongbua, Dr.rer.nat.)

THESIS COMMITTEE

.....Chairman
(Associate Professor Kejvalee Pruksathorn, Ph.D.)
.....Thesis Advisor
(Associate Professor Nuttaya Pongstabodee, Ph.D.)
.....Thesis Co-Advisor
(Associate Professor Viwat Vchirawongkwin, Dr.rer.nat.)
.....Thesis Co-Advisor
(Professor Bernd Michael Rode, Dr.rer.nat.)
.....Examiner
(Professor Tharapong Vitidsant, Ph.D.)
.....Examiner
(Assistant Professor Prasert Reubroycharoen, Ph.D.)
.....External Examiner
(Siriphong Rojluechai, Ph.D.)

ธีระทัศน์ ศักดิ์วราธรณ์ : การใช้ประโยชน์จากมีเทนและคาร์บอนไดออกไซด์ในการผลิตกระแสไฮโดรเจนเข้มข้น (UTILIZATION OF METHANE AND CARBON DIOXIDE TO PRODUCE HYDROGEN-RICH STREAM) อ.ที่ปรึกษาวิทยานิพนธ์หลัก: ณัฐธยาน์ พงศ์สถาบดี, อ.ที่ปรึกษาวิทยานิพนธ์ร่วม: วิวัฒน์ วชิรวงศ์กวิน, แบนด์ มิคาเอล โรเดอ, 194 หน้า.

ในงานวิจัยนี้ ศึกษาการผลิตไฮโดรเจนเข้มข้นจากปฏิกิริยารีฟอร์มมิงแบบแห้งโดยการใช้แก๊สเรือนกระจกเป็นสารตั้งต้น ซึ่งเป็นการใช้สารไฮโดรคาร์บอนจากบรรยากาศมาผลิตเป็นพลังงานและเป็นการลดการใช้ปริมาณไฮโดรคาร์บอนจากใต้พิภพเพื่อที่จะทำให้ภาวะโลกร้อนไม่รุนแรงไปมากกว่าปัจจุบัน ในกระบวนการกำจัดแก๊สคาร์บอนมอนอกไซด์จากปฏิกิริยารีฟอร์มมิง จะถูกกำจัดไปโดยปฏิกิริยาวอเตอร์แก๊สชิฟท์และปฏิกิริยาออกซิเดชันแบบเลือกเกิดของคาร์บอนมอนอกไซด์ รวมทั้งการใช้การดูดซับคาร์บอนมอนอกไซด์ด้วยน้ำเพื่อให้มีค่าคาร์บอนมอนอกไซด์ขาออกให้อยู่ในระดับต่ำ นอกจากนี้ยังมีการใช้การออกแบบการจำลองและวิเคราะห์ความแปรปรวนของข้อมูลเพื่อหาปัจจัยที่มีนัยสำคัญต่อปฏิกิริยา พร้อมทั้งหาค่าที่เหมาะสมที่สุดในการควบคุมแต่ละปฏิกิริยา ในปฏิกิริยารีฟอร์มมิงแบบแห้ง ตัวเร่งปฏิกิริยา 5%Ni-0.5%Mn/CeO_2 จะถูกนำมาทดสอบเพื่อหาค่าที่เหมาะสมที่สุดในการควบคุมซึ่งอยู่ที่อุณหภูมิ 820 องศาเซลเซียส สัดส่วนของมีเทนขาเข้าเท่ากับ 0.5 น้ำหนักตัวเร่งปฏิกิริยา 0.1 กรัม และอัตราการป้อนรวมเท่ากับ 30 มิลลิลิตร/นาที จะให้ค่าร้อยละการเปลี่ยนของมีเทน ร้อยละการเปลี่ยนของคาร์บอนไดออกไซด์และร้อยละการเลือกเกิดของไฮโดรเจนเท่ากับ 70 60 และ 60 ตามลำดับ ในปฏิกิริยาวอเตอร์แก๊สชิฟท์จะใช้ตัวเร่งปฏิกิริยา 1%(1:1)AuFe/CeO_2 ค่าที่เหมาะสมในการควบคุมตัวแปรที่มีนัยสำคัญ ได้แก่ อุณหภูมิ 413 องศาเซลเซียส น้ำหนักตัวเร่งปฏิกิริยา 0.2 กรัม และปริมาณน้ำที่ป้อนเป็น 2 มิลลิลิตร/ชั่วโมง จะให้ค่าร้อยละการเปลี่ยนของคาร์บอนมอนอกไซด์และร้อยละผลได้ของไฮโดรเจนเท่ากับ 70 และ 50 ตามลำดับ ส่วนกระบวนการออกซิเดชันแบบเลือกเกิดจะใช้ตัวเร่งปฏิกิริยา 1%Au/CeO_2 มาทดสอบ ซึ่งจะให้ค่าที่เหมาะสมในการป้อนดังนี้ อุณหภูมิ 90 องศาเซลเซียส อัตราส่วนของออกซิเจนต่อคาร์บอนมอนอกไซด์เท่ากับ 1.5 และไม่มีปริมาณคาร์บอนไดออกไซด์มาในกระแสป้อน จะให้ร้อยละผลได้ของปฏิกิริยาอยู่ที่ 52 การศึกษาทุกกระบวนการตั้งแต่รีฟอร์มมิงแบบแห้ง วอเตอร์แก๊สชิฟท์ และออกซิเดชันแบบเลือกเกิด สามารถลดค่าปริมาณคาร์บอนมอนอกไซด์ขาออกให้อยู่ในเกณฑ์ที่น่าพอใจ แต่ปริมาณไฮโดรเจนมีค่าน้อยเกินไป ดังนั้นการใช้ปฏิกิริยาวอเตอร์แก๊สชิฟท์สองลำดับ จะทำให้ปริมาณร้อยละการเปลี่ยนของคาร์บอนมอนอกไซด์กับร้อยละผลได้ของไฮโดรเจนมีค่าสูงขึ้นเป็น 90 และ 75 ตามลำดับ จากนั้นนำแก๊สขาออกผ่านกระบวนการดูดซับคาร์บอนมอนอกไซด์ด้วยน้ำเพื่อลดปริมาณคาร์บอนมอนอกไซด์ออกไปอีก และทำการอธิบายถึงคาร์บอนมอนอกไซด์สามารถละลายน้ำได้บางส่วนเนื่องจากมีบางพฤติกรรมของคาร์บอนมอนอกไซด์ปฏิบัติตัวคล้ายกับคาร์บอนไดออกไซด์ที่มีความสามารถในการละลายน้ำได้ สุดท้ายนี้กระบวนการผลิตไฮโดรเจนในการวิจัยนี้ให้แก๊สขาออกคือ ไฮโดรเจนร้อยละ 30 ฮีเลียมร้อยละ 60 และแก๊สอื่น ๆ ร้อยละ 10 ในอัตราการไหลขาออกที่ 90 มิลลิลิตร/นาที

ภาควิชา เคมีเทคนิค ลายมือชื่อนิสิต .....

สาขาวิชา เคมีเทคนิค ลายมือชื่อ อ.ที่ปรึกษาหลัก .....

ปีการศึกษา 2557 ลายมือชื่อ อ.ที่ปรึกษาร่วม .....

ลายมือชื่อ อ.ที่ปรึกษาร่วม .....

5273897223 : MAJOR CHEMICAL TECHNOLOGY
KEYWORDS: DRY REFORMING OF METHANE / GREENHOUSE GASES / HYDROGEN PRODUCTION / CARBON MONOXIDE REMOVAL / OPTIMUM OPERATING

THEERATHAD SAKWARATHORN: UTILIZATION OF METHANE AND CARBON DIOXIDE TO PRODUCE HYDROGEN-RICH STREAM. ADVISOR: ASSOC. PROF. NUTTAYA PONGSTABODEE, Ph.D., CO-ADVISOR: ASSOC. PROF. VIWAT VCHIRAWONGKWIN, Dr.rer.nat., PROF. BERND MICHAEL RODE, Dr.rer.nat., 194 pp.

In this research, the hydrogen production of dry reforming reaction via utilization of methane and carbon dioxide was studied. The dry reforming reaction has the advantage of reducing greenhouse gases. Other advantages are the recycle of hydrocarbons from the atmosphere to produce energy source as hydrogen, and reduce a releasing of hydrocarbons from earth drilling for fossil fuel in order to keep global warming crisis less severe than the present. Carbon monoxide from the reforming reaction will be eliminated by water gas shift reaction, preferential oxidation and carbon monoxide adsorption by water in order to reduce a carbon monoxide level. To get the maximum performance, experimental design and analysis of variance will be used to investigate significant factors; moreover, the optimum condition will be found. In the dry reforming reaction, 5%Ni-0.5%Mn/CeO_2 catalysts was tested to find the suitable condition including temperature of 820 °C, the methane fraction of 0.5, 0.1 g of catalysts weight and 30 ml/min of total feed rate given CH_4 conversion, CO_2 conversion and H_2 selectivity of 70%, 60% and 60%, respectively. The water gas shift reaction, the 1%(1:1)AuFe/CeO_2 catalyst was selected to study for experimental design. Significant factors are controlled an appropriate range of temperature 413 °C, catalyst weight of 0.2 g and water feed rate of 2 ml/h, presenting CO conversion and H_2 yield were 70% and 50%, respectively. The preferential oxidation reaction, the 1%Au/CeO_2 catalyst was investigated an optimum condition that give 90 °C, O_2/CO ratio of 1.5, and no amount of carbon dioxide in the feed stream. It gave a yield of the reaction around 52%. Integration process (DRM, WGS and PROX) can reduce the amount of carbon monoxide level into satisfactory range, but hydrogen composition is less. Thus, double stage of the water gas shift was performed to improve the performance, which gives that CO conversion and H_2 conversion increased to 90% and 75%, respectively. Then the outlet gas passed through water trap to further remove carbon monoxide. A small amount of carbon monoxide can be dissolved in water because some of its behavior similar to carbon dioxide. This research work, finally showed outlet gas component consisted of 30% H_2, 60% He, and 10% others with total flow rate around 90 ml/min.

Department:	Chemical Technology	Student's Signature	.....
Field of Study:	Chemical Technology	Advisor's Signature	.....
Academic Year:	2014	Co-Advisor's Signature	.....
		Co-Advisor's Signature	.....

ACKNOWLEDGEMENTS

I would like to express my deeply gratitude to my adviser, Associate Professor Dr. Nuttaya Pongstabodee for benefit tremendously from her emphasis on critical thinking and encouragements to innovate. I also would like to thanks Associate Professor Dr. Viwat Vchirawongkwin for his invaluable guidance, knowledge, suggestion and encouragement during my candidature. Furthermore, I would like to thank Associate Professor Dr. Kejvalee Pruksathorn, Professor Dr. Tharapong Vitidsant, Assistance Professor Dr. Prasert Reubroycharoen, and Dr. Siriphong Rojluechai for serving as chairman and thesis committees, whose comments were constructively and especially helpful. Moreover, I have to deeply thank to Professor Dr. Bernd Michael Rode and Associate Professor Dr. Thomas Hofer from University of Innsbruck, Austria, for their kindness to develop my experimental aspect and training several useful program.

Special thanks to The Royal Golden Jubilee Ph.D Program The Thailand Research Fund (RGJ.TRF.) and Mrs. Prapasri Jaruwattana Felser for funding research and general expense. Thanks to Department of Chemical technology, and Petroleum and Petrochemical College, Chulalongkorn University for their supporting the equipment and instrument.

Last but not least, I would like to sincere thank to Dr. Sutarawadee Monyanon for her helping hands, cheers up, and supports very much kind of things from start until finish of my Ph.D graduate for a long time. And also kindly thanks to Dr. Supachita Krerkkaiwan, Dr. Kitima Pinkeaw, Dr. Sakdinun Nuntang, Dr. Sasithorn Sunphorka, Dr. Supaporn Khangkham, Dr. Sompoch Pooperasupong, Dr. Nathavat Romyen and other friends for the best friendship.

Finally, I would like to dedicate this thesis to the memory of my parents and my family, who generous supported and encouraged me through the year spent on this study. I hope they would have been proud.

CONTENTS

Page

Page

Page

LIST OF FIGURES

Page

LIST OF TABLES

Page

CHAPTER 1

INTRODUCTION

1.1 Rationale

Assessment of energy demand by the International Energy Agency (1) found that the global demand for energy will increase from 85 million barrels/day to 91 million barrels/day and 107 million barrels/day in year 2015 and 2030, respectively. In addition, higher oil prices to consumers, particularly industrial and electric power. The seeking alternative fuels would have to consider the nature of the demand for fuel efficiency, comfortable to use, etc. In the future, renewable fuels will play an important role in agriculture countries. United States has produced hydrogen about 9 million tons/year, and around the world already produces 50 tons/year. The hydrogen can be used as precursors for the production of oil and chemical materials such as feedstock for ammonia production, methanol and hydrogen chloride. Liquid hydrogen is used as rocket fuel, ingredient in a nuclear reaction. As well as in the production of fertilizer, glass, metal soaps, oils, vitamins, cosmetics, electrical circuits, etc. Hydrogen as a fuel in the combustion process is a product that only water vapor and heat, which is not only polluting the environment.

From many research, the raw material which used to as a reactant to produce hydrogen are divided into 2 groups, including liquid-hydrocarbons such as methanol or ethanol and gas-hydrocarbons such as methane or ethane. These hydrocarbons can be catalytically transformed into hydrogen by reforming process. In general, nickel base catalyst is most widely used because they are cheap. Carbon monoxide is the product from this reaction same as hydrogen. The amount of carbon monoxide is an important factor for catalysts in fuel cell; however, carbon monoxide can be removed

by water gas shift and preferential oxidation process. Three processes including reforming, water gas shift and preferential oxidations are called the fuel processor as shown in Figure 1.1. This research will focus on the study of hydrocarbon conversion and carbon monoxide reduction, also known as the fuel processor, including the catalytic performance, the operating factor that controls the system.

The computational simulation of quantum mechanical charge field molecular dynamics (QMCF MD) is an interesting tool for observing a behavior of chemical material in a reaction. Computer simulations have become a popular for molecular dynamics design to solvate microspecies—molecule interaction and the acting force on other molecule. In this research, to purify the hydrogen rich stream, the more effluent is able to be routed to the water and then apply QMCF MD to determine the feasible of carbon monoxide in water.

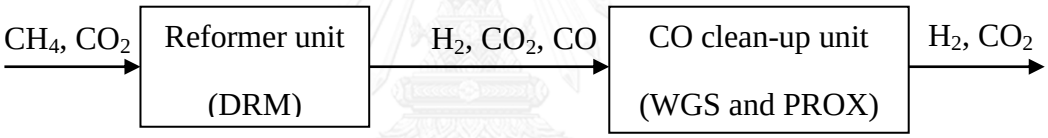

Figure 1.1 Schematic outline of fuel processor via an integration of carbon dioxide reforming of methanol (DRM) and CO clean-up (WGS and PROX) unit.

1.2 Purpose of this study

The purpose of this study is to produce high purity H_2-rich stream from methane and carbon dioxide (called dry reforming of methane; DRM). The methane is catalytically converted to H_2-rich stream via dry reforming. The CO in the reformate gas is eliminated to less than 2000 ppm via CO clean-up process. Moreover, the CO molecule was studied by quantum mechanics simulation to understand the behavior when solute in water

- *Objectives*

1. To study the process to produce H_2 from methane and carbon dioxide over nickel base catalysts.

2. To investigate the process to reduce CO level by water-gas shift and preferential oxidation processes.

3. To study the dilution of CO behavior by quantum mechanics simulation.

- *Hypothesis*

To produce pure hydrogen with CO level less than 100 ppm from carbon dioxide and methane via an integration of dry reforming of methane, water gas shift and preferential CO oxidization.

1.3 Scope of the dissertation

1.3.1 Hydrogen production via methane reforming with carbon dioxide (DRM)

To find the effective catalyst for DRM unit at constant condition of methane and carbon dioxide ratio = 1, feed rate = 60 ml/min, and 0.1 g of catalyst weight in temperature range of 500 °C to 900 °C. The prepared catalysts consist of nickel with manganese or gold promoter over ceria (CeO_2). The optimal condition for DRM was studied by statistically designed set of experiments. Four independent factors selected were the operating temperature, methane composition, catalyst weight and total feed rate. The methane conversion and carbon dioxide conversion were carried out as a response.

1.3.2 Carbon monoxide clean up via water gas shift reaction (WGS)

To find the effective catalysts for WGS unit under real condition of outlet gas from dry reforming part in temperature range of 250 °C to 450 °C. The experimental designs for a suitable condition of operating were investigated. The

factors including temperature, catalysts weight and water feed rate were determined. The CO conversion and H_2 yield were studied as a response.

1.3.3 Carbon monoxide clean up via preferential oxidation reaction (PROX)

To find the effected factor to PROX under simulated gas contain 1% CO, 1–2% O_2, 40% H_2, 0–10% H_2O, and 0–20% CO_2 with He balance in temperature range of 40 °C to 120 °C. Experimental matrix of factorial design was performed. Three independent factors selected were the operating temperature, O_2/CO ratio and CO_2 added. The CO conversion multiply with CO selectivity as yield was used as a response.

1.3.4 Integrations of hydrogen production and carbon monoxide clean up

To combine DRM, WGS and PROX unit to produce pure hydrogen by using the effective catalysts were studied, and solve the problem of CO level to below than 100 ppm.

1.3.5 Carbon monoxide clean up via water trap—a soluble explanation by quantum mechanical charge field molecular dynamics (QMCF MD)

To explanation of dynamics and behavior of CO in water was performed because in engineering field how soluble of CO in water had not been reported.

1.4 Anticipated benefits

1) To set-up a reactor of a fuel processor system for hydrogen production from green house gas including methane and carbon dioxide

2) To obtain an effective catalyst for fuel processor system

3) To perform an optimum condition for operating in each process

4) To give hydrogen rich stream without carbon monoxide from integration processes

1.5 Format of the dissertation

The dissertation was formatted in a chapter form. Chapter 1 presents background, purpose, anticipated benefits and scope of this research work. Chapter 2 mentions theoretical information and literature review. Chapter 3 describes materials used in this work and methodology, accompany with catalyst preparation, catalyst characterization, activity measurement in each process. Chapter 4 involved the results and discussion of hydrogen production and carbon monoxide clean up process. Chapter 5 quantum mechanical charge field molecular dynamics was presented. Finally conclusion and recommendations is introduced in chapter 6.

CHAPTER 2

THEORY AND LITERATURE REVIEWS

In this chapter, the explanation of the importance of hydrogen production process is presented in section 2.1. Then, CO clean up unit including water-gas shift and preferential oxidation process, which is an importance process to reduce the CO level from the hydrogen production process presented in section 2.2. Furthermore, the utilization of hydrogen will be presented in section 2.3. In section 2.4, the catalysts characterizations procedure is described. The detail in molecular dynamic is described in section 2.5. Finally, literature reviews are expressed in section 2.6

2.1 Hydrogen production process

Big business hydrogen is usually manufactured by shifting hydrocarbon-based substance such as steam reforming or dry reforming of light hydrocarbons (NG and naphtha). These reaction has several modifications depending on reactor design, type of feedstock, by-product management, heat input options, concentration of hydrogen purity, etc (2). A typical dry reforming process configuration will be reviewed in this chapter somewhere possible references on other revisions to the process will be provided.

2.1.1 Carbon dioxide reforming of methane or dry reforming (DRM)

The carbon dioxide reforming of methane is an alternative choice of hydrogen production process, which carbon dioxide is an oxidant factor. Occasionally, this process is also called stoichiometric reforming, but it is usually referred to dry reforming. It is a quite high endothermic reaction involving high

temperatures operation around 800 to 1000 °C. Due to the presence of carbon dioxide in the feedstock, the reaction produces synthesis gas with 1:1 ratio of CO and H_2 in relation to the following equation:

$$CH_4 + CO_2 \rightarrow 2CO + 2H_2 \quad \Delta H°_{298} = 247 \text{ kJ mol}^{-1} \qquad \text{(Eq. 2.1)}$$

Figure 2.1 shows the thermodynamic equilibrium result related to carbon dioxide reforming of methane at atmospheric pressure (3). It is remarkable at temperatures below 800 °C, that elemental carbon is a major component of the equilibrium mix. At higher temperatures over 800 °C, the carbon fraction drastically decrease and the H_2 and CO fractions become the major and reach to maximum value at 1000 °C.

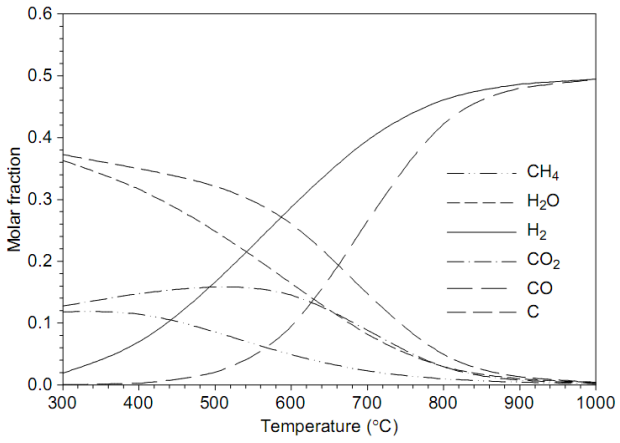

Figure 2.1 Temperature dependence of thermodynamic equilibrium composition of the products obtained from CH_4:CO_2 = 1:1 (molar) at atmospheric pressure (3).

With the rising of CO_2, world organization concerns about the negative environmental impact (i.e., global warming). The dry reforming technology is getting more attention to develop increasingly. It should be reminded, however, that if the purpose desired to produce H_2 only, this process would not be a good result in the overall reduction of CO_2 discharge compared to steam reforming process (because CO_2 is produced in the WGS stage of the process). On the other hand, if the aim

process goes for the production of synthesis gas with relatively high content of CO (e.g., for FT synthesis), then this process encourages the ratio of CO/H_2 in the synthesis gas. In this case, carbon dioxide from the feedstock will be stored in the form of synthetic fuels (diesel or FT gasoline) or oxygenated compounds (alcohols, esters, etc.). Another benefit of this process is related to the fact that carbon dioxide is produced as a co-product of the methane reforming process (4).

Practical achievements of dry reforming stand facing some key challenges such as technique and economic. From the economical viewpoint preferred pressure of the synthesis gas plant around 2.0 to 4.0 MPa, dry reforming cannot achieve the complete conversion of methane by the reason of thermodynamic limitations (5). In addition, pressure in the process strongly depends on economical status and the cost of CO_2 available. However, the most important problem hindering the practical process of dry reforming is catalysts deactivation due to the carbon formation or coke. Carbon formation can be assigned to two reactions: methane decomposition reaction and CO disproportionation reaction.

$$2CO \leftrightarrows C + CO \qquad \Delta H^{\circ}_{298} = 172 \text{ kJ mol}^{-1} \qquad \text{(Eq. 2.2)}$$

CO disproportionation is an exothermic reaction which favored high pressures and temperatures below 700 °C. From a practical dry reforming viewpoint, it is desired to operate at moderate temperatures and with the 1:1 ratio of CH_4:CO_2, which requires a catalyst that inhibits the kinetic of carbon formation on a good thermodynamic for carbon deposition (6).

2.1.2 Catalysts for carbon dioxide reforming of methane

Iron-, cobalt-, and nickel-based catalysts are mainly active in methane decomposition and CO disproportionation reactions, and noticeable carbon formations on the surface of these catalysts occur at temperatures as low as 350 °C. The carbon formation on metal surfaces is controlled by the reaction temperature around 350 °C to 600 °C, amorphous and filamentous carbons are major form of carbon, whereas an ordered graphitic structure controls at the temperatures above 700 °C (6).

Most of the reported study on dry reforming relates to Ni-based catalysts, because Ni promotes high catalytic activity with a low-priced. However, Ni catalysts are low resistance to deactivation and carbon deposition as discussed above. As a result, much research has been performed to improve the resistance of nickel catalysts to deactivation and remove carbon formation during the process. Comprehensive studies on the topic of dry reforming using Ni-based catalysts and other nonprecious metal catalysts were recently reported by Hu and Ruckenstein (6) and Bradford and Vannice (7). The surface crystallographic structure and the surface acidity are two major factors affecting the carbon deposition. It was concluded that Ni(100) and Ni(110) on surfaces are more effective in methane decomposition and carbon deposition than the Ni(111) surface (8). By controlling the size of active metal on the catalyst surface (since larger group of metal promote carbon formation), it would be prevented carbon deposition. Carbon deposition on the commercial Ni catalyst can be diminished by selectively passivating catalytically active sites. The inhibition of carbon deposition by sulfur passivation is attributed to the strong adsorption of sulfur that controls the size of active metal ensembles (i.e., it reduces larger ensembles that promote carbon deposition). Haldor Topsoe has been operating its SPARG process that applied a partially sulfided Ni catalyst (9). Nonetheless, the addition of sulfur to the catalyst reduces the catalyst activity and overall process throughput (4).

Another significant factor involving carbon deposition is the catalyst surface basicity. Especially, it was revealed that carbon formation can be reduced or controlled when the supported metal carrier with a strong Lewis basicity (10). This effect can be assinged to the fact that high Lewis basicity of the support improves the CO_2 chemisorption on the catalyst surface resulting in the elimination of coke (by surface gasification reactions). As said by Rostrup-Nielsen and Hansen (9), the quantity of carbon deposition on the metal catalysts decrease in the following order:

$$Ni >> Rh > Ir \approx Ru > Pt \approx Pd \qquad \text{(at 500 °C)}$$

$$Ni > Pd \approx Rh > Ir > Pt >> Ru \qquad \text{(at 650 °C)}$$

In addition, the rate of carbon deposition also depends on the catalysts supports and promoters. Commonly, zirconium oxide (ZrO_2) has been used as a support for Pt catalysts due to the lower rate of carbon deposition, which is compared to other supports as showed in the following order of the carbon formation rate (11):

$$Pt/Al_2O_3 >> Pt/TiO_2 > Pt/ZrO_2$$

Vanadium oxide improves catalytic activity of Rh/SiO_2 catalyst by shrinking the rate of carbon formation (7). This result was ascribed by the formation of VO_x overlayer on the metal surface (Rh), shrinking the size of the Rh cluster and, hindering carbon formation. It was mentioned that SiO_2 supported and ZrO_2 supported bimetallic Pt–Au, Pt–Sn catalysts represented a lower trend of carbon deposition during dry reforming than the respective monometallic Pt catalysts (12). In spite of the fact that noble metal catalysts are hardly sensitive to deactivation by carbon deposition compared to non-precious metal catalysts, there has a very high cost hindering to their large scale application.

2.1.3 Reaction mechanism of carbon dioxide reforming of methane

A relatively simple mechanism for CO_2 reforming of methane has been suggested by Lercher *et al.* (13):

$$CH_4 + * \rightarrow C* + 2H_2 \quad \text{(Eq. 2.3)}$$

$$CO_2 + 2* \leftrightarrows CO* + O* \quad \text{(Eq. 2.4)}$$

$$C* + O* \leftrightarrows CO* + * \quad \text{(Eq. 2.5)}$$

$$2CO* \leftrightarrows 2CO + 2* \quad \text{(Eq. 2.6)}$$

where $*$ is an active site.

The step sequence was derived from a series of pulsed adsorption tests, in which CH_4 was decomposed stoichiometrically to carbon and hydrogen, whereas carbon dioxide was presented to react stoichiometrically with the surface carbon yielding CO.

The steam addition to CH_4/CO_2 can avoid an excess carbon formation which is a widely applied in commercial systems (4). The equation of CO_2 and steam gasification of methane can be expressed by the following equation:

$$2CH_4 + CO_2 + H_2O \rightarrow 3CO + 5H_2 \qquad \text{(Eq. 2.7)}$$

The syngas performs H_2:CO ratio of 1.7. Although, there has a high relative concentration of CO in the system, coke formation has still been a problem, especially, Ni-based catalysts that commonly used for steam reforming.

2.2 Carbon monoxide clean-up

2.2.1 Water-gas shift reaction

The water-gas shift (WGS) reaction is a necessary step for the H_2 production in the industry since the 1940s (14):

$$CO + H_2O \leftrightarrows CO_2 + H_2 \qquad \Delta H°_{298} = -41.1 kJ\ mol^{-1} \qquad \text{(Eq. 2.8)}$$

The key of the WGS reaction is occupied to raise the hydrogen production for plant processes, mass storage and redistribution. This is an essential point for gases which have appropriate H_2/CO ratios in the ammonia production, methanol, and alternative hydrocarbon fuels via Fischer–Tropsch (15) synthesis. Hydrogen and carbon monoxide mixtures in manufacturing usage referred to synthetic gas are produced in large scale plants via high-temperature reaction of carbon in steam or oxygen condition (see Eq. 2.9 to Eq 2.11):

$$CH_4 + H_2O \rightarrow CO + 3H_2 \qquad \text{(Eq. 2.9)}$$

$$C_nH_m + nH_2O \rightarrow nCO + (n + m/2)H_2 \qquad \text{(Eq. 2.10)}$$

$$CH_4 + \tfrac{1}{2}O_2 \leftrightarrows CO + 2H_2 \qquad \text{(Eq. 2.11)}$$

or via coal gasification in Eq. 2.12:

$$C + H_2O \rightarrow CO + H_2 \qquad \text{(Eq. 2.12)}$$

The WGS component was considered the ratio of H_2 and CO output giving more details in literature about syngas production and application can be searched by elsewhere (16-19).

The WGS must be joined together with methanol synthesis, reforming of hydrocarbon, FT synthesis, automotive exhaust catalysis, and preferential oxidation of CO for fuel cells because the WGS reaction is not the main reaction

The WGS reaction is a vital part for decreasing the carbon monoxide level in PEM fuel cells that Pt anode cannot be tolerant to 100 ppm level of carbon monoxide. In the most condition of aim of fuel processor, the WGS reaction must reduce a CO concentration to less than 3% by volume before feed into the preferential oxidation part. And then it converts carbon monoxide to carbon dioxide by oxidation in suitable CO level. The WGS reaction has two advantages for fuel processing; first is effectively coincident decreasing the CO component and increasing H_2 component of every mole of CO and further enhance efficiency of fuel cell by generating H_2 from H_2O. Abundant utilization of the WGS reaction from understanding thermodynamics and kinetic behaviors must be considered. Operating conditions, such as temperature, steam concentration and catalysts weight must be investigated for designing system.

The WGS reaction, particularly, is an exothermic reaction, so it revealed higher CO conversions at low temperatures. An equilibrium constant of WGS reaction shifted about 80 times higher when decreasing the temperature from 600 °C to 200 °C. The WGS equilibrium constants with various temperatures are demonstrated in Table 2.1. The steam concentration in the feed stream has an important effect on CO conversion. The feeding of steam with varying the concentrations through the WGS reactor was controlled the adding by H_2O injection before or between stages of the WGS reactors. The concentrations of CO, CO_2 and H_2 in the feed have mainly dependence on the reformer operating conditions, which determines from the following thermodynamic reactions.

Table 2.1 WGS equilibrium constants (14)

Temperature °C	K_p	Temperature °C	K_p
93.3	4523	426.7	9.030
148.9	783.6	482.2	5.610
204.4	206.8	537.8	3.749
260	72.75	593.3	2.653
315.6	31.44	648.9	1.966
371.1	15.89	704.4	1.512

The effect of reaction temperature and steam concentration on the equilibrium concentration of CO is presented in Figure 2.2 and Figure 2.3 for a conventional high- and low-temperature shift reaction, respectively (14).

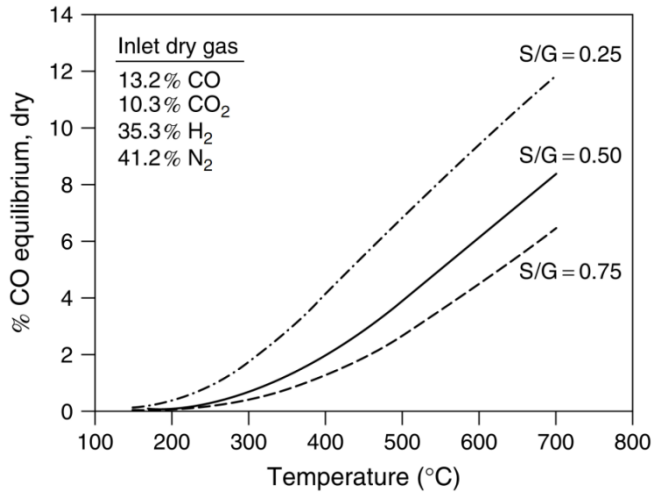

Figure 2.2 CO equilibrium of high temperature shift from auto thermal reformer at various S/G ratios (14)

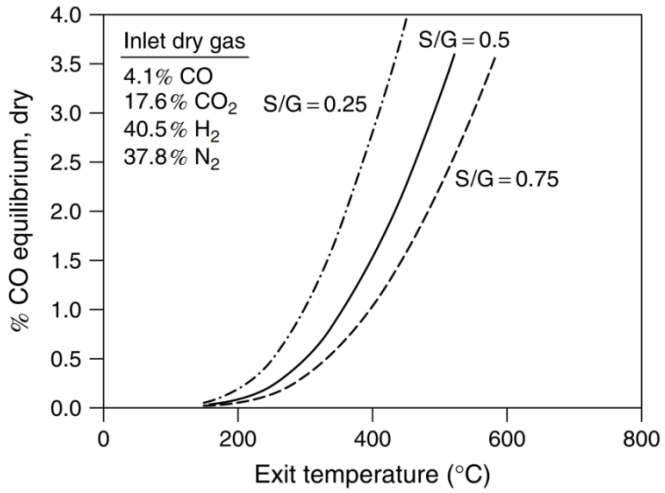

Figure 2.3 CO equilibrium of low temperature shift from auto thermal reformer at various S/G ratios (14)

The calculation from gas composition is presented in Table 2.2. The equilibrium temperature rises by 100 °C while keeping 1% CO when increasing the molar steam to dry gas ratio (S/G) from 0.25% to 0.75% (20% H_2O to 42.9% H_2O). A valuable reduction of the reactor size can be reached when operating at temperature higher than 100 °C by developing more favorable kinetics.

Table 2.2 Representative inlet gas compositions for HTS and LTS reactions, from autothermal reforming, methane free (14)

	HTS gas (%)	LTS gas (%)
CO	9	3
CO_2	7	13
H_2	24	30
N_2	28	28
H_2O	32	26

- Mechanisms and kinetics

A consideration of the mechanisms and kinetics of the WGS reaction with various catalysts by many researches was concluded in the literature (16, 20-22). Two types of mechanisms were recommended (23). The oxidation-reduction, regenerative mechanism of Rideal-Elay type, in which steam oxidizes the surface and CO reacts with the oxidized surface (20, 24) and others is a bi-functional process that oxygen in the support oxidizes the adsorbed carbon monoxide on the metal or mixed-metal oxide. Oxygen from steam, then, is filled at oxygen vacancy in the support (20, 25, 26):

$$H_2O + * \leftrightarrows H_2 + O* \quad \text{(Eq. 2.13)}$$

$$CO + O* \leftrightarrows CO_2 + * \quad \text{(Eq. 2.14)}$$

where $*$ is an active site on metal. The associative mechanism is multi-step Langmuir–Hinshelwood type which adsorbed steam. The steam is dissociated to hydroxyl group that reacts with CO to generate a formate, and then decomposed to H_2 and CO_2 and others. Hint at the nature of bi-functional, which the adsorbed CO, reacts with hydroxyl groups to generate the formate intermediate (20, 27).

In the presence of the formate intermediate, it is approved by FTIR analysis:

$$CO + * \leftrightarrows CO \quad \text{(Eq. 2.15)}$$

$$H_2O + 2* \leftrightarrows H* + OH* \quad \text{(Eq. 2.16)}$$

$$OH* + CO* \leftrightarrows HCOO* + * \quad \text{(Eq. 2.17)}$$

$$HCOO* + * \leftrightarrows CO_2* + H* \quad \text{(Eq. 2.18)}$$

$$CO_2* \leftrightarrows CO_2 + * \quad \text{(Eq. 2.19)}$$

$$2H* \leftrightarrows H_2 + 2* \quad \text{(Eq. 2.20)}$$

In equation 2.18, the formate decomposition step was noticed as the rate-determining. Increasing partial pressure of steam promoted the decomposition rate of formate with reducing the activation energy (22).

Tinkle and Dumesic have described the WGS on Fe/Cr catalyst progress by the regenerative mechanism based on adsorption/desorption measurements and inter-conversion of CO and CO_2 by isotope exchange on a Fe/Cr catalyst (28). However, the reaction mechanism over Cu based catalysts is recently debated. An importance of the catalyst composition, textural surface properties, precursors, plays a role as well as the reaction conditions clearly. The regenerative mechanism has been offered in good agreement with the results of WGS reaction achieved on single crystal surfaces of copper and water adsorption on poly-crystalline Cu (29-32). Some different kinetic demonstrations used over Cu catalysts have been concluded previously (31). The result of pressure over Cu/Zn/Al catalysts on the activation energy and reaction regulation based on macro- and micro-kinetic models has been studied (33). Grenoble *et al.* (27) studied a number of supported metals in WGS reaction at temperature between 270 °C to 380 °C under atmospheric pressure. Metals VIIB, VIII, and IB group supported on alumina displayed the range of activity differed by more than three orders of magnitude with varying the reaction orders of steam and carbon monoxide from 0 to 0.8 and –0.4 to 0.6, respectively. A level of turnover number of Pt on Al_2O_3 is higher than that of Pt on SiO_2 and active carbon. Other literatures presents reaction order CO, H_2O, CO_2 and H_2 of 0, 0–0.5, –0.5 and –1, respectively, over Pd/CeO_2 catalysts (22, 34).

- *Catalyst requirements*

Catalysts of WGS were effectively to apply in fuel processing for hydrogen production for fuel cells and those are significantly several applications of traditional industry as demonstrated in Table 2.3.

For portable applications, the operating condition included size, weight and cost targets are importance, because the prerequisite must compare with the internal combustion engines. The catalysts for stationary applications, large scale and high costs are acceptable to compare with the cost of electricity from the grid, especially in premium power applications. However, it is clear that improvement of catalyst and reactor technology for portable fuel cells will be comprised into stationary applications which make them having more economically viable.

Table 2.3 WGS catalyst requirements for mobile and stationary applications (14)

WGS catalyst attribute	Mobile application	Stationary application
Volume reduction	Critical, <0.1 l/kW	Not as constrained
Weight reduction	Critical, <0.1 kg/kW	Not as constrained
Cost	Critical, <$0.1/kW	Not as critical
Rapid response	Critical, <15s	Load following
Nonpyrophoric	Important	Eliminate purging
Attrition resistance	Critical	No constraint
Selectivity	Critical	Important
No reduction required	Critical	Important
Oxidation tolerant	Critical	Important
Condensation tolerant	Important	Important
Poison tolerant	Desired	Desired
Pressure drop	Important	Important

A purpose of WGS catalysts in the industry is efficiency of operation at long term conditions. It is estimated that a revelation of many startup/shutdown cycles over the catalysts for fuel processor will be used with described to redox cycles and condensing steam. As mentioned above, the industrial WGS catalysts must be concerned under exposed conditions. A commercial Cu/Zn/Al catalyst is drastically deactivated when exposed to condensing syngas. The reduction of the CO conversion about 40% to 50% after 3 cycles is shown in Figure 2.4. When the Cu/Zn/Al catalysts exposed to an oxidizing agent, it also shows high deactivation (35). The Cu/Zn/Al catalysts further applied in fuel processing via oxygen-assisted WGS reaction as well (36).

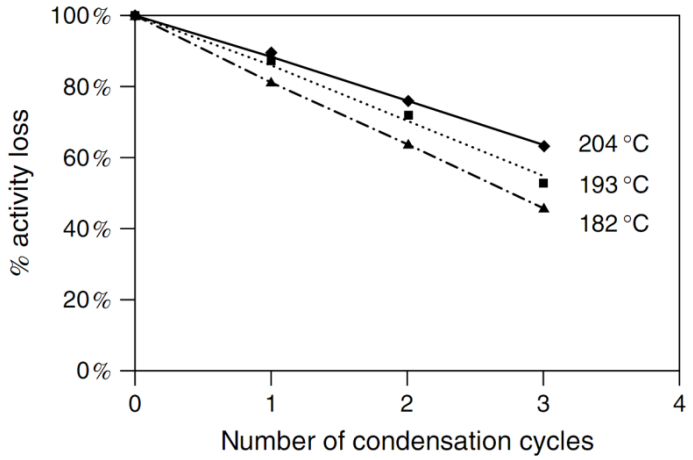

Figure 2.4 Effect of condensing synthesis gas on commercial Cu/Zn/Al catalyst (35)

2.2.2 Preferential oxidation of carbon monoxide

The principal methods for producing hydrogen including catalytic partial oxidation and steam reforming generate significant amounts of carbon monoxide. To apply the water-gas shift reaction, CO can be easily oxidized to CO_2 by reaction over an appropriate catalyst, with the coincident to hydrogen production until the reduction of CO reaches to equilibrium and kinetically conditions.

There are many processes used in an industry for the elimination of CO in the hydrogen production (37). A well-known method is that of methanation:

$$CO + 3H_2 \leftrightarrows CH_4 + H_2O \qquad \Delta H°_{298} = -206 \text{ kJ mol}^{-1} \qquad \text{(Eq. 2.21)}$$

In an industrial application, the reaction occurs in the range of 200 °C to 220 °C. There are two important disadvantages. Three moles of hydrogen are balanced with one mole of CO. Carbon dioxide, in the gas stream could react with hydrogen to produce methane. When, the level of CO_2 concentration reaches 200 ppm, it reacts with four moles of hydrogen via methanation, which is an exothermic reaction:

$$CO_2 + 4H_2 \leftrightarrows CH_4 + 2H_2O \qquad \Delta H°_{298} = -165 \text{ kJ mol}^{-1} \qquad \text{(Eq. 2.22)}$$

Clearly, it has an importance to remove CO_2 before employing a methanation step. However, this is impractical on anything less than industrial-scale compared a small fuel cell system versus a hydrogen plant; in conventional hydrogen plants, the methanation of CO is usually composed after CO_2 has been captured from an amine trap. Furthermore, the methanation catalysts are normally performed of highly active at delicately spread around reduced nickel, although ruthenium is also used as well. When exposed to oxygen, a likely scenario during a shutdown procedure or reactor leak, the oxidation of the nickel catalyst presenting in high concentration will be pyrophoric substance; the heat of reaction of the oxidation of the catalyst could result in a fire. This is reasonably an undesirable option for design of an engine that will be daily used in the homes or vehicles application.

Another method of carbon monoxide removal is adsorption. CO can be adsorbed by zeolite-containing adsorbent under high pressure, and then the pressure is released when needed to desorb CO from the adsorbent. This calls a pressure swing adsorption (PSA) system. The major downside of this process required an energy-consuming compressor, because CO would be discharged.

In addition, the hydrogen can be separated from the inlet gas by metal membranes based on palladium/silver alloys, which permeate pure hydrogen with a low amount of CO before entering to the fuel cell. The residue of hydrogen and other components discharge from the membrane module, but the cost of the membranes is a problem for low-cost fuel cell applications.

Another reaction of CO removal is preferential CO oxidation or PROX that feed an air as a source of oxygen to oxidize CO. High selectivity for CO oxidation is required, because the initial H_2/CO ratio commonly exceeds 100:1, and can rise up to 50,000:1 at the completion of reaction. Preferential CO oxidation reaction (2.23) is catalyzed with hydrogen oxidation (2.24) following by these equations:

$$1{,}000 \text{ ppmv} < CO < 5{,}000 \text{ ppmv}$$

$$CO + \tfrac{1}{2}O_2 \rightarrow CO_2 \qquad \Delta H°_{298} = -283 \text{ kJ mol}^{-1} \qquad \text{(Eq. 2.23)}$$

$$400{,}000 \text{ ppmv} < H_2 < 700{,}000 \text{ ppmv}$$

$$H_2 + \tfrac{1}{2}O_2 \rightarrow 2H_2O \qquad \Delta H°_{298} = -242 \text{ kJ mol}^{-1} \qquad \text{(Eq. 2.24)}$$

Preferential CO oxidation has been applied to eliminate CO from hydrogen prior to ammonia synthesis beginning as early as the 1960s (38-42). For example, Selectoxo^{TM}, catalysts particle composed of a Fe promoted-Pt on alumina particle (usually a tablet) removes CO to the ppm level from a hydrogen-rich stream (41).

- Purposes of PROX

The preferential CO oxidation has several objectives which are discussed in the following:

- Lowering CO concentration to <100 ppmv. The efficiency of electrochemical reaction of PEM fuel cell is reduced by the presence of CO in the hydrogen stream reacting at the anode, especially Pt-based electrode.
- To consider an undesirable of side reaction such as reverse water-gas shift (RWGS) and methanation. The relative significance of CO oxidation with RWGS and methanation, as a function of temperature for PROX catalyst is shown in Figure 2.5. The relative position of reverse water gas shift and methanation curves versus *T* is catalyst specification.

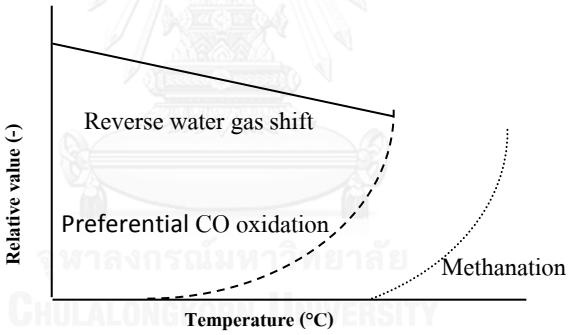

Figure 2.5 Influence of temperature on key reactions occurring with PROX (42)

- Minimal loss of hydrogen, designing a PROX system with high selectivity for CO oxidation is concerned.
- There are an importance to operation within the parameters of the fuel processor such as temperature, space velocities, high steam content and CO_2 concentration. The catalyst must become a small size to operate over a wide range of space velocities and need suitable activity to control CO level at maximum flow with tolerance in the presence of CO_2 and water.

- Catalysts for the Preferential Oxidation of Carbon Monoxide

The assembly of PROX catalyst formulations consists of a precious metal component. The catalyst-mediated oxidation of CO is a multi-stage process, particularly following Langmuir-Hinshelwood kinetics for a single site competitive mechanism between CO and O_2. In the first stage, CO is adsorbed on the surface site of active metal and coincident that oxygen has to be adsorbed on the neighboring surface site with dissociated to oxygen atoms. Then the CO* (adsorbed CO) reacts with the O* (adsorbed oxygen) to form the CO_2* (adsorbed CO_2). Finally, the CO_2* desorbs out of the active site on the active surface.

$$CO + * \leftrightarrows CO* \quad \text{(Eq. 2.25)}$$

$$O_2 + 2* \leftrightarrows 2O* \quad \text{(Eq. 2.26)}$$

$$CO* + O* \leftrightarrows CO_2* \quad \text{(Eq. 2.27)}$$

$$CO_2* \leftrightarrows CO_2 + * \quad \text{(Eq. 2.28)}$$

where $*$ is active site

For the metal oxide based catalysts commonly used CuO as an active species, the mechanism pathway is passed via oxygen lattice of the support. The CO* reacts with the oxygen lattice to the CO_2* and oxygen vacancy. Then the CO_2* desorbs and the oxygen molecule adsorbs with dissociated to oxygen atoms locating at the oxygen vacancy lattice.

$$CO + * \leftrightarrows CO* \quad \text{(Eq. 2.29)}$$

$$CO* + \text{O-lat} \leftrightarrows CO_2* + \square\text{-lat} \quad \text{(Eq. 2.30)}$$

$$CO_2* \leftrightarrows CO_2 + * \quad \text{(Eq. 2.31)}$$

$$O_2 + 2\square\text{-lat} \leftrightarrows 2\text{O-lat} \quad \text{(Eq. 2.32)}$$

where $*$ is active site and $\square$ is oxygen vacancy lattice

To become aware of the preferential oxidation catalysts behavior, the operating principle will discuss and give an explanation. The common feature of these catalysts is the preferential adsorption of CO at low temperature. Since the reaction

temperature increases, the coverage of CO decreases and reacts with oxygen (when it is present in the gas phase). At even higher temperatures and also lower coverage of active sites with CO, hydrogen oxidation occurs in coincident parallel.

Preferential CO oxidation catalysts usually include precious metals such as platinum, ruthenium, palladium, rhodium, gold and alloys of platinum with tin, ruthenium or rhodium. Particularly carrier materials are alumina and zeolites (43), such as zeolite A, mordenite and zeolite X. Other possible carriers are cobalt oxide, ceria, zirconia, titania, tin oxide, and iron oxide (44). A high precious metal loading commonly improves catalyst activity (43). The platinum on alumina catalyst often applied for the preferential CO oxidation, which contains low amounts of platinum lower than 1%wt. (45, 46), to reduce the price of the catalyst.

Catalyst improvement work on catalyst formulations as alternatives to conventional platinum/alumina catalyst for the preferential CO oxidation will be considered below. A previous study by Oh *et al.* (47) ascribed an extensive catalyst screening. The following activity ranking was followed:

$$Ru/Al_2O_3 > Rh/Al_2O_3 > Pt/Al_2O_3 > Pd/Al_2O_3 > Co/Cu/Al_2O_3 >$$
$$Ni/Co/Fe/Al_2O_3 > Ag=Al_2O_3 > Cr=Al_2O_3 > Fe=Al_2O_3 > Mn=SiO_2$$

Zhou *et al.* (46) studied various noble metal based catalysts containing 0.5 % by weight of an active species on g-alumina carrier and indicated the following activity ranking: Pt>Rh>Ru>Pd. The catalysts had been covered onto small monolithic supports. For a 1000-h test duration, CO conversion lower 150 ppm was gained over a 1%wt. platinum/alumina sample at an O/CO ratio of 2.0.

2.3 Utilization of H_2

2.3.1 Hydrogen Property

Hydrogen is an easily flammable fuel under a wide range of temperature and gas concentration. Hydrogen is well known that it has high combustion efficiency, but safety in production, storage, and transportation are generally

concerned. Hydrogen can be reacted with oxygen to generate the energy in combustion engines or PEM fuel cell producing water during the reaction. Although there has no observation of hydrogen on the earth, but also it is usually formed as compounds of carbon and oxygen, such as hydrocarbons, coal, biomass and alcohol. Hydrogen is a good alternative energy comparing with natural gas, LPG, gasoline, and diesel because of its thermal properties. The technical and economic challenges of implementing a "hydrogen economy" require a solution to the primary problem of renewable energy production. There are many concern points before hydrogen serve to a worldwide energy including hydrogen production, storage, transportation, distribution, and end user (2, 48-59).

Hydrogen has the top of energy content (on a weight basis) comparing to other fuels. Hydrogen has energy content more than gasoline around 3 times (140.4 MJ/kg versus 48.6 MJ/kg). On a volume basis, liquid hydrogen and gasoline have 8,491 MJ/m^3 and 31,150 MJ/m^3, respectively. A low density of hydrogen is a problem to storage, especially for portable applications such as automotive unit. A large container is required to stock enough hydrogen for a proper driving range. The energy density of hydrogen is also involved by the physical nature of the fuel, whether the fuel is stored as a liquid or as a gas; and if a gas, at what pressure. Characteristic of energy properties of hydrogen and other fuels are compared in Table 2.4.

Table 2.4 Comparison of hydrogen with other fuels (3)

Fuel	LHV ($MJ\ kg^{-1}$)	HHV ($MJ\ kg^{-1}$)	Stoichiometric Air/Fuel Ratio (kg)	Combustible Range (%)	Flame Temperature °C	Min. Ignition Energy (60)	Auto Ignition Temperature ©
Methane	50	55.5	17.2	5–15	1914	0.3	540–630
Propane	45.6	50.3	15.6	2.1–9.5	1925	0.3	450
Octane	47.9	15.1	0.31	0.95–6.0	1980	0.26	415
Methanol	18	22.7	6.5	6.7–36.0	1870	0.14	460
Hydrogen	119.9	141.6	34.3	4.0–75.0	2207	0.017	585
Gasoline	44.5	47.3	14.6	1.3–7.1	2307	0.29	260–460
Diesel	42.5	44.8	14.5	0.6–5.5	2327		180–320

One of the principal features of hydrogen is its electrochemical property, which can be used in a fuel cell which presents in the next part.

2.3.2 Hydrogen in proton exchange membrane fuel cell (PEMFC)

A fuel cell is a device for conversion of chemical energy to electric energy, which continuously provides electric direct current. Proton exchange membrane (PEM) fuel cell layer consists of two Pt electrode layers with central solid polymer electrolyte as seen in Figure 2.6. It normally operates at about 80 °C and atmospheric pressure. It is the most developing fuel cell system for residential and transportation applications due to its high energy density.

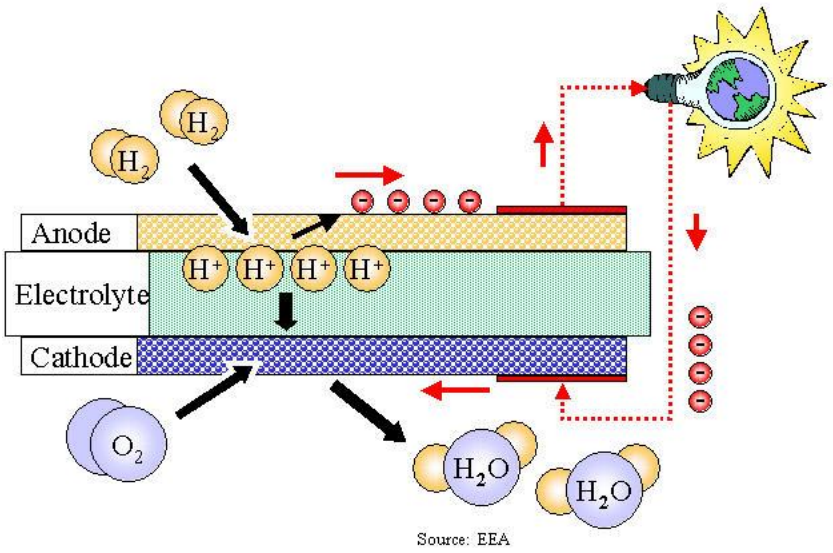

Figure 2.6 Proton exchange membrane fuel cell (PEMFC) operation *(http://www.eea.europa.eu)

In the process, the hydrogen will be fed to the anode whilst the oxygen will be routed to the cathode as well. At the anode, the hydrogen fuel will diffuse into the porous electrode to the Pt-catalyst in reaction zone, and dissociated into electrons and proton. After that, the electrons are forced to through an external circuit while the proton will pass through the electrolyte to the cathode which the oxidant reduction take places. The oxygen at the cathode will be reduced by the electrons from the external circuit to combine with the protons from the anode. The reaction for the PEM fuel cell is combined from (Eq. 2.33) and (Eq. 2.34) to become (Eq. 2.35) which releases some water, heat and current (3).

$$H_2(g) \rightarrow 2H^+(aq) + 2e^- \qquad \text{(Eq. 2.33)}$$

$$O_2(g) + 4H^+(aq) + 4e^- \rightarrow 2H_2O(l) \qquad \text{(Eq. 2.34)}$$

$$H_2(g) + \frac{1}{2}O_2(g) \rightarrow H_2O(l) + Heat + Current \qquad \text{(Eq. 2.35)}$$

For PEM fuel cell operation, the main topic is catalysts which help H_2 dissociation to proton and electron in anode reaction. The most catalysts as noble metals are widely used, especially Pt which is highly active and stable. But it can be deactivated by contaminating of CO in hydrogen-rich stream. The CO competes for the H_2 to adsorb on the active site of catalyst; therefore, molecules of H_2 cannot dissociate and the performance of fuel cell also shows less activity as shown in Figure 2.7

To solve this problem, one is a using of pure H_2 as fuel and another is a using of CO-tolerant catalysts in fuel cell. However, pure H_2 is expensive and needs high pressure to form in liquid that is dangerous for transportation. So, H_2 which is produced on-board from hydrocarbons or liquid fuels are favorable.

Presently, fuel cells are available operating at an efficiency of 50% to 60% with a lifetime of up to 3000 h. The direct current output range from 440 A/m^2 to 1720 A/m^2 of the electrode surface, which can provide a power output from 50 W to 2500 W.

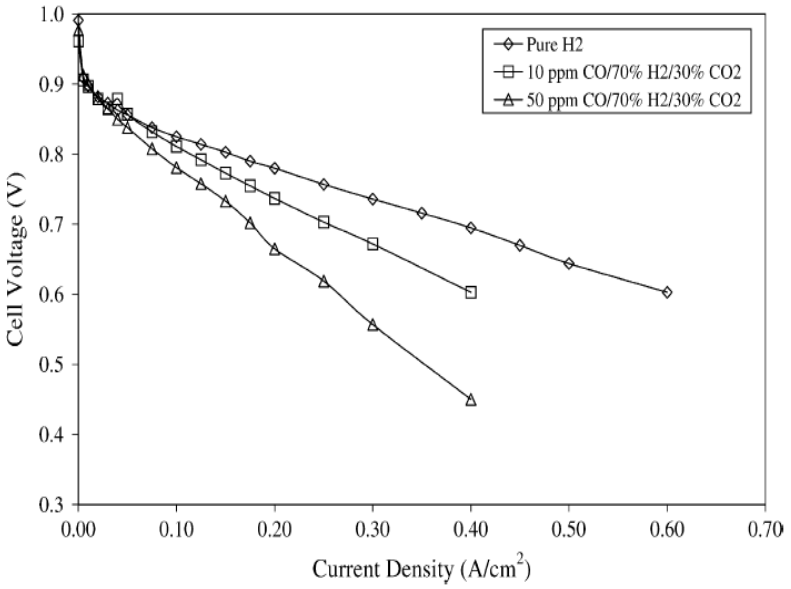

Figure 2.7 Current density of fuel cell at different CO concentration (50)

2.4 Catalyst characterization

Characterization of a heterogeneous catalyst mentions to the measurement of its ‘characteristics’, which are represented physical and chemical proprieties of the catalyst to response its performance (61). More particularly, the characteristics of a catalyst include:

- The nature of its basic building block, i.e. chemical composition
- The arrangement of these basic building blocks or architecture, e.g. structure, crystallite size and distribution, crystallite morphology, porosity, and surface area
- Surface chemical properties such as valence state, acidity, reactivity with different molecules, surface energy, and surface electronic states
- The aggregate properties such as aggregate or particle size, magnetic properties, density (bulk, particle, and skeletal), mechanical strength, and attrition resistance
- Catalytic properties, e.g. activity, selectivity, and activity stability.

The characteristics of heterogeneous catalytic materials in this work were given some of the most commonly used characterization techniques (62) and their acronyms in the following list.

- BET (Brunauer, Emmett and Teller Method): A commonly accepted method for analyzing multi-layer physisorption isotherm of nitrogen gas to investigate the surface area of solids and/or the distribution of pore sizes.
- XRD (X-ray diffraction): The characterization of bulk crystal structure and chemical phase composition by diffraction of an X-ray beam as a function of the angle of the incident beam. In the results of enlargement of the diffraction peaks can be estimated crystallite diameter. It can detect crystalline materials having crystal size greater than 3–5 nm.
- XRF (X-ray fluorescence spectroscopy): Quantitative analysis of elements composition in a solid using incident X-ray radiation to eject electrons from inner levels of the atoms.

- TPR (temperature-programmed reduction): The investigation of the reduction rate versus with function of temperature, which allows to study of the oxidation states of the surface and bulk of a solid.
- Chemisorption: It is mostly used for determination of characteristics of catalysts that are important for carrying out chemical adsorption. This makes a very necessary process for products and manufacturing processes that involved chemical adsorption.
- SEM (scanning electron microscopy): It enables the picture of the topography of a solid surface by utilize of backscattered or secondary electrons.
- TEM (transmission electron microscopy): It enables the determination of the microtexture and microstructure of electron transparent samples by transmission of a concerned parallel electron beam to a fluorescent serene, with a resolution presently better than 0.2 nm.
- FTIR (Fourier transform infrared spectroscopy): It analyzes the structures of adsorbed molecules on a catalyst surface under controlled atmosphere conditions. Principally, this technique has the same applications as IR, but FTIR spectrum is higher intensity than that produced by dispersive IR. In addition, FTIR can be used for kinetic studies because of its rapid scanning resonance (1 ms to 1 s).

2.5 Computational chemistry: Quantum Mechanic charged field molecular dynamics (QMCF MD)

2.5.1 Statistical Simulations:

A basic feature of chemical simulations is their foundation in classical physics and the calculation of many particles in order to execute a significant case for their statistical evaluation (63). Nevertheless, the only classical calculation has practical limits; therefore, the quantum mechanics will be a key method whenever high accuracy is required. These statistical methods apply a large number of molecules in a dynamic equilibrium; several types of ensemble are mentioned:

- NVE: constant number of particles, constant volume, constant energy (microcanonical ensemble).
- NVT: constant number of particles, constant volume, constant temperature (canonical ensemble).
- NμT: constant number of particles, constant chemical potential, constant temperature (grand canonical ensemble).

The NVT is definitely the most general for chemical simulations which will ascribe how this ensemble can be controlled in practice – that is, how, besides the number of particles, volume, and temperature are kept constant.

Statistical simulations are commonly applied for the calculation in liquid systems, by disorder of the gas phase combines with the density of solids, thus it makes the complicated liquid state for theoretical treatment. Alternatively, the most chemical reactions occur in solution, and biological processes take place almost in an aqueous environment; therefore, the liquid state is enormously important one for chemistry. When considering force field, the inclusion of solvent can be crucial for the quality of results, and the dynamic nature of salvation makes the statistical simulation methods are mentioned a necessary instrument.

The initial steps to perform a statistical simulation are commonly both of the Monte Carlo and Molecular Dynamics methods:

1. The choice of an appropriate ‘elementary box’
2. The definition of interaction potentials.
3. The generation of a starting structure.

2.5.2 Molecular Dynamics Simulations

Molecular dynamics consider a group of particles and all forces acting on these particles. This method attempts to solve the equations of motion for all the particles which targets a unique trajectory and predicts all future (and past) states of the system. The major difference of Molecular dynamics method compared to Monte Carlo methods is the combination of the time variable, which enables a large amount of data in the system, specifically time and dynamic data.

On the basis of the Lagragian function L=T-V, the Larangian equation of motion is defined by

$$\frac{d}{dt}\left(\frac{\partial L}{\partial \frac{\partial q_k}{\partial t}}\right) - \left(\frac{\partial L}{\partial q_k}\right) = \emptyset \qquad \text{(Eq. 2.36)}$$

where q_k are the simplified coordinates of the particles. Considering a group of atoms or molecules, it labels in Cartesian coordinates with the vectors $|r_i>$ which shows the expression as

$$m_i \frac{\partial^2 |r_i\rangle}{\partial t^2} = |f_i\rangle \qquad \text{(Eq. 2.37)}$$

where m_i is the mass of the i_{th} atom and $|f_i\rangle$ is the force acting on this atom or molecules specified as

$$|f_i\rangle = \nabla_{r_i} L = -\nabla_{r_i} V \qquad \text{(Eq. 2.38)}$$

For calculation in molecules, the center of mass presents its 'coordinate' and $|f_i\rangle$ the total force acting on the molecule.

In N-particle systems, it would have to solve second-order differential equations to compute trajectories with 3 parameters. However, one parameter is replaced by the finite difference tactic in MD simulations, by which determines from the information in the system (positions of particles and velocities) at a given time (*t)* and the values of these quantities at next time (*t + Δt)*. Normally, *Δt* will be less valuable than a typical movement time of a particle in the system. This procedure must use the predictor-corrector algorithm and the Verlet algorithin in practical implementation.

The preparatory MD simulation from an initial configuration, an appropriate number of time steps must be offered to reach an equilibrium state in range of a few ten thousand to hundred thousand steps. MD simulation has some significant different of the equilibration procedure compared with MC simulations. In MC simulation, one particle is moved/rotated every step, whereas in MD simulation, all particles of the system move simultaneously. Another important difference is that temperature is controlled, The Boltzmann factor in the Metropolis algorithm controls

the temperature in the MC simulation, but there is no such control factor to ensure a constant temperature in the MD simulation for the NVT ensemble. Along with statistical thermodynamics, temperature is a function of the velocities of the particles, and this is an easy way to handle temperature by balancing the velocities of all particles to maintain temperature constant. This process calls Berendsen algorithm corresponding to the action of an external bath to ensure isothermal state. This scaling is used in every time step which starts from the assessment of the kinetic energy as follow in (Eq. 2.39). And the scaling factor for the velocities (λ) is ascribed as (Eq. 2.40).

$$E_{kin} = \sum_i^N \frac{m_i v_i^2}{2} = \frac{3}{2} NKT \qquad \text{(Eq. 2.39)}$$

$$\lambda = \sqrt{1 + \frac{\Delta t}{\tau}\left(\frac{T}{T_o} - 1\right)} \qquad \text{(Eq. 2.40)}$$

where τ is a relaxation time, commonly chosen in the subpico- or pico-second range, and T_o is the temperature to be maintained. Although, other equivalent procedures are available to handle temperature, the Berendsen algorithm seems to be the most generally used.

The sampling phase will begin when equilibration has been accomplished. In the system of simulation, that the number of time steps require for sampling depends on the quantity of different species and their percent occurrence of data that wants to determine. In particular, if dynamic solution or structural of macromolecules require for investigation in the limit of time; therefore, one important reason should remind as preventing for long simulation times.

In the MD simulations, the trajectory is equivalent to the history file (i.e. coordinates, energies, the velocities and other dynamic data) which is stored much data, thus significantly increasing the total amount of storage also required. On the other hand, these additional data obtain much more information in the simulation than the MC simulation which could provide.

2.5.3 Quantum Mechanical Simulations

Generally, an accuracy of simulations depends on the potential functions which is calculated the energy or the forces. Even if the corresponding potential functions have been formed on the basis of *ab initio* to calculate energy surfaces for pair and 3-body interactions, in particular a liquid or a solution, the accuracy may not be enough for clear explanation of a chemical system. The reasonable solution to solve problem will evaluate all energies/forces by quantum mechanical methods in every step of the simulation, which would automatically consider all relevant polarization effects, occurring charge transfers and higher n-body effects. But, a little estimation of the required computational effort for such a procedure demonstrates that this is very difficult for the computing resources available today. Therefore, cooperation of computer must be required, and the parameters to correct the computational effort to a suitable extent are the accuracy of the quantum mechanical formalism and the size of the elementary box. The simulation would have to determine the sufficient accuracy of the calculation (as determined by quantum chemical methodology and box size) and the suitable calculating time, so Scylla and Charybdis situation has been used in generally. Although the computers are more advanced in terms of processor speed and lower cost, the computational chemist is still facing a limitation in the application of quantum mechanical simulations. Although parallel processing is helpful, it is not a complete solution for the quantum mechanical part.

In present situation, another compromise solution has been developed and has proven very successful. Instead of reducing the accuracy of the quantum mechanical method and/or the size of the elementary box (both of which would seriously deteriorate the simulation quality), the alternative way to improve the method is the separation of elementary box into two regions. The inner region which contains the chemically most relevant part of the system is treated by quantum mechanics at a sufficiently complicated level, whereas the remaining part of the elementary box is treated by conventional, potential-based molecular mechanics. These methods are usually called QM/MM.

This approach was first applied to large biomolecules, where the active center required a better description than force fields could provide. In the meantime, a

similar methodology has been developed for simulations of liquid systems and solutions that the QM/MM simulations would almost be a universal tool, supplying greatly accurate data for the liquid state. A second way to seek a compromise between accuracy and computational effort has been proposed in the form of MD simulations of relatively small molecular clusters based on density functional calculations of the forces.

2.5.4 *Ab initio* QM/MM Simulation

The QM / MM simulation system which applied by the separation of the QM and MM regions can be used both in MC and MD simulations. In the latter, more demand in terms of computer time must be required because a quantum mechanical calculation of forces will be undertaken in addition to the energy calculation. Despite the disadvantages, most QM / MM studies are conducted on the molecular dynimics in order to get access to data based on time. As mentioned above, the original method was used in the simulations of biomolecules. If a metal center is applied, then density functional methods can be alternative choice of computational simulation. However, the quality of the results depends on the suitable method, and the best functional usually do not help to save computer time in comparison with ab initio HF or even MP/2 methods.

The possibility of *ab initio* QM/MM simulations is strongly determined by the level of theory, the size of the QM region, and the selection of the basis sets. In addition to, experience has shown that the choice of basis sets is the most important point, and strongly determines the reliability of the simulation results. Double-zeta basis sets seem to be the minimal requirement, enhanced in most cases by polarization and/or diffuse functions.

An outline of the QM/MM MD formalism will discuss some further details of the methodical problems. Figure 2.8 shows the separation of a typical QM/MM simulation, presenting the spherical QM region within the cubic elementary box.

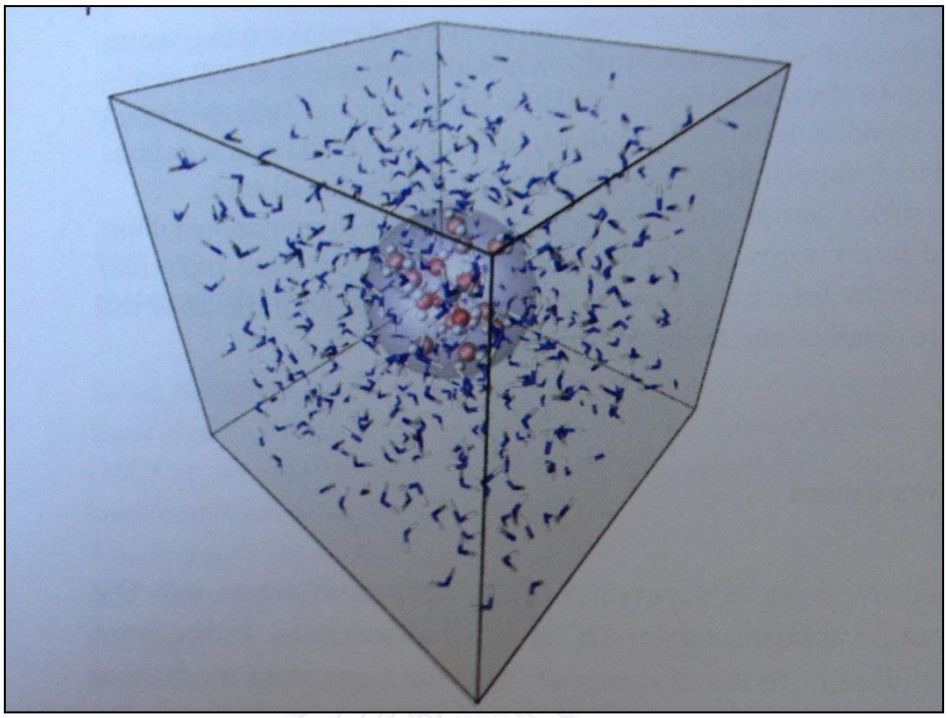

Figure 2.8 Separation scheme of a typical QM/MM simulation, presenting the spherical QM region within cubic elementary box (63)

In this scheme the forces are calculated according to

$$F_{tot} = F_{MM}^{sys} + \left(F_{QM}^{QM} - F_{QM}^{MM}\right) \cdot S(r), \qquad \text{(Eq. 2.41)}$$

where F_{tot} is the total force of the system, F_{MM}^{sys} is the MM force of the whole system, F_{QM}^{QM} is the QM force in the QM region, and F_{QM}^{MM} is the MM force of the QM region. F_{QM}^{MM} is an explanation for the coupling between the QM and MM regions. To ensure a smooth transition and continuous change of forces between the QM and MM regions, a smoothing function S(r) should be employed between the radius r_{on} and r_{off}, the difference of which is usually 0.2Å. This smoothing function is followed as Eq. 2.42.

$$S(r) = \begin{cases} 0 & for\ r < r_{on} \\ \frac{\left(r_{off}^2 - r^2\right)^2 \left(r_{off}^2 + 2r^2 - 3r_{on}^2\right)}{\left(r_{off}^2 - r_{on}^2\right)^3} & for\ r_{on} < r < r_{off} \\ 1 & for\ r > r_{off} \end{cases} \qquad \text{(Eq. 2.42)}$$

This is a particular importance when particles move between the QM and MM regions during the course of the simulation (larger molecules transiting the border imply more difficulties in achieving smooth transition).

Another problem which is clearly recognizable from the image in Figure 2.8 develops in the treatment of large biopolymers, where the QM region is only a subregion of this molecule. In this case, the separation of the QM and MM regions will cut through covalent bonds, unlike a liquid, where relatively small and weakly interacting molecules are either inside or outside the QM region. To solve this problem, the covalent bonds affected by the separation can be broken and the open valences closed by dummy atoms (usually hydrogen), at the price of a significant change of the chemical system investigated.

All types of QM/MM simulation are still extremely time-demanding, lasting from a few weeks to several months on a multi-processor, high-performance computer. The simulation time covered by this effort will still be in the picoseconds range (10-50 ps), if the time step width is selected in the sub-femtosecond range to allow for explicit movements of hydrogen atoms. On the other hand, the correct evaluation of dynamical data requires the accuracy of *ab initio* simulations, as many examples have recently presented. As already indicated, however, the quick development of computer technology and speed will most definitely lead to a rapid improvement of the simulation. One can expect, therefore, that in the near future *ab initio* simulations will become possible for systems with a large QM region and at higher levels of theory, using standard computational equipment.

Some recent methodical improvements of QM/MM simulations have also covered the way for the simulation of more complex compounds, and without the need of any potential functions except that for solvent-solvent interactions. The Quantum Mechnical Charge Field (QMCF) MD method is an example, where this improvement is achieved by a substantial extension of the QM region, a continuous consideration of the fluctuating charges within this region, and an integration of the charges in the MM region.

2.6 Literature reviews

2.6.1 Hydrogen production: Carbon dioxide reforming of methane

Laosiripojana *et al.* (64) studied the doping an additive promoter as CeO_2 on Ni/Al_2O_3 that was found to improve dry reforming activity for H_2 and CO productions at solid oxide fuel cell (SOFC) operating temperature (800–900 °C). The catalyst provides significantly higher reforming reactivity and resistance toward carbon deposition compared to conventional Ni/Al_2O_3. These enhancements are mainly due to the influence of the redox property of ceria. During dry reforming process, in addition to the reactions on Ni surface, the gas–solid reactions between the gaseous components presented in the system (CH_4, CO_2, CO, H_2O, and H_2) and the lattice oxygen on ceria surface also take place. The reactions of adsorbed methane and carbon monoxide (produced during dry reforming process) with the lattice oxygen on ceria surface can prevent the formation of carbon species on Ni surface from methane decomposition and Boudard reaction. In particular, CeO_2 doped Ni/Al_2O_3 with 8% ceria content showed the best reforming activity among those with the ceria content between 0 and 14%. The amount of carbon formation decreased with increasing Ce content.

Gonzalez-Delacruz *et al.* (65) studied of several catalysts of Ni-CeO_2 active for dry methane reforming process. The use of Ni as active phase is highly preferred, although its main lack is the coke formation on the surface of Ni metal particles, resulting in a severe deactivation. A new synthesis method that allows a simple, effective and fast way to prepare Ni-CeO_2 catalysts, in a wide range of metallic loadings, resulting in all the cases in well-formed NiO crystallites with sizes in the range of 12 nm to 18 nm. CeO_2 has been reported to have an intrinsic activity in the CH_4 reforming reaction. Besides the metallic loading, several factors that control the preparation method of the catalyst have been varied, in order to optimize their performance. Most of the catalysts prepared show a good stability on long periods of time and severe conditions. Nevertheless, formation of some carbon nano-fibers has been observed, which could result in a drawback for their application at large scale.

Kim *et al.* (66) studied the properties of a $Ni_{10}Ce_{90}$ mixed oxide relative to a Ni/Al_2O_3 catalyst and its catalytic deactivation for the CO_2 reforming of methane was investigated by XRD, XPS, pulse experimentation, and regeneration tests. Based on the results, The rapid activation of $Ni_{10}Ce_{90}$ is based on the active interfacial oxygen in the Ni–Ce boundary, which leads to the complete oxidation of methane and the creation of active sites for the subsequent reforming reaction, whereas a slow decomposition of $NiAl_2O_4$ spinel results in a long induction period of the Ni/Al_2O_3 catalyst. The coking resistance as well as the catalytic activity relies on the reactivity of lattice oxygen in the ceria. The ceria lattice oxygen participates in the reforming reaction through migration, which leads to the formation of oxygen vacancies. Subsequently, the vacancies are completely supplemented by oxygen arising from the dissociative adsorption of CO_2.

Daza *et al.* (67) studied Ni/Mg/Al/Ce mixed oxides which synthesized by thermal decomposition of layered double hydroxide-type compounds, which were obtained by the coprecipitation method at constant pH. The effect of the Ni^{2+} and Ce^{3+} incorporation methods in the hydrotalcite-type structure was studied. The solids were characterized using chemical analysis by X-ray fluorescence (XRF), X-ray diffraction (XRD), thermogravimetric analysis (TGA–DTG), diffuse reflectance infrared spectroscopy (DRIFT), temperature programmed reduction (TPR-H2), BET surface areas and scanning electron microscopy (60). The methane reforming reaction was carried out at 700 °C. The results demonstrate the formation of solids with mixed crystalline phases of NiO–MgO (periclase) type and CeO_2 (fluorite) as well as other types of reducible species. Catalysts with CH_4 conversions of 50–80%, CO_2 conversions of 80–90%, CO selectivities of 20–40% and H_2 of 18–30 % and high stability under the reaction conditions were obtained.

Kambolis *et al.* (68) studied the nickel catalysts supported on binary CeO_2-ZrO_2 which prepared and evaluated regarding their catalytic performance for the CO_2 reforming of CH_4 (Dry Reforming). The textural and structural properties of catalysts and supports were studied in their calcined, reduced and used state. It found that zirconium improves the textural properties of the CeO_2-ZrO_2 supports and the corresponding catalysts and enhances their textural stability under thermal reductive treatment. XRD analysis shows the formation of $Ce_xZr_{1-x}O_2$ solid solution for all

Ce/(Ce+Zr) ratios. Considerable alterations in the electronic environment of the cations and increased lattice defects in the binary solid solutions were detected by UV-vis DR spectroscopy. A significant increase in the reducibility of both supports and catalysts is observed in the presence of Zr. Compared to the zirconia-free sample, the Ni/CeO_2-ZrO_2 catalysts exhibited much higher activity for the title reaction, accredited to the increase of the surface concentration of the active sites. However, the amount of carbonaceous deposits is not straightforward related to the activity but depends on the Ce/Zr ratio. Among the zirconium containing catalysts, the zirconium-rich one exhibited the higher activity and the stronger resistance to the formation of carbonaceous deposits.

Cui *et al.* (69) studied the effect of La_2O_3 contents on the intrinsic activity of Ni active sites for the CO_2 reforming of CH_4 on Ni/La_2O_3. The Ni particle sizes were decreased with increasing La_2O_3 contents. And the 4-La catalyst had the most Ni–H species. The Ni active sites on the 4-La catalyst showed the highest reforming activity and the lowest activation energy. Among CH_4, CO_2, CO, and H_2, only CH_4 reaction orders were not zero and they were affected by the La_2O_3 contents. In 550–600 °C, the CH_4 dissociation is a rate-determining step for the reforming reaction on the Ni/La_2O_3/γ-Al_2O_3 catalysts. The 4-La catalyst gave the highest reforming activity because the CH_4 dissociation was a structure sensitive reaction and 4-La catalyst has the most suitable Ni particle size. In 650–750 °C, the CH_4 dissociation and the formation of Ni–H reached equilibration and the reaction between CH_x species with $La_2O_2CO_3$ became the rate-determining step. The 4-La catalyst with the most Ni–H could keep the highest x value of CH_x intermediates, leading to the highest reforming activity in 650–750 °C. Therefore, the La_2O_3 contents on the catalysts tuned the Ni particle sizes and Ni–H amounts on the catalysts, which lead to higher reforming activity on the 4-La catalyst.

Xu *et al.* (70) studied the $Ce_{1-x}Ni_xO_2$ oxides with vary x from 0.1 to 0.5 were prepared by precipitation and characterized by XRD, TPR and XPS techniques. Three kinds of Ni phases co-exist in $Ce_{1-x}Ni_xO_2$ catalysts are (i) aggregated NiO on the support CeO_2, (71) highly dispersed NiO with a strong interaction with CeO_2 and (iii) Ni atoms incorporated into the CeO_2 lattice that forms the solid solution. For the reforming of methane with CO_2 and O_2, the $Ce_{1-x}Ni_xO_2$ oxides prepared by

precipitation are superior catalysts, which had a high catalytic activity and thermal stability, especially $Ce_{0.8}Ni_{0.2}O_2$. The catalytic activity is affected by the Ni dispersion on the surface of the catalyst. The Ni–CeO_2 solid solution formed by the Ni species incorporated into CeO_2 promotes the capability of coking resistance.

2.6.2 CO clean-up: water-gas shift and preferential oxidation reaction

Deng *et al.* (72) studied the low-content (<0.6 at.%) gold-ceria samples which prepared by one-pot synthesis by the urea gelation/co-precipitation method, and by sodium cyanide leaching of high-content (5 at.%) gold-ceria materials prepared by deposition–precipitation. These catalysts, containing cationic gold in ceria, are active for both the low-temperature water–gas shift (WGS) reaction and the preferential oxidation of CO (PROX). The surface oxygen of ceria, as estimated by H_2-TPR, was used to normalize the WGS reaction rates. Cyclic temperature-programmed reduction with intermittent reoxidation showed that the surface structures of gold-ceria catalysts are highly reversible. Considerable reoxidation by oxygen or H_2O can occur even at ambient conditions. The stability of low-content gold-ceria catalysts for the PROX reaction in a realistic fuel gas mixture containing 1% CO, 0.5% O_2, 50% H_2, 10% H_2O, 15% CO_2, and He balance. No drop in activity or selectivity was found in cyclic operation up to 150 °C.

Idakiev *et al.* (73) studied the gold catalytic system prepared on ceria-modified mesoporous titania (CeMTi) used as water-gas shift (WGS) reaction. Ceria modifying additive was deposited on Mesoporous titania by deposition precipitation (DP) method. Gold-based catalysts with different gold content (1–5 wt.%) were synthesized by DP of gold hydroxide on mixed metal oxide support. The catalytic behavior of the gold-based catalysts was evaluated in WGS reaction in a wide temperature range (140–300 °C) and at different space velocities and H_2O/CO ratios. The influence of gold content and particle size on the catalytic performance was investigated. The WGS activity of the new gold/ceria-modified mesoporous titania catalysts was compared with that of gold catalysts supported on simple oxides CeO_2 and mesoporous TiO_2. A high degree of synergistic interaction between ceria and mesoporous titania and a positive modification of structural and catalytic properties

by ceria has been achieved. It is clearly revealed that the ceria-modified mesoporous titania is of much interest as potential support for gold-based catalyst.

Fu *et al.* (74) studied the nanostructured of Au–ceria catalyst for low-temperature water-gas shift (LTS). Gold–ceria was prepared by deposition–precipitation (DP), coprecipitation (75), and gelation methods. The gold loading was varied between 1% and 8.3%, while lanthanum used as a dopant in ceria, was 4% or 10%. Most gold is in metallic state, but ionic gold was also present as identified by XPS. The average ceria crystallite size in samples prepared by gelation was 4.5 nm and 7 nm, respectively, after calcination at 400 or 650 °C. The gold particle size in samples prepared by DP was <5 nm after 10 h long heating in air at 400 °C. The gold particle size did not increase with gold loading in these samples. A dramatic effect of gold on the reducibility of the surface oxygen of ceria was found by H_2- TPR. All of the available surface oxygen was reduced, while there was no effect on the bulk oxygen of ceria. The enhancement of cerium oxide reducibility by gold is independent of the method of catalyst preparation. Carbon-containing species left on the surface after the CO step, can be fully removed with O_2 or partially removed with H_2O.

Fu *et al.* (76) studied the high activity and stability of low-content gold–cerium oxide catalysts for the water–gas shift reaction. Low-content (0.2% to 0.9%) gold–ceria samples were prepared by single pot synthesis by the urea gelation/coprecipitation method; and by sodium cyanide leaching of high-content (2% to 8%) gold–ceria materials prepared by various techniques. Gold is present in oxidized form, as verified by a variety of analytical techniques. However, these materials display the same WGS activity as the high-content gold ones, and remain free of gold nanoparticles after use in a reaction gas stream composed of 11% CO, 26% H_2O, 26% H_2, 7% CO_2 and balance He up to 300 °C. The turnover frequency of WGS under the assumption of fully dispersed gold is the same for a variety of low-content gold–ceria preparations. The stability of gold–ceria in various gas compositions and temperatures was good. The most serious stability issue is formation of cerium hydroxyl carbonate in shutdown operation.

Avgouropoulos *et al.* (77) studied the catalytic performance of ceria-supported gold and copper oxide catalysts for the preferential CO oxidation (PROX) in the presence of excess hydrogen. The catalytic properties are strongly affected by

the synthesis procedure, i.e. deposition–precipitation (DP) and modified deposition–precipitation (MDP), mainly in the case of gold. The DP method leads to the preparation of more active PROX catalysts than the MDP one. Highly dispersed and more easily reducible gold or copper oxide species are formed on the catalyst surface and enhance the catalytic activity. Au/ceria catalysts are significantly more active, while CuO/ceria ones are remarkably more selective. The presence of CO_2 and H_2O causes a significant decrease in the catalytic activity, especially in the case of the gold catalyst. However, this deactivation is fully reversible. Both catalysts exhibit a perfectly constant behavior with the reaction time.

Manzoli *et al.* (78) studied the nanosized gold catalysts supported on doped ceria which prepared by deposition-precipitation method. Doping of ceria affected in different way catalytic activity towards purification of H_2 via preferential CO oxidation. The following activity order was observed: Au/Zn-CeO_2 > Au/Sm-CeO_2 > Au/CeO_2 > Au/La-CeO_2. The differences in CO oxidation rates were ascribed to different concentration of metallic gold particles on the surface of Au catalysts. Gold catalysts on modified ceria showed improved tolerance towards the presence of CO_2 and H_2O in the PROX feed. The spectroscopic experiments evidence enhanced reactivity when PROX is performed in the presence of H_2O already at 90 K.

2.6.3 Quantum mechanics charge field molecular dynamics

Rode *et al.* (79) had developed the new formalism for quantum mechanical/molecular mechanical (QM/MM) dynamics of chemical species in solution. Maintains all the advantages of large simulation boxes and ensures the accuracy of *ab initio* quantum mechanics for all forces acting in the chemically most relevant region. Solvent-solvent interaction molecules are incorporated by a dynamically adjusted force field corresponding to the actual molecular configuration of the simulated system and charges derived from the electron distribution in the solvate. The new formalism has been tested with some examples of hydrated ions, for which accurate conversional *ab initio* QM/MM simulation have been previously performed, and the comparison shows equivalence and in some aspects superiority of the new method.

Vchirawongkwin *et al.* (80) studied the structural and dynamical properties and vibrational spectra of bisulfate ion in water by *ab initio* quantum mechanical charge field molecular dynamics. The averaged geometry of bisulfate ion supports the separation of six normal modes of the $O^*–SO_3$ unit with symmetry form three modes of the OH group in the evaluation of vibrational spectra obtained from the velocity autocorrelation functions (VACFs) with subsequent normal coordinate analyses. The calculated frequencies are in good agreement with the observations in Raman and IR experiments. The mean residence time in the individual sites reveals a more complex behavior of them, in particular a strong interaction with a water molecule at the hydrogen site.

Canaval *et al.* (81) studied structural and dynamical properties of Er(III) ion by *ab initio* quantum mechanical charge field molecular dynamics (QMCF-MD) for ground and excited state. The simulation found ligand exchange and observed coordination number between eight and nine in both cases. The strength of the Er-ligand bond is considerably lower than that of trivalent transition metal ions but higher than La(III) and Ce(III) in aqueous solution. The ground state and excited state showed a different of ligand exchange rate of the first shell while the second shell was stable.

CHAPTER 3

METHODOLOGY

In this chapter, materials in this dissertation are shown in section 3.1. Experiment procedure was divided in four parts; dry reforming of methane process, water gas shift process, preferential oxidation process and quantum mechanics charge field simulation, which explains in section 3.2.

3.1 Materials & Flow diagram

3.1.1 Chemicals

- Gold (III) chloride trihydrate ($HAuCl_4.3H_2O$) from Sigma-Aldrich
- Copper (II) nitrate trihydrate ($Cu(NO_3)_2.3H_2O$) from Merck
- Cerium (III) nitrate hexahydrate ($Ce(NO_3)_3.6H_2O$) from Merck
- Zinc (II) nitrate tetrahydrate ($Zn(NO_3)_2.4H_2O$) from Merck
- Ferric (III) nitrate nonahydrate ($Fe(NO_3)_3.9H_2O$) from Merck
- Manganese (III) nitrate dihydrate ($Mn(NO_3)_3.2H_2O$) from Merck
- Nickel (II) nitrate hexahydrate ($Ni(NO_3)_2 \cdot 6H_2O$) from Ajax Finechem Pty. Ltd.
- Cerium (III) oxide anhydrous (CeO_2) from Riediel-de Haën
- Sodium carbonate anhydrous (Na_2CO_3) from APS Finechem
- XINTAO Molecular sieve 5A from GrandBiz Trading Co.,ltd

3.1.2 Gases

- Ultra high purity He from Thai Industrial Gases Public Co., Ltd.
- High purity H_2 from Thai Industrial Gases Public Co., Ltd.
- 10% CO in He from Thai Industrial Gases Public Co., Ltd.
- 5% O_2 in He from Thai Industrial Gases Public Co., Ltd.
- 20% CO_2 in He from Praxair (Thailand) Co., Ltd.
- Compressed CH_4, manufactured by The BOC Group, Inc.

3.1.3 Equipment

- Mass flow controller, AALBROG model: GFC 1715
- Temperature controller equipped with thermocouple and solenoid electric furnace
- Syringe pump
- Stainless steel 316 tube, fitting, and valve, Swagelok
- 1/4 inch and 3/8 inch I.D. quartz tubes
- Heating tab
- Pressure gauge
- Glass water trap
- Electric oven
- Static air muffle furnace
- Regulator
- Gas chromatography (GC), Thermo Finnigan 2000 and Algilent Technologies 6890N

3.1.4 Flow diagram

In this thesis, the equipment contains 3 major parts including DRM, WGS and PROX as shown in Figure 3.1. The carbon dioxide component in the effluent of WGS1 stage, WGS2 stage, and PROX stage was captured by a unit of CO_2 trap before further routing to the next stage. Furthermore, the water trap was used in last unit prior to investigate the gas composition by Gas Chromatography.

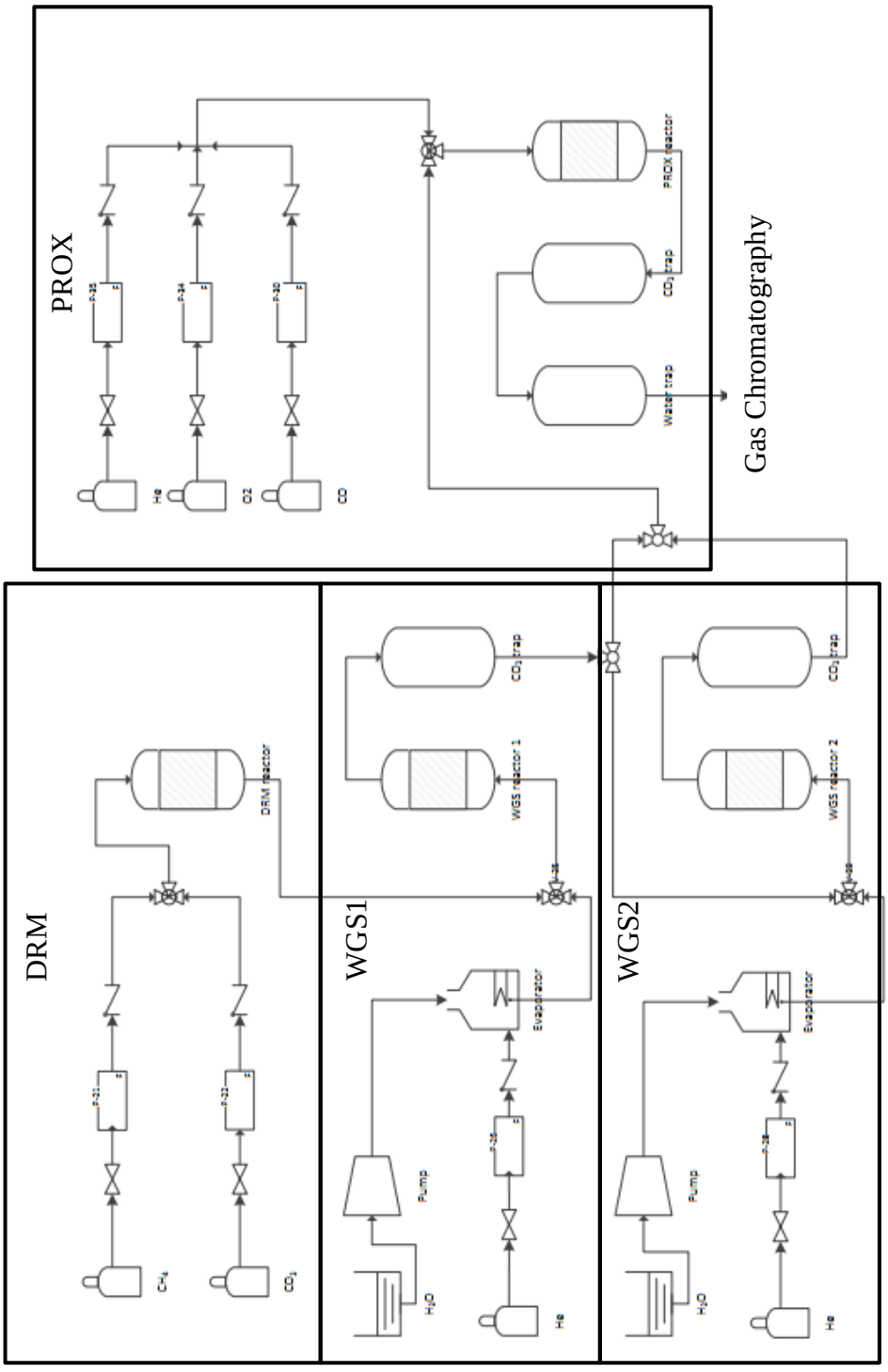

Figure 3.1 Process flow diagram of fuel processor

3.2 Experiment procedure

3.2.1 Methane reforming with carbon dioxide (Dry Reforming)

- Catalysts preparation

The catalysts were prepared by slurry impregnation method (82, 83). The calculated volume of active metal precursor as $Ni(NO_3)_2 \cdot 6H_2O$ 0.5 M was gradually dropped into a beaker of ceria-supported commercial (Riedel-de Haëh) at 60 °C during stirring at 60 rpm until the slurry was dried. To study the effect of additive promoter, the precursor either $Mn(NO_3)_2$ 0.1 M or $HAuCl_4$ 25 g/L was mixed with Ni-precursor before dropping to the beaker contained ceria-supported. The catalysts were denoted as $xNi\text{-}yMn/CeO_2$ or $xNi\text{-}yAu/CeO_2$ where x and y represented as % loading weight of Ni and % loading weight of promoter, respectively. Then, solid powder was dried overnight at 110 °C and followed by calcining at 700 °C for 5 h in air to eliminate anion precursor.

- Catalysts characterization

The crystalline structure was determined by X-ray diffractometry (XRD) using a Rigaku X-ray diffractometer system equipped with a RINT 2000 wide-angle goniometric and using CuK_α radiation (λ = 1.54 Å) and a power of 40 kV × 30 mA. The particle diameter was calculated by the Debye-Scherrer equation at the main X-ray line broadening in each phase. The reduction temperature of the catalysts was measured by temperature-programmed reduction (TPR) with pure H_2 between 100 °C to 700 °C. The particle morphology of the catalysts was observed by transmission electron microscopy (TEM) using a JEM 2010 TEM microscope operating at 200 keV in bright and dark field modes. Themogravimetric analysis (84) was used to detect carbon deposition in catalysts in O_2 air.

- Catalytic activity measurement

Catalytic activities were tested in a packed-bed reactor with 3/8 inches inner diameter quartz tube. A desire sample of the catalysts (50 mg, 100 mg and 150 mg) was packed between two layers of glass wool. The reaction temperature was controlled in a range of 500 °C to 900 °C. The feed stream composed of methane and carbon dioxide. The conditions of $CH_4/(CH_4+CO_2)$ mole ratio was maintained at 0.5. The total flow rate was hold at 60 ml/min. The catalytic activities were operated under atmospheric pressure. The reactant and product gases were analyzed by an online gas chromatography equipped with a packed carbosphere column, 80/100 mesh, and a thermal conductivity detector (TCD). The activity parameters were represented in term of CH_4 conversion (%), CO_2 conversion (%), H_2 selectivity and Carbon deposition (%) as shown in equations (3.1) – (3.4), respectively.

$$CH_4\ conversion\ (\%) = \frac{F_{in}\times[CH_4]_{in} - F_{out}\times[CH_4]_{out}}{F_{in}\times[CH_4]_{in}} \times 100 \quad \text{(Eq. 3.1)}$$

$$CO_2\ conversion\ (\%) = \frac{F_{in}\times[CO_2]_{in} - F_{out}\times[CO_2]_{out}}{F_{in}\times[CO_2]_{in}} \times 100 \quad \text{(Eq. 3.2)}$$

$$H_2\ seletivity\ (\%) = \frac{1}{2} \times \frac{F_{out}\times[H_2]_{out}}{F_{in}\times[CH_4]_{in} - F_{out}\times[CH_4]_{out}} \times 100 \quad \text{(Eq. 3.3)}$$

$$Carbon\ deposition\ (\%) = \frac{[(moleC_{in}) - (moleC_{out})]\times MW_{carbon}}{W_{catalysts}} \times 100 \quad \text{(Eq. 3.4)}$$

where F_{in} and F_{out} are the inlet and outlet flow rate (ml/min), $[CH_4]_{in}$ and $[CH_4]_{out}$ are the fraction of CH_4 in the inlet and outlet gas component, $[CO_2]_{in}$ and $[CO_2]_{out}$ are the fraction of CO_2 in the inlet and outlet gas component, $[H_2]_{out}$ is fraction of H_2 outlet gas component, $moleC_{in}$ and $moleC_{out}$ are mole of carbon from inlet and outlet gas component. MW_{carbon} means molecular weight of carbon atom and $W_{catalysts}$ is catalysts weight in gram unit (g).

A description of each parameter explains a catalytic activities feature. Methane conversion directly represents to the methane decomposition that could imply an amount of hydrogen production whereas carbon dioxide conversion relates to a depressed of coke formation as reverse Boudouard reaction. Hydrogen selectivity displays the ratio of H_2/CO product concerning to an ability of catalysts. Carbon deposition was calculated by carbon balance of the system relating to the coke

formation which was investigated by TGA. Even though, carbon deposition is not an exact value comparing with the coke formation, it still represents the trend of coke formation correlating to stoichiometry calculation. This is also wide popular accepted (64, 85).

- Experimental design and statistical analysis for optimization condition

To study an important effect on the catalytic performance of catalysts which expressed higher conversion but lower carbon deposition in their activities, experimental design was then applied. A full factorial design of 4 factors at three levels, including 2 center points were matrices in the complete randomized design as given in Table 3.1. The factors including temperature (denoted as factor A), methane composition fraction (denoted as factor B), catalysts weight (denoted as factor C), and total feed rate (denoted as factor D) were in the range of 700 °C to 900 °C, 0.3 to 0.7, 0.05 g to 0.15 g, and 30 ml/min to 90 ml/min, respectively. The software package design expert 6.0 (Stat Ease Inc. Minneapolis, USA) was used to treat the data. The CH_4 conversion, CO_2 conversion, H_2 selectivity and carbon deposition were response. An analysis of variance (ANOVA) was used to evaluate the effect factors and regression coefficient. Moreover, the Pareto's chart of absolute standardized effect at P-value = 0.05 also indicated the effect factors. The effect of each factor was tested by student's test with a corresponding P-value—less than 0.05 were considered to be "statistically significant". After screening the significant effect, 3-level design surface analysis was subsequently used in order to achieve the optimal response.

Table 3.1 Three-level factorial design and response surface method

No	A	B	C	D	No	A	B	C	D
1	700	0.3	0.05	30	43	700	0.7	0.1	60
2	800	0.3	0.05	30	44	800	0.7	0.1	60
3	900	0.3	0.05	30	45	900	0.7	0.1	60
4	700	0.5	0.05	30	46	700	0.3	0.15	60
5	800	0.5	0.05	30	47	800	0.3	0.15	60
6	900	0.5	0.05	30	48	900	0.3	0.15	60
7	700	0.7	0.05	30	49	700	0.5	0.15	60

No	A	B	C	D	No	A	B	C	D
8	800	0.7	0.05	30	50	800	0.5	0.15	60
9	900	0.7	0.05	30	51	900	0.5	0.15	60
10	700	0.3	0.1	30	52	700	0.7	0.15	60
11	800	0.3	0.1	30	53	800	0.7	0.15	60
12	900	0.3	0.1	30	54	900	0.7	0.15	60
13	700	0.5	0.1	30	55	700	0.3	0.05	90
14	800	0.5	0.1	30	56	800	0.3	0.05	90
15	900	0.5	0.1	30	57	900	0.3	0.05	90
16	700	0.7	0.1	30	58	700	0.5	0.05	90
17	800	0.7	0.1	30	59	800	0.5	0.05	90
18	900	0.7	0.1	30	60	900	0.5	0.05	90
19	700	0.3	0.15	30	61	700	0.7	0.05	90
20	800	0.3	0.15	30	62	800	0.7	0.05	90
21	900	0.3	0.15	30	63	900	0.7	0.05	90
22	700	0.5	0.15	30	64	700	0.3	0.1	90
23	800	0.5	0.15	30	65	800	0.3	0.1	90
24	900	0.5	0.15	30	66	900	0.3	0.1	90
25	700	0.7	0.15	30	67	700	0.5	0.1	90
26	800	0.7	0.15	30	68	800	0.5	0.1	90
27	900	0.7	0.15	30	69	900	0.5	0.1	90
28	700	0.3	0.05	60	70	700	0.7	0.1	90
29	800	0.3	0.05	60	71	800	0.7	0.1	90
30	900	0.3	0.05	60	72	900	0.7	0.1	90
31	700	0.5	0.05	60	73	700	0.3	0.15	90
32	800	0.5	0.05	60	74	800	0.3	0.15	90
33	900	0.5	0.05	60	75	900	0.3	0.15	90
34	700	0.7	0.05	60	76	700	0.5	0.15	90
35	800	0.7	0.05	60	77	800	0.5	0.15	90
36	900	0.7	0.05	60	78	900	0.5	0.15	90
37	700	0.3	0.1	60	79	700	0.7	0.15	90
38	800	0.3	0.1	60	80	800	0.7	0.15	90
39	900	0.3	0.1	60	81	900	0.7	0.15	90
40	700	0.5	0.1	60	**Addition center points**				
41	800	0.5	0.1	60	82	800	0.5	0.1	60
42	900	0.5	0.1	60	83	800	0.5	0.1	60

Note: A: temperature (°C), B: methane composition fraction, C: catalysts weight (g), D: feed rate (ml/min)

3.2.2 Water-gas shift process

- *Catalysts preparation*

The catalysts were prepared by impregnation method. The calculated volume of 25 g/l of $HAuCl_3.3H_2O$ aqueous solution was pipetted and dropped slowly into a calculated amount of CeO_2 commercial (Riedel-de Haëh) to prepare the desired catalysts. During dropping the solution, the mixture was stirred at 60 rpm until the slurry was dried and was kept at 60 °C. To study the additive promoter, the precursor such as $Mn(NO_3)_2$, $Cu(NO_3)_2$ or $Fe(NO_3)_3$ was mixed with gold precursor before dropped into the ceria-supported. The catalysts were separated into 2 group including high amount of promoter and low amount of promoter. The group of high amount of promoter contained 1%wt. loading of gold and 5%wt. loading of promoter. It denotes as $1Au5M/CeO_2$ (M = Mn, Cu or Fe). Others group had a ratio of gold:promoter as 1:1 denoted as $1\%(1:1)AuM/CeO_2$ (M = Mn, Cu or Fe). Then, the solid powder was dried in the oven at 110 °C overnight and calcined at 500 °C for 5 h in air.

- *Catalysts characterization*

The crystalline structure was determined by X-ray diffractometry (XRD) using a Rigaku X-ray diffractometer system equipped with a RINT 2000 wide-angle goniometric and using CuK_α radiation (λ = 1.54 Å) and a power of 40 kV × 30 mA. The particle diameter was calculated by the Debye-Scherrer equation at the main X-ray line broadening in each phase. X-ray fluorescence (XRF) (PW-2400) data was used to detect the gold and promoter content of catalysts. The Brunauer–Emmet–Teller (BET) method, using a Quantachrome Corporation Autosorb, was used to determine the specific surface area by nitrogen adsorption–desorption at 196 °C.

- *Catalysts activity measurement*

The catalysts activity was tested in a packed-bed column with ¼ inches inner diameter quartz tube. A weight of catalysts (0.1 g) was packed between the layers of glass wool. The feed steam came from outlet stream of dry reforming part. The water feed rate was 1 ml/h which was evaporated at 150 °C and mixed with an

inlet flow before feeding into the reactor. The reactant and product gases were determine by a gas chromatograph equipped with a carbosphere paced column, 80/100 mesh, and thermal conductivity detector (TCD). The activity parameters were represented in term of CO conversion and H_2 yield as shown in (Eq. 3.5) to (Eq. 3.6), respectively.

$$CO\ conversion\ (\%) = \frac{F_{in}\times[CO]_{in} - F_{out}\times[CO]_{out}}{F_{in}\times[CO]_{in}} \times 100 \qquad \text{(Eq. 3.5)}$$

$$H_2\ yield\ (\%) = \frac{F_{out}\times[H_2]_{out} - F_{in}\times[H_2]_{in}}{F_{in}\times[CO]_{in}} \times 100 \qquad \text{(Eq. 3.6)}$$

Each parameter could describe catalytic activities. CO conversion presented the ability of catalysts to convert carbon monoxide in the stream to low level as possible. H_2 yield represented the ability of catalysts to convert the CO via water gas shift reaction which is a desired reaction

- Experimental design and statistical analysis for optimization condition

The study of catalytic performance over water gas shift reaction was observed by and experimental design. A 2^k full factorial design of 3 factors with 1 center point was testing as shown in Table 3.2. The range of temperatures (A) were 250 °C to 450 °C, catalysts weight (B) were 0.1 g to 0.3 g, and water feed rate (C) were 1 ml/h to 3 ml/h. The data was evaluated results by the design expert 6.0 (Stat Ease Inc. Minneapolis, USA).

Table 3.2 The 2^3 full factorial design with 3 center points for screening factor of water-gas shift process

No	A: Temperature (°C)	B: Weight catalysts (g)	C: H_2O feed (ml/h)
1	250	0.1	1
2	250	0.2	1
3	250	0.1	3
4	250	0.2	3
5	250	0.15	2

No	A: Temperature (°C)	B: Weight catalysts (g)	C: H_2O feed (ml/h)
6	350	0.1	2
7	350	0.2	2
8	350	0.15	1
9	350	0.15	3
10	350	0.15	2
11	350	0.15	2
12	350	0.15	2
13	450	0.1	1
14	450	0.2	1
15	450	0.1	3
16	450	0.2	3
17	450	0.15	2

Table 3.3 FCC response surface analysis with 5 center points of WGS process

No	A: Temperature (°C)	B: Weight catalysts (g)
1	250	0.1
2	250	0.2
3	250	0.15
4	350	0.1
5	350	0.2
6	350	0.15
7	350	0.15
8	350	0.15
9	350	0.15
10	350	0.15
11	450	0.1
12	450	0.2
13	450	0.15

After screening of the significant effect with full factorial, then face-center-cubic design for surface analysis was performed to reach the optimal condition for operating as shown in Table 3.3.

3.2.3 Preferential oxidation process

- *Catalyst preparation*

Au/CeO_2 catalyst was synthesized by deposition-precipitation method, as mentioned in our previous work (86). Ceria support was prepared by precipitation method. Precursor of $Ce(NO_3)_3.6H_2O$ was precipitated by a drop wise of 0.1 M Na_2CO_3 in gentle sturing at 70 °C and pH 9 for 1 h. Then, a suspend solid was washed by de-ionized water until no conductivity and dried at 110 °C overnight. The dried suspend was calcined at 500 °C for 5 h. Take the support into a beaker of water at constant ratio of support (g) per water (ml) equaled to 1:100. A precursor of $HAuCl_4$ was prepared and a Na_2CO_3 aqueous solution was added simultaneously to adjust the pH in solution at 7. After that, the suspension was continuously stirred for 1 h at 70 °C. The precipitated solid was washed by de-ionized water until no chlorine ions which was detected by $AgNO_3$ solution. The sample was dried overnight at 110 °C in air and calcined at 350 °C for 2 h.

- *Catalytic activity measurement*

The Au/CeO_2 catalyst was packed into U-tube reactor (6 mm inner diameters) between quartz wool layers. A thermocouple was placed inside the reactor to control the reaction temperature. The gaseous influent contained 40% H_2, 1% to 2% O_2, 1% CO, 0% to 20% CO_2, 0% to 10% H_2O in helium balance. A total flow rate of the gaseous mixture was operated at atmospheric pressure. The catalytic activity was observed at the range of temperature over 40 °C to 120 °C. The effluent from the reactor was passed through an ice-cooled condenser to trap water vapor before entering the GC (Agilent Technologies 6890N Network GC system) equipped with a thermal conductivity detector (TCD). Helium was employed as the carrier gas. The catalytic activity was reported in term of Conversion, Selectivity, and yield as shown in (Eq. 3.7) to (Eq. 3.9).

$$CO\ conversion\ (\%) = \frac{F_{in}\times[CO]_{in} - F_{out}\times[CO]_{out}}{F_{in}\times[CO]_{in}} \times 100 \qquad \text{(Eq. 3.7)}$$

$$CO_2\ selectivity\ (\%) = \frac{1}{2}\frac{F_{in}\times[CO]_{in} - F_{out}\times[CO]_{out}}{F_{in}\times[O_2]_{in} - F_{out}\times[O_2]_{out}} \times 100 \qquad \text{(Eq. 3.8)}$$

$$\text{yield}\ (\%) = \frac{\text{CO conversion}\ (\%)\times\ CO_2\text{Selectivity}(\%)}{100} \qquad \text{(Eq. 3.9)}$$

where F_{in} and F_{out} are the inlet and outlet flow rate (ml/min) in PROX unit, $[CO]_{in}$ and $[CO]_{out}$ are the fraction of CO in the inlet and outlet gas component, $[O_2]_{in}$ and $[O_2]_{out}$ are the fraction of CO_2 in the inlet and outlet gas component.

- Experimental design and statistical analysis for optimization condition

To study the catalytic performance of Au/CeO_2 catalysts prepared by the deposition-precipitation (DP) method for PROX reaction was observed by experimental design. A full factorial design by 5 factors including 2 center points was tested in the complete randomized as shown in Table 3.4. The factor level was coded in dimensionless co-ordinate as -1, 0, 1. The software package design expert 6.0 (Stat Ease Inc. Minneapolis, USA) was used to treat the data and CO yield was response factors. An analysis of variance presented sum of square, degree of freedom, mean square, F-value, P-value and regression coefficient. The effect of each factor was tested with a corresponding P-value—less than 0.05 was considered to be statistically significant. Moreover, the Pareto chart of absolute standardized effect was an alternative selection of significant effect. After screening the significant effect with the factorial design, the Box–Behnken surface analysis was subsequently used in order to achieve the optimum condition as shown in Table 3.5.

Table 3.4 Full factorial of 5 factors with 2 center points for screening factors of preferential oxidation process in code factor

Factor	variable	unit	Low (-1)	Medium (0)	High (+1)
A	Temperature	°C	40	80	120
B	W/F ratio	g·s/ml	0.001	0.002	0.003
C	O_2/CO ratio	-	1	1.5	2
D	CO_2 added	%	0	10	20
E	H_2O added	%	0	5	10

No	A	B	C	D	E
1	-1	-1	-1	-1	-1
2	1	-1	-1	-1	-1
3	-1	1	-1	-1	-1
4	1	1	-1	-1	-1
5	-1	-1	1	-1	-1
6	1	-1	1	-1	-1
7	-1	1	1	-1	-1
8	1	1	1	-1	-1
9	-1	-1	-1	1	-1
10	1	-1	-1	1	-1
11	-1	1	-1	1	-1
12	1	1	-1	1	-1
13	-1	-1	1	1	-1
14	1	-1	1	1	-1
15	-1	1	1	1	-1
16	1	1	1	1	-1
17	-1	-1	-1	-1	1
18	1	-1	-1	-1	1
19	-1	1	-1	-1	1
20	1	1	-1	-1	1
21	-1	-1	1	-1	1
22	1	-1	1	-1	1
23	-1	1	1	-1	1
24	1	1	1	-1	1
25	-1	-1	-1	1	1
26	1	-1	-1	1	1
27	-1	1	-1	1	1
28	1	1	-1	1	1
29	-1	-1	1	1	1
30	1	-1	1	1	1
31	-1	1	1	1	1
32	1	1	1	1	1
33	0	0	0	0	0
34	0	0	0	0	0

Table 3.5 Response surface of factor A, C and D with 5 center points of preferential oxidation process in code factor

Factor	variable	unit	Low (-1)	Medium (0)	High (+1)
A	Temperature	°C	60	80	100
C	O_2/CO ratio	-	1	1.5	2
D	CO_2 added	%	0	10	20

No	A	C	D
1	-1	-1	0
2	1	-1	0
3	-1	1	0
4	1	1	0
5	-1	0	-1
6	1	0	-1
7	-1	0	1
8	1	0	1
9	0	-1	-1
10	0	1	-1
11	0	-1	1
12	0	1	1
13	0	0	0
14	0	0	0
15	0	0	0
16	0	0	0
17	0	0	0

3.2.4 Integrations of hydrogen production and carbon monoxide clean up

This section, the combination of 3 processes was studied to prove an optimization of each parts which was divided into 2 parts including 1) integration of all processes and 2) improvement of integration process by double stage of water-gas shift

- Integration of all processes

In this part, the reactant including methane and carbon monoxide was fed into the dry reforming process, and then the outlet gas was mixed with vapor and helium passing through water gas shift reactor. After water gas shift process, the outlet component was removed carbon dioxide by CO_2 trap before entering to preferential oxidation process. Prior to PROX reaction, the outlet gas from CO_2 trap was mixed with 5% oxygen in helium, and then the outlet gas from PROX reaction was detected the gas composition by GC. All of process (DRM, WGS, and PROX) operated at optimum condition investigating from experimental design and response surface analysis. A simple of flow diagram in this part is presented in Figure 3.2.

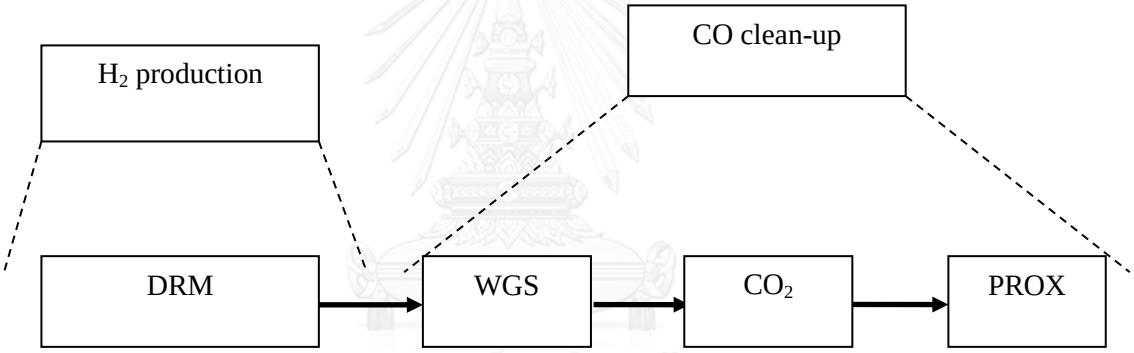

Figure 3.2 Flow diagram of section 1; integration of all processes

- Improvement of integration process by double stage of water gas shift

In this part, to improve the quality of hydrogen product was studied by additional another water-gas shift reaction called double stage of water-gas shift. Each process was operated at the same procedure with optimum condition, except second stage of WGS. The second stage of WGS was studied with 3 factors including temperature (°C), catalysts weight (g) and water feed rate (ml/h) similar to the first stage of WGS. The activity parameters were represented in term of CO conversion

and H_2 yield as shown in (Eq. 3.5) to (Eq. 3.6), respectively, as same as WGS procedure.

Prior to entering 2nd stage of WGS, the gas component was passed through CO_2 trap to set zero percent of CO_2 because the motivation of kinetic to move forward of reaction equilibrium would be required. Then the outlet gas was also passed through another CO_2 trap to remove CO_2 in order to set CO_2-free component again before entering to PROX as well. A flow diagram in this part is presented Figure 3.3. After that, the stability of integration process was tested for 20 h with optimum condition in each part.

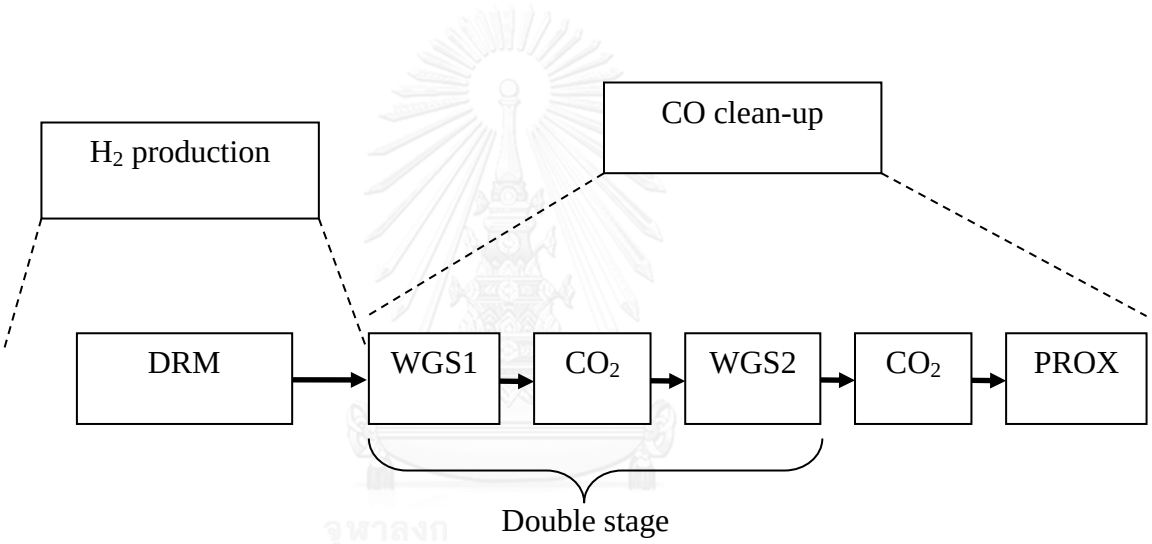

Figure 3.3 Flow diagram of section 2; improvement of integration process by double stage of water-gas shift

3.2.5 Quantum mechanics charged field molecular dynamics (QMCF MD)

In QMCF MD simulation, the layer and core regions were calculated by QM method due to the accuracy for inter-shell boundary and acceptation of ligand exchanging. The charge of all particle in MM region were calculated in Hamiltonian by a perturbation term (87) because of changing behavior in all time in MM simulation making an advantage of explanation of solvent in QM region. The QM will find a new trajectory to optimization by fluctuation from last trajectory (63, 79). Water molecules in MM region were assigned partial charge from flexible BJH-CF2

model (88, 89) to describe MM simulation. Partial charge for molecules in QM region would be calculated every simulation steps by Mulliken population analysis (90, 91) for evaluation of QM-MM Coulombic forces. The forces in each region are ascribed as follow (63):

$$\vec{F}_J^{Core} = \vec{F}_J^{QM} \quad \text{(Eq. 3.10)}$$

$$\vec{F}_J^{layer} = \vec{F}_j^{QM} + \sum_{I=1}^{M} \vec{F}_{IJ}^{BJHnC} \quad \text{(Eq. 3.11)}$$

$$\vec{F}_J^{MM} = \sum_{I=1, I\neq J}^{M} \vec{F}_{IJ}^{BJH} + \sum_{I=1}^{N_1+N_2} \frac{q_I^{QM} q_J^{MM}}{\vec{r}_{IJ}^2} + \sum_{I=1}^{N_2} \vec{F}_{IJ}^{BJHnC} \quad \text{(Eq. 3.12)}$$

$\vec{F}_J^{Core}$ indicates QM forces acting on particle *J* plus interactions between particle *J* and all MM particles. $\vec{F}_J^{layer}$ corresponds to the forces acting on a particle *J* located in the solvation layer with non-Coulombic interactions from BJH-CF2 water model. $\vec{F}_J^{MM}$ is Coulombic interactions between core and MM regions.

Particularly, the migration of particle moving between QM and MM regions are proved to smooth as a smoothing region having a normal length of 0.2 Å as (Eq. 3.13). Where the smoothing factor *S(r)* as follow (Eq. 3.14) to (Eq. 3.16) which *r* is the distance of water molecule from the ion center, r_0 is the QM radius and r_1 is the inner smoothing radius.

$$\vec{F}_J^{smoothing} = \boldsymbol{S(r)}(\vec{F}_J^{layer} - \vec{F}_J^{MM}) + \vec{F}_J^{MM} \quad \text{(Eq. 3.13)}$$

$$\boldsymbol{S(r) = 1}, \qquad \boldsymbol{for}\ \{\boldsymbol{r \geq r_1}\} \quad \text{(Eq. 3.14)}$$

$$\boldsymbol{S(r)} = \frac{(r_0^2 - r^2)^2 (r_0^2 + 2r^2 - 3r_1^2)}{(r_0^2 - r_1^2)^3}, \qquad \boldsymbol{for}\ \{\boldsymbol{r_0 < r \leq r_1}\} \quad \text{(Eq. 3.15)}$$

$$\boldsymbol{S(r) = 0}, \qquad \boldsymbol{for}\ \{\boldsymbol{r < r_1}\} \quad \text{(Eq. 3.16)}$$

Radial distribution functions (RDFs) is basic parameter to calculate forces and structures acting on solvent shell.

A mean residence times of ligand (MRTs), as a study of the dynamical properties of the hydration shell, are calculated via a direct method (90).

$$\boldsymbol{\tau^{0.5}} = \frac{\boldsymbol{t_{sim} CN_{avg}}}{\boldsymbol{N_{ex}^{0.5}}} \qquad \text{(Eq. 3.17)}$$

where t_{sim} defines the simulation time and CN_{avg} indicates the average number of particles in the concerned shell. The number of successful exchanges at 0.5 ps is denoted as $\boldsymbol{N_{ex}^{0.5}}$.

- Method and Simulation protocol

The primary study of CO and 1 water molecule for study the suitable method—such as HF, B3LYP—were calculated by GAUSSIAN03 software package (60).

QMCF MD simulation used the cubic with 24.6 Å lengths and 498 molecules of water with one molecule of carbon monoxide (CO). The charge and multiplicity of CO were 0 and 1, respectively. An equilibrium state was running at 10 ps before sampling the data. The factor of this simulation was canonical ensemble (NVT) system for calculation and time step was set at 0.2 fs. The Berendsen algorithm was a function to control the temperature with relaxation time as 0.1 ps (92). Density of the system was 0.997 g/cm^3 and reaction field method (33) were used for calculation of long-range electrostatic interaction (epsilon = 78.6 and Coulombic cutoff = 12.0). The core radius was setup at 3.0 Å and the layer zone was 3.0 Å to 5.7 Å with smoothing at 5.5 Å to 5.7 Å. The basis set of carbon monoxide and water molecules used DZP-dunning basis set. The data was collected every 5 step until the total sampling time of 16 ps. For water molecules in simulation used flexible BJH-CF2 model which can be moved between QM and MM regions. Turbomole software package (93) was selected to calculate quantum results.

CHAPTER 4

HYDROGEN PRODUCTION AND CARBON MONOXIDE CLEAN UP PROCESS

4.1 Hydrogen production via methane reforming with carbon dioxide (Dry reforming, DRM)

In this section, the hydrogen production via dry reforming of methane with carbon dioxide (DRM) over Ni/CeO_2 based catalysts with either manganese or gold promoter was studied in a range of reaction temperature from 500 °C to 900 °C at atmospheric pressure. Catalysts were synthesized by slurry impregnation method as mentioned in chapter 3. An amount of Ni loading was at 5%, 10%, and 15% by weight. An amount of Mn promoter loading were hold at 0.5%, 5%, and 10% by weight while Au promoter was loaded at 0.1% and 0.5% by weight. The characterization of catalysts is discussed and shown in section 4.1.1. The activities of Ni, Ni-Mn, Ni-Au over CeO_2-supported catalysts are represented in section 4.1.2. The activities were reported in terms of CH_4 conversion, CO_2 conversion, H_2 selectivity and carbon deposition. The catalysts which expressed higher conversion with lower carbon deposition in their activities would be selected to study in the experimental design. The experimental design was used to determine a significant factor(s) on the response and shown in section 4.1.3. Stability of the catalysts is investigated in the section 4.1.4.

4.1.1 Characterization

The XRD pattern of the catalyst is shown in Figure 4.1. The crystallite size of NiO of (1 1 1) and (2 0 0) planes were calculated by Scherrer equation. Nickel oxide peaks of (1 1 1) and (2 0 0) planes presented at 2θ = 38° and 2θ = 43°, respectively. Major of ceria characteristic peaks were attributed to (1 1 1), (2 0 0), (2 2 0), and (3 1 1) crystal planes at 28.6°, 33.1°, 47.5°, and 56.3° of 2θ, respectively. The ceria crystallite size was calculated at (1 1 1) plane which showed a high crystallinity and had a crystallite size around 55 nm of all samples. The diffraction peak of either Mn promoter or Au promoter in Ni/CeO_2 based catalysts was not observed in the XRD patterns. Two probably reasons to explain were that the promoter dispersed well over the catalysts and the crystallite size of the promoter was quite small.

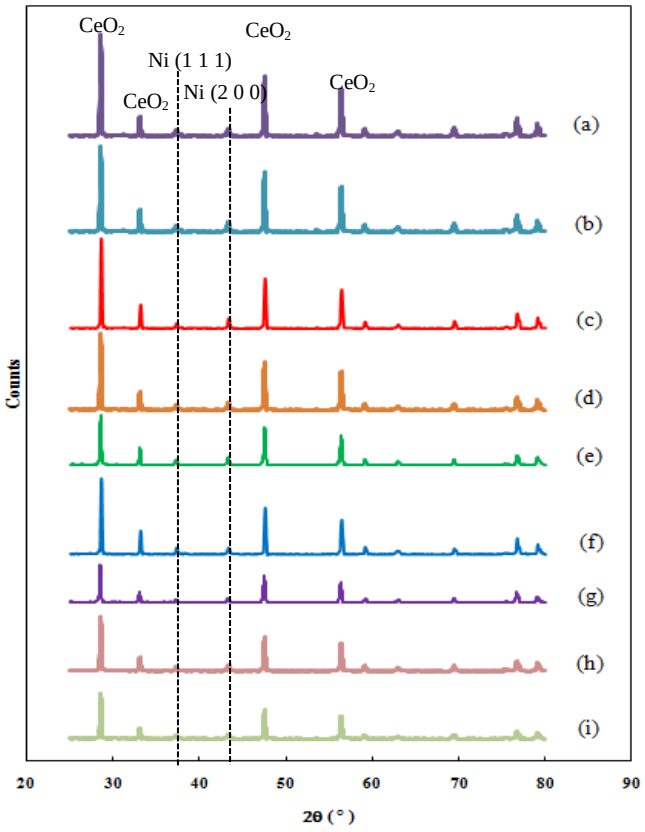

Figure 4.1 XRD pattern of Ni/CeO_2 based catalyst with various promoters: (a) $5Ni/CeO_2$; (b) $10Ni/CeO_2$; (c) $15Ni/CeO_2$; (d) $5Ni\text{-}0.5Mn/CeO_2$; (e) $15Ni\text{-}0.5Mn/CeO_2$; (f) $5Ni\text{-}0.5Au/CeO_2$; (g) $15Ni\text{-}5Mn/CeO_2$; (h) $Spent\text{-}5Ni\text{-}0.5Mn/CeO_2$; (i) $Spent\text{-}10Ni/CeO_2$

Table 4.1 represents crystallite size of nickel oxide of each catalyst. Larger crystallite size of NiO catalysts was obtained when increasing in nickel loading. When small amount of Mn promoter was added into the catalysts, a smaller crystallite size of NiO was achieved. On the other hand, the size of NiO increased when adding Au promoter. It can be suggested that Au and NiO were occurred a metal phase separately. At 15% loading weight of Ni, the average size of NiO catalysts was reduced from 7 nm to 6.3 nm when adding Mn promoter from 0% to 0.5% loading weight. Further adding Mn promoter to 5% loading weight, the average size of NiO catalysts was larger. It can be suggested that an appropriate ratio of Ni to Mn occurred a solid solution phase at low ratio of Mn:NiO (94), but increasing loading of Mn in catalysts would occurred a metal phase of MnO. Therefore, Mn promoter with an appropriate amount should be considered to get a smaller crystallite size of the catalysts. For the spent catalysts, it was found that the crystallite size of NiO was larger compared with fresh catalysts. There is a reason to explain the phenomena as a sintering of NiO in the spent catalysts. So, the sintering more occurred which effected to the larger size of NiO particle when increasing Ni loading from 5% to 10%. For surface area, 5% loading of Ni showed a lower surface area than 10% and 15% due to the optimum loading of Ni was 10% to 15%. The result agrees with Pompeo *et al.* that found 12% by weight of Ni catalysts performing highest methane conversion in dry reforming reaction due to it showed high surface area than other loading.. Surprisingly, 5Ni-0.5Mn/CeO_2 catalyst presented high surface area because NiO particle showed a smaller size than the others which detected by XRD; however, a small amount of Mn did not improve 15Ni-0.5Mn/CeO_2 catalyst. Furthermore, an increasing loading of Mn promoter, the surface area of 15Ni-5Mn/CeO_2 catalyst dropped drastically because higher loading of metal agglomerated a large particle size more easily than low loading. It can be said that Mn promoter can enhance Ni/CeO_2 catalysts at low loading of metal. In case of adding Au, the surface area slightly decreased than 5Ni/CeO_2 catalyst. It can be told that gold did not improve Ni/CeO_2 catalysts in this reaction. It can be concluded that 0.5%wt. of Mn could promote the highest surface as 5Ni-0.5Mn/CeO_2.

Table 4.1 Average crystallite size of nickel oxide (1 1 1) plane, (2 0 0) plane, NiO particle size and surface area in each catalysts in nm

Catalysts	NiO (1 1 1)[a]	NiO (2 0 0)[a]	Average[a]	NiO[b]	S_{BET}[c] (m^2/g)
5Ni/CeO_2	6.1	5.7	5.9	6.7	39.1
10Ni/CeO_2	7.3	6.2	6.8	-	44.2
15Ni/CeO_2	7.3	6.6	7.0	-	43.0
5Ni-0.5Mn/CeO_2	5.2	5.3	5.3	6.3	43.6
15Ni-0.5Mn/CeO_2	6.4	6.2	6.3	-	42.5
5Ni-0.5Au/CeO_2	7.3	6.2	6.8	7.1	38.5
15Ni-5Mn/CeO_2	7.7	6.8	7.2	-	33.6
Spent-5Ni-0.5Mn/CeO_2	7.3	7.5	7.4	-	-
Spent-10Ni/CeO_2	7.7	8.3	8.0	-	-

[a] calculated from XRD technique, [b] calculated from TEM image, [c] calculated from BET

Figure 4.2 indicated the physical image analysis by TEM technique. The particle size of ceria was about 50 nm to 200 nm as shown in Figure 4.2(a). From TEM image of 5Ni/CeO_2 as shown in Figure 4.2(b), the Ni particles in catalysts was less than 15 nm. When adding manganese to obtain 5Ni-0.5Mn/CeO_2, it found that the particle size of nickel was clearly smaller to 10 nm, as shown in Figure 4.2(c). Figure 4.2(d), the addition of gold also effected on particle size; however, the metal particle size was still larger than the addition of manganese. The distribution of NiO particle size can also see in this figure. The average NiO particle size on catalysts of 5Ni/CeO_2, 5Ni-0.5Mn/CeO_2, 5Ni-0.5Au/CeO_2 was 6.72 nm, 6.28 nm and 7.14 nm, respectively. This can be concluded that additive promoter as manganese can reduce the particle of nickel in Ni/CeO_2 catalysts.

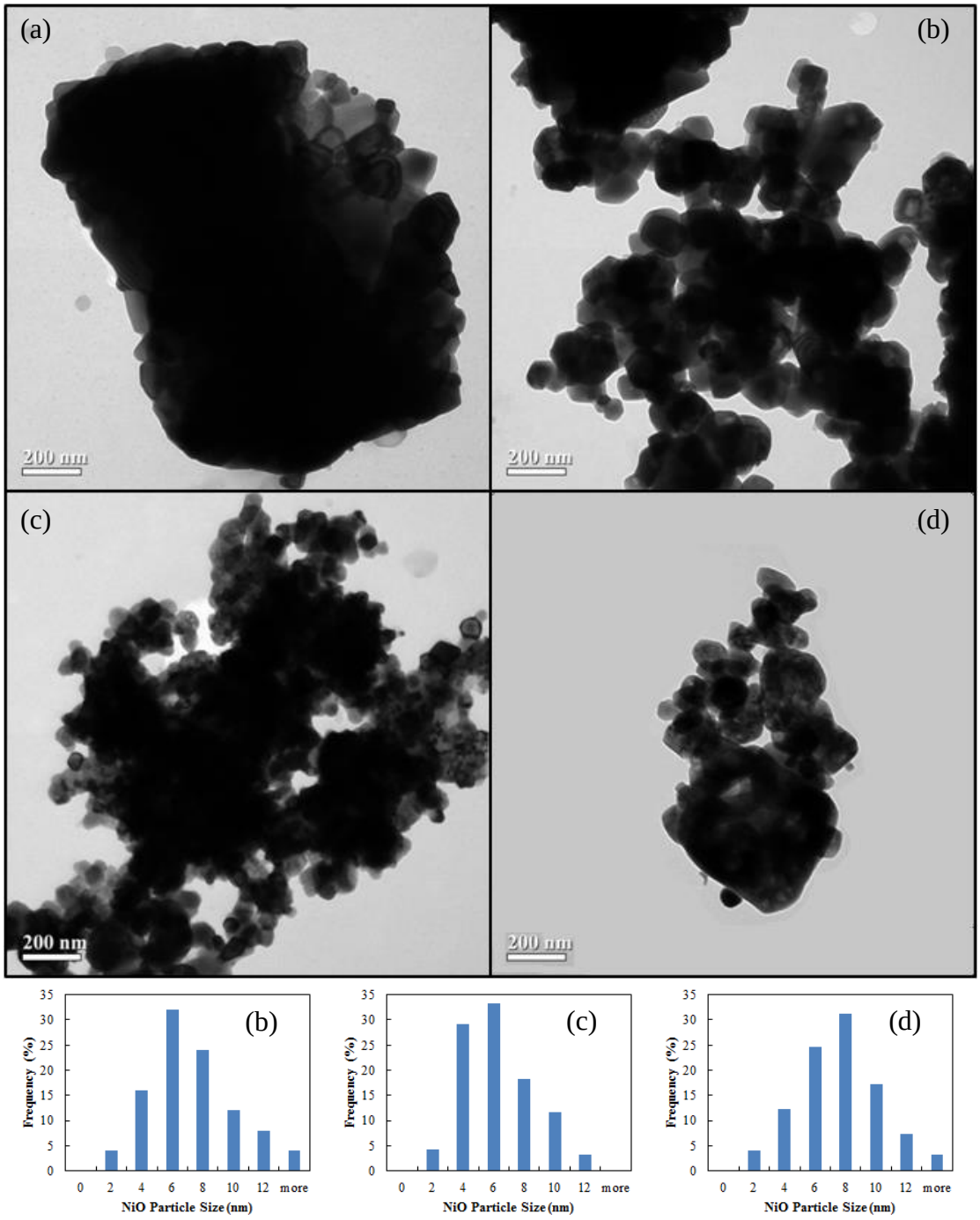

Figure 4.2 TEM image and NiO particle distribution of the catalysts: (a) CeO_2; (b) 5Ni/CeO_2; (c) 5Ni-0.5Mn/CeO_2; (d) 5Ni-0.5Au/CeO_2

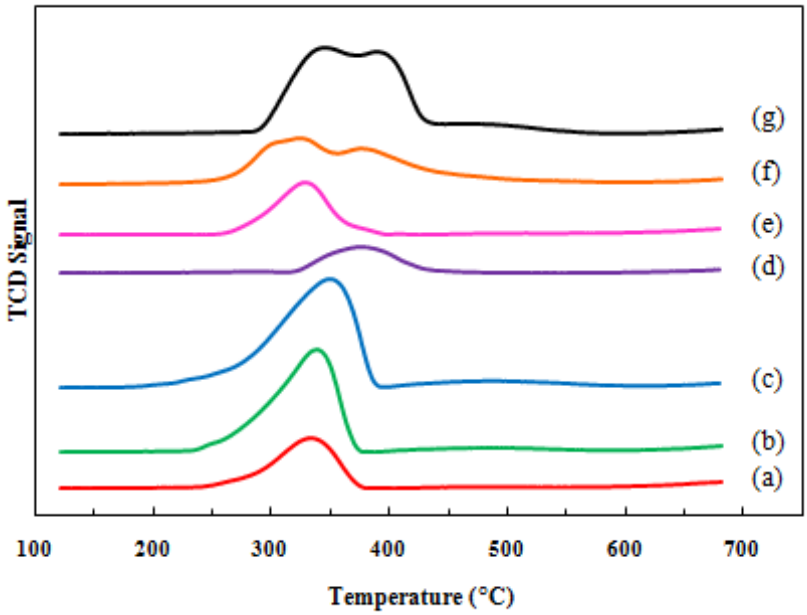

Figure 4.3 TPR profiles of Ni/CeO_2 based catalysts versus temperature with (I) different loading of Ni: (a) $5Ni/CeO_2$; (b) $10Ni/CeO_2$; (c) $15Ni/CeO_2$, and (II) various promoters: (d) $5Ni\text{-}0.5Mn/CeO_2$; (e) $5Ni\text{-}0.5Au/CeO_2$; (f) $5Ni\text{-}10Mn/CeO_2$; (g) $15Ni\text{-}0.5Mn/CeO_2$

Figure 4.3 illustrates the reduction temperature of the prepared catalysts by TPR technique. When increasing Ni loading from 5% to 15%, more amount of hydrogen was required for reducing the Ni catalysts. To consider the Ni/CeO_2 catalyst found that hydrogen was used greater amount for the Ni as line (a), (b), and (c). The larger amount of NiO clusters can shift the reduction temperature to higher temperature; particularly, nickel based catalysts are reduced around 300 °C to 400 °C (95). The addition of Mn promoter at 0.5% by weight makes the catalysts more difficult to be reduced, due to a strong of Ni–Mn bond in catalysts. It can be said that new phase between Mn-Ni formation was occurred as a solid solution (94) because the reducing temperature increased around 20 °C to 30 °C. Therefore, more difficult to reduce, more promote the oxidation reaction effecting on the methane

decomposition, reverse Boudouard and reverse water gas shift. For addition of Au promoter at 0.5% by weight, there is no change in main TPR profile, but it found small peak at 380°C which referred a gold reduction peak (86). It can be said that it was no interaction between Ni and Au. The addition of manganese at 10% by weight (f) revealed the overlapped peak clearly. The peak at the high temperature referred the peak of the Ni-Mn compound and another peak at low temperature was manganese component in the catalysts (96). When percentages of Ni loading increased to 15% by weight (g), the large amount of hydrogen was consumed for Ni and Mn which represented overlapped peak. The first peak at high temperature was the combination of nickel and manganese while the second peak was nickel peak (70).

4.1.2 Activities of Ni, Ni-Mn, Ni-Au over CeO_2-supported catalysts

The activities of Ni/CeO_2 catalysts in term of CH_4 conversion and CO_2 conversion are represented in Figure 4.4. The reactions did not observed around 500 °C to 600 °C. After increasing temperature from 600 °C until to 900 °C, the reaction was observed. They were found that CH_4 conversion and CO_2 conversion increased with an increasing reaction temperature. From the performance of $5Ni/CeO_2$ catalysts, the CH_4 conversion (%) and CO_2 conversion (%) significantly increased from 30% to 70% and from 20% to 50% when increasing temperature from 700 °C to 900 °C, respectively. The maximum conversion was obtained at 900 °C. Since reaction of dry reforming of CH_4 is a combination of CH_4 decomposition and reverse Boudouard reaction, it should concern in the performance of CH_4 conversion and CO_2 conversion, respectively. The main product of the reaction was H_2 and CO. Methane decomposes to C and H_2 which are continuously react with CO_2 via reverse Boudouard ($C + CO_2 \rightarrow 2CO$) and reverse water gas shift ($H_2 + CO_2 \leftrightarrow CO + H_2O$), respectively. The RWGS, as an undesired reaction, resulted in H_2 selectivity depletion from 100% to 70% with increasing temperature. When increasing nickel loading, CH_4 conversion was increased particularly at 800 °C to 900 °C. To consider the CO_2 conversion, it was found that the 10% by weight of nickel on the catalysts presented higher conversion than that of 15% and 5% by weight of Ni, respectively. Pompeo *et al.* (97) found that around 12% by weight of Ni catalysts performed highest methane conversion in dry reforming reaction due to it showed high surface area than other

loading. It can be suggested that 10% and 15% by weight of nickel was an appropriate content to promote a high CH_4 conversion and CO_2 conversion; however, it also promote the carbon deposition as well.

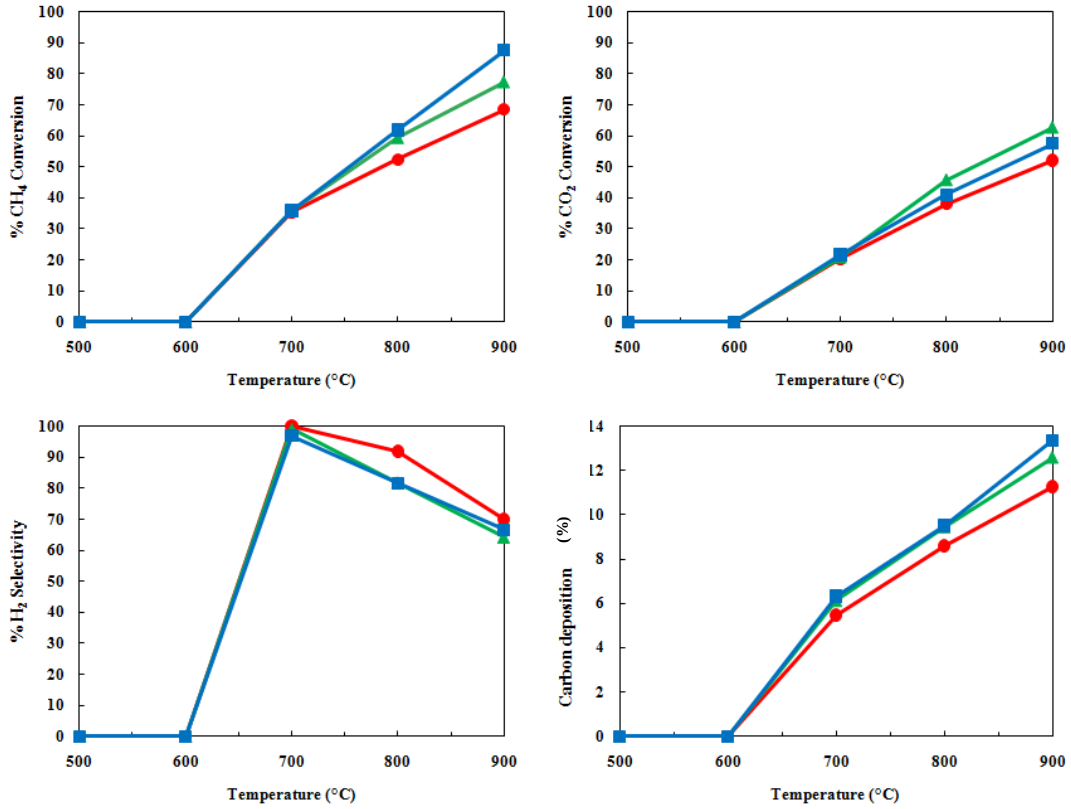

Figure 4.4 The catalysts of (●) 5%, (▲) 10% and (■) 15% weight of Ni loading versus temperature on CH_4 conversion, CO_2 conversion, H_2 selectivity and Carbon deposition

Effect of promoter on the performance of Ni/CeO_2 catalysts is presented in Figure 4.5. The manganese promoter promoted the catalytic reaction which performed for methane decomposition (CH_4 conversion), Boudouard reaction (CO_2 conversion) and reverse water gas shift (RWGS) in all Ni loading at 5%. This can be said that Mn promoter reinforced Ni/CeO_2 catalysts because Mn represented that CH_4 conversion and CO_2 conversion approximately increase to 5% and 10%, respectively, in 700 °C to 800 °C. It can be said that Mn promoted a small of active particles size of NiO which was presented in XRD and TEM results. However, H_2 selectivity would decrease about 10% because Mn promoter also promoted RWGS. To consider the

gold promoter, it gave lower activities (CH_4 conversion and CO_2 conversion, H_2 selectivity and carbon deposition). It can be suggested that gold had an ability to inhibit the CH_4 conversion and CO_2 conversion but promoted RWGS. Normally, gold based catalysts use in water gas shift reaction which performed a high performance at temperature lower than 400 °C (72, 76). These can be cleared to conclude that gold was not suitable for promoting Ni/CeO_2 catalysts for dry reforming reaction because of high temperature operating. From the Figure 4.5, it showed that the 5Ni-0.5Mn/CeO_2 catalyst activities are higher. It can be suggested that small amount of manganese in Ni/CeO_2 catalyst could develop catalysts activities. On the other word, Mn had an ability to reinforce the activities of 5%wt. of Ni based catalysts at suitable ratio.

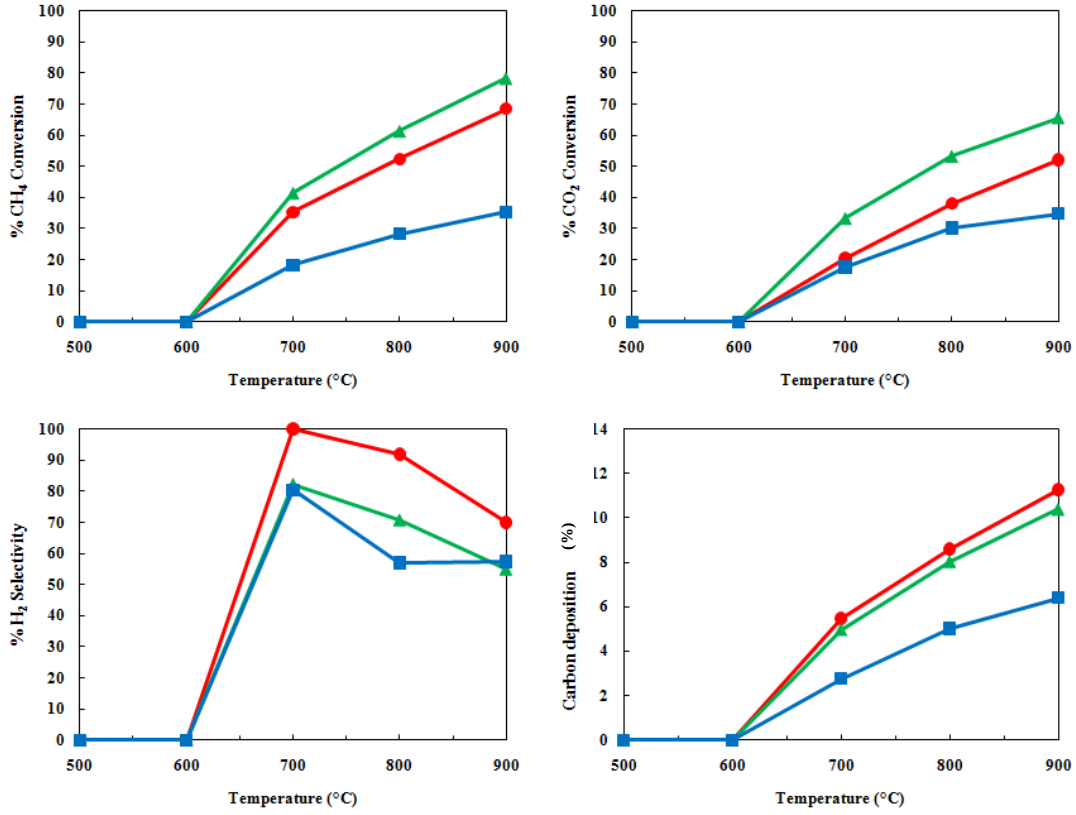

Figure 4.5 The catalysts of (●) 5Ni/CeO_2, (▲) 5Ni-0.5Mn/CeO_2 and (■) 5Ni-0.5Au/CeO_2 versus temperature on CH_4 conversion, CO_2 conversion, H_2 selectivity and carbon deposition.

Figure 4.6 shows the study of Mn promoter loading. The result showed that 0.5% by weight of manganese loading presenting the highest performance. For increasing manganese loading, the activities of Ni/CeO_2 dropped significantly because the suitable manganese for combination with nickel is a low content of manganese (Mn) per nickel (Ni) ratio of 10:90 which occurs a new phase compound as a solid solution (94).

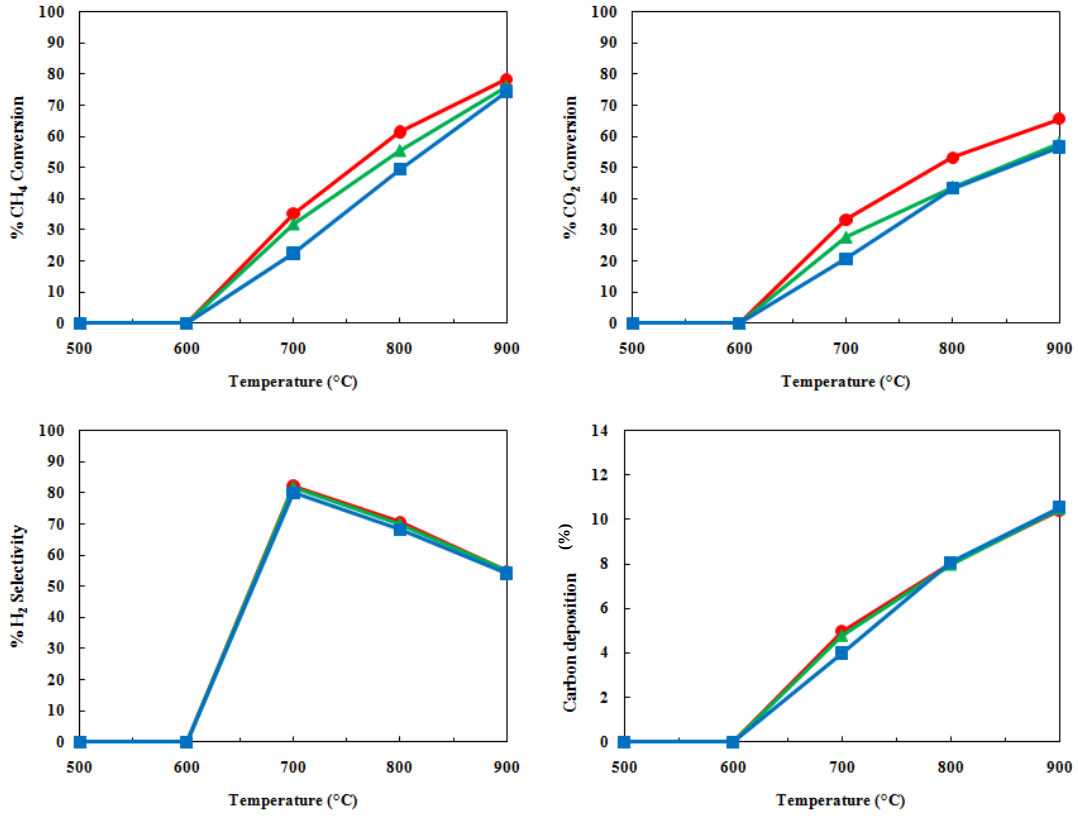

Figure 4.6 Catalytic activities of CH_4 conversion, CO_2 conversion, H_2 selectivity and Carbon deposition of Ni catalysts with various loading (%) of Mn promoter: (●) 5Ni-0.5Mn; (▲) 5Ni-5Mn; (■) 5Ni-10Mn

4.1.3 Experimental design for operating

From the catalytic activities, the $5Ni\text{-}0.5Mn/CeO_2$ catalyst which expressed higher performance is selected to study in the experimental design. The factors which have a significant effect on the catalytic activities would be screened:

temperature (denoted as factor A), CH_4 composition fraction (denoted as factor B), weight of catalysts (denoted as factor C) and feed rate (denoted as factor D). After screening, the data were analyzed by the respond surface model (RSM) for simulating the equation model to find the relation and their interaction. The responses were defined as CH_4 conversion, CO_2 conversion H_2 selectivity and carbon deposition. Table 4.2 shows full factorial with 2 additional center points of experimental data.

Table 4.2 Data for design of experimental in DRM reaction

No	A	B	C	D	CH_4 con.	CO_2 con.	H_2 sel.	C de.
1	700	0.3	0.05	30	46.5	30.5	39.0	10.4
2	800	0.3	0.05	30	72.8	46.3	45.9	13.5
3	900	0.3	0.05	30	86.8	44.9	36.8	13.8
4	700	0.5	0.05	30	27.1	32.4	75.4	2.3
5	800	0.5	0.05	30	60.7	57.9	65.6	10.4
6	900	0.5	0.05	30	81.4	67.8	54.6	12.8
7	700	0.7	0.05	30	29.0	50.0	45.0	12.9
8	800	0.7	0.05	30	51.8	74.5	51.1	15.6
9	900	0.7	0.05	30	72.9	95.3	52.3	17.7
10	700	0.3	0.1	30	52.2	37.3	40.5	6.5
11	800	0.3	0.1	30	79.1	47.8	50.5	7.4
12	900	0.3	0.1	30	91.5	45.8	45.7	7.4
13	700	0.5	0.1	30	43.8	45.2	69.2	5.2
14	800	0.5	0.1	30	69.6	64.6	60.6	6.5
15	900	0.5	0.1	30	91.8	71.4	51.9	7.5
16	700	0.7	0.1	30	35.5	52.3	45.5	4.5
17	800	0.7	0.1	30	45.0	76.2	54.1	6.6
18	900	0.7	0.1	30	73.6	97.8	61.2	9.0
19	700	0.3	0.15	30	52.5	40.7	44.4	3.7
20	800	0.3	0.15	30	86.4	49.1	56.5	4.8
21	900	0.3	0.15	30	97.3	45.8	45.6	5.0
22	700	0.5	0.15	30	44.4	45.8	63.0	2.8
23	800	0.5	0.15	30	75.1	67.5	57.0	4.2
24	900	0.5	0.15	30	97.5	72.0	44.1	5.1
25	700	0.7	0.15	30	39.7	53.2	46.0	3.8
26	800	0.7	0.15	30	52.7	77.3	54.5	4.9
27	900	0.7	0.15	30	83.4	96.9	67.3	6.5
28	700	0.3	0.05	60	30.9	8.4	32.0	3.7
29	800	0.3	0.05	60	37.2	24.1	39.3	7.4

No	A	B	C	D	CH_4 con.	CO_2 con.	H_2 sel.	C de.
30	900	0.3	0.05	60	57.4	31.3	38.7	11.4
31	700	0.5	0.05	60	12.1	16.0	87.7	5.8
32	800	0.5	0.05	60	37.6	40.9	78.5	12.6
33	900	0.5	0.05	60	60.5	58.4	58.3	18.6
34	700	0.7	0.05	60	25.1	42.5	30.9	11.7
35	800	0.7	0.05	60	38.3	58.4	35.1	15.1
36	900	0.7	0.05	60	55.3	83.0	42.7	21.0
37	700	0.3	0.1	60	37.6	30.1	33.2	6.8
38	800	0.3	0.1	60	66.4	47.1	36.9	9.1
39	900	0.3	0.1	60	81.0	46.6	52.6	9.8
40	700	0.5	0.1	60	35.5	33.3	82.1	7.0
41	800	0.5	0.1	60	61.4	53.2	70.6	8.1
42	900	0.5	0.1	60	78.5	65.7	54.9	13.4
43	700	0.7	0.1	60	25.4	48.5	38.0	6.4
44	800	0.7	0.1	60	39.2	66.9	42.5	8.7
45	900	0.7	0.1	60	61.7	91.7	45.7	11.5
46	700	0.3	0.15	60	39.3	32.6	41.3	3.7
47	800	0.3	0.15	60	66.5	49.6	45.5	5.3
48	900	0.3	0.15	60	85.7	37.6	50.7	5.9
49	700	0.5	0.15	60	37.8	35.0	73.0	4.4
50	800	0.5	0.15	60	54.4	59.1	59.7	6.7
51	900	0.5	0.15	60	85.9	71.0	49.9	8.9
52	700	0.7	0.15	60	25.6	53.0	39.4	4.7
53	800	0.7	0.15	60	43.9	74.0	42.0	6.6
54	900	0.7	0.15	60	67.3	95.0	47.7	8.9
55	700	0.3	0.05	90	2.2	15.5	17.6	11.2
56	800	0.3	0.05	90	29.8	24.4	23.0	15.9
57	900	0.3	0.05	90	50.7	30.0	36.3	22.7
58	700	0.5	0.05	90	10.1	9.0	99.3	0.0
59	800	0.5	0.05	90	6.5	15.8	100	5.7
60	900	0.5	0.05	90	31.1	40.5	63.9	17.6
61	700	0.7	0.05	90	0.3	21.9	32.9	11.4
62	800	0.7	0.05	90	18.8	40.0	37.3	18.3
63	900	0.7	0.05	90	33.5	57.1	40.4	24.4
64	700	0.3	0.1	90	21.7	22.6	38.9	8.5
65	800	0.3	0.1	90	45.5	32.7	47.5	11.8
66	900	0.3	0.1	90	65.6	37.4	48.6	14.6
67	700	0.5	0.1	90	2.1	21.0	86.6	5.5
68	800	0.5	0.1	90	32.7	41.4	73.0	10.5
69	900	0.5	0.1	90	54.7	62.0	60.3	14.7

No	A	B	C	D	CH_4 con.	CO_2 con.	H_2 sel.	C de.
70	700	0.7	0.1	90	6.4	29.7	38.9	8.0
71	800	0.7	0.1	90	30.1	52.9	45.4	13.1
72	900	0.7	0.1	90	48.6	72.0	46.3	16.8
73	700	0.3	0.15	90	28.6	25.9	68.1	4.5
74	800	0.3	0.15	90	49.4	25.4	63.5	7.6
75	900	0.3	0.15	90	76.7	42.8	56.1	10.2
76	700	0.5	0.15	90	19.8	24.5	73.8	3.4
77	800	0.5	0.15	90	51.5	40.1	67.8	7.1
78	900	0.5	0.15	90	70.5	60.5	55.5	10.4
79	700	0.7	0.15	90	9.2	39.4	50.1	6.6
80	800	0.7	0.15	90	31.2	58.8	53.9	9.0
81	900	0.7	0.15	90	57.7	84.4	50.5	13.4
Addition center points								
82	800	0.5	0.1	60	65.2	57.2	75.5	9.8
83	800	0.5	0.1	60	57.6	49.2	65.8	8.7

A –Temperature, B – CH_4 composition, C – Catalysts weight, D – Flow rate,

CH_4 con. – CH_4 conversion, CO_2 con. – CO_2 conversion, H_2 sel. – H_2 selectivity, C de. – Coke deposition

Figure 4.7 represents an analysis of the factors on the activities by 2^k experiment as CH_4 conversion and CO_2 conversion. The evaluation of each factors and there interaction in term of P-value are less than 0.05 or 95% confident interval. To consider the main factor of temperature (A), it was found that an increasing temperature gave higher CH_4 conversion, CO_2 conversion and carbon deposition. An increasing in CH_4 fraction (B) decreased CH_4 conversion but increased in CO_2 conversion and carbon deposition. Increase in catalysts weight (C) made an increase in CH_4 conversion, CO_2 conversion and H_2 selectivity. An increasing in feed rate (D) reduced CH_4 conversion and CO_2 conversion but increased in carbon deposition. The two-factor interaction factor was only AB resulting in positive effecting on CO_2 conversion. Moreover, interaction of AC and AD would be effected on carbon deposition.

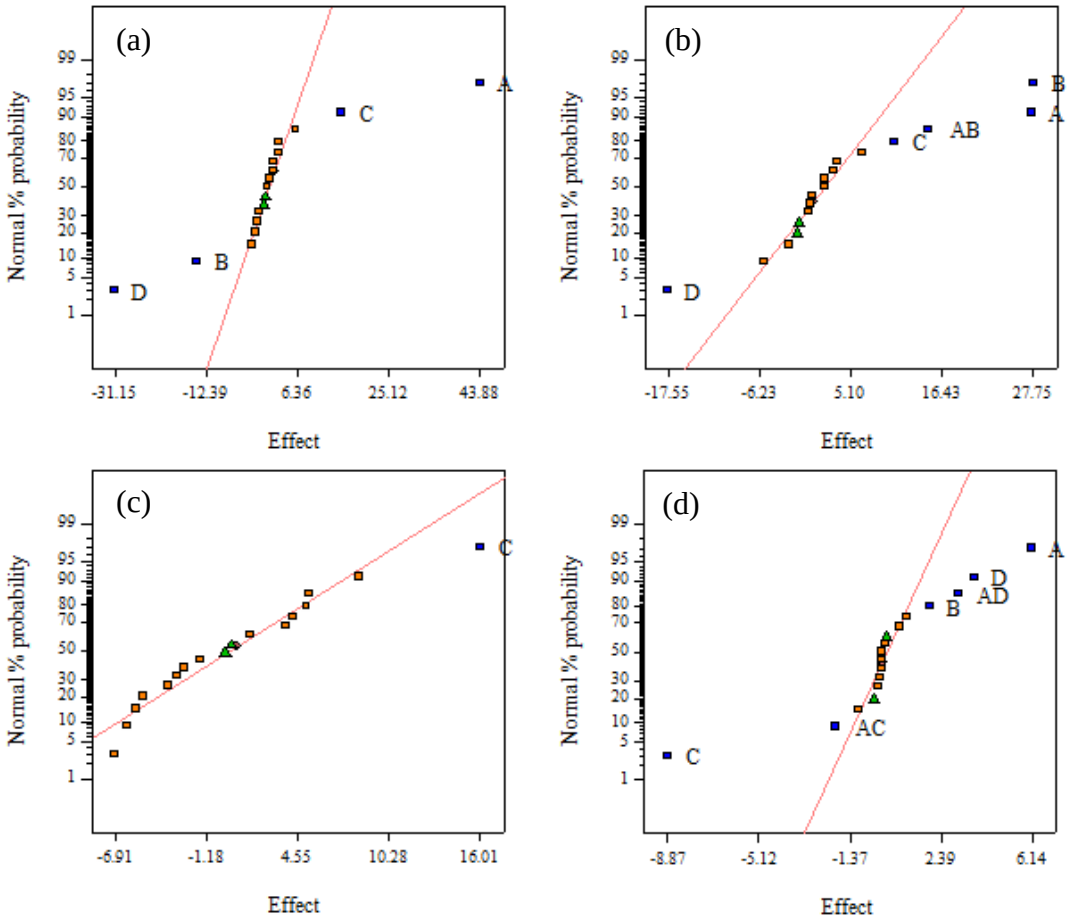

Figure 4.7 Normal probability plot of (a) CH_4 conversion, (b) CO_2 conversion, (c) H_2 selectivity and (d) Carbon deposition versus effect factors; A-temperature, B-CH_4 composition, C-catalysts weight, D-feed rate

Table 4.3 shows the absolute effect of the 2^k factors which can be assessed the significant factors by margin error (ME). The factors that absolute effect more than ME can be concluded that provide significant.

Table 4.3 Effect list of experimental data in DRM reaction

Effect term	CH_4 conversion	CO_2 conversion	H_2 selectivity	Carbon deposition
A	43.88	27.52	5.26	6.14
B	14.45	27.75	5.10	1.92
C	15.41	10.50	16.01	8.87
D	31.15	17.55	3.04	3.81
AB	1.53	14.80	3.86	0.67
AC	2.39	0.17	2.55	1.99
AD	0.74	0.39	1.61	3.09
BC	1.81	1.92	5.16	0.17
BD	0.10	5.61	6.14	0.09
CD	5.97	6.52	8.45	0.11
ABC	1.38	1.87	4.30	0.03
ABD	2.19	2.58	3.57	0.03
ACD	1.33	2.92	6.91	0.99
BCD	3.00	3.51	5.59	1.00
ABCD	2.56	0.04	1.62	0.06
Curvature	10.73	3.84	19.95	1.81
Lenth's ME	5.93	8.14	15.60	1.38

Figure **4.8** represents the absolute effect comparing with ME. The result of significant factors by ME decision was similar to %probability decision (P-value lower than 0.05) except CD factor. Only the CD factors of CH_4 conversion in ME decision was significant, but the %probability decision was not significant. It can be explained that the effect of CD was blocked by error in case of %probability decision due to the calculation from sum square (SS) divided by error. Nonetheless, the absolute effect of CD was close to magnitude of ME. However, for looking the overall screening factors by the %probability or ME decision can classify the effect factors. And another application of ME decision can specify the influence of curvature. It was found that CH_4 conversion, H_2 selectivity and carbon deposition involved a curvature which related to quadratic model. The 2^k analysis cannot explain the quadratic term; therefore, the screening factor just presents only significant factors to the activity. To get the exact equation, the respond surface model (RSM) will be used to further study in the next part.

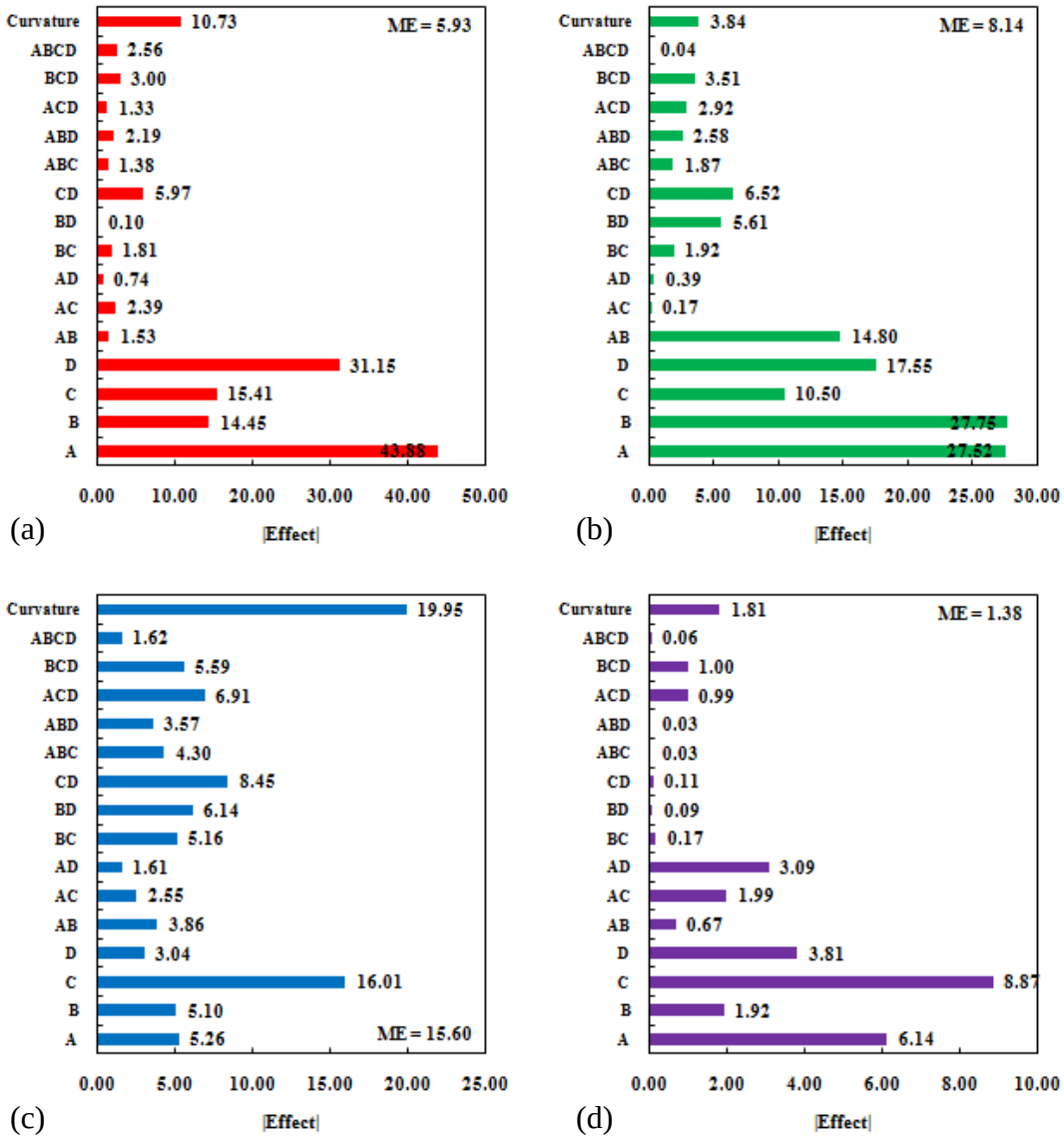

Figure 4.8 The effect list or pareto's chart of (a) CH_4 conversion, (b) CO_2 conversion, (c) H_2 selectivity and (d) carbon deposition with denoted as A-temperature effect factor, B-CH_4 composition effect factor, C-catalysts weight effect factor, D-feed rate effect factor and interaction of effect factors with Lenth's ME value

Table 4.4 Model of CH_4 conversion, CO_2 conversion, H_2 selectivity and carbon deposition in code and actual terms

Parameter	Code		Actual
CH_4 conversion =			
54.17		-156.01	
21.45	* A	0.37	* Temperature
-8.07	* B	22.72	* CH_4 composition
8.58	* C	85.90	* Catalysts weight
-15.84	* D	-0.48	* Feed rate
-3.43	* C^2	-1,370.09	* Catalysts weight^2
2.19	* A * C	0.44	* Temperature * Catalysts weight
-2.28	* B * C	-228.40	* CH_4 composition * Catalysts weight
3.10	* C * D	2.07	* Catalysts weight * Feed rate
R^2 =	0.9539	Adj R^2 =	0.9444
CO_2 conversion =			
52.62		-111.52	
14.98	* A	0.36	* Temperature
14.63	* B	-269.56	* CH_4 composition
6.30	* C	428.37	* Catalysts weight
-10.35	* D	-0.30	* Feed rate
-2.48	* A^2	0.00	* Temperature^2
2.75	* B^2	68.87	* CH_4 composition^2
-3.97	* C^2	-1,589.77	* Catalysts weight^2
7.33	* A * B	0.37	* Temperature * CH_4 composition
-2.38	* B * D	-0.40	* CH_4 composition * Feed rate
2.74	* C * D	1.83	* Catalysts weight * Feed rate
R^2 =	0.9547	Adj R^2 =	0.9545
H_2 Selectivity =			
67.86		-1,196.29	
-10.55	* A	1.90	* Temperature
-10.04	* C	1,868.77	* Catalysts weight
7.00	* D	-3.33	* Feed rate
-23.55	* B^2	-4,015.63	* CH_4 composition^2
3.52	* D^2	0.00	* Feed rate^2
-2.21	* B * C	-7,877.90	* CH_4 composition * Catalysts weight
-2.12	* B * D	9.75	* CH_4 composition * Feed rate
2.11	* C * D	5.45	* Catalysts weight * Feed rate
16.01	* A * B^2	4.00	* Temperature * CH_4 composition^2
14.62	* B^2 * C	7,309.98	* CH_4 composition^2 * Catalysts weight
-10.12	* B^2 * D	-8.44	* CH_4 composition^2 * Feed rate
-2.55	* B * C * D	-8.51	* CH_4 composition*Catalysts weight*Feed rate
R^2 =	0.9206	Adj R^2 =	0.8748

Parameter		Code	Actual
Carbon deposition =			
7.77		-39.36	
3.24	* A	0.23	* Temperature
-1.44	* C	471.23	* Catalysts weight
1.38	* D	0.11	* Feed rate
1.85	* B^2	344.91	* CH_4 composition^2
-1.49	* A * C	-0.81	* Temperature * Catalysts weight
1.47	* A * D	0.00	* Temperature * Feed rate
-0.68	* B * C	408.02	* CH_4 composition * Catalysts weight
-1.22	* A * B^2	-0.30	* Temperature * CH_4 composition^2
-2.15	* B^2 * C	-1,075.85	* CH_4 composition^2 * Catalysts weight
1.30	* B * C^2	2,598.99	* CH_4 composition * Catalysts weight^2
-1.11	* B * D^2	-0.01	* CH_4 composition * Feed rate^2
R^2 =	0.9030	Adj R^2 =	0.8470

Another reason to confirm the results is to compare of actual and predicted as shown in Figure 4.9. The results of actual value of each parameter had similar to the predict results. It could observe from the trend of plots lying on the 45° line. This can be concluded that the analysis equation was acceptable, reliable and practical for prediction activities.

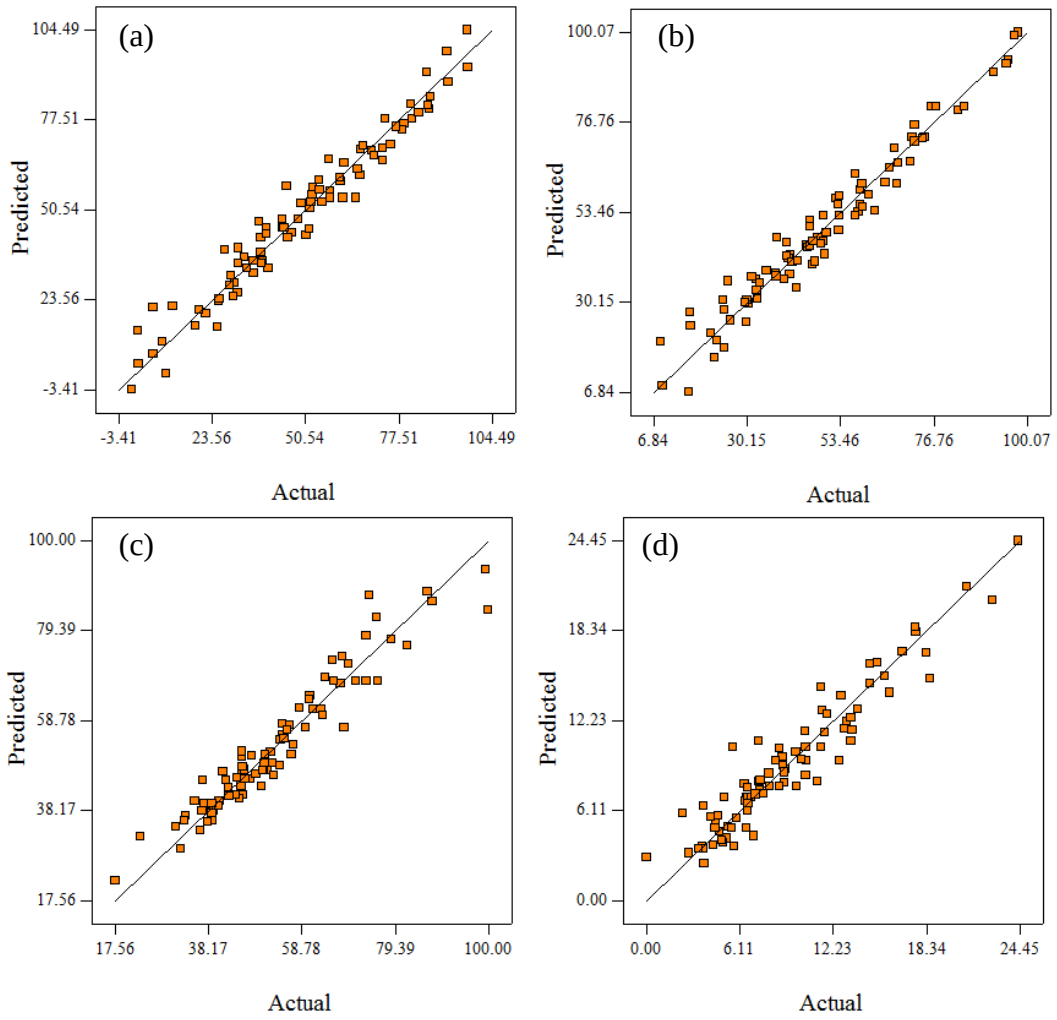

Figure 4.9 Predicted versus actual plot for (a) CH_4 conversion, (b) CO_2 conversion, (c) H_2 selectivity and (d) Carbon deposition

Figure 4.10 shows the contours of each activity. The left graph represents the effect of temperature (A) versus CH_4 composition (B) at center value of C and D factors while the right graph shows the effect of catalysts weight (C) versus feed rate (D) at center value of A and B. Figure 4.11 presents the overlays plot of the contour setting constrain of CH_4 conversion, CO_2 conversion, H_2 selectivity and carbon deposition of 70 %, 60%, 60 % and 10 mg C/g.cat·h, respectively. It can get an appropriate range of operating by fixed other factors at the suitable of other factors. This result allows the user to easily control due to the wide range of operating.

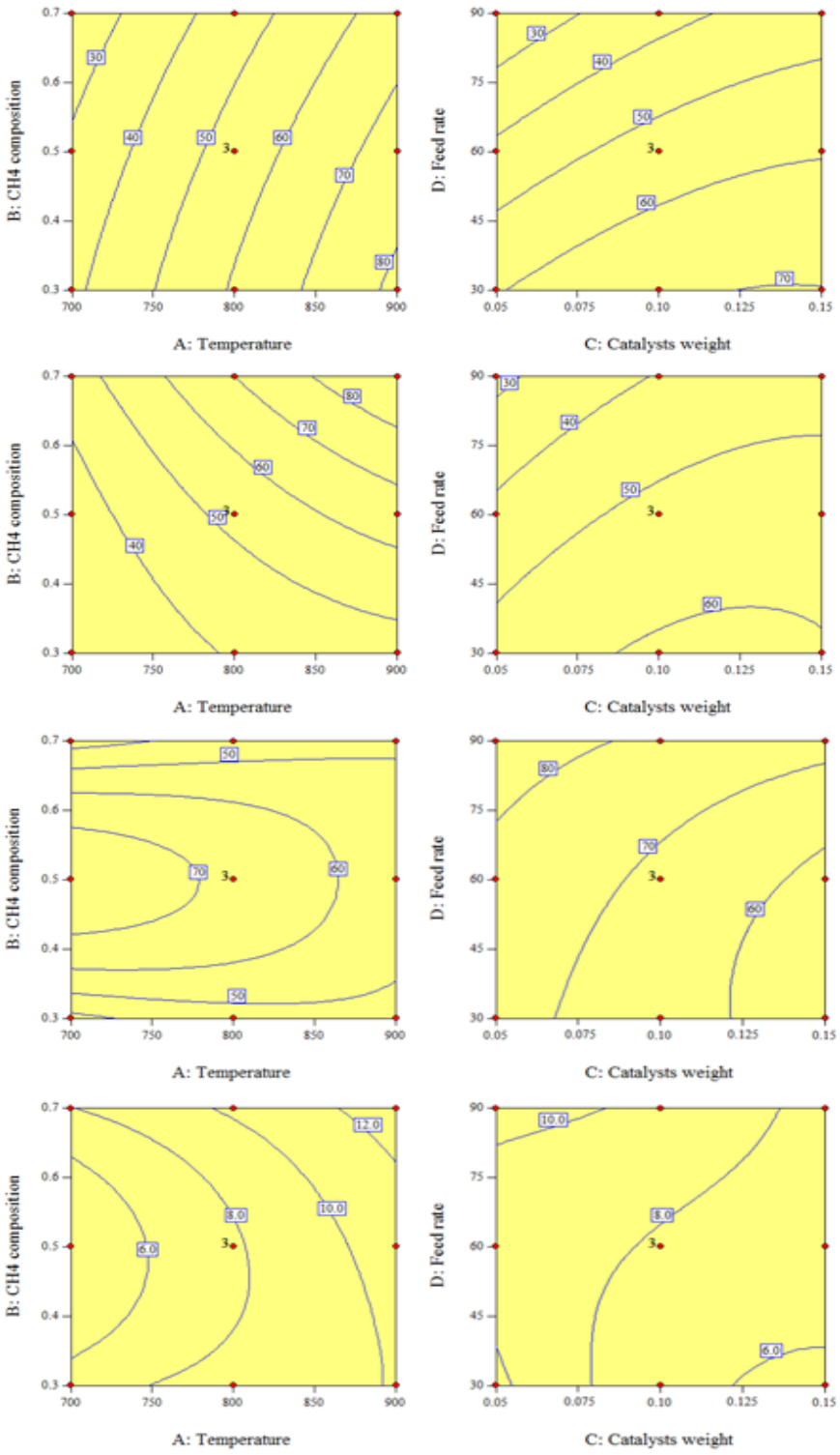

Figure 4.10 The contour plot for (a) CH_4 conversion, (b) CO_2 conversion, (c) H_2 selectivity and (d) Carbon deposition which presented effect of main factors: (left) temperature versus CH_4 composition (center value of C and D); (right) catalysts weight versus feed rate (center value of A and B)

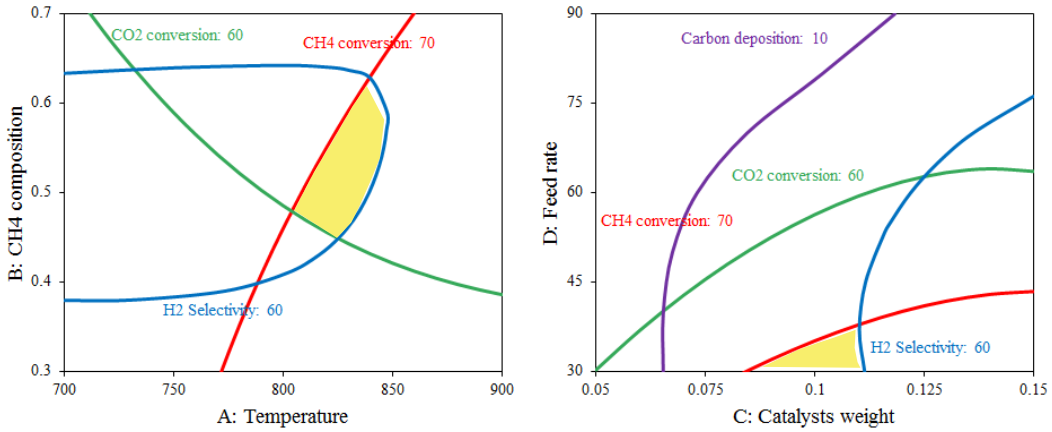

Figure 4.11 The overlay plot of CH_4 conversion, CO_2 conversion, H_2 selectivity and carbon deposition of 70%, 60%, 60% and 10 $mgC/g_{cat}{\cdot}h$ constrains, respectively: (left) temperature versus CH_4 composition (at optimum C and D); (right) catalysts weight versus feed rate (at optimum A and B)

Table 4.5 shows the actual experiment and predicted of CH_4 conversion and CO_2 conversion at optimum condition including 820 °C, 0.5 of CH_4 composition fraction, 0.1 g of catalysts and 30 ml/min total inlet feed rate. The result showed that CH_4 conversion were 72.51 and 79.21 for predicted and actual, respectively (5.2% error) while CO_2 conversion were 63.97 and 67.59 for predicted and actual, respectively (4.5% error). H_2 selectivity showed around 3% error. Finally, carbon deposition observed at 5.9% error. From experimental design analysis, it can predict the catalysts performance with accuracy that showed error around 5% or less; however, it also can evaluate the results with presented good performance.

Table 4.5 Experimental variables on CH_4 conversion, CO_2 conversion H_2 selectivity and carbon deposition compare between predicted value and actual value at optimum condition

Activity	Predicted	Actual	Error (%)
CH_4 conversion (%)	74.84	79.21	5.2
CO_2 conversion (%)	64.58	67.59	4.5
H_2 selectivity (%)	62.25	60.24	3.3
Carbon deposition (%)	7.15	7.60	5.9

4.1.4 Stability testing

Figure 4.12 shows the comparison stability. The reason for selecting 5Ni-0.5Mn/CeO_2 catalyst and 10Ni/CeO_2 catalyst were its higher performance while the later one contained optimum loading of nickel (98). Therefore, it lets us know the better performance in a long period. The results obtained that the CH_4 conversion did not show a significant difference whereas 5Ni-0.5Mn/CeO_2 catalyst represented higher CO_2 conversion than 10Ni/CeO_2 catalyst. It suggests that 5Ni-0.5Mn/CeO_2 catalyst promoted reverse Boudouard reaction to remove coke formation in the catalysts better than 10Ni/CeO_2. This result can be concluded that a small amount of manganese empowered the Ni/CeO_2 catalyst in order to improve catalytic activity and eliminate coke formation to prolong catalytic performance.

The stability performance of 10Ni/CeO_2 and 5Ni-0.5Mn/CeO_2 were compared each other which indicated by carbon deposition term (as shown in Table 4.6). The catalysts were tested at optimum condition for 20 h. The 10Ni/CeO_2 catalyst showed carbon deposition (%) of 11.7 and 12.4 by TGA and mass balance, respectively, while 5Ni-0.5Mn/CeO_2 showed 10.1 and 9.5, respectively. It can be said that 5Ni-0.5Mn/CeO_2 gave higher tolerance to the carbon deposition than 10Ni/CeO_2 catalyst due to the fact that manganese promoter promoted reverse Boudouard reaction to reduce the carbon deposition in the catalysts.

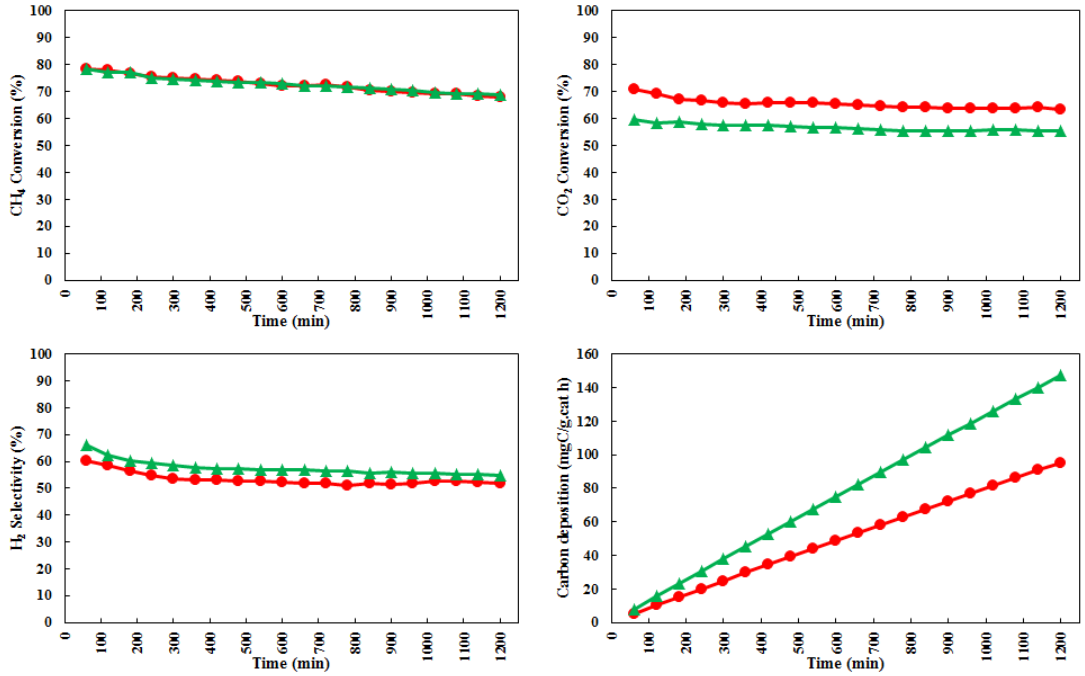

Figure 4.12 comparison stability plot of (●) 5% Ni-0.5Mn/CeO_2 and (▲) 10% Ni/CeO_2 catalysts on CH_4 conversion,CO_2 conversion, H_2 selectivity and carbon deposition

Table 4.6 Carbon deposition (%) in the catalysts after testing at 20 h which is calculated from TGA analysis and carbon mass balance

Catalysts	Carbon deposition (%)	
	TGA	Carbon mass balance
10Ni/CeO_2	11.7	12.4
5Ni-0.5Mn/CeO_2	10.1	9.5

4.2 Carbon monoxide clean up via water gas shift and preferential oxidation

4.2.1 Water gas shift reaction (WGS)

In this section, to reduce the carbon monoxide level via water gas shift reaction over Au/CeO_2 based catalysts with manganese, copper or iron promoter was investigated. The studied temperature was from 250 °C to 450 °C in atmospheric pressure. The catalysts were synthesized by slurry impregnation method. The activity of Au/CeO_2 based catalysts is presented in section 4.2.1.1. The experimental design investigates as shown in section 4.2.1.2.

4.2.1.1 Activities of Au/CeO_2 base catalysts with Mn, Cu or Fe promoter

Figure 4.15 represents the activities of 1% loading of gold catalysts effecting to CO conversion and H_2 yield. Promoters were studied including manganese (Mn), copper (Cu), and iron (Fe). Catalysts characterizations are presented in Table 4.7. The catalysts would be expressed into 2 groups of low content of promoter and high content of promoter. It found that the gold component contained an actual loading lower than the calculated amount. It can be suggested that preparation method as impregnation would lose some gold component, even this method has no washing catalysts after preparation. To consider high promoter loading, it showed a lower actual amount compared with the calculated amount of promoter; however, the error of loading was quite low. To consider (1:1) atom ratio of gold per promoter, promoter loading presented quite similar value to each other. Moreover, the gold per promoter ratio represented nearly 1:1 ratio in term of molar ratio. For surface area, S_{BET} of catalysts with promoter had slight higher value than no promoter. It seems that promoter occured a small size effecting to surface area.

Table 4.7 Characteristics of prepared catalysts

Catalysts	Au[a] (%wt.)	Promoter[a] (%wt.)	Ratio[b] (Ni:M)	S_{BET}[c](m^2/g)
1%Au/CeO_2	0.93	-	-	42.3
1Au5MnO_2/CeO_2	0.87	3.37	-	45.8
1Au5CuO/CeO_2	0.82	4.88	-	49.9
1Au5Fe_2O_3/CeO_2	0.74	5.58	-	57.9
1%(1:1)AuMn/CeO_2	0.63	0.26	1 : 0.94	40.6
1%(1:1)AuCu/CeO_2	0.64	0.25	1 : 0.98	48.3
1%(1:1)AuFe/CeO_2	0.60	0.26	1 : 1.07	48.1

[a] calculated from XRF, [b] calculated by mole ratio, [c] calculated from BET

Figure 4.13 presents TPR profile of catalysts in WGS part. The 1%Au/CeO_2 catalyst (line a) did not show any peak due to Au is oxidized normally below 100 ºC or interacts with sunlight to become Au^0 (86). In high content of promoter, Mn consumed the lowest amount of hydrogen while Fe consumed the highest amount of hydrogen followed by Cu, respectively, because a board peak related to the loading of promoter in the catalysts. The 1%(1:1)AuMn/CeO_2 catalyst showed a small peak around 270 ºC which referred to MnO_2 phase. The 1%(1:1)AuCu/CeO_2 catalyst showed 2 peak at 150 ºC and 180 ºC referred to Cu^{2+} and small cluster of copper, respectively (100). The 1%(1:1)AuFe/CeO_2 catalyst presented a minor peak at 260 ºC and a major peak 400 ºC which represented to Fe_3O_4 and Fe_2O_3, respectively. It can be said that Fe promoter showed a difficult reduction than Mn promoter and Cu promoter, respectively. For the low content of promoter (line e, f and g), they showed the TPR pattern the same with high promoter loading but lower intensity. It can be conclude that Fe showed higher reduction temperature than other promoters in either high content or low content in the catalysts.

To study activities of promoter loading at 5% weight is presented in Figure 4.14. The 1%Au/CeO_2 catalyst showed that the CO conversions was around 10%, 25%, 50%, 71%, 75% at temperature of 250 °C, 300 °C, 350 °C, 400 °C, and 450 °C, respectively, while H_2 yields was 10%, 25%, 41%, 51%, 45% at the same temperature in that order.

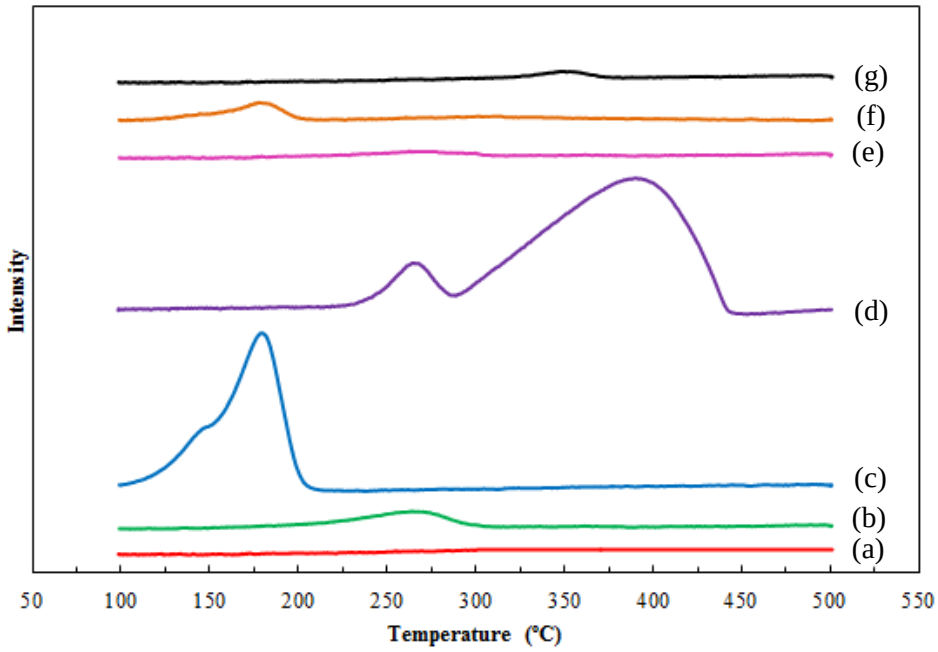

Figure 4.13 TPR profiles of (a) 1%Au/CeO_2 based catalysts versus temperature with (I) high loading of promoter: (b) 1Au5Mn/CeO_2; (c) 1Au5Cu/CeO_2; (d) 1Au5Fe/CeO_2, and (II) low loading of promoters: (e) 1%(1:1)AuMn/CeO_2; (f) 1%(1:1)AuCu/CeO_2; (g) 1%(1:1)AuFe/CeO_2

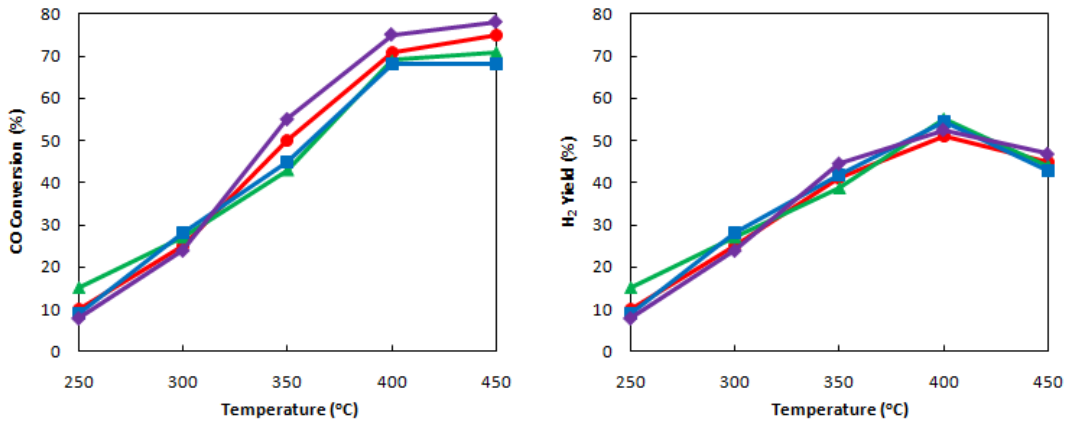

Figure 4.14 Comparison activities as CO conversion and H_2 yield of catalysts: (●) 1%Au/CeO_2; (▲) 1Au5Mn/CeO_2; (■) 1Au5Cu/CeO_2; (♦) 1Au5Fe/CeO_2 in real reforming condition

It was found from Figure 4.14 that the activity of gold catalysts was improved around 5% in a temperature range of 350 °C to 450 °C when adding 5%wt. Fe promoter. The CO conversion increased from 55% at 350 °C to 75% at 400 °C to 78% at 450 °C. When adding either Mn or Cu promoter at 5%wt. loading to the gold catalysts, the performance was dropped slightly in the temperature range of 350 °C to 450 °C (the CO conversion was 40% at 350 °C and 65% at 400 °C to 450 °C for both Mn or Cu promoter). Furthermore, the gold catalyst with adding different promoter and without promoter did not show differ in their performance in term of H_2 yield. Murugan *et al.* (99) studied the Mn catalysts over CeO_2-TiO_2 supported that Mn species presented +2 and +3 oxidation states. Especially prepared by impregnation method, manganese presented Mn^{3+} exclusively; therefore, highly reversible redox properties were an influence of Ce^{2+} and Ce^{3+} instead of manganese. It can be implied that the Mn species did not play a role of redox properties even it can be occurred in solid solutions phase. Lui *et al.* (100) explained that a part of smaller size Cu^{2+} could enter the CeO_2 lattice to form a solid solution and the rest of the Cu^{2+} forms metal oxide particles on the surface of the CeO_2 lattice. Papavasiliou *et al.* (101) reported that a smaller dispersion of CuO may be attributed to the perturbation of the interaction between copper and cerium ions. It can be said that Cu species can promote redox property in catalysts; however, it did not significantly show higher performance in the result. Fe promoter, it is a functional promoter in Au/CeO_2 catalysts, especially enhancing redox property of ceria support. The Fe element can replace in ceria lattice to promote redox transfer between Ce^{2+} and Ce^{3+} resulting in an increasing of driving force in the system. Moreover, it improves the reducibility of Au/CeO_2 catalysts which enhances CO oxidation in lattice oxygen to increase the selectivity (102). On the other hand, the gold is a stabilizer that prevents the thermal sintering of Fe (102). Another idea of Fe promoter occurs redox property of ferrite formation between Fe^{3+} and Fe^{2+} (103). Khan *et al.* (104) revealed that both Fe and Ce represented a facile charge transfer of Ce^{4+}/Ce^{3+} and Fe^{3+}/Fe^{2+} performing the synergism of them which could be improved a responsible of WGS activity. From the reasons, Mn was not an appropriate promoter in WGS catalysts due to the lack of redox ability and less surface area while Cu or Fe could improve redox properties of ceria supported and presented high surface area. For copper promoter, it did not

observe higher activities even though Cu can promote redox properties. It can be suggested that an excessive of promoter loading did not improve catalysts activities.

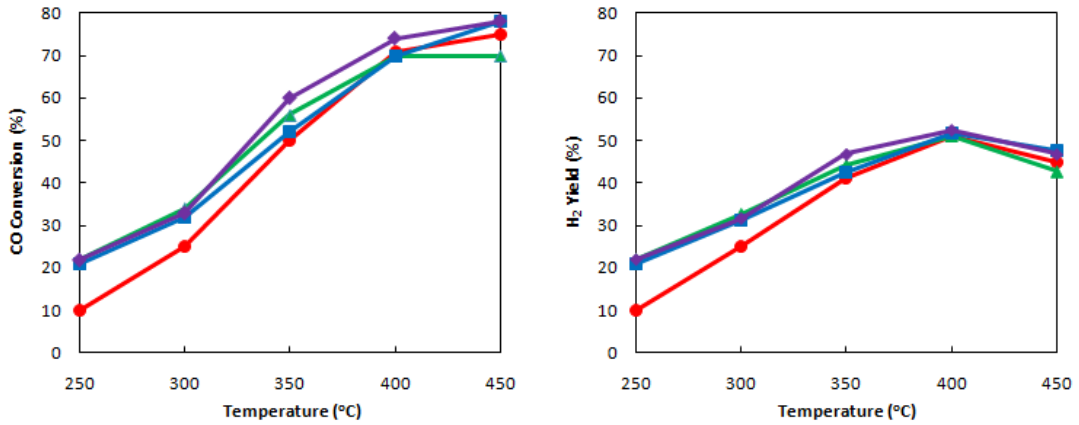

Figure 4.15 Comparison activities as CO conversion (%) and H_2 yield (%) of catalysts: (●) 1%Au/CeO_2; (▲) 1%(1:1)AuMn/CeO_2; (■) 1%(1:1)AuCu/CeO_2; (♦) 1%(1:1)AuFe/CeO_2 in real reforming condition

To study the low amount of promoter loading, the catalytic activities of the gold catalysts with promoter at 1:1 molar ratio and 1%wt. of total loading are shown in Figure 4.15. All catalysts with promoter presented higher CO conversion than the catalysts without promoter. At 250 °C to 300 °C, the catalysts with promoter gave higher conversion around 10% than without promoter. However, a difference in CO conversion slightly decreased when temperature was increased more than 350 °C. In this work, it is noted that the catalysts with Fe promoter represented the higher CO conversion in whole temperature range. The catalysts with Fe promoter presented CO conversion as 22%, 33%, 60%, 74%, 78% at the temperature 250 °C, 300 °C, 350 °C, 400 °C, 450 °C, respectively. Since Fe enhances redox property of CeO_2 support to promote CO oxidation comparing CO conversion from gold based catalysts, the result showed an increasing of CO conversion around 5% to 10% in low temperature. Particularly, the promoter could present higher activity because the system did not reach to a thermodynamic equilibrium at low temperature. But in this reaction, the thermodynamic equilibrium is observed at high temperature from 350 °C to 400 °C.

Considering H_2 yield, it was found that the small amount of promoter improved the gold catalysts performance to 22%, 31%, 46%, 52%, 46% at temperature of 250 °C, 300 °C, 350 °C, 400 °C, 450 °C, respectively. However, it is surprised that activity of gold catalysts with different promoter had a slight difference in terms of H_2 yield. H_2 yield was increased when rising temperature from 250 °C to 400 °C. Further increasing temperature to 450 °C, H_2 yield was decreased due to the reaction are exothermic reaction.

From the results, it can be concluded that the low amount of promoter had an importance to improve catalytic activity. Particularly, the lattice oxygen in CeO_2 easily converts an adsorbed CO to CO_2, and restores the lattice oxygen by releasing H_2 from H_2O. The basic objectives of promoter are, first, to improve metal dispersion over a support, second, to prevent a sintering from active site, and third, to improve the transfer rate of lattice oxygen which increases the selectivity and suppress undesired reaction as methanation (102). Normally, increasing temperature moves the forward reaction over catalysts which are proposed by kinetics control; however, the kinetic of reaction limits WGS equilibrium at high temperatures (105). So, the promoter on the catalysts did not show significant performance clearly in equilibrium state of reaction because the reaction was controlled by temperature control. However, the 1%(1:1)AuFe/CeO_2 catalyst was selected to study the experimental design to find the suitable operating condition because Fe promoter represented the higher activities and the others.

4.2.1.2 Experimental design for operation

Three independent factors based on classical experiments above were studied under experimental design. The factors were temperature (A), catalysts weight (B) and water feed rate (C). Normally, temperature, as the first main factor, directly performs the kinetic activity in the system. In exothermic reaction, the equilibrium temperature is an importance for controlling the reaction to get higher product rate. For view of competition reaction, it is really necessary to concern in temperature in order to promote a desired reaction but prohibit an undesired reaction. Catalysts weight, as the second main factor, is the necessary factor to prolong the contact time between the reactant gas and active surface area in the catalysts. Some literature study

W/F ratio instead of catalysts weight; however, it also seems to elongate a residence time of the reaction to increase the catalytic activity. Water feed rate, as the last factor, is an importance to CO conversion since it is a major driving force to forward the WGS reaction. Some search used steam/CO ratio instead of water feed rate to obtain its optimum ratio. The WGS reaction, particularly, should add excess water vapor to drive the forward reaction. However, the steam/CO ratio should be at least 1:1 due to the stoichiometry of the WGS reaction. Shido and Iwasawa (22) confirmed that the water vapor enhanced a decomposition of formate to H_2. Additionally, Li *et al.* (106, 107) studied Fe species that improved the covering of hydroxyl groups by redox behavior to reinforce the forward reaction. The output parameters were CO conversion and H_2 yield performing as a catalytic activity. CO conversion means the ability of catalysts to convert CO to CO_2 while H_2 yield means receiving an actual hydrogen product or losing of hydrogen to become methane by methanation reaction.

Table 4.8 presents design of experiment data. It shows the independent factors and their levels in term of coded and actual. The temperature (A) range was 250 °C to 450 °C, the catalysts weight (B) was 0.1 g to 0.2 g and the water feed rate (C) was 1 ml/h to 3 ml/h (as equal steam/CO ratio of 1:1 to 3:1).

Table 4.8 Experimental data in coded and actual unit for a full 2^3 factorial design with one center point

No	A: temperature (°C)	B: weight catalysts (g)	C: H_2O feed (ml/h)	CO Conversion	H_2 Yield
1	–1 (250)	–1 (0.1)	–1 (1)	18.8	18.8
2	–1 (250)	–1 (0.1)	+1 (3)	17.7	17.7
3	–1 (250)	+1 (0.2)	–1 (1)	23.8	23.8
4	–1 (250)	+1 (0.2)	+1 (3)	21.4	21.4
5	+1 (450)	–1 (0.1)	–1 (1)	78.7	55.6
6	+1 (450)	–1 (0.1)	+1 (3)	81.3	52.9
7	+1 (450)	+1 (0.2)	–1 (1)	82.2	68.7
8	+1 (450)	+1 (0.2)	+1 (3)	86.3	47.5
9	0 (350)	0 (0.15)	0 (108)	56.9	46.4

The data evaluated the significant factors on CO conversion and H_2 yield. The result found that temperature (A) was the main effect which was observed in normal probability plot as shown in Figure 4.16. This might be explained that temperature, normally, directly effects on the kinetic reaction in the system. The graph presents that not only the temperature (A) but also catalysts weight (B) were significant factors on CO conversion. Only temperature was significant factor on H_2 yield. The water feed rate (C) was not significant factor in this work. Actually, excess water vapor enhances coverage of hydroxyl group on catalysts surface, then it reacts with adsorbed CO to become H_2 and CO_2. Nevertheless, this work studied the real reforming gas with 50% CO (dry basis); therefore, the least of water vapor to balance the reaction was also the same with CO component (50% H_2O). When increasing water, the catalysts became a soaking sludge in the reactor due to the water vapor in the system was quite high. Thus, the water feed rate (or steam/CO ratio) did not present a significant effect on the catalytic activity in this work. Moreover, too much of water vapor in the system presents the blocking of water on the catalysts surface lead to reduce the catalytic activity such as CO conversion and H_2 yield (109).

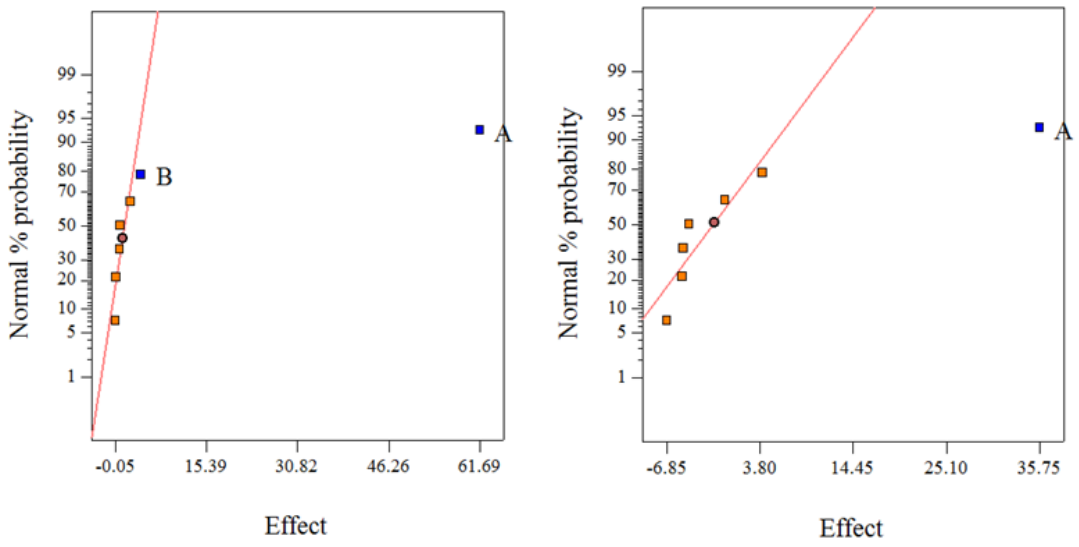

Figure 4.16 Normal probability plot of (left) CO conversion and (right) H_2 yield for full 2^3 factorial designs

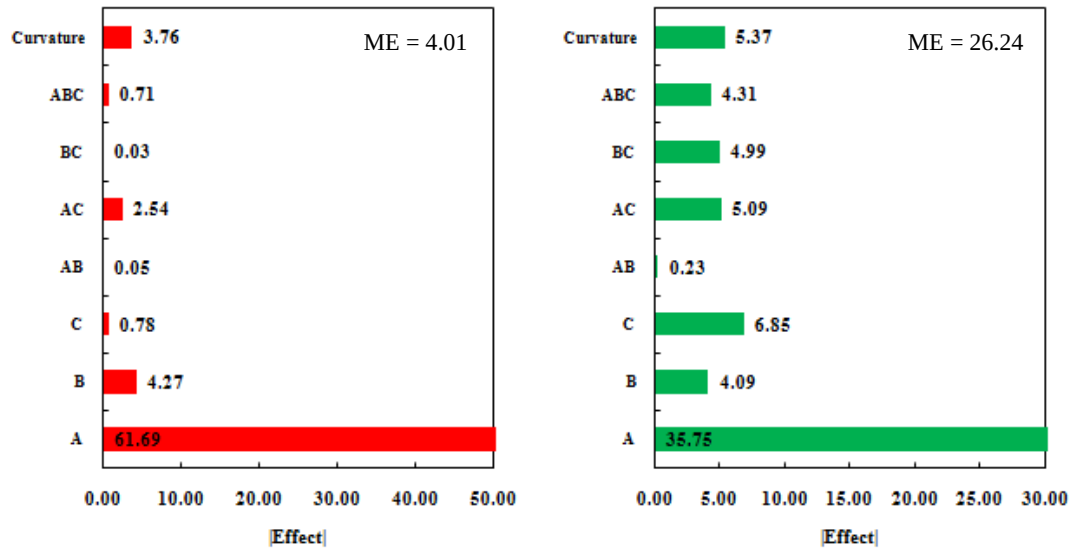

Figure 4.17 Effect list or Pareto diagrams of CO conversion and H_2 yield for full 2^3 factorial designs

The next evaluate was the consideration of absolute standard effect using on Pareto chart as shown in Figure 4.17. The CO conversion and H_2 yield parameters showed the margin error (ME) of 4.01 and 26.24, respectively. To consider on CO conversion, the temperature (A) and catalysts weight (B) showed the absolute standard effect of 61.69 and 4.27, respectively, presenting higher value than ME whereas the absolute standard effect of temperature on H_2 yield was 35.75 which also showed higher value than ME. The absolute standard effect decision represented the result as same as the normal probability evaluation. Beside, this evaluation also investigated the curvature effect. The absolute standard effect of curvature on CO conversion showed 3.76 which a slightly lower than ME value of 4.01. However, re-checking the curvature factors for an accuracy model was performed on the next part as respond surface methodology.

After screening effect factor, the respond surface methodology was studied. The factors that studied in this part were temperature (A) and catalysts weight (B) while the water feed rate (C) was not significant factor to the CO conversion and H_2 yield. The design of experiment for respond surface analysis—which used the face-centered cube design (FCC)—was shown in Table 4.9 with 5 center points (The water feed rate (C) was set at 2 ml/min as a constant value).

Table 4.9 Experimental data for response surface methodology by the face-centered cube (FCC) design with 5 center points and water feed (C) was kept at 2 ml/h as a constant value

No	A: Temperature (°C)	B: Weight catalysts (g)	CO Conversion	H_2 Yield
1	–1 (250)	–1 (0.1)	18.8	18.8
2	–1 (250)	+1 (0.2)	23.8	23.8
3	+1 (450)	–1 (0.1)	70.7	42.8
4	+1 (450)	+1 (0.2)	72.2	45.9
5	–1 (250)	0 (0.15)	15.9	15.9
6	+1 (450)	0 (0.15)	72.6	47.7
7	0 (350)	–1 (0.1)	56.0	44.3
8	0 (350)	+1 (0.2)	60.8	45.7
9	0 (350)	0 (0.15)	59.2	49.1
10	0 (350)	0 (0.15)	58.2	46.0
11	0 (350)	0 (0.15)	56.9	46.4
12	0 (350)	0 (0.15)	57.1	44.8
13	0 (350)	0 (0.15)	56.5	42.6

Table 4.10 presents ANOVA of factors that effect to CO conversion and H_2 yield. When focusing on CO conversion, factors A, B, AB, A^2, B^2 showed p-value <0.0001, 0.0319, 0.2037 , <0.0001, 0.3438, respectively, It can be said factor A, B, A^2 had a significant effect because of p-value less than 0.05 while factors B^2 and AB were not significant factors on CO conversion. The influence factors A and A^2 on H_2 yield represented a significant effect due to their p-value less than 0.0001. So, it can be concluded that factors A, B, A^2 had a significant effect on CO conversion while factors A and A^2 had a significant effect to H_2 yield. For residual, it divided to lack of fit and pure error. Lack of fit means the tests of data of a null hypothesis that presented statistical model was fitted well. Lack of fit did not present a significant P-value (not lower than 0.05) meaning that the models were acceptable for both CO conversion and H_2 yield. Besides, R^2 indicates that the sum square of main effects and

their interactions divided by the sum square of model. Particularly, the value of 0.95 or higher of R^2 investigates good agreement of experimental data. Moreover, adj-R^2 corrects the R^2 by expressed a smaller value than R^2 because it calculates from error and degree of freedom in the experimental results. CO conversion and H_2 yield presented the R^2 more than 0.95 which also confirmed the model could be reliable.

Table 4.10 Analysis of variance for CO conversion and H_2 yield of response surface analysis for quadratic model

Source	SS	DF	MS	F-Value	P-Value
CO conversion (%)					
Model					
A	4106.59	1	4106.59	1373.6632	<0.0001
B	21.36	1	21.36	7.1444	0.0319
A^2	446.43	1	446.43	149.3325	<0.0001
B^2	5.88	1	5.88	1.9656	0.2037
AB	3.08	1	3.08	1.0308	0.3438
Residual	20.93	7	2.99		
Lack of Fit	16.11	3	5.37	4.4606	0.0913
Pure Error	4.82	4	1.20		
Total	4635.40	12			
R^2	0.9955				
Adj-R^2	0.9923				
H_2 yield (%)					
Model					
A	1013.16	1	1013.16	136.7148	<0.0001
B	15.25	1	15.25	2.0581	0.1945
A^2	472.57	1	472.57	63.7685	<0.0001
B^2	0.03	1	0.03	0.0037	0.9534
AB	0.92	1	0.92	0.1239	0.7352
Residual	51.88	7	7.41		
Lack of Fit	29.64	3	9.88	1.7776	0.2904
Pure Error	22.23	4	5.56		
Total	1630.83	12			
R^2	0.9682				
Adj-R^2	0.9455				

As an explanation before, the temperature is the major factor that directly affects to the catalytic activity. Furthermore, the WGS reaction is an exothermic reaction when increasing temperature the reaction will perform backward reaction. It can be confirmed that A^2 controlled the temperature to reach an optimum point, and then the catalytic activities as CO conversion and H_2 yield were moderately reduced when temperature still increased. For catalysts weight, it represents an elongation of residence time in the reaction which directly effects to CO conversion. The H_2 yield means the catalysts ability of both reaction as water gas shift and methanation reaction; therefore, an increasing of catalysts weight implied that a residence time of both reactions were increased together and did not present significant effect on H_2 yield. The equation model, that predicted the CO conversion and H_2 yield, is shown in Table 4.11 (as code and actual factors).

Table 4.11 Summaries of equation model in code and actual factors by face-centered cube design of response surface methodology

Parameter	Code		Actual	
CO conversion (%) =	57.83		–188.34	
	26.16	* A	1.11	* Temperature
	1.89	* B	37.73	* Catalysts Weight
	–12.16	* A^2	–0.0012	* $Temperature^2$
H_2 yield (%) =	45.54		–159.71	
	12.99	* A	1.04	* Temperature
	–13.04	* A^2	–0.0013	* $Temperature^2$

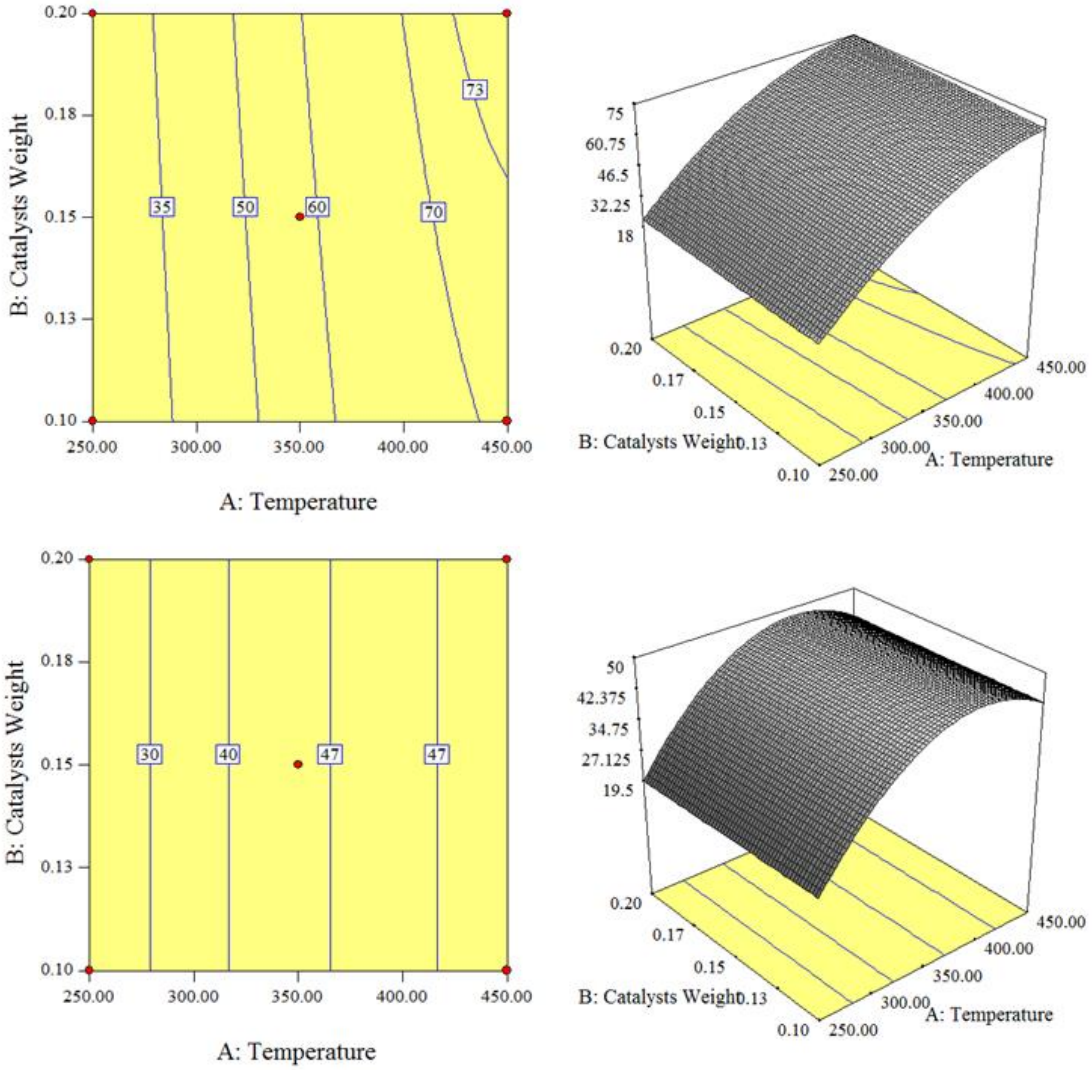

Figure 4.18 Response surface of contour and 3D plot of (top) CO conversion and (bottom) H_2 yield

Figure 4.18 shows contours and 3D plots of CO conversion and H_2 yield between temperatures (A) versus catalysts weight (B) and their interactions. It found that the temperature around 400 °C to 450 °C gave CO conversion more than 60% and the catalysts weight promoted CO conversion around 5% when used 0.2 g of catalysts. For H_2 yield, the temperature range of 350 °C to 450 °C gave H_2 yield more than 40% while the catalysts weight did not present an effect to H_2 yield.

As the results of equation model, it could predict the suitable operating condition for WGS reaction at the temperature of 413 °C and 0.2 g of catalysts. Table 4.12 presents the validation of model equation at suitable condition for operating. The optimum condition performed 71.9% of CO conversion from equation (74.2% for experiment) and 47.2% of H_2 yield from equation (52.1% for experiment). So the study of catalysts on water gas shift reaction over the CO conversion and H_2 yield can be evaluated by equation to find the optimal condition for operating.

Table 4.12 Validation of model at optimum condition at constant water feed rate at 2 ml/h.

No	Temperature (°C)	Catalysts Weight (g)	CO conversion (%)		H_2 yield (%)	
			Predicted	Actual	Predicted	Actual
1	413	0.20	71.9	74.2	47.2	52.1

4.2.2 Preferential oxidation (PROX)

In this section, the reduction of carbon monoxide was studied via preferential oxidation reaction over 1% by weight of Au/CeO_2 catalyst prepared by deposition–precipitation method. The activities of catalysts were studied under influence of various factors as presented in section 4.2.2.1. The effect of these factors (temperature, catalysts weight, oxygen per carbon monoxide ratio, carbon dioxide addition and water addition) was evaluated by statistical analysis (the full 2^k factorial design) as shown in section 4.2.2.2. The respond surface analysis is an advance method to investigate the data to give more explanation detail of significant factors. This respond surface study used Box-Behnken theory to determine the new model to get more precision. The last section involves a validation of model.

4.2.2.1 Activities of Au/CeO_2 catalysts

Figure 4.19 shows activities of Au/CeO_2 catalysts with various temperatures. It presented that conversion increased when increased temperature because the kinetic of CO and O_2 molecules had high enough energy to converse to CO_2. On the other hand, selectivity represented the opposite way, compared to the conversion behavior. So, temperature is an important factor on the PROX reactions because many researchers studied of this factor (15, 110, 111). Furthermore, this behavior can be described to the competition of O_2 consuming by H_2 and CO molecules in order to forward reaction. It is well known that everyone needs to perform high conversion and high selectivity, but which is the appropriate point during the conversion and selectivity. The yield demonstrates the maximum value which indicates the suitable point between conversion and selectivity. Thus, considering the yield is very interesting for the best operating condition.

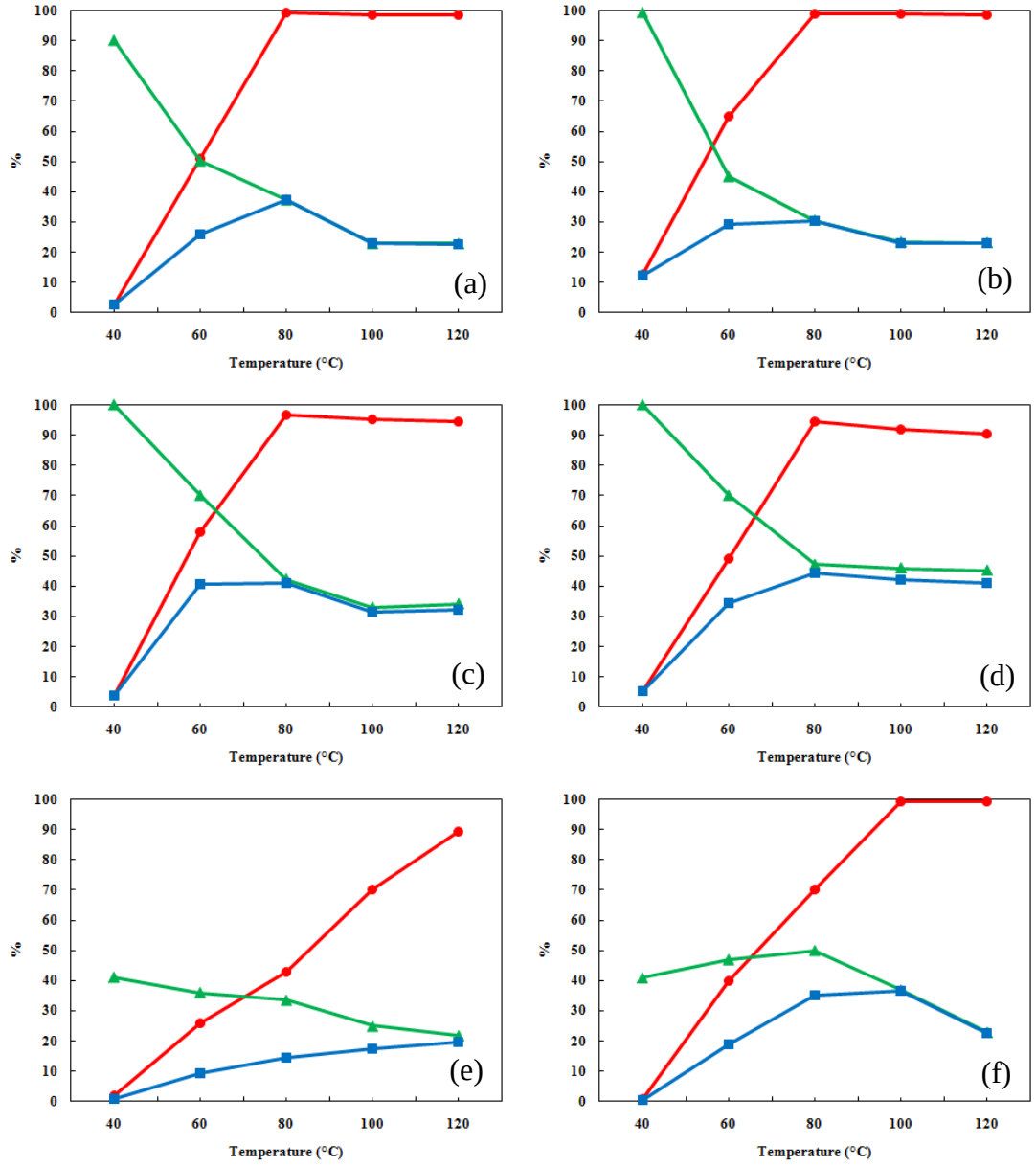

Figure 4.19 The activity of (●) conversion (%), (▲) selectivity (%), and (■) yield (%) over Au/CeO_2 catalysts at various conditions

Condition	Wt. of catalysts (g)	feed stream composition (%v/v) in He balance				
		H_2	O_2	CO	CO_2	H_2O
a	0.05	40	2	1	-	-
b	0.15	40	2	1	-	-
c	0.05	40	1.5	1	-	-
d	0.05	40	1	1	-	-
e	0.05	40	2	1	20	-
f	0.05	40	2	1	-	10

Figure 4.19(a) and Figure 4.19(b) represent the influence of weight of Au/CeO_2 catalyst. We can see that 0.5 g of Au/CeO_2 catalyst gave higher selectivity and yield than 1.5 g of Au/CeO_2 catalyst at 80 °C. Particularly, the relation between catalyst weights with catalyst performance refers to contact time (W/F ratio) or gas hourly space velocity (GHSV). This can be said that an increasing catalysts weight promote H_2 oxidation more than CO oxidation resulting in decreasing of selectivity and yield. Therefore, the weight of catalyst is also an important variable, Avgouropoulos *et al.* (112) confirmed that the weight of the catalyst effected to the CO conversion reaction in PROX reaction.

Figure 4.19(a), (c) and (d) represent the effect of O_2/CO ratio at 2.0, 1.5 and 1.0, respectively. O_2/CO ratio at 2.0 presented an increasing conversion from 40 °C to 80 °C and performed complete conversion above 80 °C. And it ratio at 1.5 and 1.0 also showed the same trend but presented nearly complete conversion at 80 °C. Considering selectivity, O_2/CO ratio at 1.0 presented higher selectivity than its ratio at 2.0 in whole temperature range. The results showed a different activity because of a competition between H_2 oxidation and CO oxidation. The portion of O_2/CO was confirmed by some researchers that effect to the conversion of this reaction. Avgouropoulos *et al.* (112) studied O_2/CO ratio at 1.25 while Arena *et al.* (113) used the O_2/CO ratio = 2. So the ratio of O_2/CO should be studied for finding the optimum point.

The influents of CO_2 and H_2O on the catalytic performance were shown in Figure 4.19(e) and Figure 4.19(f), respectively. It can be observed that CO_2 addition could depress the catalysts activities in all range of temperature and H_2O addition also showed less activity at 40 °C to 60°C. However, H_2O addition could reach the complete CO conversion at 100 °C and showed highest CO_2 selectivity at 80 °C. Figure 4.20 represents the FTIR pattern of spent catalysts under CO_2 and H_2O on these catalysts. The carbonate specie bands presented at 1200 cm^{-1} to 1800 cm^{-1}. It referred to an intermediate reactant of CO oxidation while CO reacting at surface of catalysts representing two quite board peaks at 1343 cm^{-1} and 1544 cm^{-1}. The more concentration of O_2 could release carbonate species greater than lower of O_2 due to a promotion of O_2 converting CO to CO_2. The present of CO_2 in the feed stream showed the highest peak as can be said that the CO_2 competed to cover an active site

to form carbonate intermediate species, which especially presented at 1343 cm^{-1} peak. The water showed a slight decline peak than free water. It can be concluded that the result confirmed with Gamarra *et al.* (114) which explained the path way of CO oxidation by the reaction of carbon monoxide and oxygen molecule from hydroxyl species.

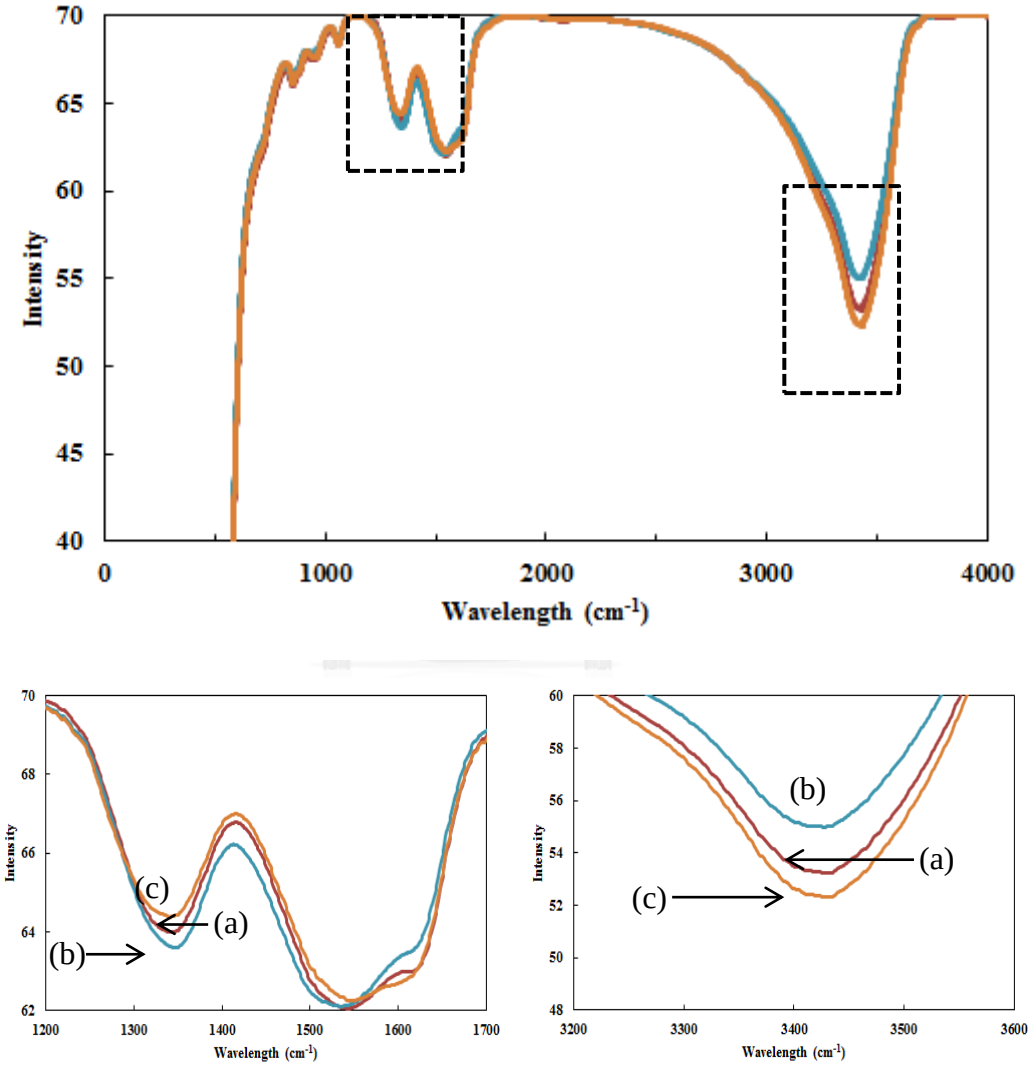

Figure 4.20 The intensity of FTIR over Au/CeO_2 on the condition: (a) spent catalyst at feed composition was 40% H_2, 2% O_2, 1% CO and He balance; (b) spent catalyst at feed composition was 40% H_2, 1% O_2, 1% CO, 20% CO_2 and He balance; (c) spent catalyst at feed composition was 40% H_2, 1% O_2, 1% CO, 10% H_2O and He balance.

The band between 2500 cm^{-1} to 3700 cm^{-1} represented hydroxyl specie. It can be seen that the reduction of O_2 conformed to the reduction of OH species. The hydrogen oxidation which demonstrates hydroxyl specie was decreased because of the lower O_2 in the feed stream. The present of CO_2 in feed stream, it showed less hydroxyl species than free CO_2 due to the CO_2 obstructed O_2 molecules to react with hydrogen to form hydroxyl intermediate on catalysts surface. The present of H_2O at 1% O_2 (O_2/CO ratio = 1) displayed the OH species substantial near free water at 2% O_2 (O_2/CO ratio = 2) at wavelength around 3300-3500 cm^{-1}. This can be explained that water could promote OH species to cover catalysts surface which confirm OH species reinforce the CO molecule to CO_2 like reason of carbonate species. The conclusion of hydroxyl intermediate species can be described that it could promote the CO oxidation at suitable amount of water. However, the excess of water would restrain the CO oxidation because the catalysts surface would lose some active sites for this application. Some researcher explained the behavior of CO_2 and H_2O. Arena *et al.* (113) and Moretti *et al.* (115) found that added CO_2 in feed stream would decrease the conversion and selectivity. It can be explained that the containing of CO_2 in H_2-rich stream affects to catalysts performance due to competition to cover the surface of the catalysts. Deng *et al.* (72) studied that the existence of water in the stream could increase the selectivity. But Avgouropoulos *et al.* (112) found that water could decrease the conversion and selectivity due to the condensation of water onto an active surface effecting on the PROX reaction at O_2/CO ratio = 1.25. Therefore, the CO_2 addition and H_2O addition were importance factor to study optimum operation.

4.2.2.2 Experimental design for operating

This section would like to study the appropriate condition in the PROX reaction over 1%Au/CeO_2 catalysts in plug flow reactor. Temperature (defined as variable A), W/F ratio (defined as variable B), the O_2/CO ratio (defined as variable C), CO_2 added (defined as variable D) and H_2O added (defined as variable E) were several factors for screening. The optimization of variables was screened in a running of 32 runs for 5 factors and 2 center points. Table 4.13 represents the factor levels for screening experiment which is coded as -1 (low), 0 (center point) and 1 (top). The yield was selected as response.

Table 4.13 Experimental variables in coded and actual units for the 2^5 factorial design with two center points

Factor	variable	unit	Low (-1)	Medium (0)	High (+1)
A	Temperature	°C	40	80	120
B	W/F ratio	g·s/ml	0.001	0.002	0.003
C	O_2/CO ratio	-	1	1.5	2
D	CO_2 added	%	0	10	20
E	H_2O added	%	0	5	10

No	A	B	C	D	E	Conversion (%)	Selectivity (%)	Yield (%)
1	-1	-1	-1	-1	-1	5.2	100.0	5.2
2	1	-1	-1	-1	-1	90.6	45.2	41.0
3	-1	1	-1	-1	-1	7.5	100.0	7.5
4	1	1	-1	-1	-1	91.7	45.8	42.0
5	-1	-1	1	-1	-1	2.7	90.3	2.5
6	1	-1	1	-1	-1	98.4	23.0	22.6
7	-1	1	1	-1	-1	9.0	99.4	9.0
8	1	1	1	-1	-1	98.8	23.1	22.8
9	-1	-1	-1	1	-1	5.0	31.8	1.6
10	1	-1	-1	1	-1	57.4	26.4	15.2
11	-1	1	-1	1	-1	5.3	35.0	1.8
12	1	1	-1	1	-1	64.9	32.8	21.3
13	-1	-1	1	1	-1	1.8	41.0	0.7
14	1	-1	1	1	-1	89.4	21.9	19.6
15	-1	1	1	1	-1	2.0	29.0	0.6
16	1	1	1	1	-1	91.0	22.3	20.3
17	-1	-1	-1	-1	1	1.7	80.0	1.4
18	1	-1	-1	-1	1	87.2	44.9	39.2
19	-1	1	-1	-1	1	5.6	100.0	5.6
20	1	1	-1	-1	1	91.2	47.0	42.9
21	-1	-1	1	-1	1	0.9	40.9	0.4
22	1	-1	1	-1	1	99.2	22.9	22.7
23	-1	1	1	-1	1	10.2	44.5	4.5
24	1	1	1	-1	1	99.1	22.9	22.7
25	-1	-1	-1	1	1	10.6	45	4.8
26	1	-1	-1	1	1	62.2	29.1	18.1
27	-1	1	-1	1	1	7.9	46.8	3.7
28	1	1	-1	1	1	69.4	32.5	22.6
29	-1	-1	1	1	1	1.0	34.0	0.3
30	1	-1	1	1	1	90.4	22.1	20.0
31	-1	1	1	1	1	1.4	27.0	0.4
32	1	1	1	1	1	90.9	22.2	20.2
33	0	0	0	0	0	78.3	46.0	36.0
34	0	0	0	0	0	74.5	46.4	34.8

The normal probability plot of the effect is shown in Figure 4.21. The graph can be separated into two zones: a primary zone with upper than 50% probability where the effect and interactions present positive coefficients; a secondary zone with lower than 50% probability where the effect and interactions present negative coefficients. The combination between conversion and selectivity was shown in term of yield. The effects and interactions located out of a straight line having a significant effect to the yield. The significant effect of the yield was A, C, D, AC, AD, CD and ACD (A, CD, ACD were positive effect and C, D, AC, AD were negative effect).

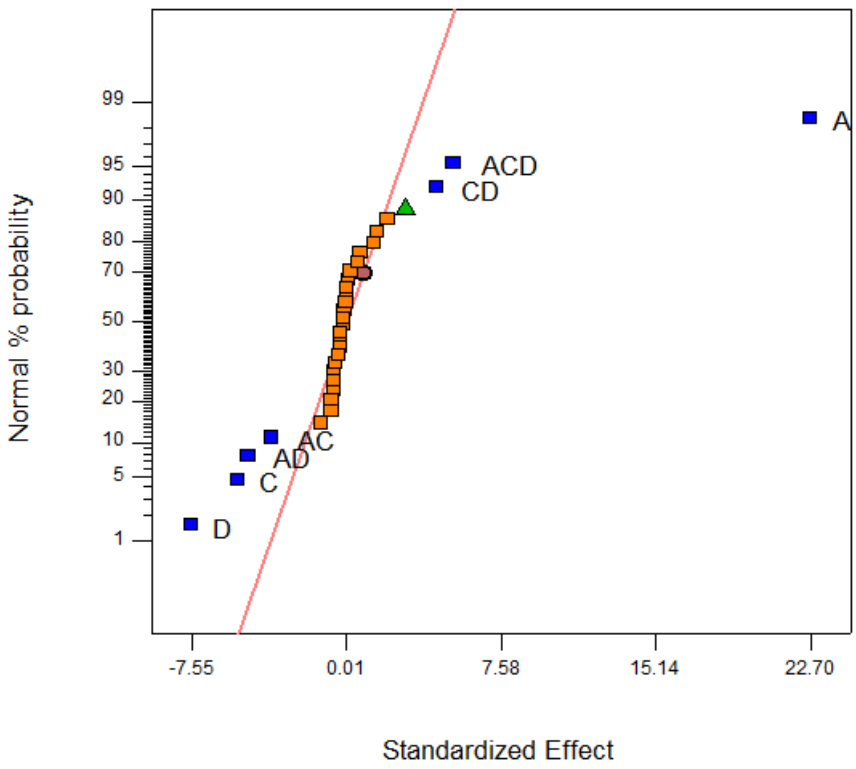

Figure 4.21 Normal probability plot of yield (%) of the effects for the 2^5 factorial designs: A–temperature; B–W/F ratio; C–O_2/CO ratio; D–CO_2 added; E–H_2O added; and their interaction

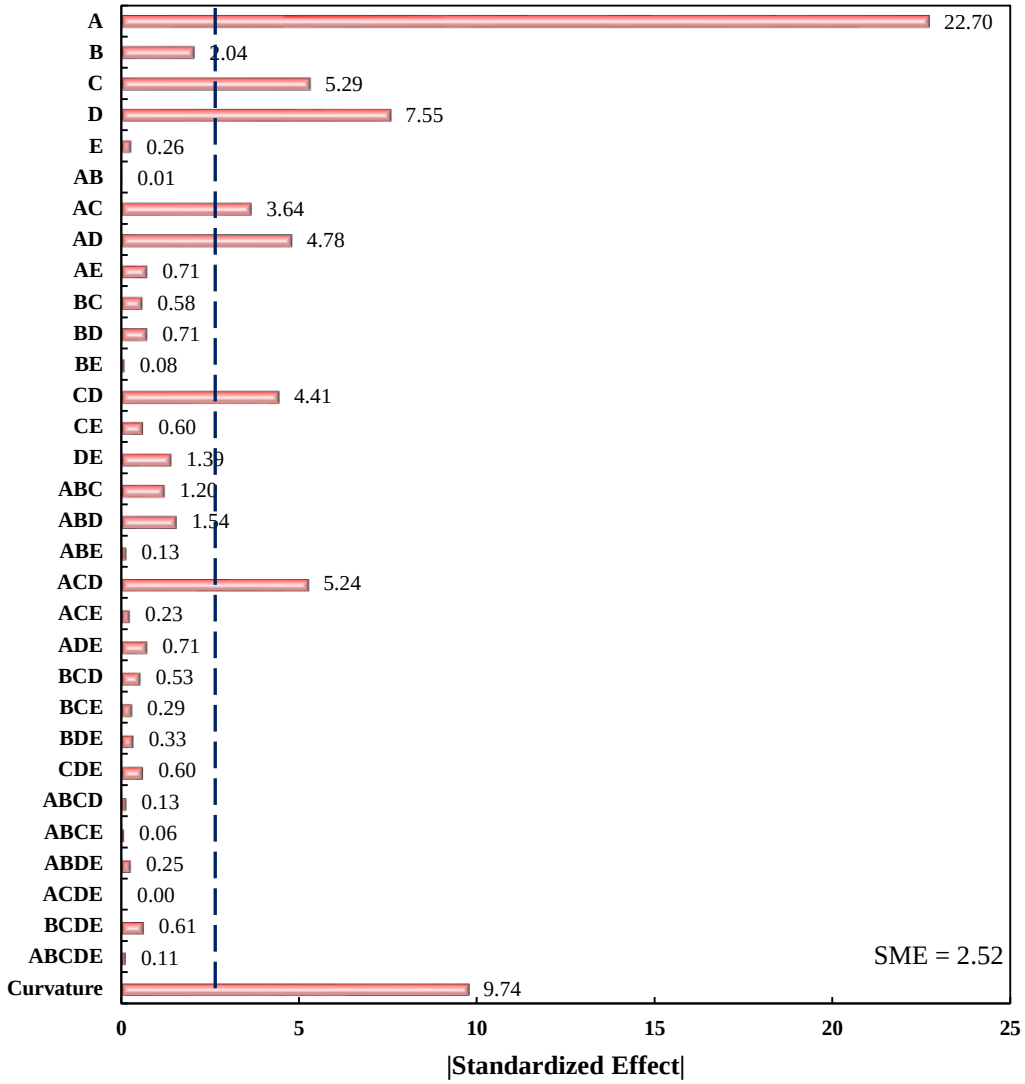

Figure 4.22 Pareto's chart of yield (%) of absolute standardized effects on the factors: A–temperature; B–W/F ratio; C–O_2/CO ratio; D–CO_2 added; E–H_2O added; their interaction; and curvature with SME value

Figure 4.22 represents the Pareto chart of the absolute standardized effect at P-value = 0.05 on yield. Absolute standardized effects would become a significant effect which had higher value than simultaneous margin error (SME of yield is 2.52). By analyzing the graph, it can be concluded that the reaction temperature (A), CO_2 added (D), the O_2/CO ratio (C), interaction between ACD, AC, CD, AC were an important effect on yield in that order.

Table 4.14 ANOVA of the full 2^5 factorial designs for yield

Term	SS	DF	MS	F	P-value	Coefficient	Significant
A	4122.3	1	4122.3	5725.4	0.01	11.35	significant
B	33.2	1	33.2	46.1	0.09	1.02	
C	223.7	1	223.7	310.6	0.04	-2.64	significant
D	456.0	1	456.0	633.4	0.03	-3.78	significant
E	0.6	1	0.6	0.8	0.54	-0.13	
AB	0.0	1	0.0	0.0	0.97	0.01	
AC	105.9	1	105.9	147.0	0.05	-1.82	significant
AD	182.4	1	182.4	253.3	0.04	-2.39	significant
AE	4.1	1	4.1	5.6	0.25	0.36	
BC	2.6	1	2.6	3.7	0.31	-0.29	
BD	4.1	1	4.1	5.6	0.25	-0.36	
BE	0.0	1	0.0	0.1	0.84	-0.04	
CD	155.8	1	155.8	216.3	0.04	2.21	significant
CE	2.9	1	2.9	4.0	0.30	-0.30	
DE	15.4	1	15.4	21.4	0.14	0.69	
ABC	11.5	1	11.5	16.0	0.16	-0.60	
ABD	18.9	1	18.9	26.3	0.12	0.77	
ABE	0.1	1	0.1	0.2	0.75	0.06	
ACD	219.5	1	219.5	304.8	0.04	2.62	significant
ACE	0.4	1	0.4	0.6	0.59	0.11	
ADE	4.1	1	4.1	5.6	0.25	-0.36	
BCD	2.2	1	2.2	3.1	0.33	-0.26	
BCE	0.7	1	0.7	0.9	0.51	-0.14	
BDE	0.8	1	0.8	1.2	0.47	-0.16	
CDE	2.9	1	2.9	4.0	0.30	-0.30	
ABCD	0.1	1	0.1	0.2	0.75	-0.06	
ABCE	0.0	1	0.0	0.0	0.87	0.03	
ABDE	0.5	1	0.5	0.7	0.56	-0.13	
ACDE	0.0	1	0.0	0.0	1.00	0.00	
BCDE	3.0	1	3.0	4.2	0.29	0.31	
ABCDE	0.1	1	0.1	0.1	0.77	-0.06	
Curvature	824.2	1	824.2	1144.7	0.0188	824.2	significant
Residual	0.7	1	0.7			0.7	
Total	6398.6	33				6398.6	
R^2 (significant term)			0.9805	Adj R^2 (significant term)		0.9750	

An analysis of variance (ANOVA) on yield is shown in Table 4.14. The sum of squares, degree of freedom, mean square, F-value, P-value, and regression coefficient were calculated. The significant effect were determined from P-value which was lower than 0.05. These effects were confirmed with %normal probability plot and absolute standardized effect. The relative importance of these effects is also guided by the %contribution relating to the total sum of squares. A curvature is obtained by the difference between the average of the factorial points and the average of the center points. Besides, the analysis of variance reported a curvature of the model. It can be concluded that the curvature of the model could not be neglect.

The R^2 value provides a measure of how much variability that can be told by main effects and their interactions to a significant model. The R^2 was 0.9805 which indicated a good agreement between the experimental and the regression equation model. The adj-R^2 corrects the R^2 value for the sample size and for the number of terms in the model because degree freedom of effect is considered in the model. If there are many terms in the model and if the sample size is not very large, the adj-R^2 may be expressed as smaller than the R^2. In this study, both of R^2 and adj-R^2 (adj-R^2 = 0.9750) were more than 0.9. This can be implies that, the selected significant effect confirmed a regression model. From a full factorial experimental design, the W/F ratio (B) and H_2O added (E) were not significant factors to yield compared with other variables.

Figure 4.23 shows normal probability plot of residuals with R^2 more than 0.9. This result confirmed that the experiment was reliable (116). However, when focus on the existence of curvature of yield was shown in Figure 4.22, standard effect was displayed more than SME value. This can be suggested that a respond surface analysis design should be undertaken to achieve a better understanding of PROX condition.

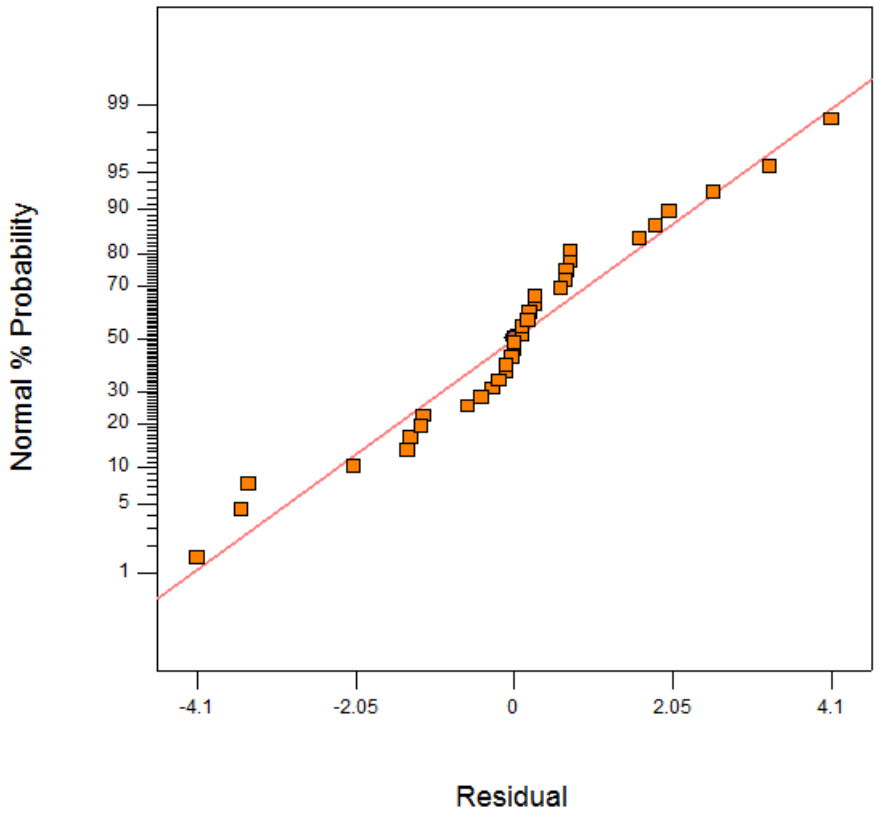

Figure 4.23 Normal plot of residual of yield selecting A–temperature, C–O_2/CO ratio, and D–CO_2 added as a significant factor

Box-Behnken design is a class of rotatable or nearly rotatable second-order designs based on three-level incomplete factorial designs. A comparison between the Box-Behnken design and three-level full factorial design has demonstrated that the Box-Behnken design is much more effectiveness than the three-level full factorial designs where the effectiveness of one experimental design is defined as the number of coefficients in the predict model divided by the number of runs. A comparison among the efficiencies of Box-Behnken disign for the quadratic model found that is a good response surface for three factors. Another advantage is that it does not contain combinations for which all factors are simultaneously at their highest or lowest levels. The Box-Behnken is a good design for response surface methodology because it permits estimation of the parameters of the quadratic model and building of sequential designs (117). The application of Box-Behnken design for optimization of analytical methods is presented in this section.

From a screening 2^5 factorial design, we found the factors A, C and D as good as the factor that effect to the yield; therefore, the variable A, C and D were great to do respond surface analysis. Figure 4.24 shows the influence of main factors on yield of a screening that the factor B and E could be neglected due to the lack of significance term. Respond surface analysis could adjust the level of temperature factor. Because the range of temperature was quite broad or the slope was high, the more error of yield would be found in this range.

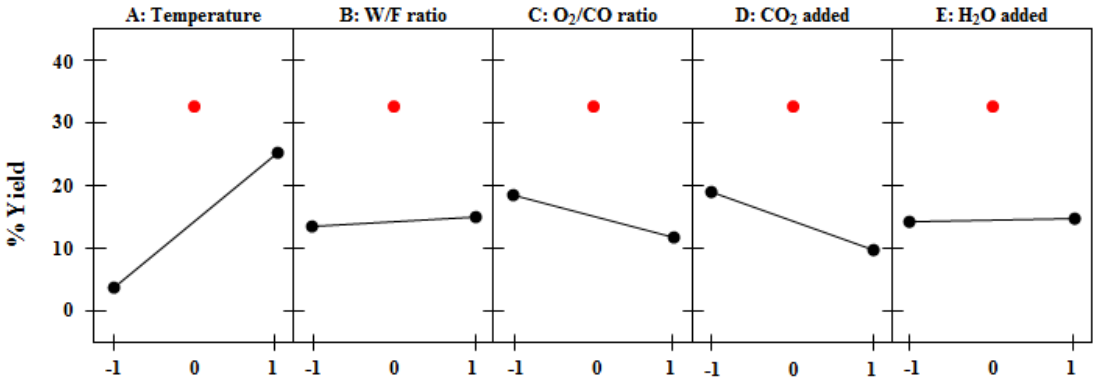

Figure 4.24 Main effect plots for yield (%) response for 2^5 factorial designs, each factor plot are low (-1) and high (1) with center value of other factor and 2 average center points.

Table 4.15 shows the number of Box-Behnken experiment with 17 trials. From a screening, low and high level of temperature (A) would change from 40 °C and 120 °C to 60 °C and 100 °C, respectively. The range of O_2/CO ratio (C) and CO_2 added (D) had still been the same range. W/F ratio (B) was set at 0.001 g and 0% H_2O added (E).

Table 4.15 Experimental variables in coded and actual units for Box-Behnken design of 3 factors containing 17 trials with 5 center points.

Factor	variable	unit	Low (-1)	Medium (0)	High (+1)
A	Temperature	°C	60	80	100
C	O_2/CO ratio	-	1	1.5	2
D	CO_2 added	%	0	10	20

Note: Factor B was kept at 0.001 g·s/ml and Factor E was kept at 0% H_2O.

No	A	C	D	Conversion (%)	Selectivity (%)	Yield (%)
1	-1	-1	0	20.2	94.6	19.1
2	1	-1	0	66.5	33.4	22.2
3	-1	1	0	26.2	82.5	21.5
4	1	1	0	85.7	25.4	21.6
5	-1	0	-1	58.2	70.0	40.7
6	1	0	-1	95.3	33.1	31.5
7	-1	0	1	16.1	89.2	14.4
8	1	0	1	72.0	27.7	20.0
9	0	-1	-1	94.4	47.1	44.5
10	0	1	-1	99.3	37.5	37.2
11	0	-1	1	38.0	38.7	14.7
12	0	1	1	43.0	33.5	14.4
13	0	0	0	73.3	43.7	32.1
14	0	0	0	73.0	42.2	30.8
15	0	0	0	68.5	46.2	31.6
16	0	0	0	65.2	46.5	30.3
17	0	0	0	66.1	46.4	30.7

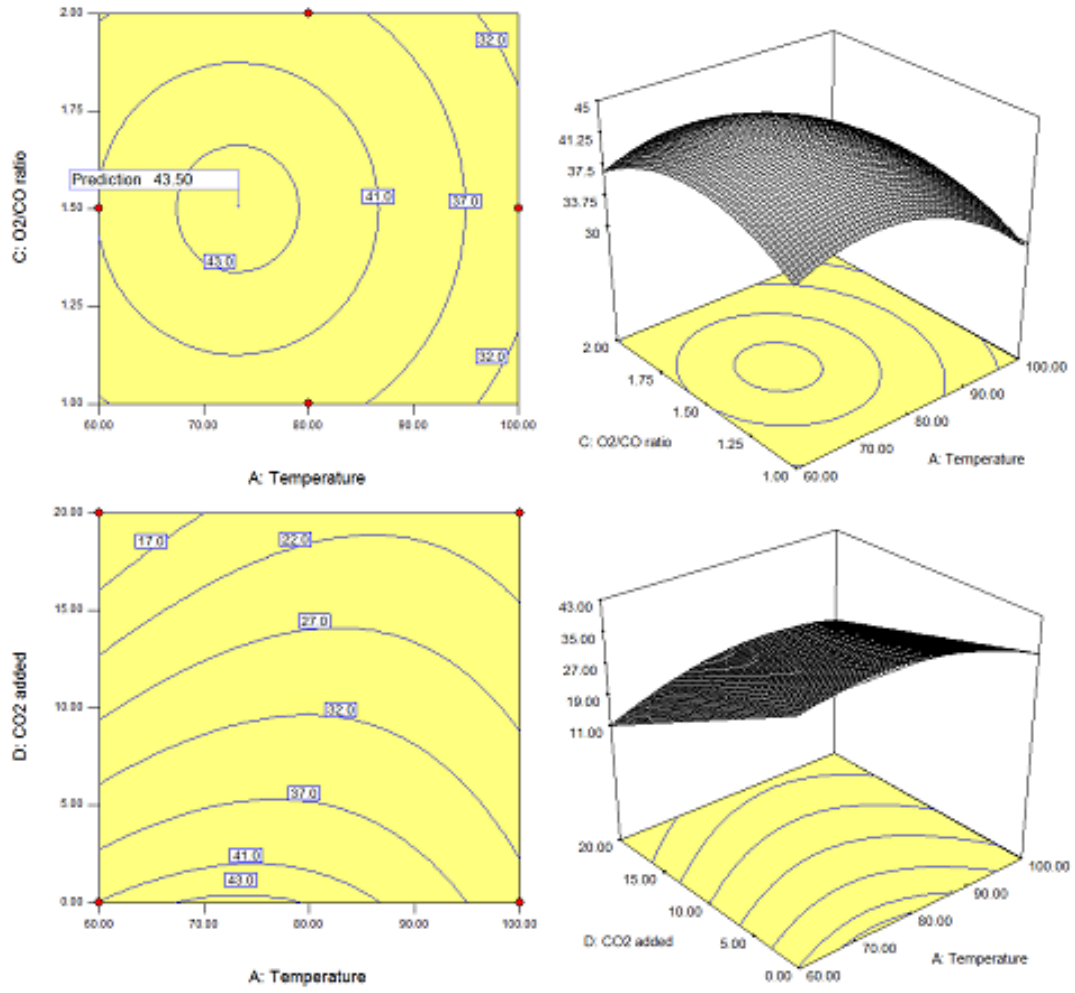

Figure 4.25 Contour plot (left) and 3D-diagram (right) of % yield on: (top) Temperature vs O_2/CO ratio with 0% CO_2; (bottom) Temperature vs. CO_2 added with O_2/CO ratio equal 1.5

Figure 4.25 shows 3D diagram and contour of the temperature factor (A) versus the O_2/CO ratio (C) (with 0 % CO_2 added). It found that the temperature and yield increased together until the optimum point. After that, an increasing temperature would show contrast with yield. The range of optimum temperature was around 68 °C to 78 °C and the range of O_2/CO ratio was around 1.35 to 1.65. The 3D diagram and contour of the temperature factor (A) versus CO_2 added (D) (with center value of O_2/CO ratio) found that the existence of CO_2 represented negative effect to the yield

in all temperatures. From the results, it can be concluded that the proper temperature was around 73 °C, O_2/CO ratio of 1.50 and no amount of CO_2 entering with the stream. The value of yield was increased up to 43.50% at optimum condition (analyzed by design expert 6.0). Figure 4.26 shows normal probability plot of residuals as same pattern like Figure 4.23. It can be suggested that the equation was validity and reliable. Considering the yield, it was the most basic as finding the best condition for PROX reaction because the yield represented the importance of conversion and selectivity.

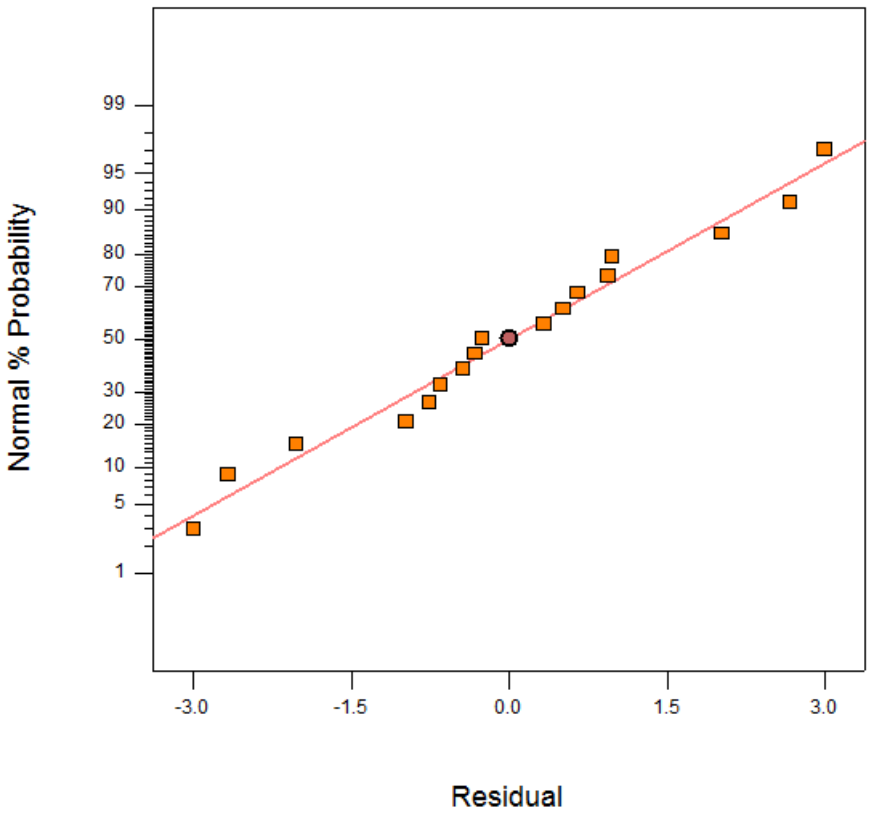

Figure 4.26 Normal plot of residual of Box-Behnken respond surface of yield by select D, A^2, C^2 and AD as a significant factor

From Box-Behnken respond surface analysis, the ANOVA table of significant factors is shown in Table 4.16. The different of R^2 and adj-R^2 of significant factors were less than the Box-Behnken full model. This reason believes that the full model could be reduced to the new model which had still been a reliable and an acceptable. The final equation of yield was presented following in term of code factor;

$$\text{Yield (\%)} = 31.56 - 11.31*D - 5.47*A^2 - 4.41*C^2 + 3.71*A*D$$

Table 4.16 ANOVA of significant factors of Box-Behnken designs to the yield

Term	SS	DF	MS	F	P-value	Coefficient (code-factor)
D	1024.2	1	1024.2	175.6	<0.0001	-11.31
A^2	126.5	1	126.5	21.69	0.0006	-5.47
C^2	82.1	1	82.1	14.07	0.0028	-4.41
AD	55.1	1	55.1	9.45	0.0097	3.71
Residual	70.0	12	5.8			
Total	1369.9	16				
R^2	0.9489				Intercept	31.56
Adj R^2	0.9319					

To validate at optimum condition of significant factors, confirmable model was carried out and compared between experimental data and equation model which is shown in Figure 4.27. Validation of equation was tested in the range of study. The optimum condition for maximized yield was found in this condition range. The accuracy of the model equation with the actual experiment was acceptable because it rarely deviated from 45° line.

Table 4.17 represents the yield at optimum point as can be seen that the models were close to actual values with 4.40 % error. Thus, the results confirmed that the temperature (A), the O_2/CO ratio (C) and CO_2 added (D) were significant factors to the yield.

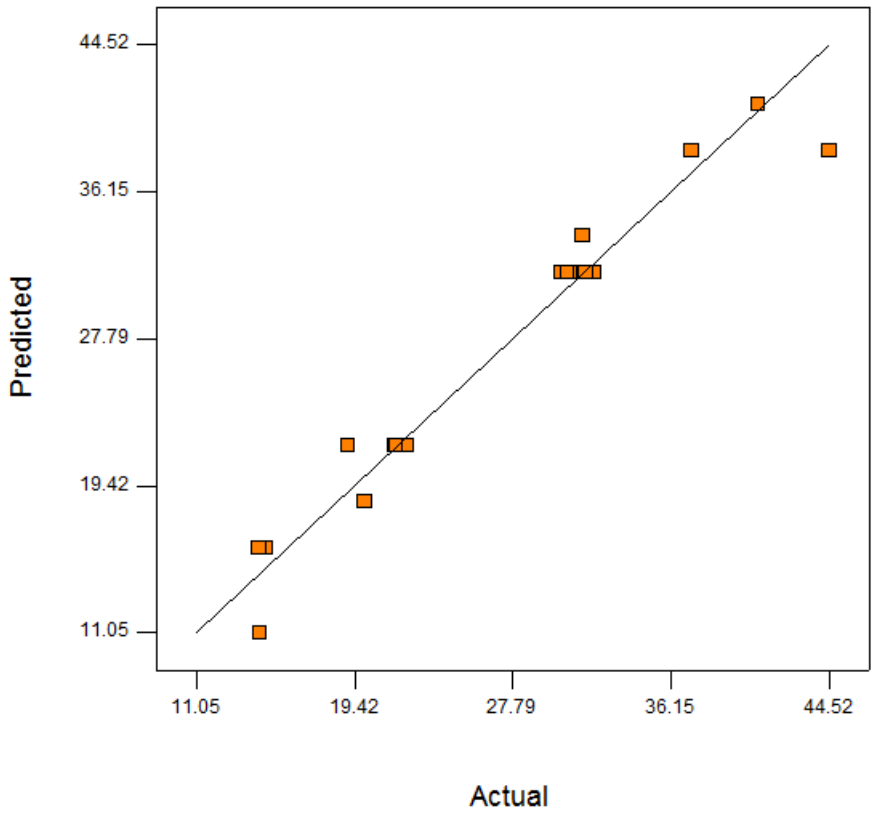

Figure 4.27 Validation between predicted values and actual values of Au/CeO_2 catalysts on the yield

Table 4.17 Experimental variables on yield (%) compared between predicted value and actual value at optimum point

	A	C	D	Yield (%)		Error (%)
				Predicted	Actual	
Optimum	73	1.5	0	43.5	45.5	4.40

Finally, a reliable model can predict the data resulting in the development of the PROX system. Moreover, this can reduce the trial and also give the necessary information. And, it also reduces costs and waste which released to the environment as well.

4.3 Integrations of hydrogen production and carbon monoxide clean up

This section studied a combination of H_2 production part (DRM) and CO clean up part (WGS and PROX) based on the results of experimental design. In DRM reaction, the 5Ni-0.5Mn/CeO_2 catalysts was selected as condition of 800 °C, CH_4 composition of 0.5, 0.1 g of catalysts weight and 30 ml/min of total feed rate. In WGS process, the 1%(1:1)AuFe/CeO_2 was chosen for both of WGS1 and WGS2. The optimum condition of 413 °C, 0.2 g of catalysts and 2 ml/h of water feed rate was operated for WGS1. The PROX reaction used an Au/CeO_2 catalyst which was operated at 73 °C and O_2/CO ratio of 1.5. The study of DRM, WGS and PROX are determined in section 4.3.1 (as shown in Figure 3.2). In section 4.3.2, the DRM, double WGS, and PROX are investigated and also show in Figure 3.3. The last section 4.3.3, the study of stability test of best condition is observed and presents in all components in each process.

4.3.1 Integration of all processes (DRM, single WGS, and PROX)

In this section, the addition of CO_2 trap between WGS and PROX for removal CO_2 component before entering PROX was set up to improve the ability of PROX catalysts and set the optimum constrain as no CO_2 component in an inlet feed. The substance for CO_2 capture was molecular sieve 5A commercial. The performances of catalysts in each part are presented in Figure 4.28. The inlet gas before entering into DRM contains 50% methane and 50% carbon dioxide at 30 ml/min. The DRM reaction gave 80% CH_4 conversion, 70% CO_2 conversion and 60% H_2 selectivity. The composition of outlet gas from DRM contained 6.5% CH_4, 9.7% CO_2, 31.2% H_2 and 52.6% CO with total flow around 46 ml/min. The outlet gas from DRM was mixed with water vapor (at steam/CO ratio = 2) in 10 ml/h of helium before entering WGS reactor. The catalysts in WGS performed 70% CO conversion and 55% H_2 yield containing 4.6% CH_4, 30.6% CO_2, 39.8% H_2 and 9.7% CO (dry basis) in helium.

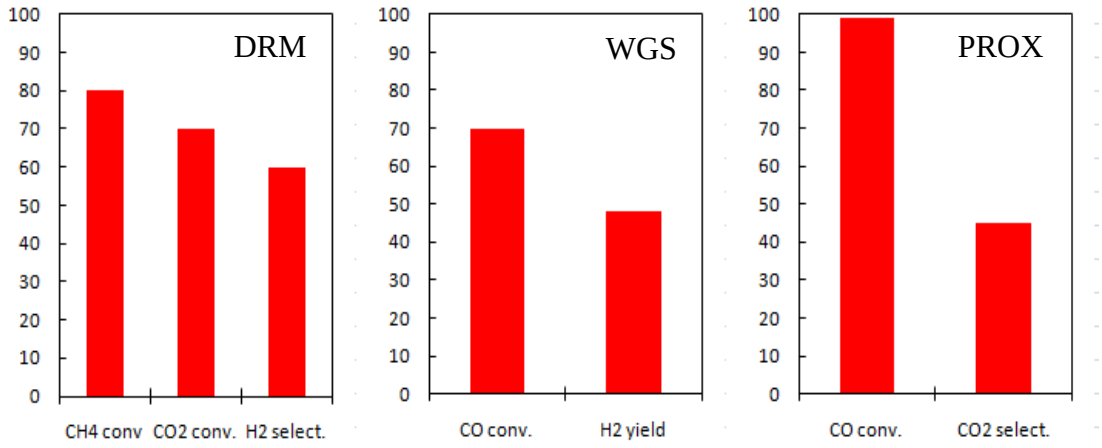

Figure 4.28 Catalysts performance of integration of DRM, WGS and PROX processes with CO_2 trap unit between WGS and PROX process
*Reaction condition was the optimal condition with suitable catalysts in each process.

The outlet gas of WGS part entered to CO_2 trap using 100 g of molecular sieve 5A as CO_2 absorber before routing to PROX process. Complete CO_2 removal from the stream via adsorption on molecular sieve 5A was observed in a whole period of 20 h. The new composition of outlet stream from CO_2 trap was 6.6% CH_4, 57.5% H_2, and 13.9% CO in helium at 45 ml/min total flow. Before entering to PROX, the outlet gas from CO_2 trap was mixed with oxygen at the optimum ratio (O_2/CO ratio = 1.5) in helium. The catalysts activities of PROX reaction became 99% CO conversion and 45% CO_2 selectivity which presented the outlet component as 3.4% CH_4, 7.2% CO_2, 28.7% H_2, CO lower than 0.01% and 3.0% O_2 in helium (around 87 ml/min outlet flow) which is shown in Figure 4.28 and Figure 4.29.

This section showed complete CO removal from DRM process, but, the hydrogen product presented quite low concentration. It can be said that the outlet gas from WGS reaction still contained high CO level. The O_2 feed must be high in order to remove CO residue in PROX, so undesired reaction as hydrogen oxidation would be increased as well. Further enhanced the hydrogen productivity, double stage of WGS was studied to reduce CO level before entered the PROX in order to reduced hydrogen oxidation reaction as side reaction.

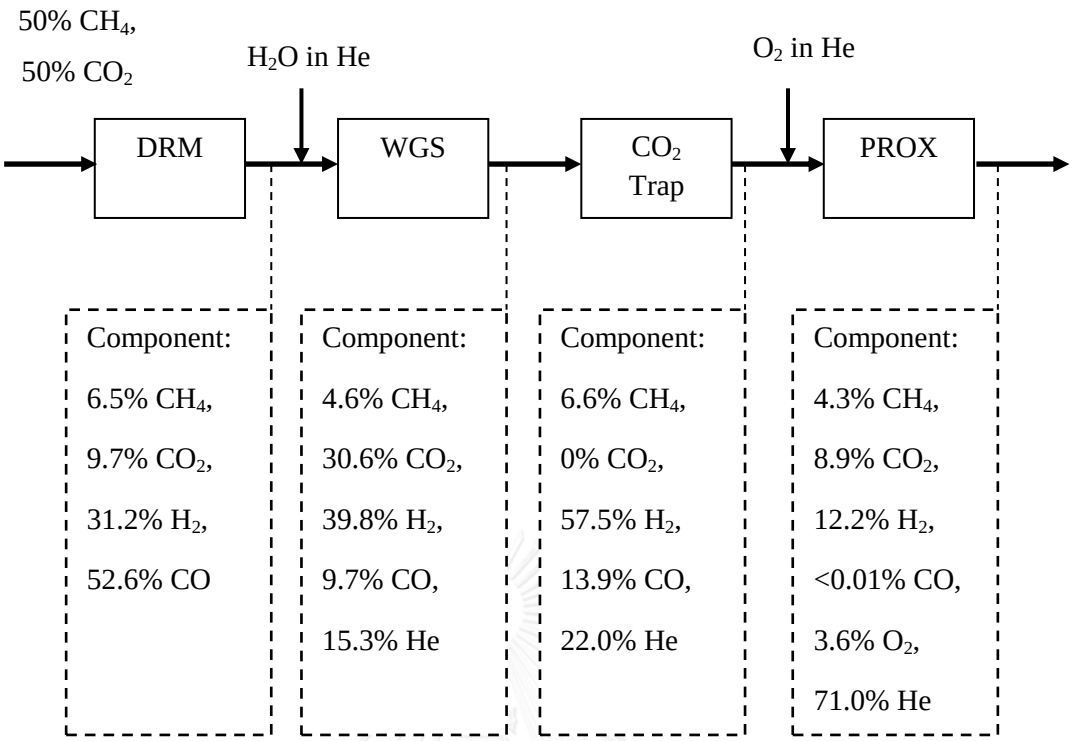

Figure 4.29 Outlet gas composition in DRM, single WGS and PROX processes with CO_2 trap between WGS and PROX process

*Reaction condition was the optimal condition with suitable catalysts in each process.

4.3.2 Improvement of integration process by double stage of water gas shift

4.3.2.1 The second stage of water gas shift part

From the WGS results, it found that outlet composition had a quite high of CO content around 10%. Generally, a high level of CO directly affect to PROX process due to the oxygen will be more required. Otherwise, more oxygen must be provided which leads to loss some hydrogen to become water vapor from side reaction as hydrogen oxidation. Therefore the study of repeating WGS unit for continuity of CO reduction was performed to control CO level before entering to PROX process and to avoid the losing of hydrogen product. The each unit of WGS processes denoted as WGS1 and WGS2, respectively.

An inlet gas composition of WGS2 came from an outlet gas of WGS1 as can be seen in Figure 4.30. Prior to WGS2 process, the stream passed into the

absorber to remove CO_2 component to keep straight forward reaction by Le Chatelier's principle because CO_2 is a common product in water gas shift reaction. The inlet composition of WGS2 was 5.4% CH_4, 47.1% H_2, 11.4% CO in He (dry basis). In WGS2 process, the studied factors and parameters had still been the same as WGS1 part which were temperature, catalysts weight, water feed rate (related S/C ratio), CO conversion and H_2 yield.

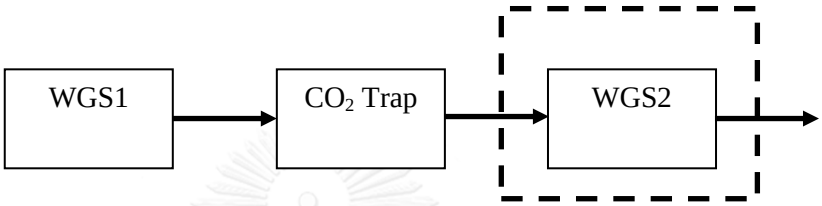

Figure 4.30 Scheme of the study of WGS2 part

Normally, the reaction should present low temperature in WGS2 which is called low-temperature water gas shift due to WGS process is separated into high-temperature and low-temperature water gas shift (HT WGS and LT WGS). The HT WGS and LT WGS control the reaction by kinetic control and temperature control, respectively, which maintains around 400 °C and 250 °C for HT WGS and LT WGS in that order. Idakiev *et al.* (118) studied LT WGS reaction by using gold catalysts and found that the catalysts performed wide temperature range of 140 °C to 300 °C.

Figure 4.31 presents the temperature factor that affected to activities. Temperature at 200 °C, 250 °C, 300 °C, 350 °C, 400 °C and 450 °C represented CO conversion to be 19.9%, 25.4%, 40.5%, 57.6%, 80.0% and 76.8%, respectively, and H_2 yield of 19.9%, 25.4%, 36.0%, 50.6%, 55.5% and 48.7%, respectively. To consider at 400 °C, the activities still showed the best results; therefore, it can be said that the WGS2 was controlled by kinetic control due to the still quite high of CO level in the stream. Particularly, LT WGS operates the condition that has CO component lower than 5% and maintains at temperature lower 300 °C. This can be ascribed that rich-stream hydrogen production in this work used methane with carbon dioxide or DRM to study which DRM reaction produced a lot of hydrogen and carbon monoxide

leading to a quite high CO level in the system. The WGS2 had still been HT WGS instead of LT WGS; therefore, it called double stage of HT WGS as well.

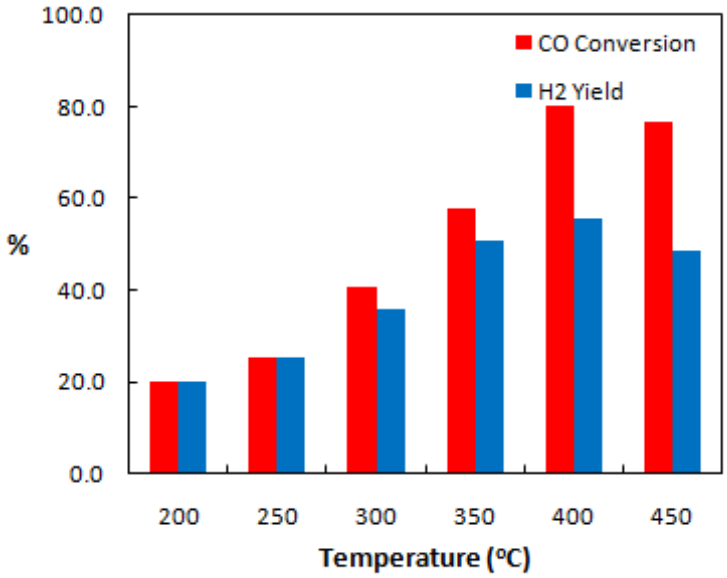

Figure 4.31 Influence of temperature to (■) CO conversion and (■) H_2 yield on 2nd stage of WGS which set 0.2 g of catalysts and 1.05 ml/h of water feed rate (S/C = 4.5) and inlet gas composition (dry basis): 5.4% CH_4, 47.1% H_2, 11.4% CO in He balance

Another study factor was catalysts weight because the WGS1 found the CO conversion significantly depend on the catalysts weight. Thus, the catalyst weight could not deny to study. Figure 4.32 shows the various catalysts weight onto catalytic activities which found that catalysts weight of 0.1 g, 0.15 g and 0.2 g showed 69.1%, 72.0% and 75.5% of CO conversion, and 47.2%, 48.9% and 50.3% of H_2 yield, respectively.

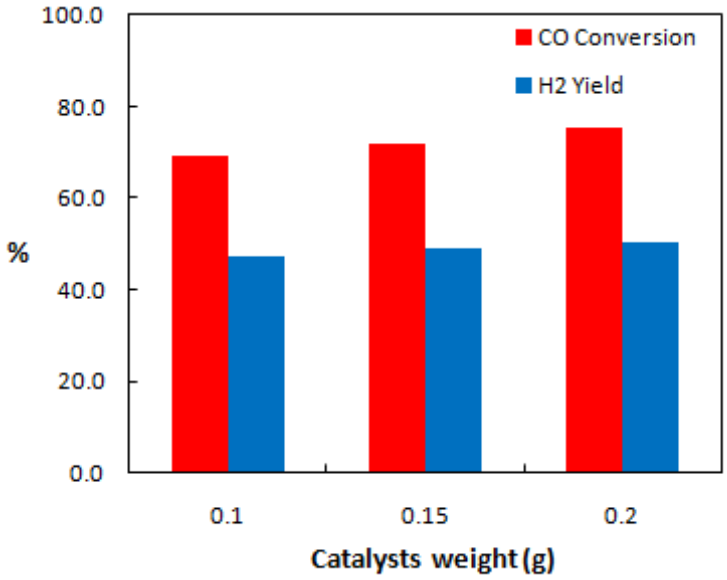

Figure 4.32 Influence of catalysts weight to (■) CO conversion and (■) H_2 yield on 2nd stage of WGS which set temperature at 400 °C and 1.05 ml/h of water feed rate (S/C = 4.5) and inlet gas composition (dry basis): 5.4% CH_4, 47.1% H_2, 11.4% CO in He balance

Increasing catalysts weight refer to an increasing of contact time—the contact time describes that how long molecules can react with each other at active site on surface catalysts. However, WGS2 did not present the different clearly compared with WGS1 due to the reaction reached to equilibrium faster than WGS1. It can be explained that the total flow rate of WGS2 had lower than WGS1 around 20% affecting to catalytic activities (flow rate of WGS1 and WGS2 were 105 ml/min and 84 ml/min, respectively).

The last factor in this part was water feed rate which related with steam to carbon ratio (S/C ratio) in the system. An increasing of water feed rate changed the inlet gas composition to move forward reaction by chemical equilibrium like removal CO in the stream by absorber before entering into WGS2. Although WGS1 found that the water feed rate or S/C ratio were not an influent to CO conversion and H_2 yield because of a high level of CO inlet. An increasing amount of water lead to some water vapor condensed and blocked active surface on catalysts and prohibited reaction move forward. However, the water vapor should be lower than 30%; otherwise, the reaction cannot even take place for long period.

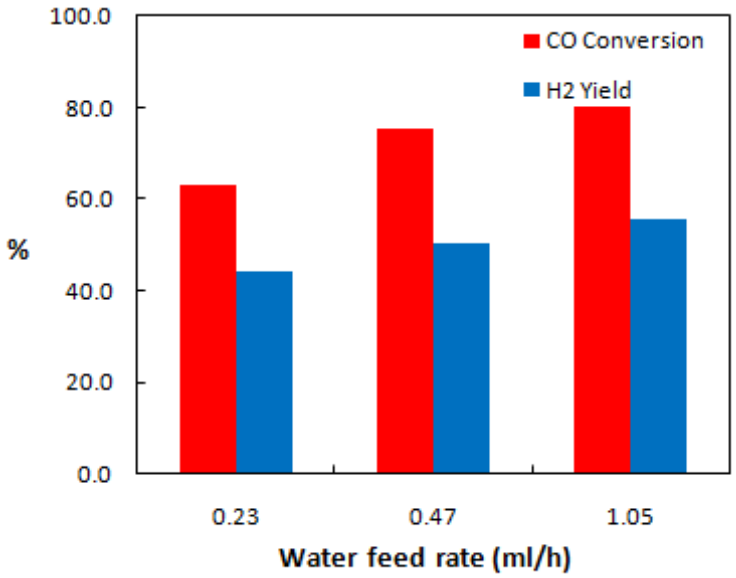

Figure 4.33 Influence of water feed rate of 0.23, 0.47 and 1.05 ml/h (S/C = 1, 2, 4.5, respectively) to (■) CO conversion and (■) H_2 yield on 2nd stage WGS which set temperature at 400 °C and 0.2 g of catalysts and inlet gas composition (dry basis): 5.4% CH_4, 47.1% H_2, 11.4% CO in He balance

In WGS2, the water feed rate was set at 0.23, 0.47 and 1.05 ml/h which related to S/C ratio of 1, 2 and 4.5, in that order, presenting CO conversion as 63.2%, 75.5% and 80.0%, respectively and H_2 yield as 44.2%, 50.3% and 55.5%, respectively, as shown in Figure 4.33. The result found that water feed rate showed significant effect to CO conversion and H_2 yield which confirmed by Le Chatelier's principle. Shido and Iwasaw (22) confirmed that the water vapor enhanced catalytic activity. Moreover, an increasing of S/C ratio could inhibit the methanation which observed by a decreasing of H_2 yield. The water feed rate of 1.05 ml/h (S/C ratio equal at 4.5) gave the best result. However, an increasing of water more than 1.05 ml/h (around 33 % of vapor in the system) presented that some vapor condensed and blocked active site of catalysts.

4.3.2.2 Double stage of water gas shift

In this section, the integration of WGS1 and WGS2 called double stage of WGS. The double stage of WGS has much benefit to remove CO component in the stream because the reaction reaches to equilibrium 2 times by changing chemical equilibrium or Le Chatelier's principle to drive the reaction forward. The cause of studying double stage was the still high value of CO in the system.

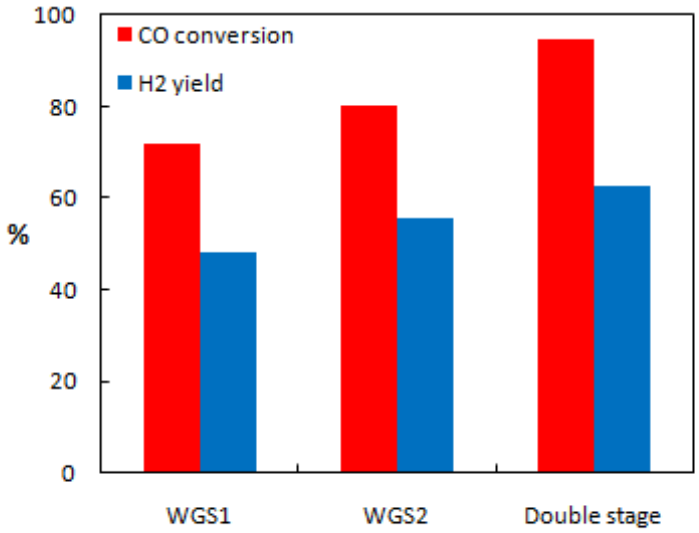

Figure 4.34 Activities performance of WGS1[a], WGS2[b] and double stage to (■) CO conversion and (■) H_2 yield

[a]WGS1 condition: temperature at 413 °C, 0.2 g of catalysts and 2 ml/h of water feed rate (S/C = 2), inlet gas composition (dry basis): 5.3% CH_4, 8.0% CO_2, 25.6% H_2, 43.2% CO in He balance

[b]WGS2 condition: temperature at 400 °C, 0.2 g of catalysts and 1.05 ml/h of water feed rate (S/C = 4.5), inlet gas composition (dry basis): 5.4% CH_4, 47.1% H_2, 11.4% CO in He balance

Figure 4.34 represents CO conversion and H_2 yield of catalysts over the part of WGS1, WGS2 and double stage at optimum condition. The operating condition of WGS1 was 413 °C, 0.2 g of catalysts and 2 ml/h water feed rate and operating condition of WGS2 was 400 °C, 0.2 g of catalysts and 1.05 ml/h water feed rate. Both WGS1 and WGS2 represented CO conversion around 74% and 80%, respectively, (equilibrium conversion around 85%). For WGS2, it showed higher CO conversion than WGS1 because of the removal of CO_2 before entering to the reactor.

To consider H_2 yield, WGS2 presented higher than WGS1 because the S/C ratio in WGS2 showed higher value than WGS1 which inhibited the side reaction as methanation in the reaction. However, both WGS1 and WGS2 performed good activity for converting CO to CO_2. When consider to double stage, it found that CO conversion shifted to higher value of 95% which reduced CO level in the stream to become 1.4%. Furthermore, H_2 yield was 62% which gave 35.9% of hydrogen outlet from double stage of WGS. Two stages of WGS had enough units for reduction of CO level in the stream because the CO composition was suitable for further process of PROX.

4.3.2.3 Integration of DRM, double WGS, and PROX processes

In this section, DRM part still presented the same pattern of catalytic performance. The activity of catalysts and outlet component over each processes are presented in Figure 4.35 and Figure 4.36, respectively. The catalytic activity on double WGS performed 94.8% CO conversion and 62.4% H_2 yield presenting 4.6% CH_4, 30.6% CO_2, 39.8% H_2, 9.7% CO and 15.3% He on dry basis which total flow around 59 ml/min. The outlet gas from WGS was mixed with oxygen at O_2/CO ratio of 1.5 before entering into PROX reactor. The PROX catalysts still presented 99% CO conversion and 45% CO_2 selectivity which contained outlet gas as 3.4% CH_4, 1.4% CO_2, 31.5% H_2, 0.6% O_2 and <0.01% CO in helium balance. The total flow of outlet gas from PROX was around 85 ml/min. To compare the results between single or double WGS in overall processes, it found that both of them presented a complete conversion of CO. However, double stage showed a better perfomance—hydrogen was produced about 31.5% instead of 12.2% on single stage of WGS. It can be said that double stage of WGS could perform a good CO conversion and hydrogen selectivity than single stage of WGS.

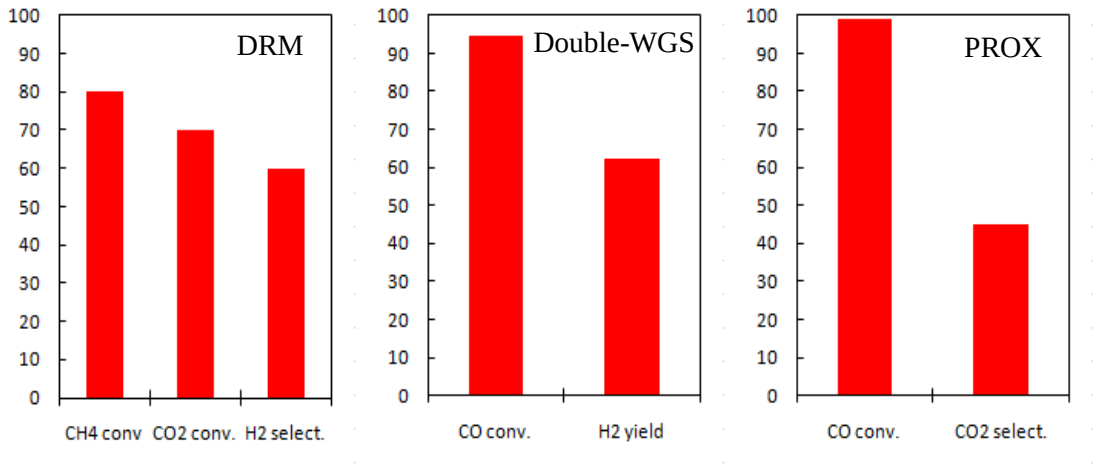

Figure 4.35 Catalytic performance of integration of DRM, WGS (double stage) and PROX processes with CO_2 trap unit between WGS and PROX process

*Reaction condition was the optimal condition with suitable catalysts in each process.

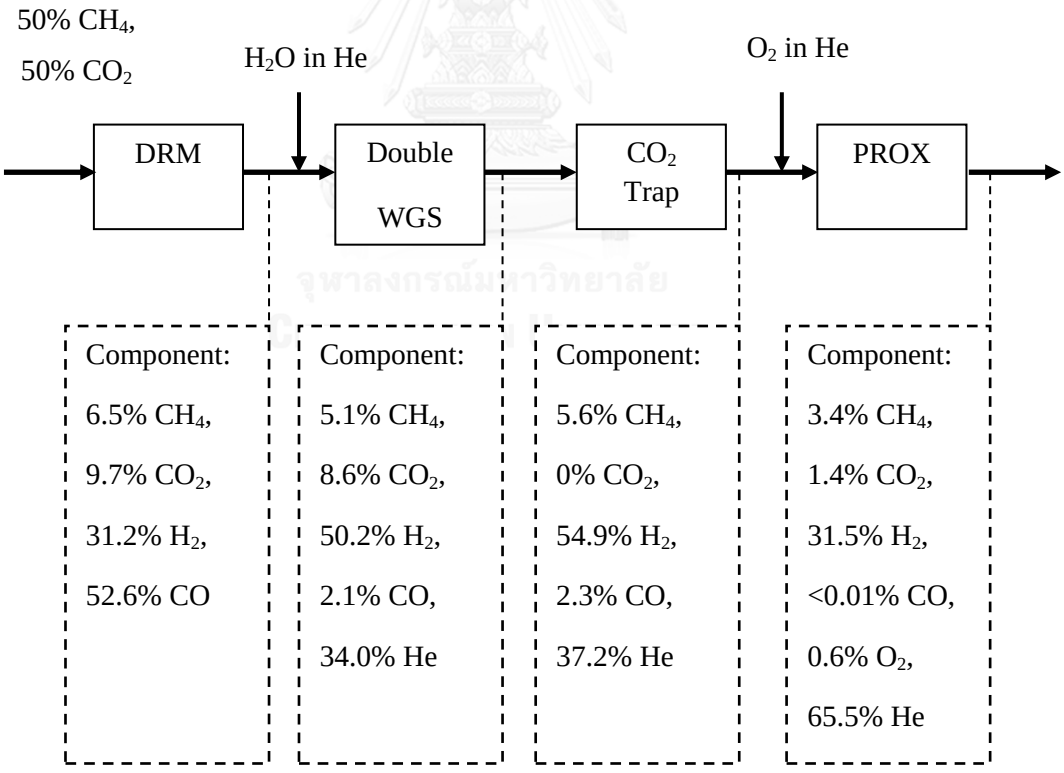

Figure 4.36 Outlet gas compositions in DRM, double WGS and PROX processes with CO_2 trap between WGS and PROX process

*Reaction condition was the optimal condition with suitable catalysts in each process.

4.3.3 Stability test of integration process

Stability of the catalytic performance for DRM, WGS1, WGS2 and PROX under suitable condition is shown in Figure 4.37.

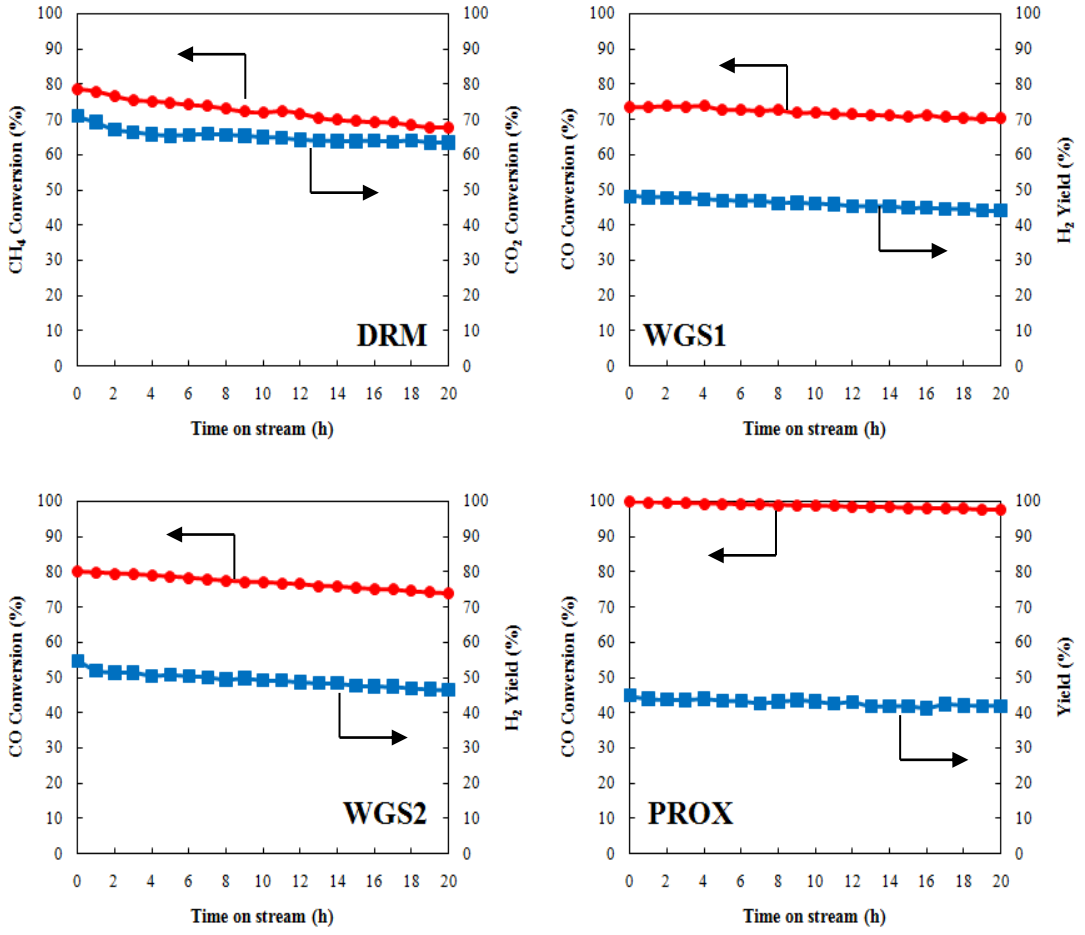

Figure 4.37 Stability tests of DRM, WGS1, WGS2 and PROX processes over catalytic performance versus time on stream in each process

*Reaction condition was the optimal condition with suitable catalysts in each process.

The catalytic performance was tested along the time on stream of 20 h. It can be observed that all parameter of catalytic performance slightly decreased along with time on stream. However, the maximum of decreasing activity was investigated at DRM process around 10% of CH_4 conversion due to the gas composition contained reactant gas without inert, which maximized kinetic reaction more than other processes. Moreover, the DRM process accumulated carbon deposition along the time

on stream via reverse Boudouard reaction that directly performed a deactivation of catalysts. Other processes presented a quite stable of catalytic performance because it had little water blocking an active surface on WGS and became a side product on PROX, respectively.

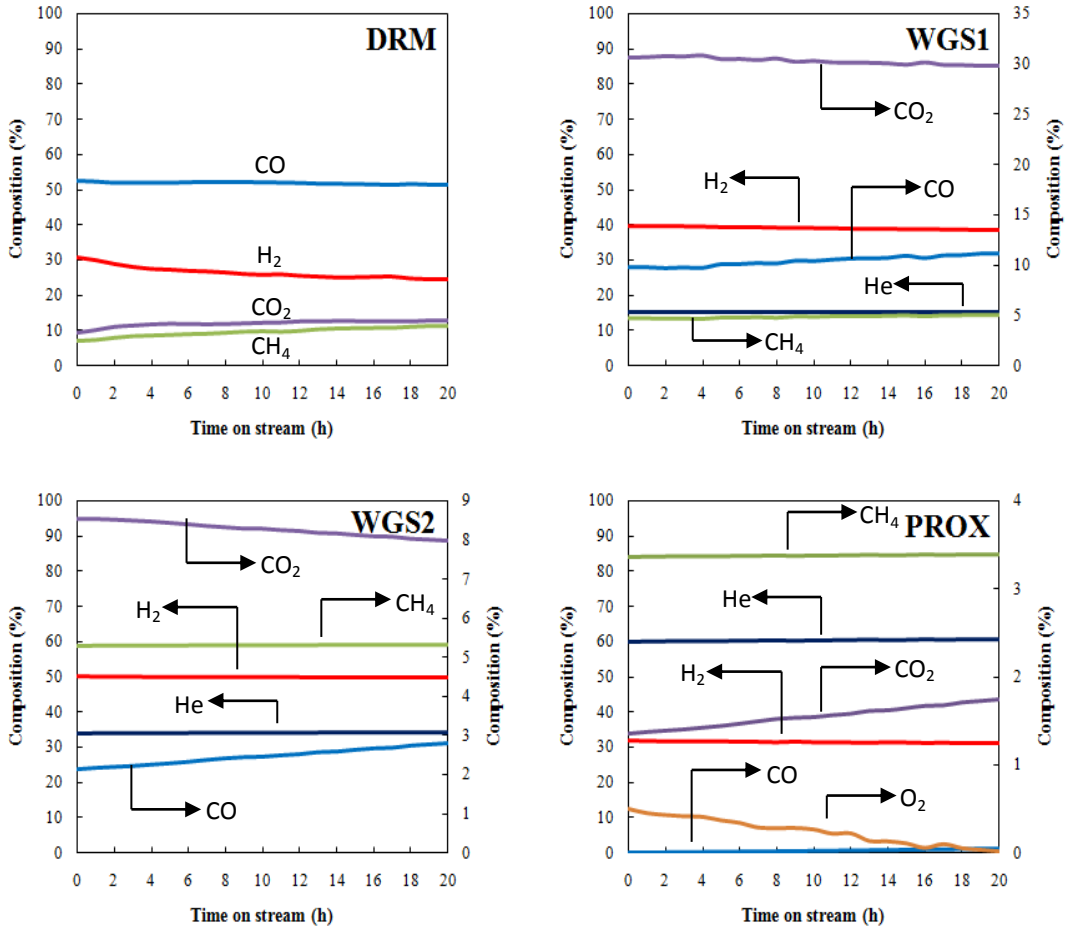

Figure 4.38 Gas compositions (%) of outlet from DRM, WGS1, WGS2 and PROX processes versus time on stream

*Reaction condition was the optimal condition with suitable catalysts in each process.

The outlet gas compositions are also presented in Figure 4.38 of all processes. The CO component showed a quite constant along the time on stream in DRM process while H_2, CO_2 and CH_4 components presented slight different especially at first 5 h. It can be concluded that the carbon deposition inhibited the methane decomposition and reverse Boudouard reaction. Furthermore, the reverse

water gas shift was also occurred in this process (83, 85). To consider outlet gas of WGS processes, it presented an increasing CO along the time on stream while others components kept constant value because a decreasing rate of CO reaction on active surface was blocked from excess water effecting to a decreasing of CO conversion around 3% on both WGS1 and WGS2 processes. The CO outlet component along with the time on stream increased from 9.8% to 11.1% in WGS1 and 2.1% to 2.8% (dry basis) in WGS2, respectively.

In the PROX process, the CO_2 component showed an increasing of 1.3% to 1.7% while O_2 showed a decreasing of 0.5% to 0% along the time on stream. This result can be explained that an increasing of CO_2 composition caused from the inlet gas composition before entering to PROX containing more CO level along the time on stream which led to an increasing of O_2 consumption in the reaction. However, the PROX process still kept CO conversion more than 99.9% which released CO composition lower than 0.01%. Scheme of effluent outlet gas and theirs activities in DRM, WGS and PROX processes with CO_2 trap can see in the appendix.

CHAPTER 5

QUANTUM MECHANICAL CHARGE FIELD MOLECULAR DYNAMICS—CARBON MONOXIDE CEAN UP VIA WATER TRAP

Hydrogen production from dry reforming, to eliminate CO is more difficult than steam reforming, because it releases large amount of CO. Therefore, the removal CO by the water is a topic of great interesting, because this process just only uses the solubility property that is rarely requires energy to operate. In addition to the catalysts in fuel cells, the existence of some water can promote the catalytic reaction performing a high efficiency of electrical production (119). This has double benefit from removal CO by water—first, to prolong the lifetime of the catalysts, and second, to increase the catalytic performance in fuel cell. In the engineering field, carbon monoxide is capable of dissolving approximately 40 mg/kg at 0 °C, but no one explained that how CO soluble in water. Interestingly, the computational simulation can explain some phenomenon of molecules in water; therefore, to study of CO in water to investigate the phenomenon and its properties will be performed by QMCF MD simulation in term of dynamic structure and behavior explanation.

Firstly, Table 5.1 summarizes a bond length between C-atom and O-atom of carbon monoxide molecule to ensure a suitable basis set, which were performed on gas phase comparing bond length with the experimental values of carbon monoxide. The level of theory found that Hartree–Fock (HF) was an appropriate level more than B3LYP; therefore, HF level was calculated for quantum mechanical calculations in this work.

Table 5.1 Comparison of C—O bond length in CO molecule at different levels of theory

	Method	Basis set	Bond distance (Å)
C—O	HF	6-31++G(d,p)	1.115
C—O	B3LPY	6-31++G(d,p)	1.138
C—O	Standard*		1.12

* http://en.wikipedia.org/wiki/Carbon_monoxide

The radius distribution function (RDF) of CO molecule, which was calculated at the midpoint of the molecular geometry, is shown in Figure 5.1. The distance of CO molecule and water was attributed to $g_{CO\text{-}O}$ and $g_{CO\text{-}H}$ that referred to the distance between the center of CO molecule to O or H of water, respectively.

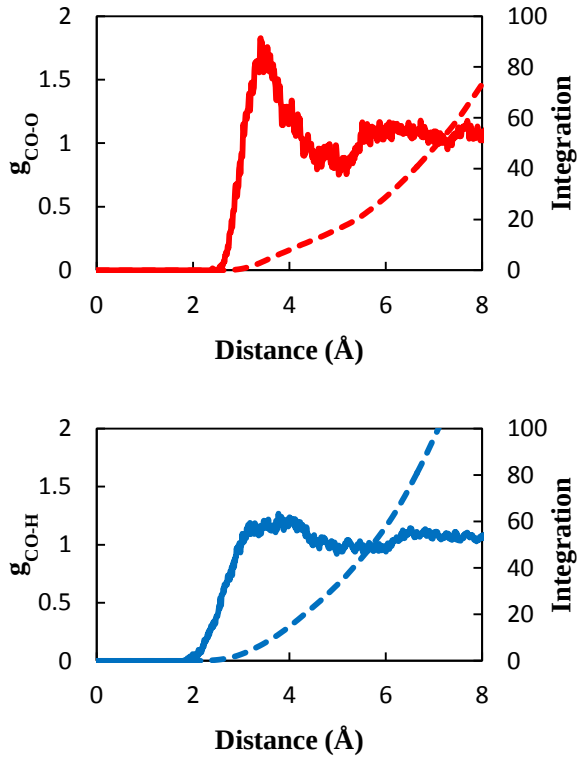

Figure 5.1 RDF and its integration of CO molecule to water's (top) oxygen atom and (bottom) hydrogen atom in the simulation time of 16 ps

Initially, it can be roughly explained that the water molecules presenting H of water toward to the CO molecule. C_{CO} and O_{CO} atoms had a dominant negative charge involving a dominant negative charge more than H_{wat} (The electronegativity values of H, C, and O are 2.1, 2.5, and 3.5, respectively).

To find a hydration shell of carbon monoxide molecule, since the CO molecule seems to be a straight line and symmetry structure; therefore, hydration shell should be a spherical shape. But, in fact, a linear molecule of CO contained different type of atoms, which affected to the distance of water surrounding toward to CO molecule on each side including C atom or O atom. So, the hydration shell was performed a new shape instead of spherical shape by considering the RDF of each atoms calculated from gC_{CO}-O_{wat} and gO_{CO}-O_{wat} (C_{CO}, O_{CO}, and O_{wat} refer to C atom of CO, O atom of CO and O atom of water, respectively).

Radial distribution function (RDF) of each atom of CO molecule to the water, which were calculated the distance from C_{CO} to O_{wat} and O_{CO} to O_{wat} shown in Figure 5.2. The data was smoothed and separated in 2 peaks by Gauss functions (in origin software package). The results represented 2 peaks in the first shell which could be described that a close side of O_{wat} had a short distance less than an opposite side of O_{wat}. Figure 5.2(top) shows RDF of C_{CO}-O_{wat}, which represented the distance between C_{CO} and water at close- and opposite-side of 3.555 Å and 4.495 Å, respectively. Besides, Figure 5.2(bottom) could be explained in the same way as in Figure 5.2(top) which was calculated from O_{CO} and O_{wat} presenting the distance at close- and opposite-side of 3.345 Å and 4.395 Å, respectively. Consider to water molecules that located in the first shell found that the distance of close- and opposite-side of water to C_{CO} or O_{CO} were not the same values; therefore, it can be predicted that the shape of the first shell was not generally spherical like a symmetrical molecules. The distance of the water in the first hydration shell was determined by the selection point from RDF in the Figure 5.2. The selection point investigating from a destination of first peaks—which could be referred that some water surrounded close to C_{CO} and O_{CO} side of carbon monoxide molecule as 4.45 Å and 4.00 Å, respectively.

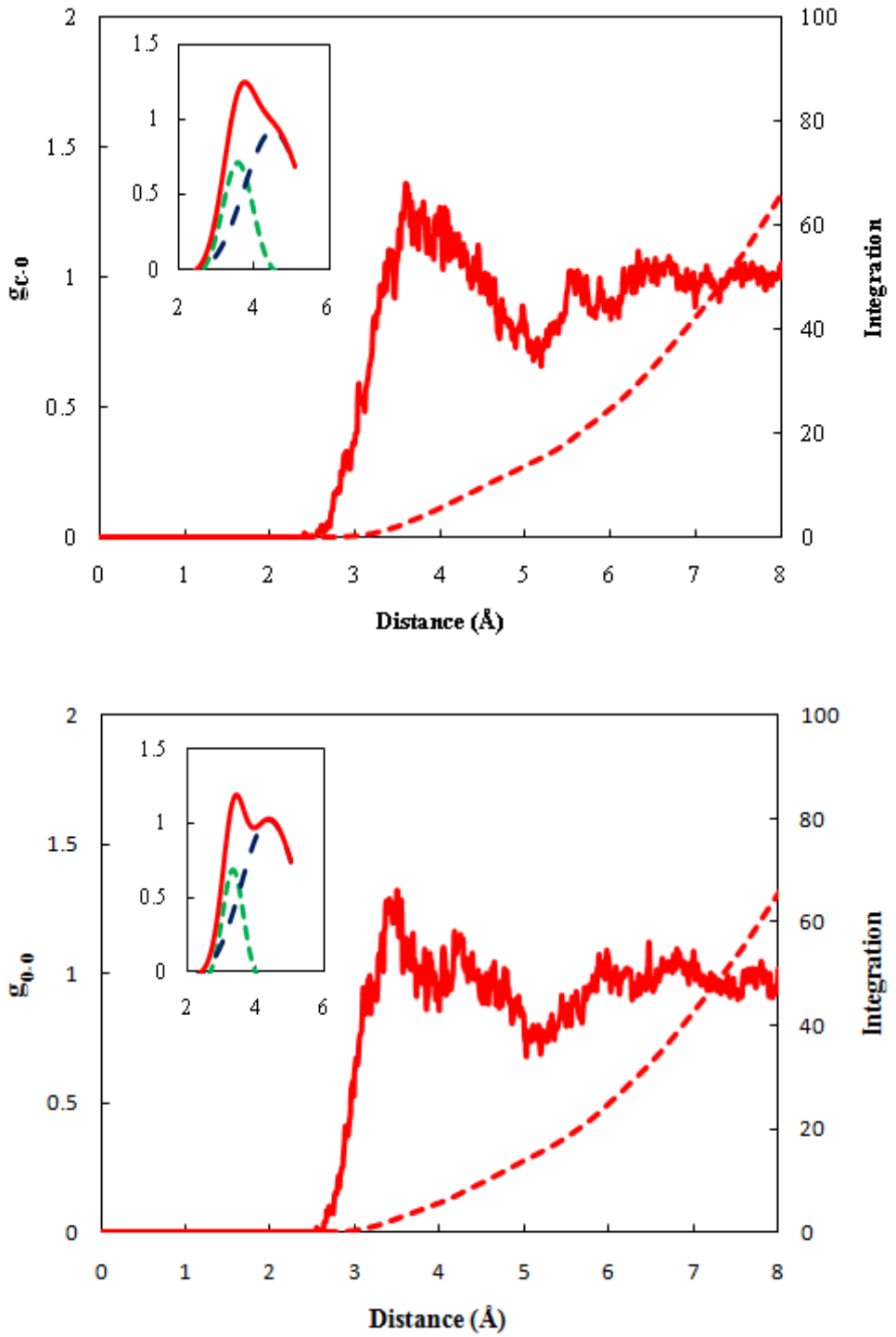

Figure 5.2 RDF of (top) C_{CO} and (bottom) O_{CO} atom of carbon monoxide and O_{wat} of water in the simulation time of 16 ps with smooth graph and separated peak into 2 peaks of first hydration shell

Figure 5.3 shows the coordination number distribution (CND) of CO molecule which represented amount of water surrounding C atom, O atom and CO molecule by considering the distance of first hydration shell. The results presented an average of water surrounding C atom and O atom at 10 and 6 molecules, respectively. But considering the CO molecule, it found that an average of water surrounding about 11 molecules. It can be describe that some water close to C atom and O atom caused a duplication counting of water surrounding. If CND were determined as the symmetry molecule like a spherical shape, the first hydration shell would be larger than usual. Otherwise, the distance of first shell was large enough at around 5 Å before modified the hydration shell.

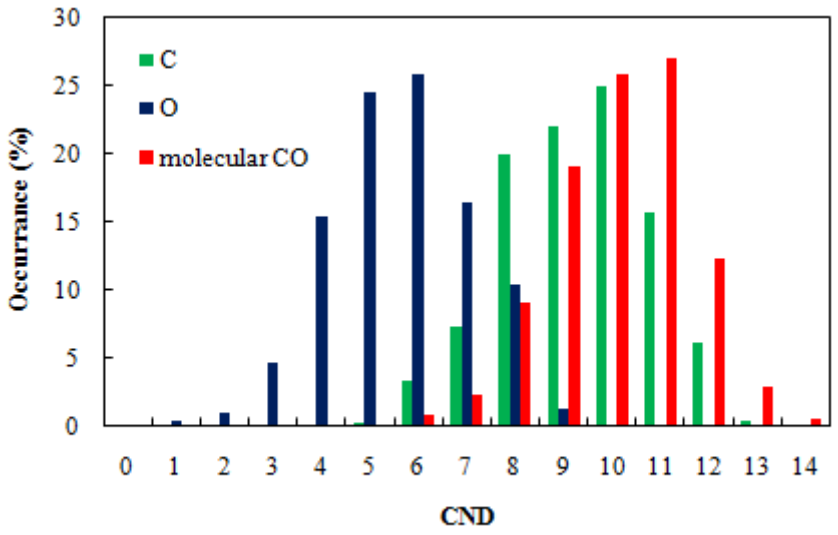

Figure 5.3 Coordination number of first hydration shell of carbon monoxide focus on C atom, O atom and CO molecule

Figure 5.4 is the consideration of water structure in the first hydration shell comparing with bulk water. Figure 5.4(top) presents a distance of O_{wat}-H_{wat} and Figure 5.4(bottom) presents water angle of H-O-H. It can be seen that water molecules in the first shell and bulk represented quite similar structure, which would imply that CO affects to the water extremely least. Concerning to other molecules like metal ions, they showed a capable of easily soluble, for example, the water molecules in the first shell significantly showed a different structure comparing with bulk (81,

120, 121). So, it can be indicated that why carbon monoxide has an ability to dissolve in water less than 27 ppm at 25 °C (122).

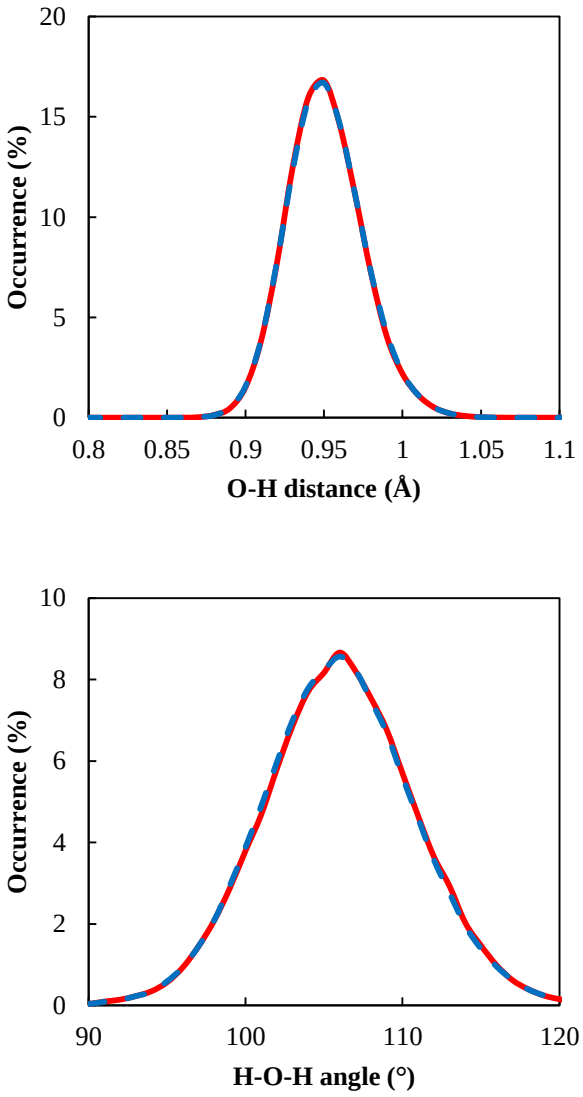

Figure 5.4 Comparisons of water molecule at first hydration shell and bulk representing (top) O-H distance and (bottom) H-O-H angle

Table 5.2 shows some characteristic data of carbon monoxide in water comparing with a carbon dioxide in water calculated by QMCF MD (123). MRT of both C_{CO} and O_{CO} referred that water molecules could occur easily an exchange state, because they had a small value. N_{ex} presented high value meaning that water occurred an exchange state around 80 times in simulation time of 16 ps. The results confirmed

that carbon monoxide showed hardly dilution in the water. This was consistent with the characteristics of the surrounding water structure virtually unchanged compared to bulk water. Considering CND, the CO molecule had a less water surrounding in first shell than CO_2 due to CO structure are smaller than CO_2 molecule.

Table 5.2 Characteristic data for the water dynamics surrounding CO from QMCF simulation time for 16 ps

	C	O	CO	CO_2*
MRT	1.75	1.17	1.76	1.72
N_{ex}	85	77	89	82
CND	9.31	5.65	9.81	~14

*data from Moin *et al.* (123)

Figure 5.5 shows the distance between C_{CO}-O_{CO} which collected the dynamic data time at 16 ps. The distance of C_{CO}-O_{CO} bond presented a main peak at 1.12 Å and minor peak at 1.17 Å, respectively. The behavior of bond distance of 1.12 Å is a common triple bond which showed a highest value of occurrence, because this bond length is the most stable than the others.

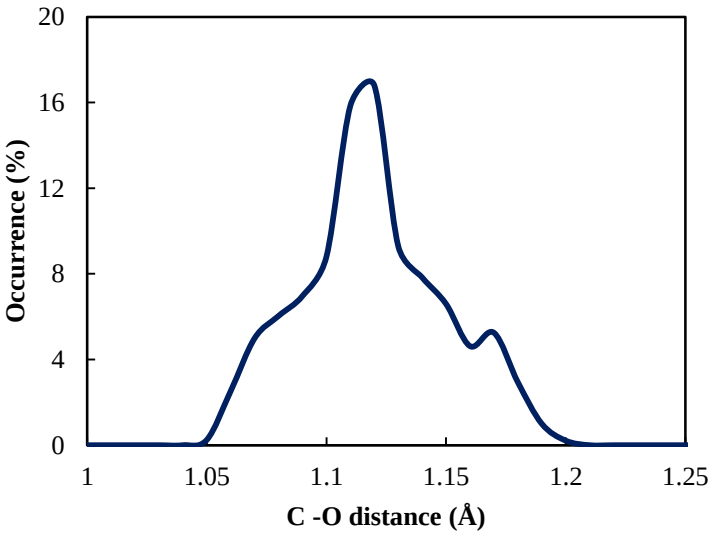

Figure 5.5 Summation of dynamical C-O bond length in simulation time of 16 ps

From the simulation, it was found that the bond in Gaussview was estimated at 1.11 Å (Table 5.1) and the distance of the triple bond of CO is typically located at 1.12 Å. However, the calculation from simulation is a slightly less value than expected value due to the water molecules surrounding. The bond distance at 1.17 Å can be implied that the C atom and O atom of CO molecule connected each other by double bond, because this distance is in the range of double bond length. Interestingly, Moin *et al.* (123) studied the simulation of CO_2 in the water, which found the distance of C=O bond at 1.15 Å to 1.17 Å and readily associated to water molecules by hydrogen bonds. It is well known that carbon dioxide has an ability to dissolve in water to become carbonic acid (124-126). So, this is evidence that CO, sometimes, had a same structure or same behavior like CO_2. In other words, carbon monoxide could stretch the bond, which was changing form from the triple bond to double bond and had ability to dilute in the water.

CHAPTER 6

CONCLUSIONS

6.1 Hydrogen production via methane reforming with carbon dioxide (DRM)

From the DRM results, it was surprising that adding a small amount of manganese to nickel based catalysts (denoted as 5Ni-0.5Mn/CeO_2) expressed the performance as high as the Ni/CeO_2 with optimum loading at 10% to 15% by weight, because manganese promotes the dispersion of nickel metal in catalysts. Besides, the combination of manganese and nickel at proper ratio performs a new phase in catalysts. On the other hand, the gold additive decreases the catalysts performance. So, the appropriated catalyst in this work is 5Ni-0.5Mn/CeO_2 to study the optimization of operating. The factors including temperature, CH_4 composition fraction, catalysts weight and feed rate were studied in design of experiments analysis as full factorial design with center point. The results found that the suitable model for CH_4 conversion and CO_2 conversion are a quadratic model, whereas H_2 selectivity and carbon deposition are a cubic model that can be seen in chapter 4. The optimum condition for operating should be 820 °C, 0.5 methane composition fraction, 0.1 g of catalysts weight and 30 ml/min of total feed rate to give 70% CH_4 conversion, 60% CO_2 conversion, 60% H_2 selectivity. Then, the stability testing presented carbon deposition around 10% for 20 h. This means that the catalysts have a tolerance to coke formation when manganese is presented in the catalysts. Moreover, the prediction of catalysts activity to CH_4 conversion and CO_2 conversion are acceptable which presented less than 10% error.

6.2 Carbon monoxide clean up via water gas shift (WGS) and preferential oxidation (PROX) reactions

The Fe promoter represents the higher CO conversion and H_2 yield, because the combination of redox behavior between Ce and Fe. For screening factors, a temperature directly represents to the kinetic of the reaction; therefore, this factor is a significant effect on the CO conversion and H_2 yield. Catalysts weight is an influence of only CO conversion in this section, because the contact time between reactant and active surface on catalysts is increased. While catalysts weight did not present a significant effect on H_2 yield, because the contact time of reactant gas promotes both water gas shift (desired reaction) and methanation (undesired reaction) together. The steam/CO ratio, as represented in term of water feed rate, was not a significant factor to both CO conversion and H_2 yield. Actually, steam/CO ratio should be a significant factor to catalytic activity; however, the high level of CO in the inlet feed lead to water vapor feed is also high. It can be said that a steam/CO ratio is not a significant factor in high CO level system. Moreover, too much amount of water vapor shows a negative effect by condensing and blocking the catalysts surface. In response surface methodology part, the face-centered cube design was applied to evaluate the data. After interpreting data to find suitable optimum point, the temperature and catalysts weight should be 413 °C and 0.2 g, respectively, which presented 74.2% of CO conversion and 52.1% of H_2 yield. Furthermore, the evaluation model presented a small deviation when comparing to the actual data lower than 5% error.

The magnitude of the PROX reaction increases both of conversion and selectivity. However, an increasing temperature enhance conversion but not for selectivity. These importance parameters (conversion and selectivity) could not be neglect, so the combined parameter called yield applied to control a condition to give highest activity of catalysts. The study of Au/CeO_2 catalyst for evaluation the significant factors were performed. The temperature (A), the O_2/CO ratio (C) and CO_2 added (D) were the significant factors on the yield, while W/F ratio (B) and H_2O added (E) were not. In order to continue the optimization, Box-Behnken response surface analysis was applied. Temperature (A), the O_2/CO ratio (C) and CO_2 added (D) achieve the optimum condition at a suitable range. From an experimental design

results, Au/CeO_2 catalyst performed the range of condition as: 68 °C to 78 °C of temperature; 1.35 to 1.65 of O_2/CO ratio; no or little of CO_2 added. The result elucidates a validation of the model representing that the maximum of yield is 45.5% (4.40% error), and also can estimate the yield at any points by equation model in this section.

6.3 Integrations of hydrogen production and carbon monoxide clean up

The integration of each process by set an operating condition can determine the final product composition and catalytic activity. It found that the capable of reducing carbon monoxide is almost exhausted. However, a hydrogen composition was not enough for practical using (around 10% hydrogen); therefore, it is necessary to improve the hydrogen concentration output. Double stage of water gas shift is a good way to increase the hydrogen concentration output. However, the second stage of WGS did not use an experimental design to analysis an optimum condition, because the carbon monoxide had been completely removed already. Therefore an increasing the hydrogen content does not need to perform experimental design, the study of effect factors and analysis data by conventional method are enough to find the suitable range for operating. The suitable operating condition of 2^{nd} WGS was 400 °C, 0.2 g of catalysts and 1.05 ml/h of water feed rate (as equal S/C ratio = 4.5) giving 80% CO conversion and 55% H_2 yield. When combine WGS1 and WGS2, the performance of double stage further enhanced CO conversion and H_2 yield more than single stage around 20% and 15%, respectively, promoting hydrogen composition of output stream to become 30% by volume.

6.4 Quantum mechanical charge field molecular dynamics (QMCF MD)— Carbon monoxide clean up via water trap

Characteristics of carbon monoxide including structure and dynamic were evaluated by *ab initio* QMCF MD simulation. Radial distribution function of each side such as C_{CO} and O_{CO} calculated an appropriate first hydration shell. The distance of C and O found triple bond which is the most stable in CO molecule; however, it can be changed to double bond when stretching its bond. It can be confirmed the data comparing with CO_2 bond length. This simulation studied the CO molecule in water that confirmed and provided a helpful explanation data for a further discussion of CO soluble in water.

6.5 Recommendations

Although, the fuel processor in this dissertation consisting of DRM, WGS, and PROX reactions with water trap showed a good performance to produce hydrogen and almost completely removed carbon monoxide in the stream, nevertheless, it was tested the system in a lab scale. To apply in an industry, more parameters have to continue for further study. Moreover, the life time in the system was not enough for hydrogen production on-board PEMFC or practical usage, because this process was stable on 20 h time on steam. However, the hydrogen production from methane and carbon dioxide is one of the potential candidates to steam reforming due to this is the utilization of greenhouse gas to generate a new source of energy with clean output.

REFERENCES

1. IEA. World energy outlook 2009. IEA, Paris; 2006.
2. Ogden JM. Prospects for building a hydrogen energy infrastructure. Annual Review of Energy and the Environment. 1999;24(1):227-79.
3. Gupta RB. Hydrogen fuel: production, transport, and storage: CRC Press; 2008.
4. Armor JN. The multiple roles for catalysis in the production of H_2. Applied Catalysis A-General. 1999;176(2):159-76.
5. Rostrup-Nielsen JR. New aspects of syngas production and use. Catalysis Today. 2000;63(2-4):159-64.
6. Hu YH, Ruckenstein E. Catalytic conversion of methane to synthesis gas by partial oxidation and CO2 reforming. Advances in Catalysis. 2004;48:297-345.
7. Bradford MCJ, Vannice MA. CO_2 reforming of CH_4. Catalysis Reviews-Science and Engineering. 1999;41(1):1-42.
8. Schouten FC, Gijzeman OLJ, Bootsma GA. Reaction of methane with nickel single crystal surfaces and the stability of surface nickel carbides. Bulletin des Sociétés Chimiques Belges. 1979;88(7-8):541-7.
9. Rostrup-Nielsen JR, Hansen JHB. CO_2 Reforming of Methane over Transition-Metals. Journal of Catalysis. 1993;144(1):38-49.
10. Zhang ZL, Verykios XE. Carbon-Dioxide Reforming of Methane to Synthesis Gas over Supported Ni Catalysts. Catalysis Today. 1994;21(2-3):589-95.
11. Bitter JH, Seshan K, Lercher JA. Deactivation and coke accumulation during CO_2/CH_4 reforming over Pt catalysts. Journal of Catalysis. 1999;183(2):336-43.
12. Stagg SM, Resasco DE. Effect of promoters on supported Pt catalysts for CO_2 reforming of CH_4. Natural Gas Conversion V. 1998;119:813-8.
13. Lercher JA, Bitter JH, Hally W, Niessen W, Seshan K. Design of stable catalysts for methane-carbon dioxide reforming. 11th International Congress on Catalysis - 40th Anniversary, Pts A and B. 1996;101:463-72.

14. Ladebeck JR, Wagner JP. Catalyst development for water-gas shift. In: Vielstich W, Lamm A, Gasteiger HA, editors. Handbook of Fuel Cells – Fundamentals, Technology and Applications. 3. Chichester, UK: John Wiley & Sons, Ltd.; 2003. p. 190-201.
15. Pozdnyakova O, Teschner D, Wootsch A, Krohnert J, Steinhauer B, Sauer H, et al. Preferential CO oxidation in hydrogen (PROX) on ceria-supported catalysts, part I: Oxidation state and surface species on Pt/CeO_2 under reaction conditions. Journal of Catalysis. 2006;237(1):1-16.
16. Ertl G, Knözinger H, Weitkamp J. Handbook of Heterogeneous Catalysis. Weinheim, Germany.: Wiley-VCH Verlag GmbH; 1997.
17. Kohle R. Eigenschaften, Gewinnung, Veredelung (Hrsg. F. Benthaus). Verlag Chemie. Weinheim; 1978.
18. Hawker P. Shift CO Plus Steam to H_2. Hydrocarbon Processing. 1982;61(4):183-7.
19. Stitt E, Abbott P, Cromarty B, Crewdson B, editors. Emerging Trends in Syngas and Hydrogen. Worldwide Catalyst Industry Conference—CatCon; 2000.
20. Barbier-Jr J, Duprez D. Steam Effects in 3-Way Catalysis. Applied Catalysis B-Environmental. 1994;4(2-3):105-40.
21. Newsome DS. The water-gas shift reaction. Catalysis Reviews: Science and Engineering. 1980;21(2):275-318.
22. Shido T, Iwasawa Y. Reactant-Promoted Reaction-Mechanism for Water Gas Shift Reaction on Rh-Doped CeO_2. Journal of Catalysis. 1993;141(1):71-81.
23. Newsome DS. The water-gas shift reaction. Catalysis Reviews Science and Engineering. 1980;21(2):275-318.
24. Lloyd L, Ridler D, Twigg M. The water-gas shift reaction. Catalyst handbook. 1996;2:283-338.
25. Bunluesin T, Gorte RJ, Graham GW. Studies of the water-gas-shift reaction on ceria-supported Pt, Pd, and Rh: implications for oxygen-storage properties. Applied Catalysis B-Environmental. 1998;15(1-2):107-14.

26. Li Y, Fu Q, Flytzani-Stephanopoulos M. Low-temperature water-gas shift reaction over Cu- and Ni-loaded cerium oxide catalysts. Applied Catalysis B-Environmental. 2000;27(3):179-91.
27. Grenoble D, Estadt M, Ollis D. The chemistry and catalysis of the water gas shift reaction: 1. The kinetics over supported metal catalysts. Journal of Catalysis. 1981;67(1):90-102.
28. Tinkle M, Dumesic J. Isotopic exchange measurements of the rates of adsorption/desorption and interconversion of CO and CO_2 over chromia-promoted magnetite: Implications for water-gas shift. Journal of Catalysis. 1987;103(1):65-78.
29. Campbell CT, Daube K. A surface science investigation of the water-gas shift reaction on Cu (111). Journal of Catalysis. 1987;104(1):109-19.
30. Colbourn E, Hadden R, Vandervell H, Waugh K, Webb G. Adsorption of water on polycrystalline copper: relevance to the water gas shift reaction. Journal of Catalysis. 1991;130(2):514-27.
31. Van Herwijnen T, De Jong W. Kinetics and mechanism of the CO shift on CuZnO: 1. Kinetics of the forward and reverse CO shift reactions. Journal of Catalysis. 1980;63(1):83-93.
32. Ovesen C, Stoltze P, Nørskov J, Campbell C. A kinetic model of the water gas shift reaction. Journal of Catalysis. 1992;134(2):445-68.
33. Ovesen C, Clausen B, Hammershøi B, Steffensen G, Askgaard T, Chorkendorff I, et al. A microkinetic analysis of the water–gas shift reaction under industrial conditions. Journal of Catalysis. 1996;158(1):170-80.
34. Hilaire S, Wang X, Luo T, Gorte RJ, Wagner J. A comparative study of water-gas-shift reaction over ceria supported metallic catalysts. Applied Catalysis A-General. 2001;215(1-2):271-8.
35. Xue EZ, Ross J. The use of membrane reactors for catalytic n-butane oxidation to maleic anhydride with a butane-rich feed. Catalysis Today. 2000;61(1-4):3-8.
36. Utaka T, Sekizawa K, Eguchi K. Co removal by oxygen-assisted water gas shift reaction over supported Cu catalysts. Applied Catalysis A-General. 2000;194:21-6.

37. Larminie J, Dicks A, McDonald MS. Fuel cell systems explained: Wiley New York; 2003.
38. Brown ML. Heater. Google Patents; 1963.
39. Shore L, Farrauto R. PROX catalysts. Handbook of fuel cells. 2003.
40. Cohn JG. Process for Selectivity Removing Carbon Monoxide from Hydrogen-Containing Gases. Google Patents; 1965.
41. Cohn JG. Process for Oxidation of Carbon Monoxide. Google Patents; 1971.
42. Johann G. Process for selectivity Removing Carbon. Google Patents; 1965.
43. Ghenciu AF. Review of fuel processing catalysts for hydrogen production in PEM fuel cell systems. Current Opinion in Solid State & Materials Science. 2002;6(5):389-99.
44. Trimm DL, Onsan ZI. Onboard fuel conversion for hydrogen-fuel-cell-driven vehicles. Catalysis Reviews-Science and Engineering. 2001;43(1-2):31-84.
45. Choudhary TV, Goodman DW. CO-free fuel processing for fuel cell applications. Catalysis Today. 2002;77(1-2):65-78.
46. Zhou SL, Yuan ZS, Wang SD. Selective CO oxidation with real methanol reformate over monolithic Pt group catalysts: PEMFC applications. International Journal of Hydrogen Energy. 2006;31(7):924-33.
47. Oh SH, Sinkevitch RM. Carbon-Monoxide Removal from Hydrogen-Rich Fuel-Cell Feedstreams by Selective Catalytic-Oxidation. Journal of Catalysis. 1993;142(1):254-62.
48. Romm JJ. The hype about hydrogen: fact and fiction in the race to save the climate: Island Press; 2004.
49. DoE U. A national vision of America's transition to a hydrogen economy—to 2030 and beyond. United States Department of Energy, Washington, DC. 2002.
50. Ogden JM, Dennis E, Steinbugler M, Strohbehn J, editors. Hydrogen energy systems studies. Proceedings of the 1999 US DOE Hydrogen Program Review Denver, CO; 1999.
51. Szklo A, Schaeffer R. Fuel specification, energy consumption and CO_2 emission in oil refineries. Energy. 2007;32(7):1075-92.

52. Davis SC, Diegel SW, Boundy RG. Transportation energy data book: Edition 23. United States. Department of Energy, 2003.
53. Johnson W, Kaelin T, Tohi G. Chemical Economics Handbook. SRI International, Menlo Park, Calif; 2001.
54. Scholz WH. Processes for industrial production of hydrogen and associated environmental effects. Gas separation & purification. 1993;7(3):131-9.
55. Kermode R. Hydrogen: Its Technology and Implications: Hydrogen Production Technology: CRC; 1977.
56. Spath PL, Mann MK. Life cycle assessment of hydrogen production via natural gas steam reforming: National Renewable Energy Laboratory Golden, CO; 2000.
57. Shirasaki Y, Tsuneki T, Ota Y, Yasuda I, Tachibana S, Nakajima H, et al. Development of membrane reformer system for highly efficient hydrogen production from natural gas. International Journal of Hydrogen Energy. 2009;34(10):4482-7.
58. Yacobucci BD. Alternative Fuels and Advanced Technology Vehicles: Issues in Congress: DIANE Publishing; 2006.
59. Wee J-H. Applications of proton exchange membrane fuel cell systems. Renewable and sustainable energy reviews. 2007;11(8):1720-38.
60. Frisch M, Trucks G, Schlegel HB, Scuseria G, Robb M, Cheeseman J, et al. Gaussian 03. Gaussian. Inc: Wallingford, CT. 2004.
61. Bartholomew CH, Farrauto RJ. Fundamentals of industrial catalytic processes: John Wiley & Sons; 2011.
62. Ertl G, Knözinger H, Schüth F, Weitkamp J. Handbook of Heterogeneous Catalysis., 2008. John Wiley & Sons ISBN978-3-527-31241-2; 1955.
63. Rode BM, Hofer TS, Kugler MD. The Basics of Theoretical and Computational Chemistry. : WILEY-VCH Verlag GmbH & Co. KGaA.; 2007.
64. Laosiripojana N, Sutthisripok W, Assabumrungrat S. Synthesis gas production from dry reforming of methane over CeO_2 doped Ni/Al_2O_3: Influence of the doping ceria on the resistance toward carbon formation. Chemical Engineering Journal. 2005;112(1-3):13-22.

65. Gonzalez-Delacruz VM, Ternero F, Pereñíguez R, Caballero A, Holgado JP. Study of nanostructured Ni/CeO_2 catalysts prepared by combustion synthesis in dry reforming of methane. Applied Catalysis A: General. 2010;384(1):1-9.

66. Kim DK, Stöwe K, Müller F, Maier WF. Mechanistic study of the unusual catalytic properties of a new NiCe mixed oxide for the CO_2 reforming of methane. Journal of Catalysis. 2007;247(1):101-11.

67. Daza CE, Gallego J, Moreno JA, Mondragón F, Moreno S, Molina R. CO_2 reforming of methane over Ni/Mg/Al/Ce mixed oxides. Catalysis Today. 2008;133:357-66.

68. Kambolis A, Matralis H, Trovarelli A, Papadopoulou C. Ni/CeO_2-ZrO_2 catalysts for the dry reforming of methane. Applied Catalysis A-General. 2010;377(1-2):16-26.

69. Cui Y, Zhang H, Xu H, Li W. The CO_2 reforming of CH_4 over Ni/La_2O_3/α-Al_2O_3 catalysts: the effect of La_2O_3 contents on the kinetic performance. Applied catalysis A, General. 2007;331:60-9.

70. Xu S, Yan X, Wang X. Catalytic performances of NiO–CeO_2 for the reforming of methane with CO_2 and O_2. Fuel. 2006;85(14):2243-7.

71. Sakurai R, Hongo Y, Honda Y, Cutlip D, Popma JJ, Zimetbaum P, et al. A randomized comparison of ABT-578 eluting phosphorylcholine-coated cobalt-chromium stents with bare metal stents in de novo coronary lesions: Final intravascular ultrasound results from the ENDEAVOR II trial. Circulation. 2005;112(17):U748-U.

72. Deng WL, De Jesus J, Saltsburg H, Flytzani-Stephanopoulos M. Low-content gold-ceria catalysts for the water-gas shift and preferential CO oxidation reactions. Applied Catalysis A-General. 2005;291(1-2):126-35.

73. Idakiev V, Tabakova T, Tenchev K, Yuan Z-Y, Ren T-Z, Su B-L. Gold nanoparticles supported on ceria-modified mesoporous titania as highly active catalysts for low-temperature water-gas shift reaction. Catalysis Today. 2007;128(3):223-9.

74. Fu Q, Kudriavtseva S, Saltsburg H, Flytzani-Stephanopoulos M. Gold–ceria catalysts for low-temperature water-gas shift reaction. Chemical Engineering Journal. 2003;93(1):41-53.

75. MacPhail RC, Farmer JD, Jarema KA. Effects of acute and weekly episodic exposures to anatoxin-a on the motor activity of rats: Comparison with nicotine. Toxicology. 2007;234(1-2):83-9.

76. Fu Q, Deng W, Saltsburg H, Flytzani-Stephanopoulos M. Activity and stability of low-content gold–cerium oxide catalysts for the water–gas shift reaction. Applied Catalysis B: Environmental. 2005;56(1):57-68.

77. Avgouropoulos G, Papavasiliou J, Tabakova T, Idakiev V, Ioannides T. A comparative study of ceria-supported gold and copper oxide catalysts for preferential CO oxidation reaction. Chemical Engineering Journal. 2006;124(1):41-5.

78. Manzoli M, Avgouropoulos G, Tabakova T, Papavasiliou J, Ioannides T, Boccuzzi F. Preferential CO oxidation in H_2-rich gas mixtures over Au/doped ceria catalysts. Catalysis Today. 2008;138(3):239-43.

79. Rode BM, Hofer TS, Randolf BR, Schwenk CF, Xenides D, Vchirawongkwin V. Ab initio quantum mechanical charge field (QMCF) molecular dynamics: a QM/MM–MD procedure for accurate simulations of ions and complexes. Theoretical Chemistry Accounts. 2006;115(2-3):77-85.

80. Vchirawongkwin V, Kritayakornupong C, Rode BM. Structural and Dynamical Properties and Vibrational Spectra of Bisulfate Ion in Water: A Study by Ab Initio Quantum Mechanical Charge Field Molecular Dynamics. Journal of Physical Chemistry B. 2010;114(35):11561-9.

81. Canaval LR, Sakwarathorn T, Rode BM, Messner CB, Lutz OMD, Bonn GK. Erbium(III) in Aqueous Solution: An Ab Initio Molecular Dynamics Study. Journal of Physical Chemistry B. 2013;117(48):15151-6.

82. Wang HY, Ruckenstein E. Carbon dioxide reforming of methane to synthesis gas over supported rhodium catalysts: the effect of support. Applied Catalysis A-General. 2000;204(1):143-52.

83. Ozkara-Aydinoglu S, Ozensoy E, Aksoylu AE. The effect of impregnation strategy on methane dry reforming activity of Ce promoted Pt/ZrO_2. International Journal of Hydrogen Energy. 2009;34(24):9711-22.

84. Dombradi Z, Elekes Z, Kanungo R, Baba H, Fulop Z, Gibelin J, et al. Decoupling of valence neutrons from the core in B-17. Physics Letters B. 2005;621(1-2):81-8.

85. Laosiripojana N, Assabumrungrat S. Catalytic dry reforming of methane over high surface area ceria. Applied Catalysis B-Environmental. 2005;60(1-2):107-16.

86. Sakwarathorn T, Luengnaruemitchai A, Pongstabodee S. Preferential CO oxidation in H_2-rich stream over Au/CeO_2 catalysts prepared via modified deposition-precipitation. Journal of Industrial and Engineering Chemistry. 2011;17(4):747-54.

87. Hofer TS, Pribil AB, Randolf BR, Rode BM. Ab Initio Quantum Mechanical Charge Field Molecular Dynamics-A Nonparametrized First-Principle Approach to Liquids and Solutions. Advances in Quantum Chemistry, Vol 59. 2010;59:213-46.

88. Bopp P, Jancs G, Heinzinger K. An improved potential for non-rigid water molecules in the liquid phase. Chemical Physics Letters. 1983;98(2):129-33.

89. Stillinger FH, Rahman AJ. Journal of Chemical Physics. 1978;68(2):666-70.

90. Hofer TS, Tran HT, Schwenk CF, Rode BM. Characterization of dynamics and reactivities of solvated ions by ab initio simulations. Journal of Computational Chemistry. 2004;25(2):211-7.

91. Mulliken RSJ. Journal of Chemical Physics. 1955;23(10):1841-6.

92. Berendsen HJC, Postma JPM, van Gunsteren WF, DiNola A, Haak JR. Molecular dynimics with coupling to an external bath. Journal of Chemical Physics. 1984;81(8):3684-90.

93. Bhattacharjee A, Hofer TS, Rode BM. Local density corrected three-body distribution functions for probing local structure reorganization in liquids. Physical Chemistry Chemical Physics. 2008;10(44):6653-7.

94. Morales MR, Barbero BP, Cadus LE. Combustion of volatile organic compounds on manganese iron or nickel mixed oxide catalysts. Applied Catalysis B-Environmental. 2007;74(1-2):1-10.

95. Montoya JA, Romero-Pascual E, Gimon C, Del Angel P, Monzon A. Methane reforming with CO_2 over Ni/ZrO_2-CeO_2 catalysts prepared by sol-gel. Catalysis Today. 2000;63(1):71-85.

96. Chen HY, Lin J, Tan KL, Li J. Comparative studies of manganese-doped copper-based catalysts: the promoter effect of Mn on methanol synthesis. Applied Surface Science. 1998;126(3-4):323-31.

97. Pompeo F, Nichio NN, Gonzalez MG, Montes M. Characterization of Ni/SiO_2 and Ni/Li-SiO_2 catalysts for methane dry reforming. Catalysis Today. 2005;107-08:856-62.

98. Montoya J, Romero-Pascual E, Gimon C, Del Angel P, Monzon A. Methane reforming with CO_2 over Ni/ZrO_2–CeO_2 catalysts prepared by sol–gel. Catalysis Today. 2000;63(1):71-85.

99. Murugan B, Ramaswamy A. Chemical States and Redox Properties of Mn/CeO_2− TiO_2 Nanocomposites Prepared by Solution Combustion Route. The Journal of Physical Chemistry C. 2008;112(51):20429-42.

100. Liu Y, Hayakawa T, Suzuki K, Hamakawa S. Production of hydrogen by steam reforming of methanol over Cu/CeO_2 catalysts derived from $Ce_{1-x}Cu_xO_{2-x}$ precursors. Catalysis Communications. 2001;2(6):195-200.

101. Papavasiliou J, Avgouropoulos G, Ioannides T. Effect of dopants on the performance of CuO–CeO_2 catalysts in methanol steam reforming. Applied Catalysis B: Environmental. 2007;69(3):226-34.

102. Lee DW, Lee MS, Lee JY, Kim S, Eom HJ, Moon DJ, et al. The review of Cr-free Fe-based catalysts for high-temperature water-gas shift reactions. Catalysis Today. 2013;210:2-9.

103. Khan A, Chen P, Boolchand P, Smirniotis PG. Modified nano-crystalline ferrites for high-temperature WGS membrane reactor applications. Journal of Catalysis. 2008;253(1):91-104.

104. Khan A, Smirniotis PG. Relationship between temperature-programmed reduction profile and activity of modified ferrite-based catalysts for WGS reaction. Journal of Molecular Catalysis A-Chemical. 2008;280(1-2):43-51.

105. Thouchprasitchai N, Luengnaruemitchai A, Pongstabodee S. Water-gas shift reaction over Cu-Zn, Cu-Fe, and Cu-Zn-Fe composite-oxide catalysts prepared

by urea-nitrate combustion. Journal of Industrial and Engineering Chemistry. 2013;19(5):1483-92.

106. Li JW, Zhan YY, Mang FL, Lin XY, Zheng Q. Au/Fe_2O_3 water-gas shift catalyst prepared by modified deposition-precipitation method. Chinese Journal of Catalysis. 2008;29(4):346-50.

107. Li JW, Zhan YY, Lin XY, Zheng Q. Influence of calcination temperature on properties of Au/Fe2O3 catalysts for low temperature water gas shift reaction. Acta Physico-Chimica Sinica. 2008;24(6):932-8.

108. Frisch MJea, GAUSSIAN 09, Revision A.02 GAUSSIAN, Inc., Wallingford, CT. 2009.

109. Tanaka Y, Utaka T, Kikuchi R, Sasaki K, Eguchi K. CO removal from reformed fuel over Cu/ZnO/Al_2O_3 catalysts prepared by impregnation and coprecipitation methods. Applied Catalysis a-General. 2003;238(1):11-8.

110. Panzera G, Modafferi V, Candamano S, Donato A, Frusteri F, Antonucci PL. CO selective oxidation on ceria-supported Au catalysts for fuel cell application. Journal of Power Sources. 2004;135(1-2):177-83.

111. Ayastuy JL, Gonzalez-Marcos MP, Gutierrez-Ortiz MA. Promotion effect of Sn in alumina-supported Pt catalysts for CO-PROX. Catalysis Communications. 2011;12(10):895-900.

112. Avgouropoulos G, Manzoli M, Boccuzzi F, Tabakova T, Papavasiliou J, Ioannides T, et al. Catalytic performance and characterization of Au/doped-ceria catalysts for the preferential CO oxidation reaction. Journal of Catalysis. 2008;256(2):237-47.

113. Arena F, Famulari P, Interdonato N, Bonura G, Frusteri F, Spadaro L. Physico-chemical properties and reactivity of Au/CeO_2 catalysts in total and selective oxidation of COD. Catalysis Today. 2006;116(3):384-90.

114. Gamarra D, Martinez-Arias A. Preferential oxidation of CO in rich H_2 over CuO/CeO_2: Operando-DRIFTS analysis of deactivating effect of CO_2 and H_2O. Journal of Catalysis. 2009;263(1):189-95.

115. Moretti E, Storaro L, Talon A, Patrono P, Pinzari F, Montanari T, et al. Preferential CO oxidation (CO-PROX) over CuO-ZnO/TiO_2 catalysts. Applied Catalysis A-General. 2008;344(1-2):165-74.

116. Montgomery DC. Design and analysis of experiments. 7th edn. ed. Hoboken, NJ: John Wiley & Sons; 2009. xvii, 656 p p.

117. Box GEP, Behnken DW. Some new three level designs for the study of quantitative variables. Technometrics. 1960;2(4):455-75.

118. Idakiev V, Tabakova T, Tenchev K, Yuan ZY, Ren TZ, Su BL. Gold nanoparticles supported on ceria-modified mesoporous titania as highly active catalysts for low-temperature water-gas shift reaction. Catalysis Today. 2007;128(3-4):223-9.

119. Hou JB, Yi BL, Yu HM, Hao LX, Song W, Fu Y, et al. Investigation of resided water effects on PEM fuel cell after cold start. International Journal of Hydrogen Energy. 2007;32(17):4503-9.

120. Canaval LR, Weiss AKH, Rode BM. Structure and dynamics of the Th^{4+}-ion in aqueous solution - An ab initio QMCF-MD study. Computational and Theoretical Chemistry. 2013;1022:94-102.

121. Moin ST, Hofer TS, Pribil AB, Randolf BR, Rode BM. A Quantum Mechanical Charge Field Molecular Dynamics Study of Fe^{2+} and Fe^{3+} Ions in Aqueous Solutions. Inorganic Chemistry. 2010;49(11):5101-6.

122. Wiesenburg DA, Guinasso Jr NL. Equilibrium solubilities of methane, carbon monoxide, and hydrogen in water and sea water. Journal of Chemical and Engineering Data. 1979;24(4):356-60.

123. Moin ST, Pribil AB, Lim LHV, Hofer TS, Randolf BR, Rode BM. Carbon Dioxide in Aqueous Environment-A Quantum Mechanical Charge Field Molecular Dynamics Study. International Journal of Quantum Chemistry. 2011;111(7-8):1370-8.

124. Brucato JR, Palumbo ME, Strazzulla G. Carbonic acid by ion implantation in water/carbon dioxide ice mixtures. Icarus. 1997;125(1):135-44.

125. Baltrusaitis J, Grassian VH. Carbonic Acid Formation from Reaction of Carbon Dioxide and Water Coordinated to Al(OH)(3): A Quantum Chemical Study. Journal of Physical Chemistry A. 2010;114(6):2350-6.

126. Jiao D, Rempe S. Thermodynamic studies of carbon dioxide and carbonic anhydrase with quasichemical theory. Abstracts of Papers of the American Chemical Society. 2010;240.

127. Sakwarathorn T, Pongstabodee S, Vchirawongkwin V, Canaval LR, Tirler AO, Hofer TS. Characteristics of selenate in aqueous solution–An ab initio QMCF-MD study. Chemical Physics Letters. 2014;595:226-9.
128. Vchirawongkwin V, Rode BM, Persson I. Structure and dynamics of sulfate ion in aqueous solution - An ab initio QMCF MD simulation and large angle X-ray scattering study. Journal of Physical Chemistry B. 2007;111(16):4150-5.
129. Stillinger FH, Rahman AJ. Revised central force potentials for water. Journal of Chemical Physics. 1978;68:666-70.
130. DeFrees DJ, McLean AD. Molecular orbital predictions of the vibrational frequencies of some molecular ions. J Chem Phys. 1985;82(1):333-41.
131. Scott AP, Radom L. Harmonic vibrational frequencies: An evaluation of Hartree-Fock, Moller-Plesset, quadratic configuration interaction, density functional theory, and semiempirical scale factors. Journal of Physical Chemistry. 1996;100(41):16502-13.
132. Daszkiewicz M, Marchewka MK. Crystallographic, vibrational and theoretical studies of 2,3-diaminopyridinium selenate. Vibrational Spectroscopy. 2011;57(2):326-33.
133. Dammak M, Mhiri T, Cousson A. Neutron structural and vibrational studies of dipotassium selenate tellurate. Journal of Alloys and Compounds. 2006;407(1-2):176-81.
134. Gupta MK, Surendra L, Kaushik SM, Jere GV. Solid-state effects on selenate vibrations in yttrium and some rare earth selenates. Journal of Solid State Chemistry. 1982;43(3):359-63.
135. Frost RL, Weier ML, Kloprogge JT. Raman spectroscopy of some natural hydrotalcites with sulphate and carbonate in the interlayer. Journal of Raman Spectroscopy. 2003;34:760-8.
136. Xenides D, Randolf BR, Rode BM. Structure and ultrafast dynamics of liquid water: A quantum mechanics/molecular mechanics molecular dynamics simulations study. Journal of Chemical Physics. 2005;122(17).
137. Dolg M, Stoll H, Preuss H, Pitzer RM. Relativistic and correlation effects for element 105 (hahnium, Ha): a comparative study of M and MO (M= Nb, Ta,

Ha) using energy-adjusted ab initio pseudopotentials. The Journal of Physical Chemistry. 1993;97(22):5852-9.

138. Lutz O, Hofer TS, Randolf BR, Rode BM. Hydration of trivalent lanthanum revisited–An ab initio QMCF-MD approach. Chemical Physics Letters. 2012;536:50-4.

139. Lutz O, Hofer TS, Randolf BR, Rode BM. Computational study of the cerium (III) ion in aqueous environment. Chemical Physics Letters. 2012;539:50-3.

140. Kanno H, Hiraishi J. Raman study of aqueous rare earth nitrate solutions in liquid and glassy states. The Journal of Physical Chemistry. 1984;88(13):2787-92.

APPENDIX

APPENDIX A

CATALYSTS CALCULATION

Preparation catalysts by impregnation method

Sample: 1%(1:1)AuFe/CeO_2 1000 mg

In part of active metal;

1 g of catalyst consists of 10 mg of Au and Fe

M.W. of Au = 197 g

M.W. of Fe = 55.9 g

At Au : Fe = 1 : 1 atomic ratio;

Au	:	Fe	
1	:	1	atom by mole
$1\times\frac{197}{197}$	:	$1\times\frac{55.9}{197}$	by weight
1	:	0.284	by weight

Total amount of Au–Fe = 10 mg; so,

$1\times\frac{10}{(1+0.284)}$	:	$0.284\times\frac{10}{(1+0.284)}$	
7.79	:	2.21	mg

Stock solution:

M.W. of $HAuCl_4.3H_2O$ = 395 g

M.W. of $Fe(NO_3)_3.9H_2O$ = 404 g

$HAuCl_4.3H_2O$ solution contains 5 g in 200 ml = 25 mg/ml

So, concentration of Au = $\frac{197}{395}$ x 25

= 12.47 mg/ml

$Fe(NO_3)_3.9H_2O$ solution has 0.1 M

So, concentration of Fe = 5.59 mg/ml

From stock solution;

Au 7.79 mg = $\frac{7.79}{12.47}$

= 0.625 ml of solution

Fe 2.21 mg = $\frac{2.21}{5.59}$

= 0.395 ml of solution

Therefore, the solution for 1%(1:1)$AuFe/CeO_2$ preparation by slurry impregnation method are:

Ce support	=	990 mg
$HAuCl_4.3H_2O$ solution	=	0.625 ml
$Fe(NO_3)_3.9H_2O$ solution	=	0.395 ml

APPENDIX B

X-RAY DIFFRACTION CALCULATION

XRD calculation for crystallite size particle from Debye Scherrer's equation as

$$D_b = \frac{K \times \lambda}{\beta \times cos\theta}$$

Where

$D_b =$ Crystallite diameter (Å)

K = Scherrer constant =0.9

λ = X-ray wave length (Å) = 1.54

β = angular width of peak in term of 2θ

θ = Bragg's angle of reflection (degree)

For example: 1% Au/CeO_2 catalyst

To calculate CeO_2 crystallite size from the XRD pattern of Au/CeO_2 is presented in Figure B with given some data.

At center of major peak, (1 1 1) plane,

$$2\theta = \frac{\text{Left angle + Right angle}}{2}$$

$$= \frac{27.20 + 30.56}{2}$$

$$= 28.88^{o}$$

$$\theta = \frac{28.88}{2} \times \frac{\pi}{180}$$

$$= 0.25 \text{ rad}$$

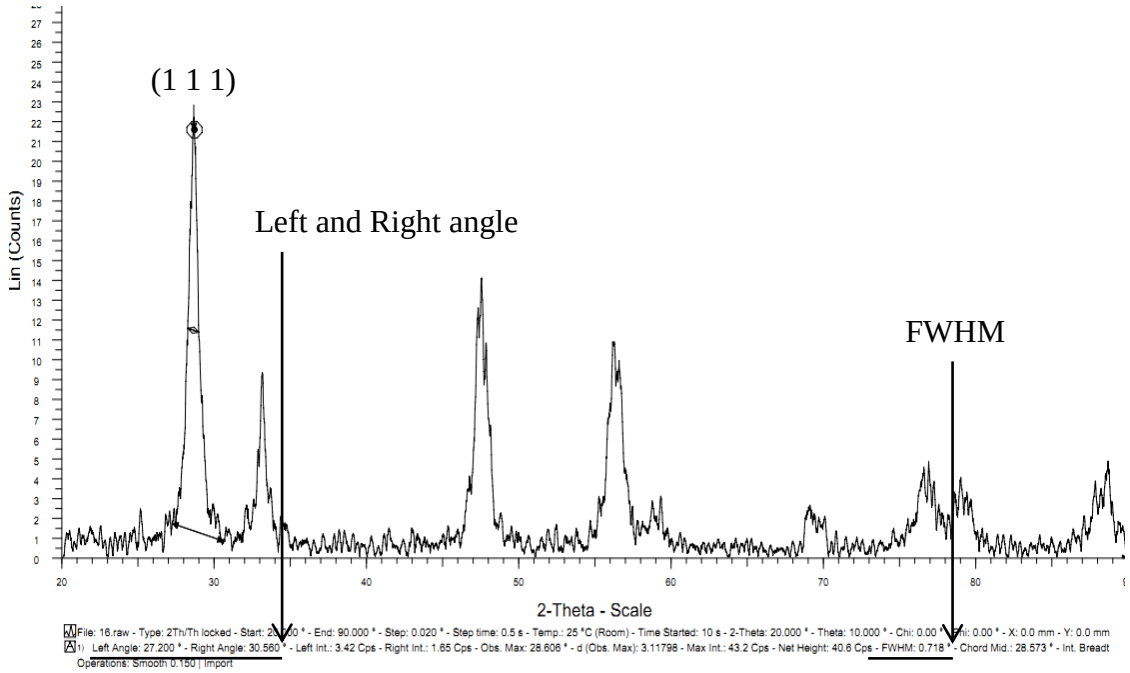

Figure B.1 XRD pattern of 1% Au/CeO_2 catalyst for calculate crystallite size

From Figure B.1,

Full width at half maximum (FWHM) = 0.718 º

So, β = $0.718 \times \frac{\pi}{180}$

= 0.01 rad

Therefore,

CeO_2 crystallite size (D_b) = $\frac{K \times \lambda}{\beta \times cos\theta}$

= $\frac{0.9 \times 1.54}{0.01 \times cos\ 0.25}$

= 138.6 Å

= 13.9 nm

APPENDIX C

ADDITIONAL EXPERIMENTAL DESIGN DATA

C.1 Additional data in DRM part

In DRM part, the CO concentration effluent in each catalyst versus temperature is shown in Figure C.1 to Figure C.3. When increasing temperature, the methane decomposition and reverse Boudouard reaction move forward effecting on an increasing of CO component. These figures represent why carbon monoxide should remove in the next process. When hydrogen product increases at high temperature, the carbon monoxide also increases.

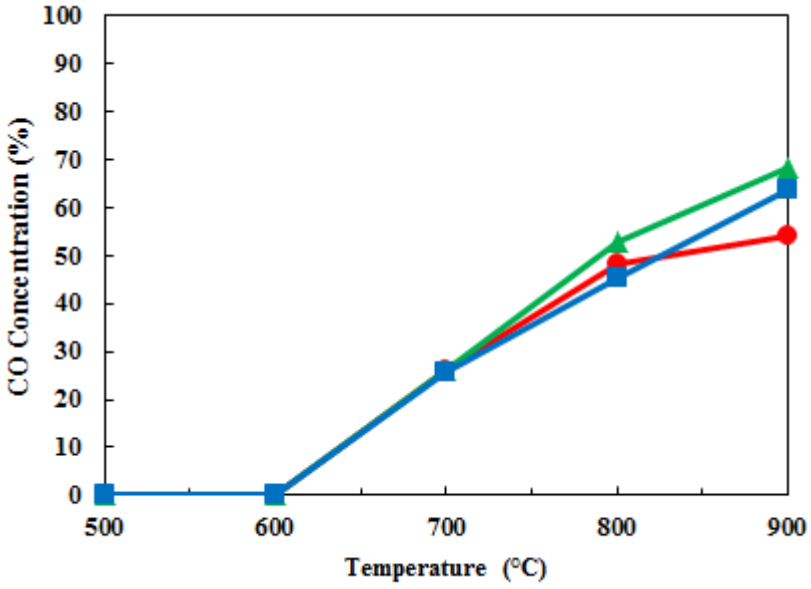

Figure C.1 CO concentration effluent from DRM over catalysts of (●) 5%, (▲) 10% and (■) 15% weight of Ni loading versus temperature

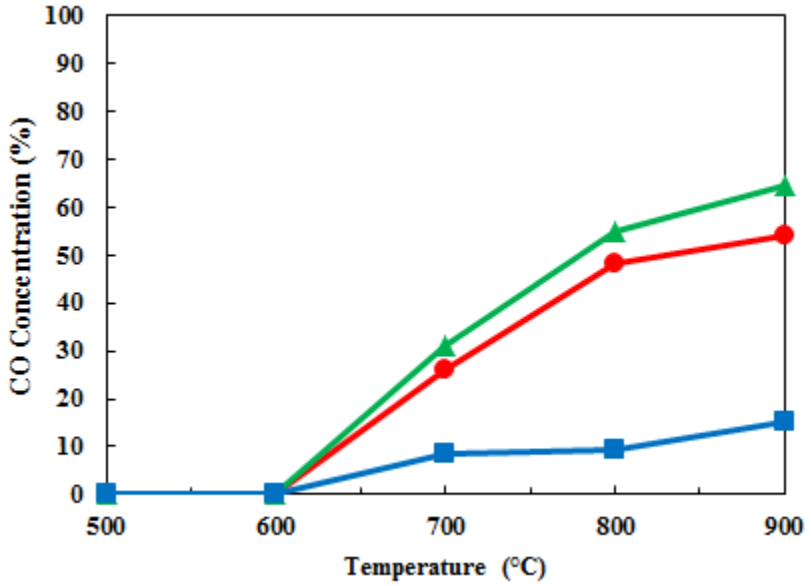

Figure C.2 CO concentration effluent from DRM over catalysts of (●) 5Ni/CeO_2, (▲) 5Ni-0.5Mn/CeO_2 and (■) 5Ni-0.5Au/CeO_2 versus temperature

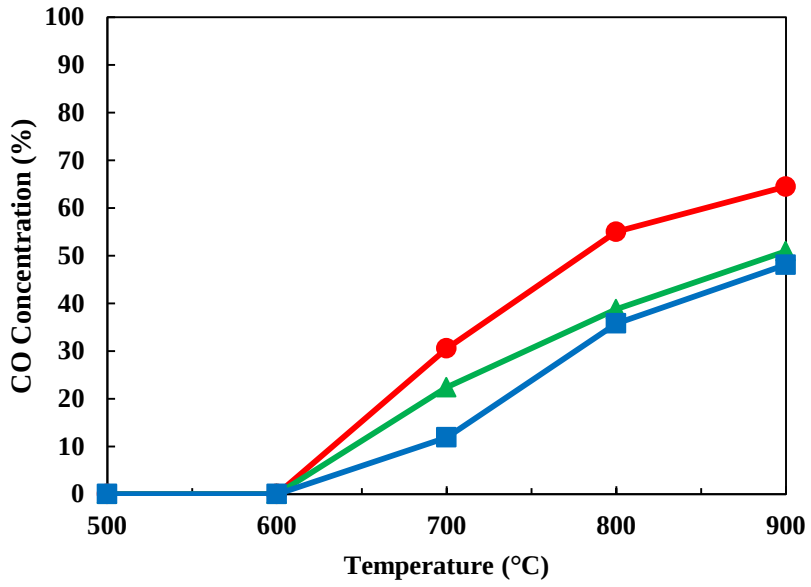

Figure C.3 CO concentration effluent from DRM over Ni catalysts with various loading (%) of Mn promoter: (●) 5Ni-0.5Mn; (▲) 5Ni-5Mn; (■) 5Ni-10Mn

Figure C.4 shows each main factors effecting to the activities including CH_4 conversion, CO_2 conversion, H_2 selectivity and carbon deposition. It presented that the center value was located outside of the straight line drawn through the (-1) to (+1). This result confirmed with the influence of curvature. Only CO_2 conversion, the center point did not locate far from the linear line resulting curvature did not effect to these activity. This consistent line showed that the curvature did not significantly effect to CO_2 conversion.

From 2^k experiment to screen factors, the final equation could not find an exact model; therefore, the role of RSM is very important to determine the effects of the curvature. In this study, the 3-level factorial theory was applied for RSM analysis.

Table C.1 shows the analysis of the activities including CH_4 conversion, CO_2 conversion, H_2 selectivity and carbon deposition. The equation model can be divided into four categories such as linear, 2FI, quadratic and cubic sources. Linear source represents the main factors consists of A, B, C and D. The 2FI source refers to the influence of the combination effects including AB, AC, AD, BC, BD and CD interaction. The quadratic source represents the influence of the main effect square, which directly affects to the curvature, including A^2, B^2, C^2 and D^2. The cubic source means the influence effect of the combination factors power of three degree total such as A^3, B^3, C^3, D^3, A^2B, A^2C, A^2D, AB^2, AC^2, AD^2, B^2C, B^2D, BC^2, BD^2, C^2D, CD^2, ABC, ABD, ACD and BCD. To consider CH_4 conversion, it was found that the model composed with linear, 2FI and quadratic sources (P-value less than 0.05). To determine the R^2 and adj-R^2, CH_4 conversion gave 0.9539 and 0.9444 of the quadratic source, respectively, which remained acceptable and CO_2 conversion showed 0.9547 and 0.9454, respectively. This result agreed with the previous screening. Focus on the H_2 selectivity and carbon deposition found that the suitable model consists of quadratic and cubic. Especially H_2 selectivity, the result agree with the previous screening that it found the linear and interaction were not significant excepting factor C. The main factor of C and C^3 were an alias.

ANOVA of the activities are represented in Table C.2 to Table C.5. The factor that shows P-value less than 0.05 would be significant effects on the response as shown in Table 4.4.

To present some character of analysis to confirm the equation model including normal plots of residuals, predicted vs residuals, run number vs residuals, run number vs out liner T, and main effect vs residuals of CH_4 conversion and CO_2 conversion determined by 3^k factorial calculation as shown in Figure C.5 and Figure C.6. It showed some results that confirmed the equation after RSM by 3^k factorial theory in DRM part. For H_2 selectivity and carbon deposition, it did not show a confirmation graph in this thesis; however, it presented the same trend that similar to CH_4 conversion and CO_2 conversion.

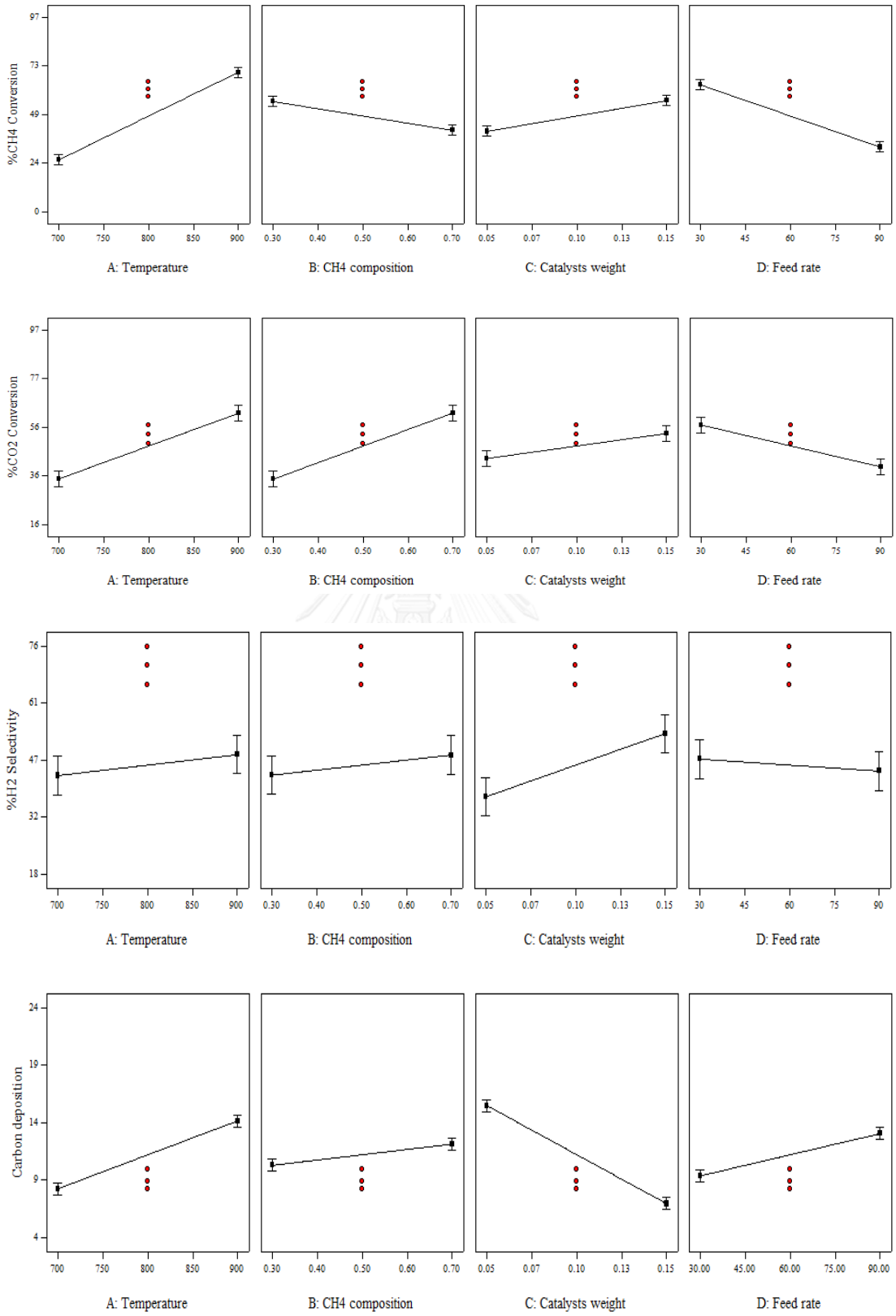

Figure C.4 The main factor plot for (a) CH_4 conversion, (b) CO_2 conversion, (c) H_2 selectivity and (d) carbon deposition for 2^4 factorial designs with 3 center points

Table C.1 Sequential model of CH_4 conversion, CO_2 conversion, H_2 selectivity and carbon deposition to select the highest order polynomial

Source	SS	DF	MS	F–Value	Prob	R^2	Adj-R^2	
CH_4 conversion								
Mean	202088.68	1	202088.68					
Linear	45897.92	4	11474.48	261.11	< 0.0001	0.9305	0.9269	
2FI	790.11	6	131.68	3.59	0.0036	0.9465	0.9391	
Quadratic	361.37	4	90.34	2.70	0.0378	0.9539	0.9444	Selected
Cubic	811.79	16	50.74	1.80	0.0565	0.9703	0.9532	
Residual	1464.43	52	28.16					
Total	251414.29	83	3029.09					
CO_2 conversion								
Mean	199925.97	1	199925.97					
Linear	31599.61	4	7899.90	130.78	< 0.0001	0.8702	0.8636	
2FI	2456.28	6	409.38	13.07	< 0.0001	0.9379	0.9293	
Quadratic	612.05	4	153.01	6.33	0.0002	0.9547	0.9454	Selected
Cubic	994.10	16	62.13	4.98	< 0.0001	0.9821	0.9718	
Residual	649.21	52	12.48					
Total	236237.23	83	2846.23					
H_2 Selectivity								
Mean	232057.61	1	232057.61					
Linear	435.90	4	108.98	0.42	0.7963	0.0209	-0.0293	
2FI	568.34	6	94.72	0.34	0.9113	0.0482	-0.0840	
Quadratic	10782.67	4	2695.67	20.23	< 0.0001	0.5654	0.4760	
Cubic	7403.32	16	462.71	14.53	< 0.0001	0.9206	0.8748	Selected
Residual	1655.63	52	31.84					
Total	252903.48	83	3047.03					
Carbon deposition								
Mean	7244.34	1	7244.34					
Linear	1343.01	4	335.75	42.93	< 0.0001	0.6876	0.6716	
2FI	188.49	6	31.41	5.37	0.0001	0.7842	0.7542	
Quadratic	71.52	4	17.88	3.47	0.0122	0.8208	0.7839	
Cubic	160.60	16	10.04	2.76	0.0030	0.9030	0.8470	Selected
Residual	189.44	52	3.64					
Total	9197.39	83	110.81					

Table C.2 Analysis of variance of CH_4 conversion as the response for quadratic regression model

Source	SS	DF	MS	F–Value	Prob	Coefficient
Model	47049.39	14	3360.67	100.40	< 0.0001	Intercept 54.17
A	24846.80	1	24846.80	742.27	< 0.0001	21.45
B	3518.72	1	3518.72	105.12	< 0.0001	-8.07
C	3979.85	1	3979.85	118.89	< 0.0001	8.58
D	13552.55	1	13552.55	404.87	< 0.0001	-15.84
A^2	20.95	1	20.95	0.63	0.4316	-1.06
B^2	22.83	1	22.83	0.68	0.4117	-1.10
C^2	220.07	1	220.07	6.57	0.0126	-3.43
D^2	62.98	1	62.98	1.88	0.1747	-1.83
AB	14.91	1	14.91	0.45	0.5068	-0.64
AC	172.30	1	172.30	5.15	0.0265	2.19
AD	7.61	1	7.61	0.23	0.6350	-0.46
BC	187.79	1	187.79	5.61	0.0207	-2.28
BD	61.65	1	61.65	1.84	0.1792	1.31
CD	345.85	1	345.85	10.33	0.0020	3.10
Residual	2276.22	68	33.47			
Lack of Fit	2247.45	66	34.05	2.37	0.3428	
Pure Error	28.77	2	14.38			
Total	49325.61	82				

R^2 0.9539 Adj-R^2 0.9444

Table C.3 Analysis of variance of CO_2 conversion as the response for quadratic regression model

Source	SS	DF	MS	F–Value	Prob	Coefficient
Model	34667.94	14	2476.28	102.47	< 0.0001	Intercept 52.62
A	12110.14	1	12110.14	501.12	< 0.0001	14.98
B	11564.17	1	11564.17	478.52	< 0.0001	14.63
C	2143.85	1	2143.85	88.71	< 0.0001	6.30
D	5781.46	1	5781.46	239.24	< 0.0001	-10.35
A^2	115.08	1	115.08	4.76	0.0326	-2.48
B^2	142.36	1	142.36	5.89	0.0179	2.75
C^2	296.30	1	296.30	12.26	0.0008	-3.97
D^2	57.29	1	57.29	2.37	0.1283	-1.75
AB	1936.20	1	1936.20	80.12	< 0.0001	7.33
AC	18.78	1	18.78	0.78	0.3812	-0.72
AD	20.24	1	20.24	0.84	0.3634	0.75
BC	6.60	1	6.60	0.27	0.6029	0.43
BD	203.50	1	203.50	8.42	0.0050	-2.38
CD	270.97	1	270.97	11.21	0.0013	2.74
Residual	1643.31	68	24.17			
Lack of Fit	1611.31	66	24.41	1.53	0.4774	
Pure Error	32.00	2	16.00			
Total	36311.25	82				

R^2 0.9547 Adj-R^2 0.9454

Table C.4 Analysis of variance of H_2 selectivity as the response for quadratic regression model

Source	SS	DF	MS	F–Value	Prob	Coefficient
Model	19190.23	30	639.67	20.09	< 0.0001	Intercept 67.85
A	859.03	1	859.03	26.98	< 0.0001	-10.55
B	6.79	1	6.79	0.21	0.6461	-0.93
C	777.40	1	777.40	24.42	< 0.0001	-10.03
D	377.83	1	377.83	11.87	0.0011	6.99
A^2	117.40	1	117.40	3.69	0.0603	-2.50
B^2	10403.03	1	10403.03	326.74	< 0.0001	-23.54
C^2	4.56	1	4.56	0.14	0.7065	-0.49
D^2	232.45	1	232.45	7.30	0.0093	3.52
AB	26.95	1	26.95	0.85	0.3618	0.86
AC	0.44	1	0.44	0.01	0.9068	0.11
AD	43.63	1	43.63	1.37	0.2471	-1.10
BC	175.87	1	175.87	5.52	0.0226	-2.21
BD	161.32	1	161.32	5.07	0.0286	-2.11
CD	160.13	1	160.13	5.03	0.0292	2.10
A^2B	14.84	1	14.84	0.47	0.4978	1.11
A^2C	10.51	1	10.51	0.33	0.5681	0.93
A^2D	0.29	1	0.29	0.01	0.9239	0.15
AB^2	3075.92	1	3075.92	96.61	< 0.0001	16.01
AC^2	28.76	1	28.76	0.90	0.3463	-1.54
AD^2	5.36	1	5.36	0.17	0.6833	-0.66
B^2C	2564.92	1	2564.92	80.56	< 0.0001	14.61
B^2D	1229.71	1	1229.71	38.62	< 0.0001	-10.12
BC^2	0.53	1	0.53	0.02	0.8982	-0.20
BD^2	60.12	1	60.12	1.89	0.1753	2.23
C^2D	10.27	1	10.27	0.32	0.5726	0.92
CD^2	74.10	1	74.10	2.33	0.1332	2.48
ABC	33.21	1	33.21	1.04	0.3119	1.17
ABD	71.90	1	71.90	2.26	0.1389	-1.73
ACD	66.60	1	66.60	2.09	0.1541	-1.66
BCD	156.27	1	156.27	4.91	0.0311	-2.55
Residual	1655.63	52	31.84			
Lack of Fit	1607.91	50	32.16	1.35	0.5187	
Pure Error	47.73	2	23.86			
Total	20845.87	82				

R^2 0.9206 Adj-R^2 0.8748

Table C.5 Analysis of variance of carbon deposition as the response for quadratic regression model

Source	SS	DF	MS	F–Value	Prob	Coefficient
Model	1763.62	30	58.79	16.14	< 0.0001	7.76
A	81.06	1	81.06	22.25	< 0.0001	3.24
B	3.95	1	3.95	1.08	0.3024	0.71
C	16.07	1	16.07	4.41	0.0406	-1.44
D	14.77	1	14.77	4.05	0.0492	1.38
A^2	0.29	1	0.29	0.08	0.7796	-0.12
B^2	64.31	1	64.31	17.65	0.0001	1.85
C^2	1.67	1	1.67	0.46	0.5019	0.29
D^2	2.96	1	2.96	0.81	0.3714	0.39
AB	8.30	1	8.30	2.28	0.1373	0.48
AC	79.54	1	79.54	21.83	< 0.0001	-1.48
AD	78.03	1	78.03	21.42	< 0.0001	1.47
BC	16.64	1	16.64	4.57	0.0373	-0.67
BD	0.69	1	0.69	0.19	0.6659	0.13
CD	5.30	1	5.30	1.45	0.2333	0.38
A^2B	0.75	1	0.75	0.21	0.6516	0.25
A^2C	0.01	1	0.01	0.00	0.9581	-0.02
A^2D	2.42	1	2.42	0.66	0.4189	0.44
AB^2	17.82	1	17.82	4.89	0.0314	-1.21
AC^2	11.24	1	11.24	3.09	0.0849	0.96
AD^2	0.51	1	0.51	0.14	0.7099	0.20
B^2C	55.56	1	55.56	15.25	0.0003	-2.15
B^2D	13.34	1	13.34	3.66	0.0612	1.05
BC^2	20.26	1	20.26	5.56	0.0221	1.29
BD^2	14.68	1	14.68	4.03	0.0499	-1.10
C^2D	12.44	1	12.44	3.41	0.0703	-1.01
CD^2	3.53	1	3.53	0.97	0.3298	-0.54
ABC	0.00	1	0.00	0.00	0.9883	0.00
ABD	0.06	1	0.06	0.02	0.8958	-0.05
ACD	4.56	1	4.56	1.25	0.2685	-0.43
BCD	3.42	1	3.42	0.94	0.3372	0.37
Residual	189.44	52	3.64			
Lack of Fit	187.87	50	3.76	4.80	0.1873	
Pure Error	1.57	2	0.78			
Total	1953.06	82				
R^2 0.9030		Adj-R^2	0.8470			

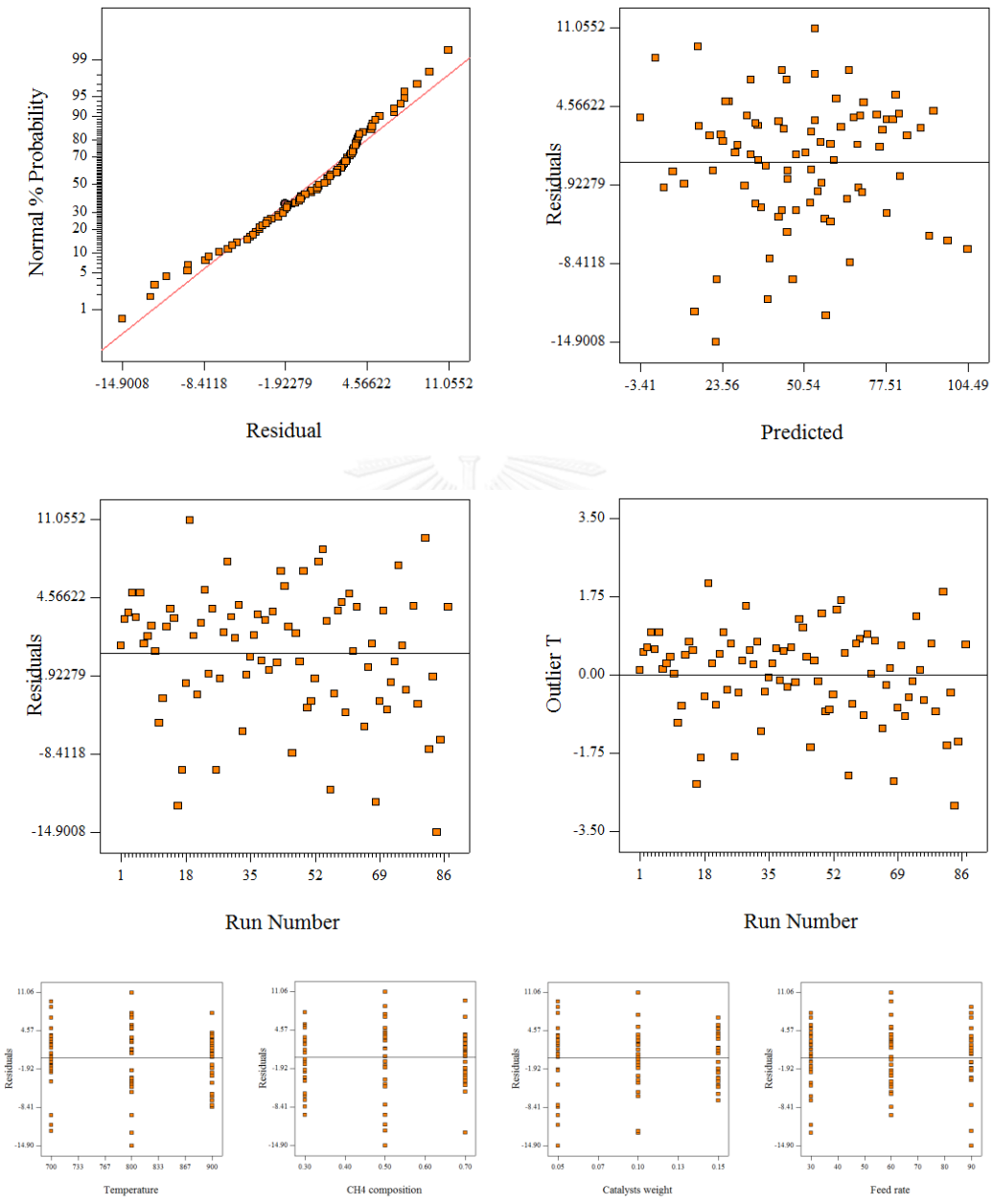

Figure C.5 Normal plots of residuals, predicted vs residuals, run number vs residuals, run number vs out liner T, and main effects vs residuals of CH_4 conversion calculated from 3^k factorial.

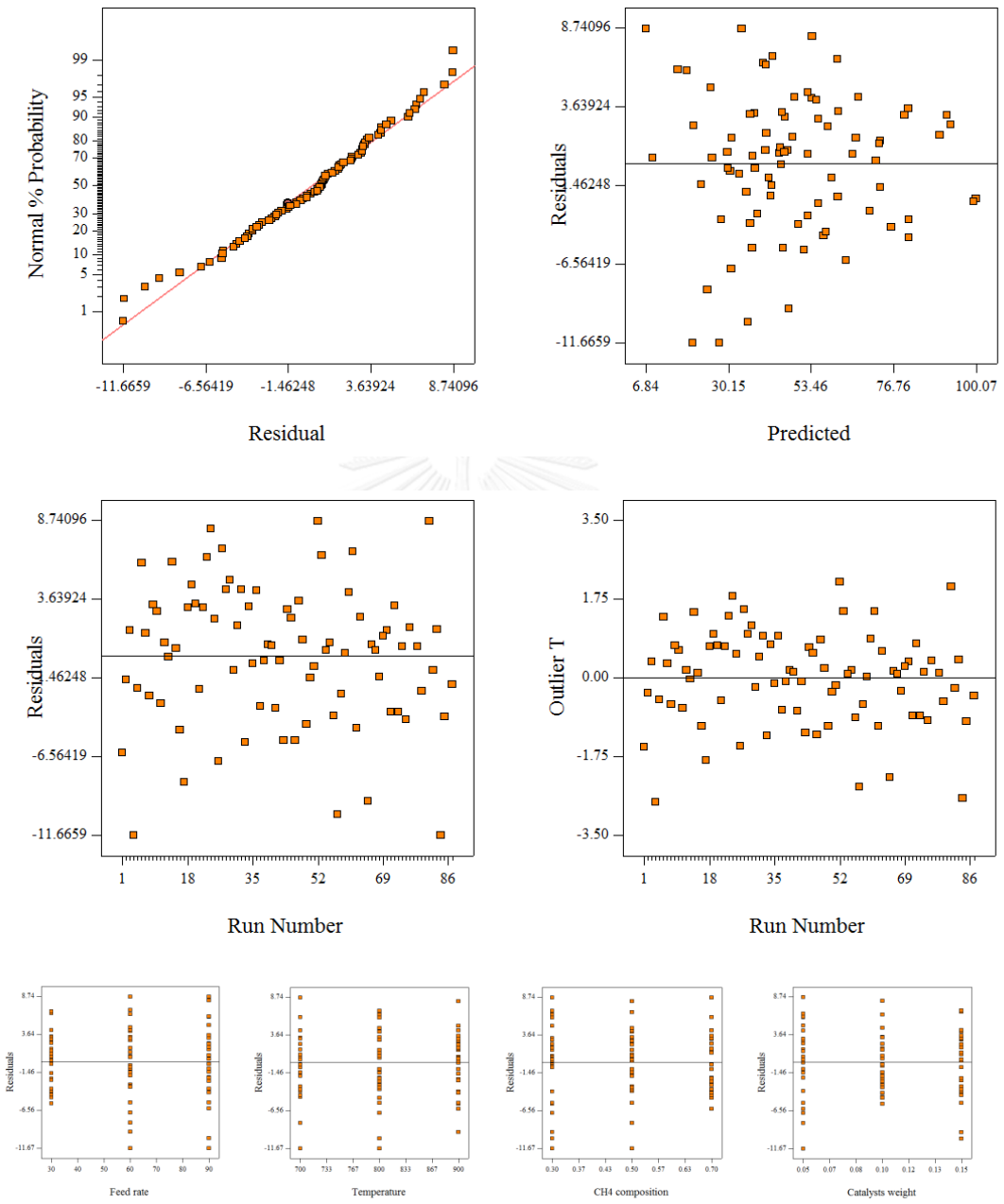

Figure C.6 Normal plots of residuals, predicted vs residuals, run number vs residuals, run number vs out liner T, and main effects vs residuals of CO_2 conversion calculated from 3^k factorial.

C.2 Additional data in WGS part

To consider the degree of factors effecting to CO conversion and H_2 yield found that the source of linear and quadratic presented clearly significant (p-value < 0.05). Thus, the appropriated source was a quadratic model due to it showed the higher degree than linear (as shown in Table C.6).

Table C.6 Analysis of variance of the response surface for CO conversion and H_2 yield regressions to select the highest order polynomial

	Source	SS	DF	MS	F-Value	P-Value	
CO Conversion							
	Mean	35442.73	1	35442.73			
	Linear	4127.94	2	2063.97	40.6733	<0.0001	
	2FI	3.08	1	3.08	0.0550	0.8198	
	Quadratic	483.44	2	241.72	80.8565	<0.0001	Suggested
	Cubic	14.98	2	7.49	6.2936	0.0431	
	Residual	5.95	5	1.19			
	Total	40078.12	13	3082.93			
H_2 Yield							
	Mean	20307.87	1	20307.87			
	Linear	1028.41	2	514.20	8.5356	0.0069	
	2FI	0.92	1	0.92	0.0137	0.9093	
	Quadratic	549.63	2	274.82	37.0834	0.0002	Suggested
	Cubic	27.43	2	13.72	2.8061	0.1524	
	Residual	24.44	5	4.89			
	Total	21938.70	13	1687.59			

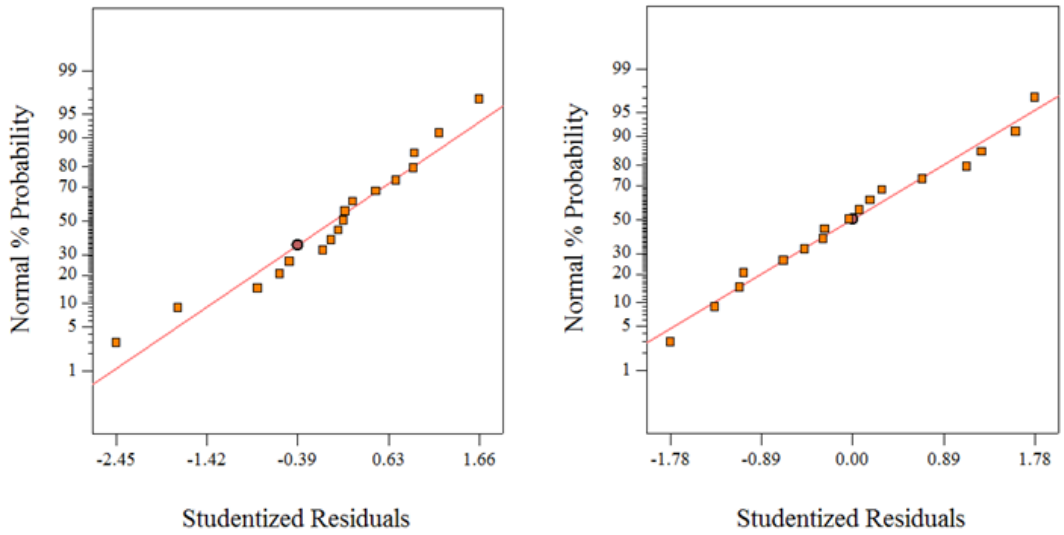

Figure C.7 Normal probability plot of (left) CO Conversion and (right) H_2 Yield of selected factor of model

Figure C.7 presents %normal probability plot of residue of CO conversion and H_2 yield. It represented the linear line that had R^2 and adj-R^2 of 0.9955 and 0.9923, respectively, for CO conversion while R^2 and adj-R^2 of H_2 yield were 0.9682 and 0.9455, respectively. Generally, due to R^2 and adj-R^2 are higher than 0.95, the model can be accepted.

C.3 Additional data in PROX part

Table C.7 demonstrates source of factor which select the additional terms. The highest order polynomial was significantly selected including quadratic source such as A^2, C^2 and D^2 terms. Linear (A, C and D) and 2FI (AC, AD and CD) sources were also selected because of the lower degree or equal the quadratic order. The cubic model was an aliased model which did not necessary to select these factors consisting of A^3, C^3, D^3, A^2C, A^2D, AC^2, AD^2, C^2D, CD^2 and ACD.

Table C.7 Sequential model sum of squares of Box-Behnken design

Source	SS	DF	MS	F	P-value	Note
Mean	12304.97	1	12304.97			
Linear	1028.41	3	342.80	13.04	0.0003	
2FI	69.38	3	23.12	0.85	0.4978	
Quadratic	225.43	3	75.14	11.25	0.0046	suggested
Cubic	44.70	3	14.90	29.09	0.0035	aliased
Residual	2.04	4	0.51			
Total	13674.95	17	804.40			

Table C.8 represents ANOVA of quadratic factor in Box-Behnken design. We know that factors of CO_2 added (D) was the highest effected to the yield (P-value <0.05 or highest code coefficient). The observations terms of A^2 and C^2 were significant in the model. It confirmed the results from screening effects indicating the influent of the curvature. For the temperature effect (A), P-value in this design was less than in 2^k design. It can be explained by the changing of the range of temperature from screening test.

Table C.8 ANOVA of all effects of Box-Behnken designs to the yield

Term	SS	DF	MS	F	P-value	Coefficient (code factor)	Significant
A	0.03	1	0.03	0.00	0.9504	-0.06	
C	4.1	1	4.1	0.62	0.4563	-0.72	
D	1024.2	1	1024.2	153.35	0.0001	-11.31	significant
A^2	128.8	1	128.8	19.28	0.0032	-5.53	significant
C^2	83.9	1	83.9	12.57	0.0094	-4.47	significant
D^2	4.7	1	4.7	0.72	0.4249	1.07	
AC	2.2	1	2.2	0.34	0.5775	-0.75	
AD	55.1	1	55.1	8.25	0.0239	3.71	significant
CD	12.0	1	12.0	1.80	0.2221	1.73	
Residual	46.7	7	6.6				
Total	1369.9	16					
R^2	0.9659				Intercept	31.11	
R^2_{adj}	0.9220						

APPENDIX D

OVERVIEW OF OVERALL PROCESS

To overview overall process including feed stream component, reactor unit, catalysts activity and gaseous component output in this dissertation are shown in this appendix.

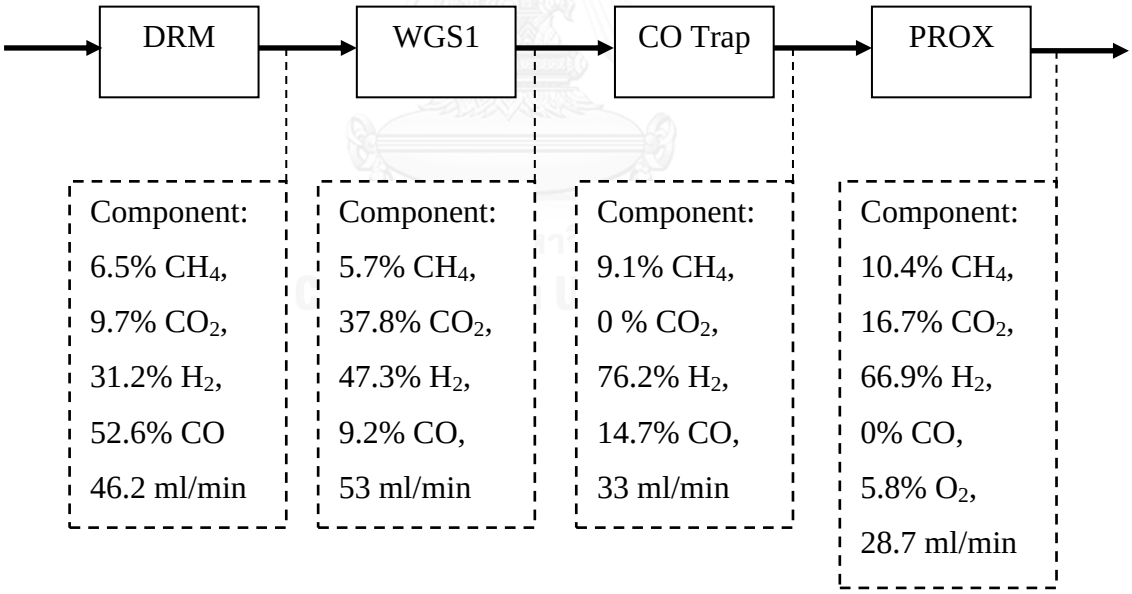

Figure D.1 Overview of effluent component without helium over DRM, WGS1, CO trap and PROX process

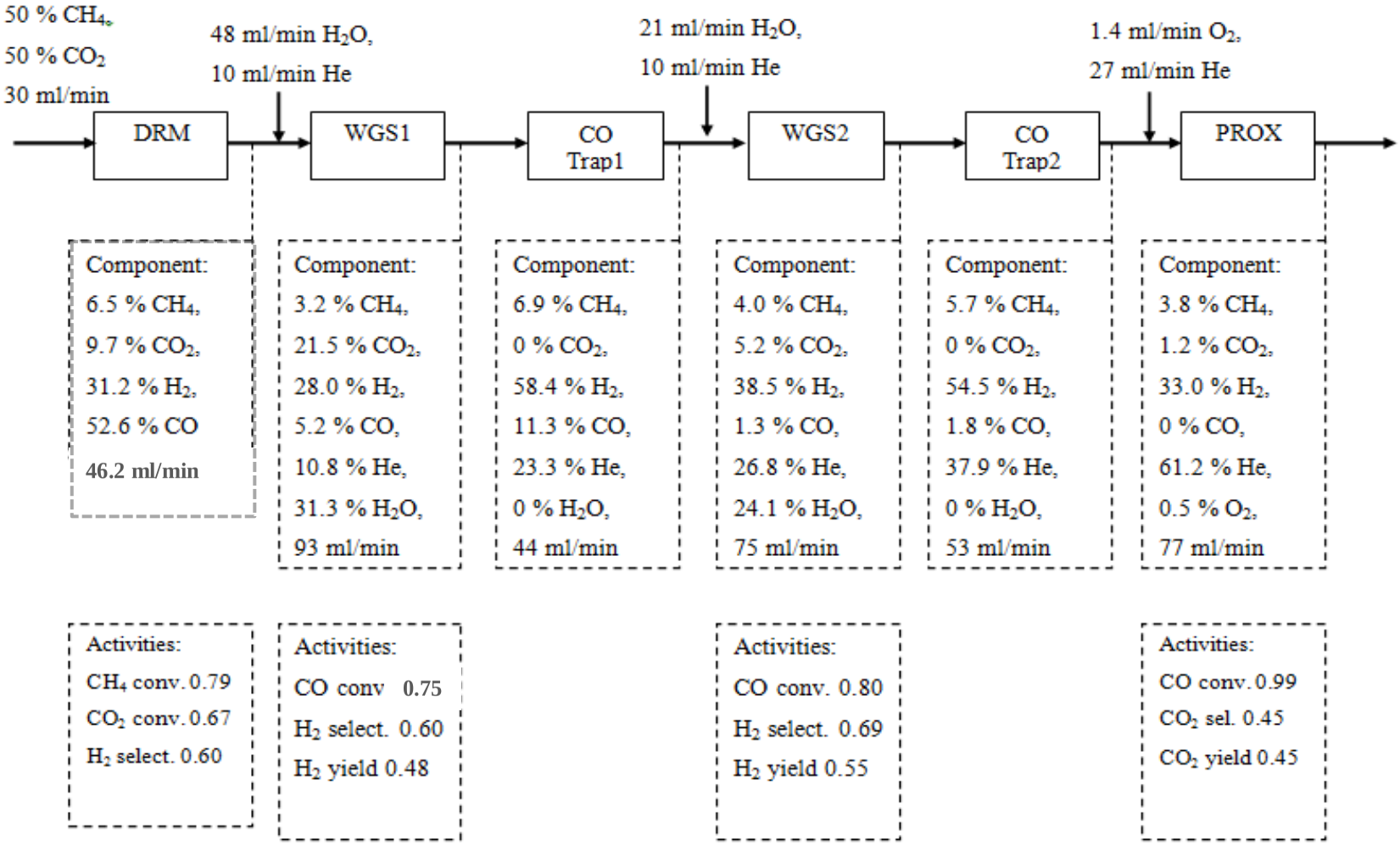

Figure D.2 Overview of overall process in term of feed stream, catalysts activities and output composition

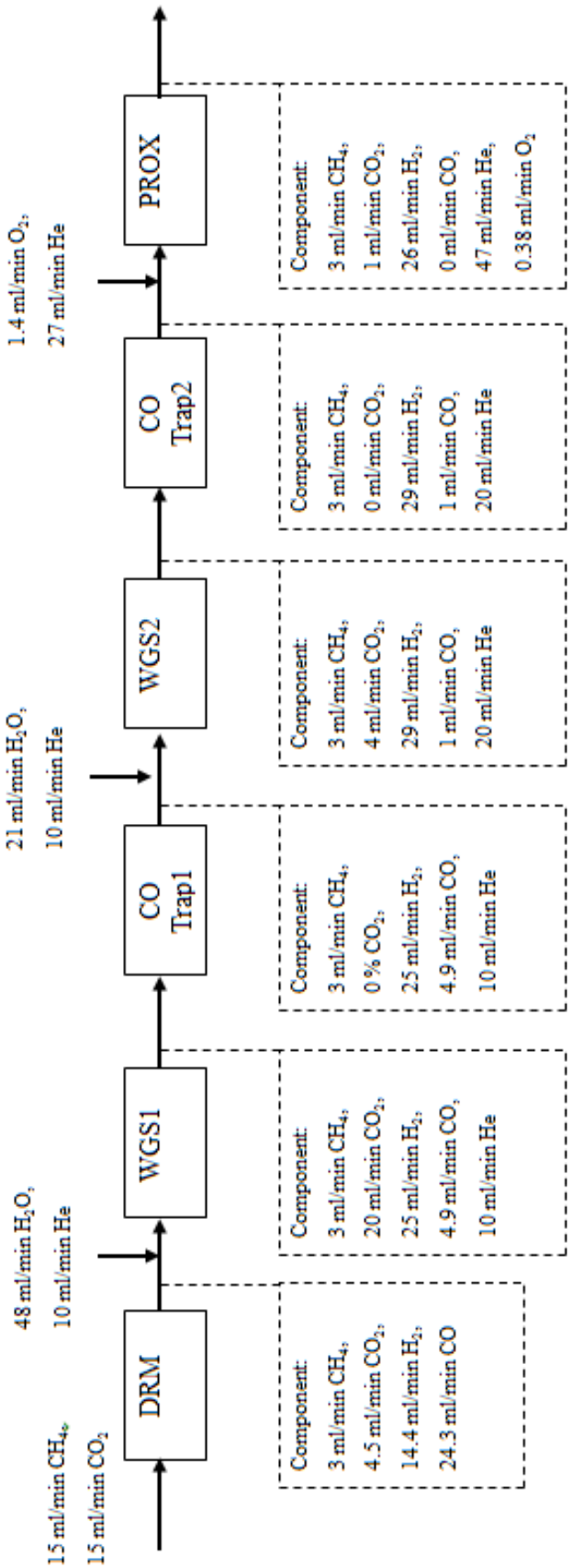

Figure D.3 Overview of overall process of output composition in term of mole balance (ml/min)

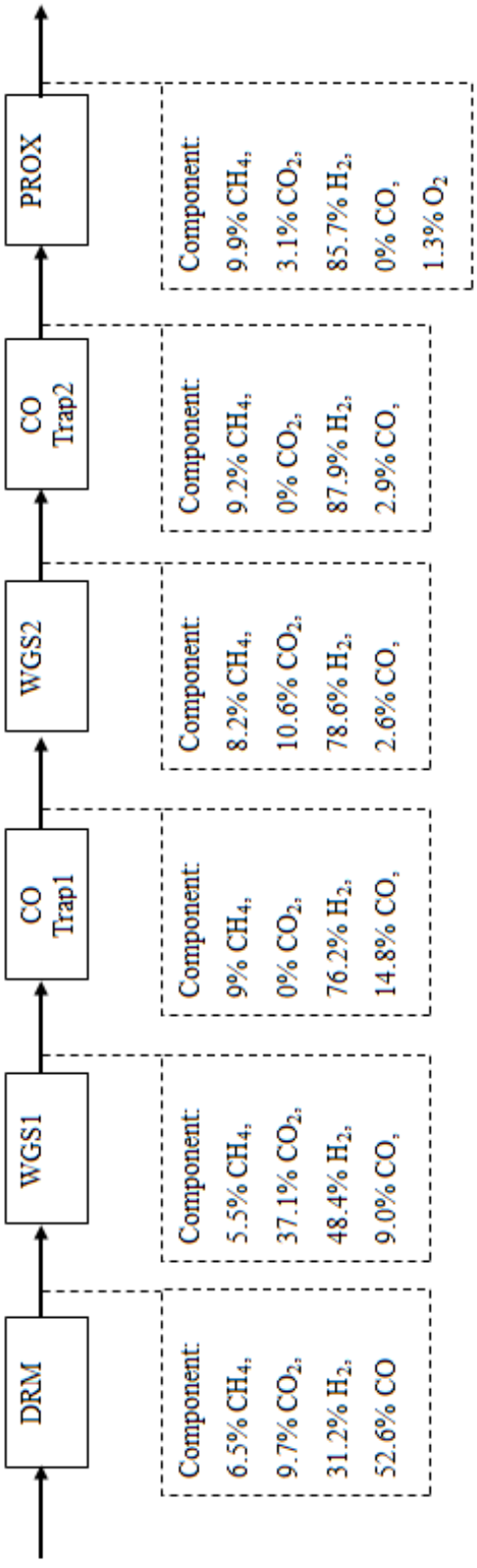

Figure D.4 Overview of overall process in term of output composition without helium component

APPENDIX E

QUANTUM MECHANICAL CHARGE FIELD MOLECULAR DYNAMIC: THE SIMULATION OF SELENATE AND ERBIUM IN AQUEOUS SOLUTION

This part is the study of quantum mechanical charge field (QMCF) in Innsbruck University, Austria. The simulation and interpretation of selenate and erbium ions were studied for further explanation of CO simulation in water which was presented in CHAPTER 5.

E.1 Simulation of selenate ion in aqueous solution

In this study, the structure and dynamics of the selenate ion and its hydration were investigated with regard to molecular vibrations (υ), force constants (f), coordination number distribution (CND) and mean residence times (MRT), comparing these data with those for SO_4^{2-}. This section has been public in Chemical Physics Letters, 2013 (127).

E.1.1 Method

The details of the QMCF MD framework have been published earlier (128). The main improvement of the QMCF approval compared to conventional quantum mechanical/molecular mechanical (QM/MM) MD methods are an increased size of the QM region, which is separated into a core zone and a layer zone. The latter contains only solvent molecules. Thus non-Coulombic interactions between the solute located in the core zone and solvent molecules in the MM region become negligible

and the only potential functions required are for interactions between solvent molecules. A perturbation term in the core Hamiltonian includes all point charges of solvent molecules in the MM region, while the partial charges of all atoms in the QM region are determined via population analysis and applied to calculate the Coulombic interactions with atoms in the MM region. In this work a periodic cubic box contains selenate water molecules in the NVT ensemble. The temperature controlled by the Berendsen algorithm (92) at 298 K was employed. The density was set to that of pure water. The MD time-step was set to 0.2 fs. For the *ab initio* calculations, the 6-31G(d,p) basis sets were chosen for Se, O and H atoms. All QM computations were executed using the GAUSSIAN 09 package (108). The radius of the QM region was set to 7.3 Å, the radius of the core region was 4.6 Å. In this condition the forces between the solute and particles located in the MM region are only determined by population-derived quantum mechanical charges in the QM region and the charges of the BHJ-CF2 (88, 129) model assigned to atoms in the MM region. A smoothing region, adjusting the forces of particles migrating between the QM and MM regions was employed with thickness 0.2 Å. The flexible BJH-CF2 (88, 129) water model also ensures that no abrupt geometrical changes occur during such transitions.

Normally, tetrahedral anions yield four Raman active modes for internal vibration, one of which is IR active (T_2). The correlation length and the window size for the Fourier transformation was set to 500 steps in addition to an applied blackman window, using 500 data in each transformation. The vibrations can also be obtained from *ab initio* gas-phase calculations at Hartree-Fock (HF) level (108, 130, 131). A study of the sulfate anion (128) has used the same framework to investigate the frequencies of vibrations.

E.1.2 Results and Discussions

Figure E.1 displays the variations of the Se–O distance and the O_{se}–Se–O_{se} angle. The distance distribution shows a maximum peak at 1.64 Å with the full width at half-height (fwhh) as 0.06 Å, and the angle distribution peaks at 109° with the fwhh as 9°, in good agreement with experiment (132, 133) as can be seen in Table E.1.

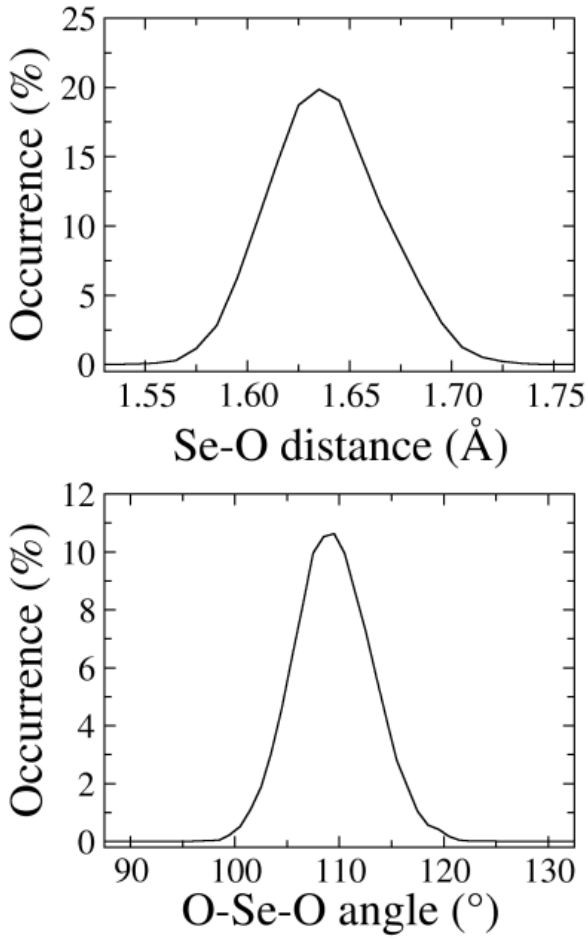

Figure E.1 Variation of Se–O bond length (a) and O–Se–O angle (b) of selenate ion in water obtained from the QMCF MD simulation.

Table E.1 Comparison of intramolecular geometry of SeO_4^{2-}

Method	Se–O distance (Å)	O–Se–O angle (°)
QMCF MD	1.64 ± 0.09	109.0 ± 10
Experiment. (132)	1.64 ± 0.02	109.5 ± 3
Experiment (133)	1.64 ± 0.01	110.0 ± 3

Experimentally, Dammak *et al.* (133) studied the selenate vibrational frequencies of yttrium selenate ($Y_2(SO_4)_3.7H_2O$) prepared by dissolving the respective carbonates in a little excess of selenic acid. Gupta *et al.* (134) studied the selenate frequencies of evaporated dipotassium selenate tellurate which was prepared by the stoichiometric ratio of H_6TeO_6 and K_2SeO_4. Due to composition and concentration of the studied systems, deviation from the simulation data valid for very dilute aqueous solution had to be expected.

The vibrational power spectra for SeO_4^{2-} obtained from the QMCF MD simulation are displayed in Figure E.2. The frequencies of the symmetric stretching $\upsilon_1(A_1)$, the asymmetric stretching $\upsilon_3(T_2)$, the angle bending modes $\upsilon_2(E)$ and $\upsilon_4(T_2)$ modes were located at 902 cm^{-1}, 953 cm^{-1}, 359 cm^{-1} and 440 cm^{-1}, respectively.

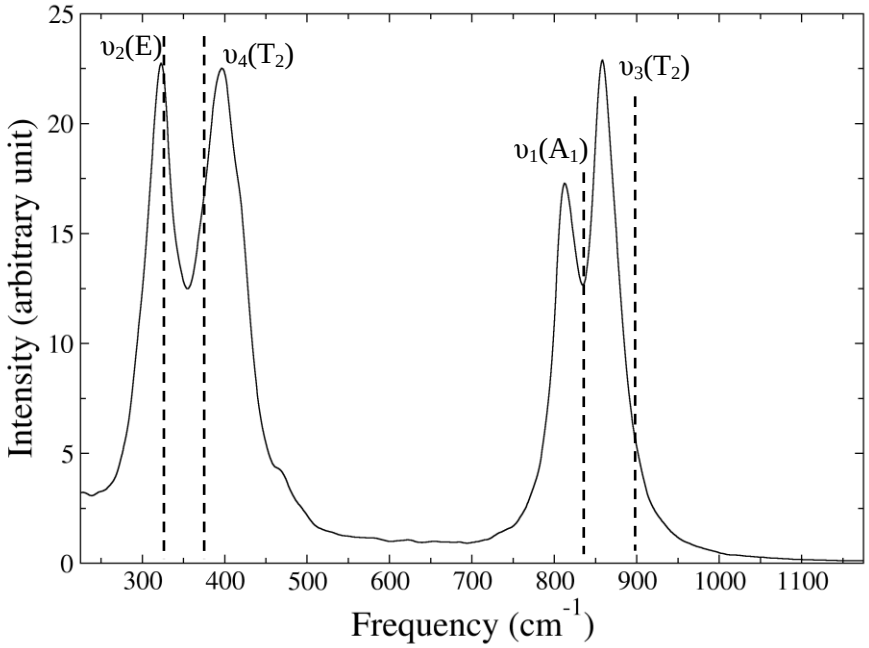

Figure E.2 The power spectrum of Se–O vibration modes $\upsilon_1(A_1)$, $\upsilon_2(E)$, $\upsilon_3(T_2)$ and $\upsilon_4(T_2)$ of T_d symmetry of the selenate ion scaled by the standard factor 0.90 comparing with experimental data (dash peak line)

The original values for all modes of the selenate ion (υ_1, υ_2, υ_3 and υ_4 modes) are higher than the experimental ones, but the application of standard scaling for HF calculated values of 0.90 (131) leads to a quite satisfactory agreement, in particular for υ_2 and υ_4 (812, 323, 858 and 396 cm^{-1}). The vibrational frequencies obtained from QMCF MD and Raman spectroscopy are compared in Table E.2. Moreover, the corresponding force constants are also shown with gas-phase values from *ab initio* calculation and comparison between SO_4^{2-} (135) and SeO_4^{2-} demonstrates weaker bonding of oxygen in the case of selenate.

Table E.2 Vibrational frequencies (cm^{-1}) and force constant of the selenate ion evaluated from the VACFs obtained from the QMCF MD simulation and for gas phase (scaled by f = 0.90), compared to experimental data and sulfate data.

Method	$\upsilon_1(A_1)$	$\upsilon_2(E)$	$\upsilon_3(T_2)$	$\upsilon_4(T_2)$	Force con. (mDyn/Å)
SeO_4^{2-}					
QMCF	812	323	858	369	5.16
Gas phase	824	332	890	430	5.32
Exp. $Y_2(SeO_4)_3 \bullet 7H_2O$ (132)	835	325	890	376	5.36
Exp. $K_2SeO_4 \bullet Te(OH)_6$ (133)	836	330	894	400	5.37
SO_4^{2-}					
QMCF (128)	968	454	1118	635	5.89
Gas phase	923	422	1093	601	5.36
Exp. SO_4^{2-} in hydrotalcite (134)	981	451	1104	613	6.05

Figure E.3 shows water molecules in hydration shell and bulk. The intramolecular geometry in terms of O–H distance and H–O–H angle distribution predicts most probable values in the hydration shell of 0.96 Å with fwhh of 0.07 Å which is only slightly different compared to bulk water (0.97 Å with fwhh of 0.06 Å). The HOH angle of 105° with fwhh of 14° is marginally larger than for water in bulk (101° with the fwhh of 11°). The shortened distance and the widened angle in the first hydration shell indicate the influence of the selenate ion on nearest neighbor water molecules by hydrogen bonding similar to a previous study of SO_4^{2-} in water (128).

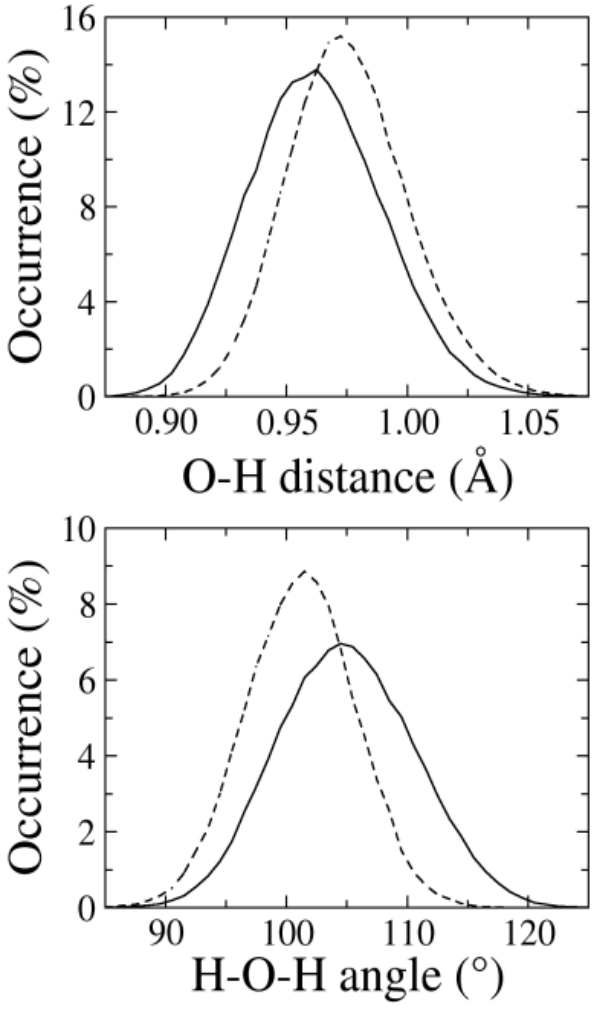

Figure E.3 Distributions of the O–H bond length (a) and H–O–H angle (b) of water molecules in the hydration shell (solid line) and bulk (dashed line) of selenate ion

Figure E.4 presents the charge variations of each atom of selenate during the simulation time of 8 ps. The charge of the selenium atom fluctuates between 1.95 and 2.10 while the charges of the oxygen atoms fluctuate between -1.00 and -0.85. The average charge of selenium is 2.02 and that of oxygen -0.91. The total charge of the selenate ion is, therefore, -1.63, and thus considerably different from the formal value of -2.0 resulting from charge transfer between water molecules in the first shell hydrogen bonded to selenium oxygens (48). Table E.3 shows the comparing of the charge between aqueous SeO_4^{2-} and SO_4^{2-}, that sulfate is more strongly polarized than selenate. This finding is in contrast to the gas phase values, which can be attributed to

the stronger ion–water interaction of SO_4^{2-}. This can be seen as another factor determining the ease of redox processes in case of SeO_4^{2-}.

Table E.3 Charge of atoms of selenate ion and sulfate ion in water compared with gas phase values.

	Charge						
	Se, S	O_1	O_2	O_3	O_4	O_{avg}	total
SeO_4^{2-}							
QMCF	2.02	-0.92	-0.91	-0.91	-0.91	-0.91	-1.63
Gas phase	1.81	-0.95	-0.95	-0.95	-0.95	-0.95	-2.00
SO_4^{2-} (128)							
QMCF	2.12	-0.97	-1.00	-0.99	-0.98	-0.98	-1.82
Gas phase	1.50	-0.87	-0.88	-0.87	-0.88	-0.87	-2.00

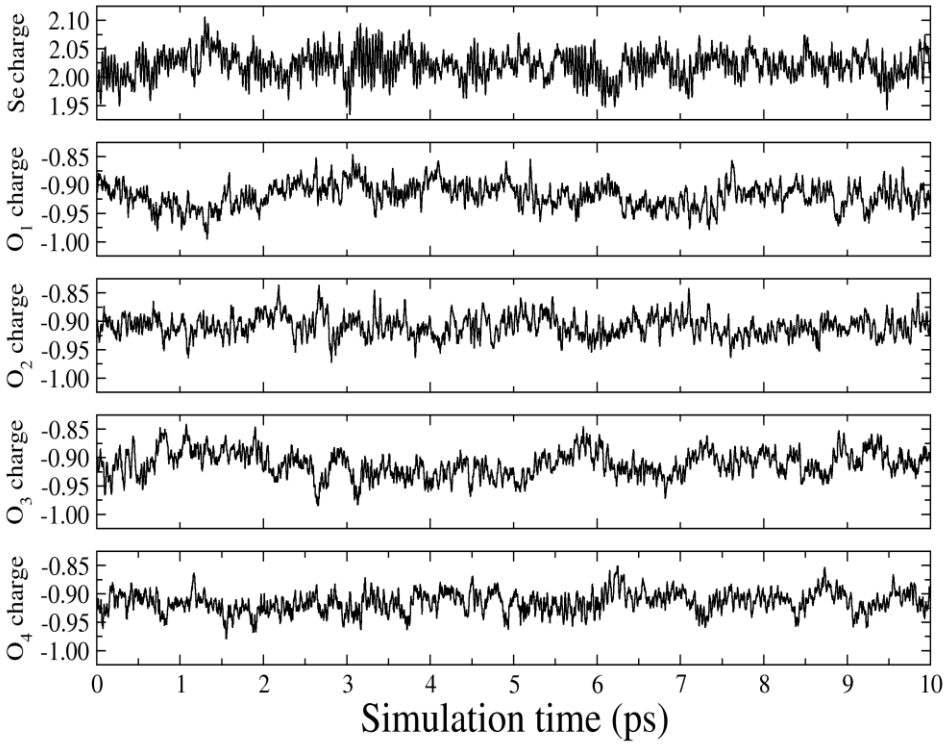

Figure E.4 Time series of the atomic partial charges obtained from the QMCF MD simulations

The radial distribution functions (RDFs) for Se–O_{water} and O_{se}–H_{water} are shown in Figure E.5. The O_{se}–H_{water} RDF indicates hydrogen bonding to the O_{se} atoms of selenate ion with a peak between 1.5 Å and 2.65 Å, having a mean bond distance of 1.9 Å. Integration of this peak yields an average coordination number of each oxygen atom of 2.8, i.e. each O_{se} atom forms approximately three hydrogen bonds to the first shell. The Se–O_{water} RDF clearly displays the first hydration shell, while a second shell cannot be observed. The Se–O_{water} RDF shape represents a flexible first hydration shell with its maximum located at 4.9 Å. The minimum between the first shell and bulk is far from the baseline, indicating frequent ligand exchanges in the hydration shell. Integration of the Se–O_{water} RDF determines an average coordination number of 12.8 for the first shell, close to the value resulting from the O_{se}–H RDFs together, namely 11.2. Apparently, H-bonding is by far dominating the hydration shell formation.

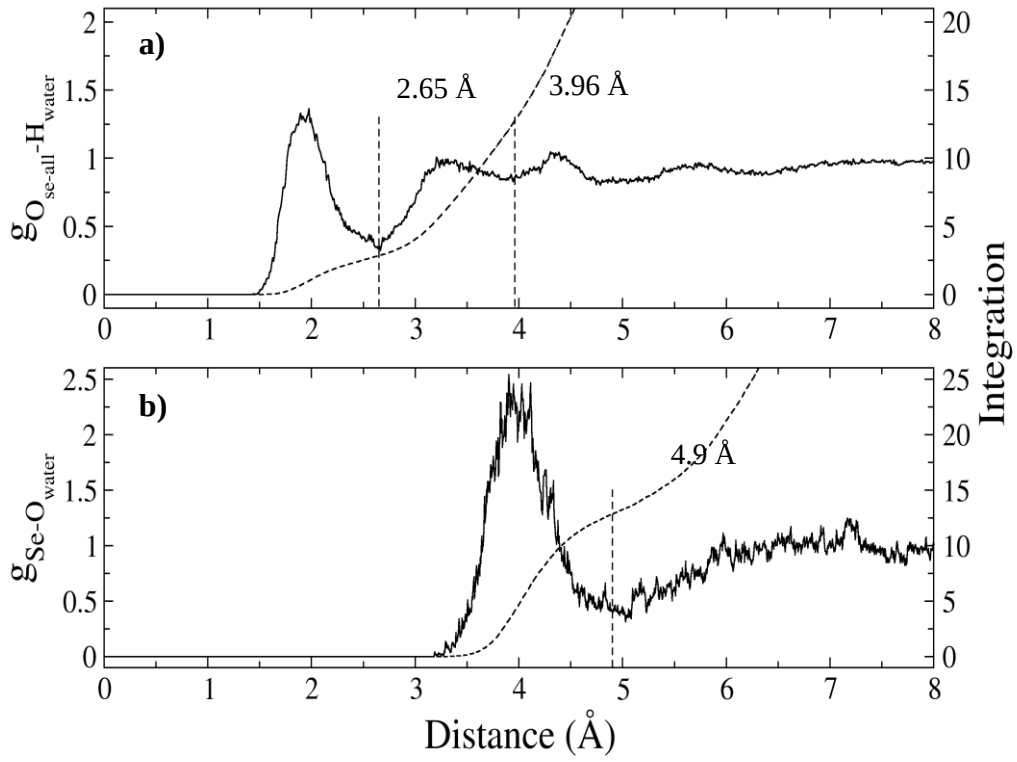

Figure E.5 Radial distribution of (a) O_{se}–H_{water} and (b) Se–O_{water} of selenate ion in aqueous solution

The coordination number distribution (CND) plot of selenate oxygen with regard to water hydrogen (O_{se}–H_{water}) is displayed in Figure E.6. The CND varies from 1 to 5 per oxygen atom, showing a maximum of three occurring with percent probability of 52 followed by coordination numbers 2, 4, 1, and 5 occurring (probabilities of 27, 16, 3, and 2 percent), respectively. The coordination number distribution of O_{water} around Se in the first shell is shown in figure 6b, varying from 10 to 16, with percent probabilities of 0.5, 12, 25, 37, 20, 5 and 0.5, thus 13 being the most populated coordination number. These results also confirm rapid ligand migration between the solvation shell and bulk.

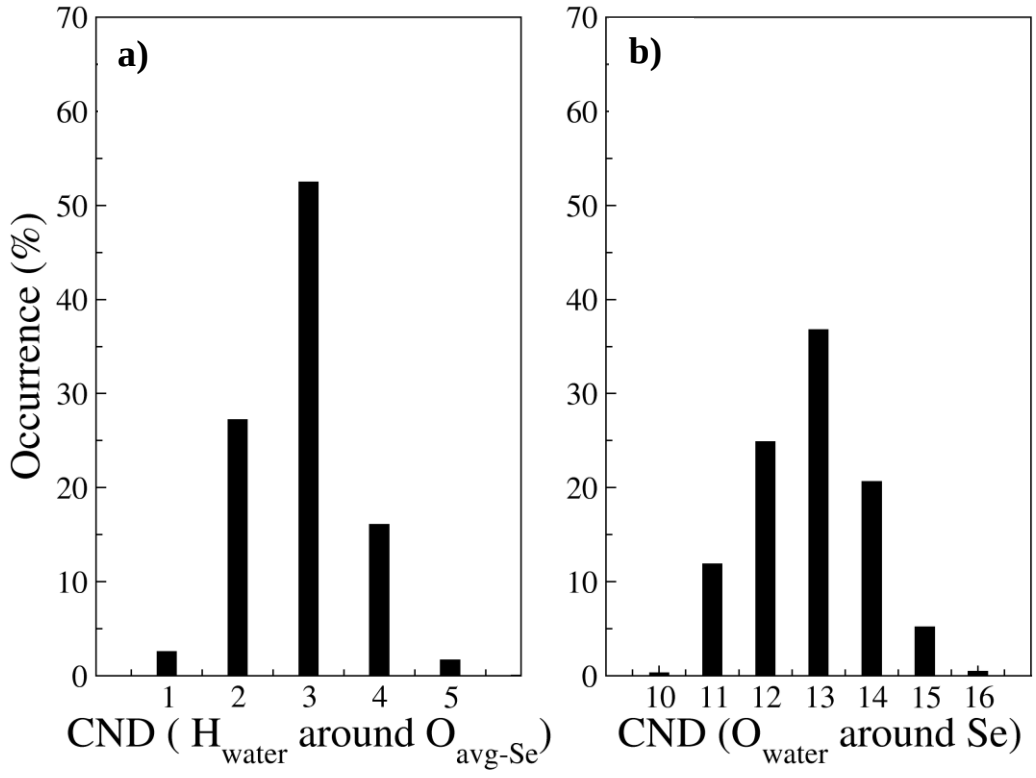

Figure E.6 Comparison of coordination numbers for (a) $O_{avg,Se}$–H_{water} per oxygen and (b) Se–O_{water} of selenate ion in the first shell

These water exchange processes between first shell and bulk were further characterized by mean residence times (MRT) of water molecules. The MRT was calculated by the direct method (128), from the average number of water molecules in the hydration shell and the number of exchange phenomenon for two time parameters (128) τ^* set to 0.0 and 0.5 ps, respectively. The R_{ex} value is the average number of attempts needed for one successful ligand exchange process.

Table E.4 shows coordination number averages (CN_{avg}), mean residence times (MRT) and R_{ex} comparing SeO_4^{2-} with SO_4^{2-} and pure water. The CN_{avg} of SeO_4^{2-}, as 12.8, is slightly higher than that of SO_4^{2-}, corresponding to the larger bond distance of Se–O than S–O (average $Se–O_{water}$ distance = 4.0 Å, $S–O_{water}$ distance = 3.8 Å (128)). The MRT values—also related to hydrogen bond lifetime—in the first hydration shell of SeO_4^{2-} and SO_4^{2-} are similar (MRT of SeO_4^{2-} = 3.05 ps, MRT of SO_4^{2-} = 2.57 ps (128)) and significantly higher than that of pure water (1.7 ps (90, 136)). The number of attempts needed for successful exchange (R_{ex}) of SeO_4^{2-} of 3.7 is half the R_{ex} value of SO_4^{2-} (R_{ex} of SO_4^{2-} = 7.4). This data means that three to four attempts to move water in or out around selenate's first shell are required to achieve a successful exchange process while seven to eight attempts are needed in case of SO_4^{2-}. This implies ligand transition processes are easier and smoother at the larger selenate ion. From the comparison with the value for pure water the selenate ion can be classified as a structure making ion even slightly stronger than sulfate (128).

Table E.4 Average coordination number (CN), mean residence times (MRT) and R_{ex} obtained by QMCF MD simulation

	CN_{avg}	MRT (ps)	R_{ex}
SeO_4^{2-}	12.8	3.05	3.7
SO_4^{2-} (128)	11.1	2.57	7.4
Water (90)	-	1.7	11.2

E.1.3 Conclusion

The quantum mechanical charge field (QMCF) molecular dynamic simulation of the selenate ion in water delivered data close to experimental ones,

where available. Water molecules in the first hydration shell show significant differences from bulk characterizing a distinct, but flexible hydration shell based on hydrogen bonding in average approx three water molecules per O_{se}. The total first shell consists of 11 to 12 water molecules. The mean residence times (MRT) of a water ligand attached to SeO_4^{2-} is 3.05 ps, which classifies the ion as a structure-maker. A further improvement of these data can only be expected from an analogous simulation using a correlated *ab initio* method for the QM region, which is currently still beyond computational facility limits.

E.2 Simulation of erbium ion in aqueous solution

The erbium simulation in this part is the part of "Erbium(III) in aqueous solution: an *ab initio* molecular dynamics study" which public in Journal of Physical Chemistry B, 2013 (81). This work studied an erbium ion in ground state which presented some structural and dynamical properties.

E.2.1 Method and Simulation protocol

The primary study of $[Er(H_2O)_n]^{3+}$ (n= 1, 2, 3, 4, 6, 8, 9) for study the suitable method—such as HF, MP2 and CCSD—were calculated by GAUSSIAN09 software package (108). The results of distance of Er–O bond length and also binding energies per water ligand in each method were considered to decision method for appropriated QMCF MD simulation.

QMCF MD simulation used the cubic with 31.2 Å length and a thousand of water molecule with one molecule of erbium ion. An equilibrium state was running at 3 ps, after that heated up to 798 K, then cooled down to 298 K, and re-equilibrated at 3 ps before sampling the data. The factors of this simulation were canonical ensemble (NVT) system for calculation and time steps setting at 0.2 fs. The Berendsen algorithm was a function to control the temperature with relaxation time as 0.1 ps (92). Density of the system was 0.997 g/cm^3 and reaction field method (33) were used for calculation of long-range electrostatic interaction (epsilon = 78.35 and Coulombic cutoff = 15.0). The core radius was setup at 3.3 Å and the layer zone was

3.3 Å to 5.7 Å with smoothing at 5.5 Å to 5.7 Å. For water molecules in simulation used flexible BJH-CF2 model which can be moved between QM and MM regions. Turbomole software package (93) was selected to calculate quantum results. Partial charge in QM region would be evaluated from mullike population which applied to BJH-CF2 model of water molecules. The basis set of erbium(III) was Stuttgart ECP basis set (137) and water molecules used DZP-dunning basis set. The data were collected every 5 step until the total sampling time of 10 ps.

E.2.2 Results and Discussion

Table E.5 presents the comparison of Er^{3+}–O distance and binding energy per in each method including HF, MP2 and CCSD. It can be seen that each method had a same trend. Increasing of water ligand around erbium presented more distance between Er and O while it showed the decreasing of binding energy. Considering the same number of water ligand found that HF gave the lowest energy than MP2 and CCSD, respectively; but, it did not show too difference which can be concluded that no significant difference. Moreover, the significant useful of HF method showed the lowest computational time for simulation. It can be concluded that HF method appropriated to calculation in QMCF MD because of accuracy, time- and cost-saving. Moreover, the numbers of water ligand shows 8 or 9 water surrounded erbium were more stable which presented lowest energy.

Table E.5 Binding energies per water ligand in kcal/mol of $[Er(H_2O)_n]^{3+}$ at HF, MP2 and CCSD methods.

n	HF	MP2	CCSD	%Diff MP2	%Diff CCSD
1	-100	-105	-107	4.3	6.5
2	-94	-98	-101	4.5	7.8
3	-89	-93	-	4.8	-
4	-83	-71	-	14.4	-
6	-65	-70	-	9.1	-
8	-60	-61	-	1.7	-
9	-62	-65	-	5.9	-

Figure E.7 represents the dynamics of water ligand as the distance between Er^{3+} and O at 10 ps. It can be seen that, normally, the Er had 8-waters ligand as the 1st shell with 3.6 Å from the center (Er). But in around times at 2.5 ps and 6 ps, the exchange of ligand was happened (as associative exchange type) to become 9-water ligand a few moment and got the same back to 8-water ligand. From the result, the Er^{3+} can contain 8- or 9-water ligand; however, a 8-water ligand was a more stable than a 9-water ligand because one exceed water was moved out from the 1st shell to 2nd shell.

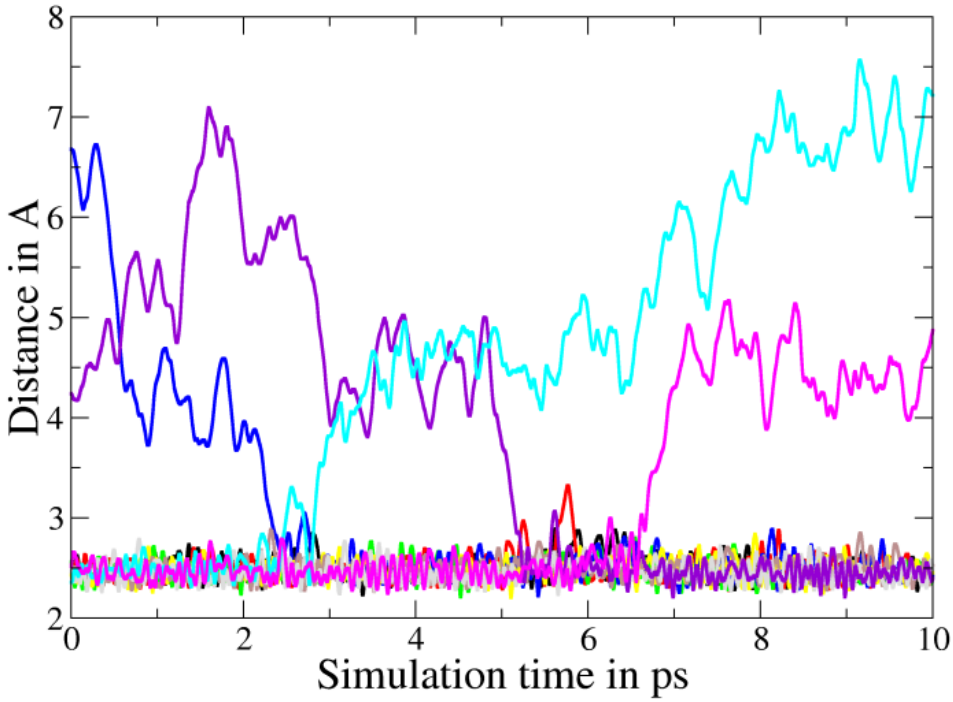

Figure E.7 Dynamics of ion–ligand distance plot from 10 ps trajectory

Figure E.8 shows coordination number distribution (CND) of 1st shell and 2nd shell of Er with water ligand. The average of water ligand in 1st shell and 2nd shell was 8.2241 and 20.8379, respectively. In 1st shell, it found that CND had 8 and 9 water ligand as 79% and 21% by occurrence, respectively. It can be said that 8-water ligand was stable than 9-water ligand. This result confirmed the dynamic of distance of Er^{3+}–O in Figure E.7

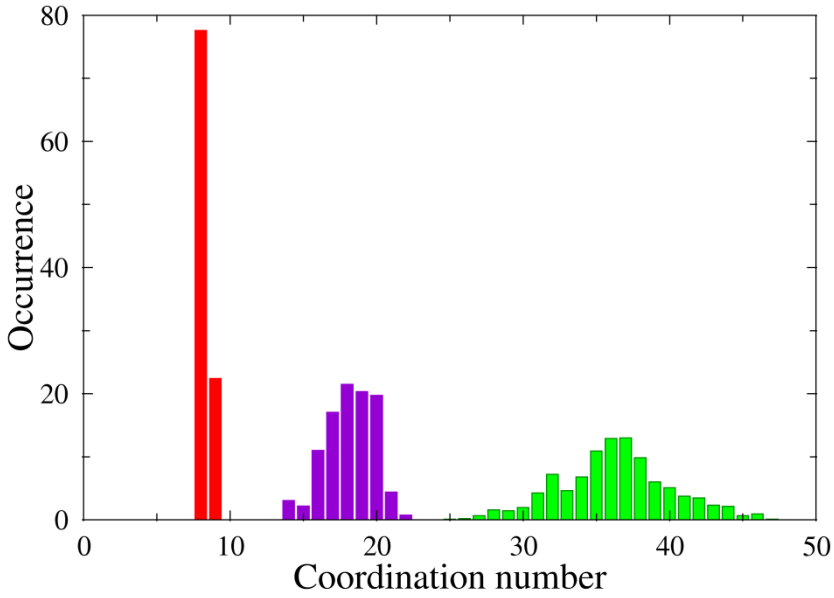

Figure E.8 Coordination number distributions for first, second and third hydration shell of Er for 10 ps

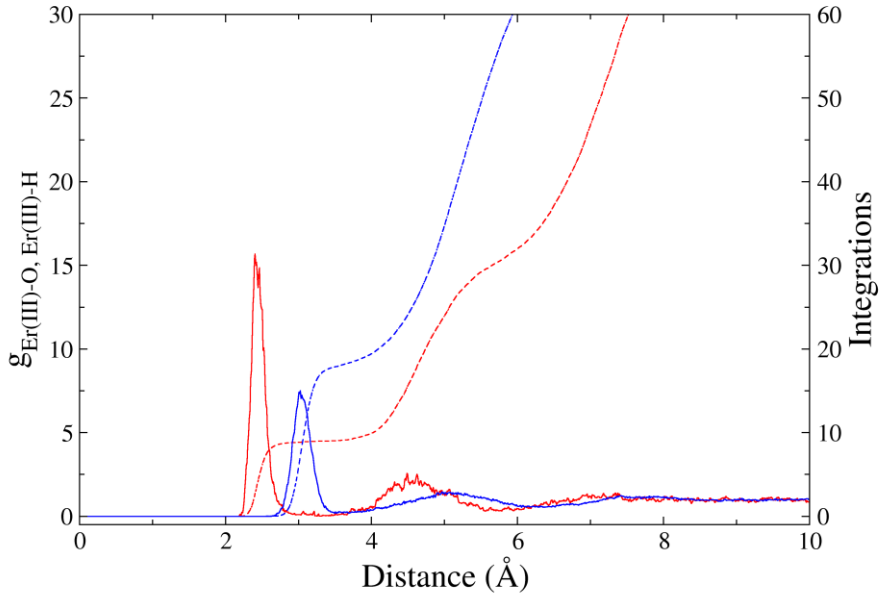

Figure E.9 The radial distribution functions and corresponding integrations of Er–O (solid line) and Er–H (dashed line) obtained from QMCF MD simulation

Figure E.9 represents radial distribution function (RDF) of erbium oxygen and erbium hydrogen and their integrations. Considering erbium oxygen RDF found 2 maximum peaks at 2.45 Å and 4.7 Å. That means this result can observe 1st and 2nd shell whereas 3rd and 4th shell cannot observe the major peak in this range. However, the 3rd and 4th shell can identify by local density corrected three-body distribution which present in Figure E.10. The results confirmed that there presented almost the same with water bulk density: therefore, it can be said that erbium are only significant effect to the 1st and 2nd shell.

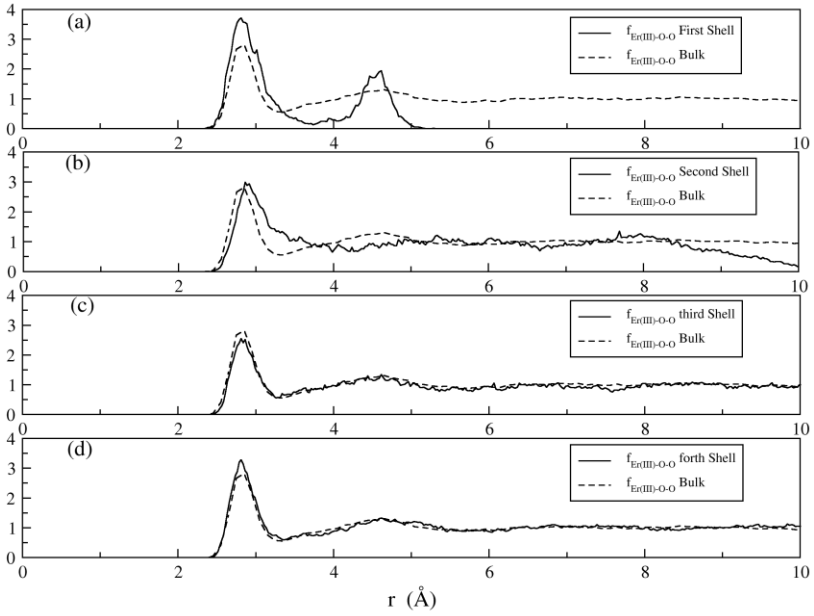

Figure E.10 Local density corrected three-body distributions for first (a), second (b), third (c) and fourth (d) shell of Er^{3+} compared with bulk water

Figure E.11 shows angel distribution function (ADF) of 1st shell of water ligand comparing with tricapped trigonal prism, square antiprism and dodecahedron. The graphs appeared board peaks because water ligands vibrated and fluctuated around themselves. Figure E.11(a) shows ADF of 8-water ligand which represents the peaks as same position as a square antiprism. On the other hand, Figure E.11(b) shows ADF of 9-water ligand which was represented that the peaks position similarly

appeared as tri-capped trigonal prism more than other structure. From this graph, it can be implied that the structure of erbium with water ligand can be changed between square antiprism and tricapped trigonal prism.

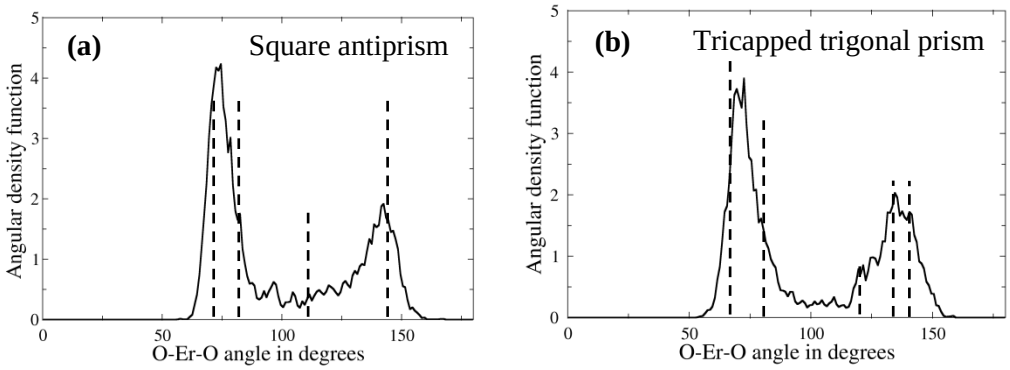

Figure E.11 The angular distribution function (ADF) of Er^{3+} in solution overlaid by peaks for ideal coordination polyhedral: (a) 8-ligand in a square antiprism and (b) 9-ligands in a tricapped trigonal prism

Comparison of QMCF MD simulation of other ions in the lanthanide group in water such as La (138) and Ce (139) were shown in Table E.6. It can be observed that the mean residence time (MRT) and R_{ex} value of erbium on 1^{st} shell were 20.6 ps and 1.0, respectively, while 2^{nd} shell were 3.0 ps and 5.4. The coordination ligand number distribution of La, Ce and Er were 9.5, 9.1 and 8.2, respectively. It shows the trend of decreasing water ligand when increasing molecular weight. It can be suggested that increasing of molecular weight in the same series made a smaller atom size promoting lower average of coordination number. The wave number and force constant of ion-oxygen bond are shown in ผิดพลาด! ไม่พบแหล่งการอ้างอิง. he erbium presented the stretching frequency equal 315 cm^{-1} which can be agreed with Kanno and Hiraishi who reported frequency of lanthanide series (140). The force constant of La, Ce and Er were similar value as 110 N/m^{-1}, 106 N/m and 85 N/m, respectively. It can be implied that the force constant of ion-oxygen bond was related to ability of exchange water ligand.

Table E.6 Mean residence times ($\tau^{0.5}$), coordination number and R_{ex} values of 1st and 2nd shell, frequency (Q_{ion}) and force constants ($k_{ion–O}$) of some element in lanthanide series obtained from QMCF MD simulation

Ion	$\tau_1^{0.5}$ (ps)	$\tau_2^{0.5}$ (ps)	CN_1	CN_2	$R_{ex,1}$	$R_{ex,2}$	Q_{ion} (cm^{-1})	$k_{ion–O}$ (N/m)
La (138)	16.6	2.3	9.5	25.6	2.4	2.3	360	110
Ce (139)	>118	2.6	9.1	21.4	30	5.5	354	106
$Er_{this\ work}$	20.6	3.0	8.4	18.23	1	5.4	315	85

E.2.3 Conclusion

The quantum mechanical charge field (QMCF) molecular dynamic simulation of the hydrated erbium ion has an interesting data. Any methods (HF, MP2 and CCSD) were not too different, so the HF was selected to calculate because of time saving. The structures of hydrated erbium presented the square antiprism or tricapped trigonal prism which depended on the number of 8 water ligands or 9 water ligands. The forces constant value of La, Ce and Er were more closely which is a probable reason that La, Ce and Er showed similar phenomenon as exchange ligand. Furthemore, the frequency of Er presented the same trend with lanthanide series reported by Kanno and Hiraishi (140). However, this simulation used ground state of Er, the exited state of it must be studied.

VITA

Mr. Theerathad Sakwarathorn was born on October 11, 1984 in Ratchaburi, Thailand. He finished the Bachelor's Degree and Master Degree at Department of Chemical Technology, Faculty of Science, Chulalongkorn University in 2007 and 2009, respectively. He has received a scholarship from The Royal Golden Jubilee Ph.D. Program to study the Philosophy of Science in Chemical Technology at Chulalongkorn University. He had spent eight months research at Institute of General, Inorganic and Theoretical Chemistry, University of Innsbruck, Austria during his Ph.D. program.